frontiers | Research Topics

Functional materials with charge transfer properties and their application in photoelectric devices

Edited by
Meng Zheng, Teresa Gatti, Yue Liu and Yongtao Qu

Published in
Frontiers in Chemistry

ISSN 1664-8714
ISBN 978-2-83250-986-9
DOI 10.3389/978-2-83250-986-9

About Frontiers

Frontiers is more than just an open access publisher of scholarly articles: it is a pioneering approach to the world of academia, radically improving the way scholarly research is managed. The grand vision of Frontiers is a world where all people have an equal opportunity to seek, share and generate knowledge. Frontiers provides immediate and permanent online open access to all its publications, but this alone is not enough to realize our grand goals.

Frontiers journal series

The Frontiers journal series is a multi-tier and interdisciplinary set of open-access, online journals, promising a paradigm shift from the current review, selection and dissemination processes in academic publishing. All Frontiers journals are driven by researchers for researchers; therefore, they constitute a service to the scholarly community. At the same time, the *Frontiers journal series* operates on a revolutionary invention, the tiered publishing system, initially addressing specific communities of scholars, and gradually climbing up to broader public understanding, thus serving the interests of the lay society, too.

Dedication to quality

Each Frontiers article is a landmark of the highest quality, thanks to genuinely collaborative interactions between authors and review editors, who include some of the world's best academicians. Research must be certified by peers before entering a stream of knowledge that may eventually reach the public - and shape society; therefore, Frontiers only applies the most rigorous and unbiased reviews. Frontiers revolutionizes research publishing by freely delivering the most outstanding research, evaluated with no bias from both the academic and social point of view. By applying the most advanced information technologies, Frontiers is catapulting scholarly publishing into a new generation.

What are Frontiers Research Topics?

Frontiers Research Topics are very popular trademarks of the *Frontiers journals series*: they are collections of at least ten articles, all centered on a particular subject. With their unique mix of varied contributions from Original Research to Review Articles, Frontiers Research Topics unify the most influential researchers, the latest key findings and historical advances in a hot research area.

Find out more on how to host your own Frontiers Research Topic or contribute to one as an author by contacting the Frontiers editorial office: frontiersin.org/about/contact

Functional materials with charge transfer properties and their application in photoelectric devices

Topic editors

Meng Zheng — Qingdao Haiwan Science and Technology Industry Research Institute Co., Ltd, China

Teresa Gatti — University of Giessen, Germany

Yue Liu — Liaoning Technical University, China

Yongtao Qu — Northumbria University, United Kingdom

Citation

Zheng, M., Gatti, T., Liu, Y., Qu, Y., eds. (2022). *Functional materials with charge transfer properties and their application in photoelectric devices*. Lausanne: Frontiers Media SA. doi: 10.3389/978-2-83250-986-9

Table of contents

frontiers | Frontiers in Chemistry

TYPE Editorial
PUBLISHED 23 November 2022
DOI 10.3389/fchem.2022.1094264

OPEN ACCESS

EDITED AND REVIEWED BY
Nosang Vincent Myung,
University of Notre Dame, United States

*CORRESPONDENCE
Meng Zheng,
zhengmeng.555@hotmail.com

SPECIALTY SECTION
This article was submitted to Electrochemistry, a section of the journal Frontiers in Chemistry

RECEIVED 09 November 2022
ACCEPTED 14 November 2022
PUBLISHED 23 November 2022

CITATION
Zheng M, Gatti T, Liu Y and Qu Y (2022), Editorial: Functional materials with charge transfer properties and their application in photoelectric devices. *Front. Chem.* 10:1094264. doi: 10.3389/fchem.2022.1094264

Editorial: Functional materials with charge transfer properties and their application in photoelectric devices

Meng Zheng[1]*, Teresa Gatti[2,3], Yue Liu[4] and Yongtao Qu[5]

[1]R&D Center of Polymer Materials, Qingdao Haiwan Science and Technology Industry Research Institute Co., Ltd. (HWSTI), Qingdao Haiwan Chemistry Co., Ltd. (QHCC), Qingdao, China, [2]Institute of Physical Chemistry, Justus Liebig University, Giessen, Germany, [3]Center for Materials Research, Justus Liebig University, Giessen, Germany, [4]College of Material Science Engineer, Liaoning Technical University, Fuxin, China, [5]Department of Mathematics, Physics and Electrical Engineering, Northumbria University, Newcastle Upon Tyne, United Kingdom

KEYWORDS

charge transfer properties, structure-property relationships, applications, photoelectric devices, device performance

Editorial on the Research Topic
Functional materials with charge transfer properties and their application in photoelectric devices

Introduction

Charge transfer is an extensively studied issue as this property enables molecular components to manipulate and tune the properties of materials. This is achieved through a systematic variation of the molecular components, which allow for a molecular-level control of the structural-property *via* an arrangement of the functional molecular components into a defined architecture by charge generation and extraction.

In our topic "*Functional Materials with Charge Transfer Properties and Their Application in Photoelectric Devices*", we received 14 interesting articles which concerned more on perspectives and new developments of functional material with charge transfer properties, leading to good performance in different type of devices, such as fluorescence sensor, organic field effect transistors, solar cells, lithium storage, nanocomposite supercapacitor, etc. Strategies of molecular design and simulation to improve device performance were also discussed in this topic as well as some extensive research work relating to charge transfer properties.

Charge transfer properties and device applications

Hou et al. reviewed the application of biological sensing based on dicyanomethylene-4H-pyran (DCM) derivatives with intramolecular charge transfer (ICT) properties. The luminescence mechanism of DCM probes mainly depends on the ICT properties. By regulating the ICT process, the DCM probes have been constructed to detect the ions, reactive oxygen species (ROS), and biological macromolecules in cells. DCM derivatives modified with fluorescence-quenching group have shown typical off–on characteristics.

Meanwhile, Cai et al. designed and synthesized DCM-based derivatives, enable to fluorescence enhancement in solid state for visualization of latent fingerprints (LFP). In this study, the authors prepared DCM derivatives with strong emission in solid state by introducing Boc group, which provides strategies for the fluorescence enhancement of aggregation-caused quenching dyes in solid state. LFP fluorescent developers were prepared by blending Boc-PZ-DCM with montmorillonite (MMT). It showed that LFP can be clearly developed by dusting method with 3% dye content Boc-PZ-DCM/MMT developer. Boc-PZ-DCM/MMT developer for LFP reduced the content of fluorescent materials to 3%, greatly reducing the consumption of fluorescent materials and increasing the safety of LFP fluorescent developer.

Zhang et al. designed a pyrrolopyrrole-based aza-BODIPY (PPAB) small molecule for organic field-effect transistors based on thiophene-substituted diketopyrrolopyrrole (DPP). Due to large conjugated molecular skeleton, the PPAB units exhibited a broad absorption range in the visible and near-infrared regions, which enable it to be a new chromophore with electron-deficient ability. The OFETs constructed by PPAB as the semiconductor layer present a clear p-type behavior with a maximum electron mobility of 1.5×10^{-3} $cm^2 V^{-1} s^{-1}$, indicating that PPAB is a promising electron-deficient chromophore to construct semiconductors for OFETs.

Another application of OFETs based on small molecular design was taken by Dai et al. A novel alternating donor–acceptor polymer PQ1 is designed and synthesized by palladium-catalyzed Stille coupling. Polymer PQ1 presents not only a strong intramolecular charge transfer effect, but also a narrow electrochemical band gap and a high highest occupied molecular orbital (HOMO) energy level. The optical absorption study indicates that the PQ1 film exhibits good aggregation, which is an advantage for the charge transport between neighboring molecules. PQ1 presents p-type semiconductor properties with a high hole mobility of up to 0.12 $cm^2 V^{-1} s^{-1}$.

Campbell et al. created routes to increase performance for antimony selenide solar cells using inorganic hole transport layers. In this work, solar cell capacitance simulator (SCAPS) is used to interpret the effect of hole transport layers (HTL), they demonstrated the critical role of NiO and MoO_x in altering the energy band alignment and increasing device performance by the introduction of a high energy barrier to electrons at the rear absorber/metal interface. CSS-based Sb_2Se_3 solar cells with NiO HTL showed average improvements in open circuit voltage, short circuit current density and power conversion efficiency of 12%, 41%, and 42%, respectively, over the standard devices. Similarly, using a NiO HTL in TE-based Sb_2Se_3 devices improved open circuit voltage, short circuit current density and power conversion efficiency by 39%, 68%, and 92%, respectively.

Yang et al. reported a flexible Asymmetric organic-inorganic composite solid-state electrolyte based on PI membrane for solid-state Lithium metal batteries. This lightweight solid electrolyte is stable at a high temperature of 150°C and exhibits a wide electrochemical window of more than 6 V. Furthermore, the high ionic conductivity of the flexible solid electrolyte was 7.3×10^{-7} S/cm. The solid-state batteries assembled with this flexible asymmetric organic-inorganic composite solid electrolyte exhibit excellent performance at ambient temperature.

Wang et al. designed one kinds of Co_3O_4-doped $Li_4Ti_5O_{12}$ (LTO) composites by the hydrothermal reduction and metal doping modification method. The $Li_4Ti_5O_{12}$ particles attached to lamellar Co_3O_4 constituted a heterostructure and Co ion doped into $Li_4Ti_5O_{12}$ lattice. This Co ion-doped microstructure improved the charge transportability of $Li_4Ti_5O_{12}$ and inhibited the gas evolution behavior of $Li_4Ti_5O_{12}$, which enhanced the lithium storage performance. It had an excellent rate performance and long cycle stability, in which the capacity reached 174.6 mA h/g, 2.2 times higher than that of $Li_4Ti_5O_{12}$ at 5 A/g.

Xu et al. designed a Nano-petal nickel hydroxide on multilayered modified montmorillonite (M-MMT) using one-step hydrothermal method. This nano-petal multilayered nanostructure dominated the ion diffusion path to be shorted and the higher charge transport ability, which caused the higher specific capacitance. The results showed that in the three-electrode system, the specific capacitance of the nanocomposite with 4% M-MMT reached 1068 F/g at 1 A/g and the capacity retention rate was 70.2% after 1,000 cycles at 10 A/g, which was much higher than that of pure $Ni(OH)_2$ (824 F/g at 1 A/g), indicating that the $Ni(OH)_2$/M-MMT nanocomposite would be a new type of environmentally friendly energy storage supercapacitor.

Strategies of molecular design and simulation

For better OLED performance, Liu et al. stated the strategy of molecular design in the conception of hydrogen bond interactions. By regulating the H-bond interaction, the desired properties could be obtained through restricting the rotation between different donor/acceptor moieties and inhibiting the

vibrational coupling of excited states, which could obtain high luminous efficiency and color purity. Also, the multiple H-bonds interactions could further enhance horizontal orientation in amorphous organic semiconductor films and significantly increase hole and electron mobilities, which is beneficial for efficiency stability with negligible roll-off.

Sun et al. summarized a mini-review introducing strategies to improve the thermoelectric figure of merit in thermoelectric functional materials. The strategies refer to optimize the carrier concentration to improve the Seebeck coefficient, improve the steady of carrier mobility, modify the energy band to achieve expected thermoelectric performance, reduce lattice thermal conductivity, seek intrinsically low thermal conductivity thermoelectric materials and Electron-phonon decoupling.

For solar cells, where charge transport across several heterojunction interfaces is a pre-requisite for working devices. For better performance of thin-film photovoltaic devices, Jones et al. reviewed the interfaces behaviors through modelling simulation. In this review they have discussed several approaches for modelling interface processes at various length and timescales, and have split these into data-driven approaches, atomistic approaches and continuum level models. These approaches enabled better understanding of material or device performance, alongside their key limitations.

Xu et al. surveyed both theoretical calculations and experimental works to provide reference and inspiration for the rational design of multifunctional memristors, which intend to promote the increments in the memristor fabrications. As discussed in the review, the rational fabrication of memristors with Cints may give rise to remarkable enhancement in resistive switching performance with better stability and endurance, lower operation voltage, higher ON/OFF ratio, faster device speed, etc. By adjusting the Cints, suitable electric structures would be established in the metal oxides, which helps improve the performance of the electronic devices.

Other research work relating to charge transfer properties

Some extensive research work relating to charge transfer properties were also collected in this topic. Tang et al. studied the adsorption characteristics and charge transfer kinetics of fluoride in water by different adsorbents, Zhang et al. constructed TaPP/DiDOPO conjugated flame retardant composites, which they believe the absorption properties and flame retardancy effect were enhanced due to the conjugated structure of the composites.

Author contributions

MZ, TG, YL, and YQ conceptualized the Research Topic, wrote and approved the editorial.

Conflict of interest

Author MZ was employed by Qingdao Haiwan Science and Technology Industry Research Institute Co., Ltd. (HWSTI), Qingdao Haiwan Chemistry Co., Ltd. (QHCC).

The remaining authors declare that the research was conducted in the absence of any commercial or financial relationships that could be construed as a potential conflict of interest.

Publisher's note

frontiers in Chemistry

ORIGINAL RESEARCH
published: 23 March 2022
doi: 10.3389/fchem.2022.855800

Flexible Asymmetric Organic-Inorganic Composite Solid-State Electrolyte Based on PI Membrane for Ambient Temperature Solid-State Lithium Metal Batteries

Ruilu Yang[1], Zheng Zhang[1], Qi Zhang[1], Jian Shi[1], Shusen Kang[2]* and Yanchen Fan[2]**

[1]Analysis and Testing Center, Nantong University, Nantong, China, [2]SUSTeach Academy for Advanced Interdisciplinary Studies and Department of Materials Science and Engineering, Southern University of Science and Technology, Shenzhen, China

Solid-state lithium metal batteries have attracted more and more attention in recent years because of their high safety and energy density, with developments in the new energy industry and energy storage industry. However, solid-state electrolytes are usually symmetric and are not compatible with the cathode and anode at once. In this work, a flexible asymmetric organic-inorganic composite solid-state electrolyte consisting of PI membrane, succinonitrile (SN), LiLaZrTaO(LLZTO), Poly (ethylene glycol) (PEO), and LiTFSI were prepared by solution casting successfully. This lightweight solid electrolyte is stable at a high temperature of 150°C and exhibits a wide electrochemical window of more than 6 V. Furthermore, the high ionic conductivity of the flexible solid electrolyte was 7.3×10^{-7} S/cm. The solid-state batteries assembled with this flexible asymmetric organic-inorganic composite solid electrolyte exhibit excellent performance at ambient temperature. The specific discharge capacity of coin cells using asymmetric organic-inorganic composite solid-state electrolytes was 156.56 mAh/g, 147.25 mAh/g, and 66.55 mAh/g at 0.1, 0.2, and 1C at room temperature. After 100 cycles at 0.2C, the reversible discharging capacity was 96.01 mAh/g, and Coulombic efficiency was 98%. Considering the good performance mentioned above, our designed flexible asymmetric organic-inorganic composite solid electrolyte is appropriate for next-generation solid-state batteries with high cycling stability.

Keywords: Asymmetrical structure, solid-state electrolyte, solid-state lithium metal batteries, Poly(ethylene glycol), PI membrane

OPEN ACCESS

Edited by:
Yue Liu,
Liaoning Technical University, China

Reviewed by:
Zhixin Xu,
Shanghai Jiao Tong University, China
Chunrong Ma,
Shandong University, China

****Correspondence:***
Jian Shi
shi.j1@ntu.edu.cn
Shusen Kang
kshusen@163.com
Yanchen Fan
fanyc@sustech.edu.cn

Specialty section:
This article was submitted to Electrochemistry, a section of the journal Frontiers in Chemistry

Received: *16 January 2022*
Accepted: *07 February 2022*
Published: *23 March 2022*

Citation:
Yang R, Zhang Z, Zhang Q, Shi J, Kang S and Fan Y (2022) Flexible Asymmetric Organic-Inorganic Composite Solid-State Electrolyte Based on PI Membrane for Ambient Temperature Solid-State Lithium Metal Batteries. Front. Chem. 10:855800. doi: 10.3389/fchem.2022.855800

INTRODUCTION

Lithium-ion batteries (LIB) are widely applied in electric vehicles, portable devices, and smart grids because of their good performance (Lu et al., 2013; Humana et al., 2016; Liu et al., 2019; Sheng et al., 2019). In recent decades, researchers around the world have made tremendous progress on every component of batteries. However, the safety problems of high energy density LIB remain a problem (Wang et al., 2012; Eshetu et al., 2013; Xie and Lu, 2020), especially because the lithium metal anode is expected to be used in the high energy LIB, as more serious safety issues affect its highest capacity density and lowest potential. Li dendrites formed during electrochemical Li plating and stripping can penetrate the separator, leading to battery short-circuiting, and eventually fire and tragedies (Zhang, 2018; Wan et al., 2019; Wang et al., 2019).

To improve the safety of LIB, solid-state batteries have attracted significant attention, because they can replace the flammable liquid electrolyte in the current LIB (Jung et al., 2016; Gai et al., 2019; Xiao et al., 2020; Yu et al., 2020; Yu et al., 2021). The key component of solid-state batteries is a solid-state electrolyte (SSE). A perfect SSE should have high ionic conductivity, good interfacial stability and adhesion with the electrodes, a wide electrochemical window, good chemical stability, strong mechanical stability, nonvolatility, and nonflammability (Quartarone and Mustarelli, 2011; Judez et al., 2019; Xia et al., 2022). A great deal of research has been devoted to the various SSE materials, which can be summarized into three kinds, inorganic (oxides/sulfide) solid electrolytes, solid polymer electrolytes (SPEs), and their hybrids. There are advantages and disadvantages to the three kinds of solid-state electrolytes (Porz et al., 2017; Chua et al., 2018; Sen et al., 2021).

The ionic conductivity of inorganic SSEs is the highest. Some sulfide SSEs even have higher ionic conductivity than that of liquid electrolytes (Lian et al., 2019; Reddy et al., 2020). While there is large interfacial resistance in solid-state lithium metal batteries, which has prompted the leap in SSEs towards applications in lithium metal batteries. The inorganic SSEs are not flexible and thick. An increasing numbers of studies have found that the intrinsic high electronic conductivity in certain inorganic SSEs, especially at grain boundaries, leads to hazardous direct Li deposition inside of them (Dawson et al., 2017; Soares et al., 2019). Polymer electrolytes are flexible, lightweight, and have easy scalability (Manthiram et al., 2017). SPEs contain polymers, Li salts, and plasticizers. However, their application was limited by moderate ionic conductivity and narrow electrolyte windows. The low mechanical strength of the SPEs hinders their practical application in electric vehicles. Polyethylene oxide solid-state electrolyte system is the most widely studied, while the PEO itself is flammable. This is a giant leap to its practical application in LIBs (Zhang et al., 2016; Ding et al., 2021). A composite solid electrolyte containing organic and inorganic solid electrolytes has attracted more and more attention because of its high ionic conductivity and flexibility. However, the ionic conductivity of the composite solid electrolyte is usually below 10^{-4} S/cm and cannot be applied in solid-state batteries at room temperature.

It is therefore necessary to develop a solid-state electrolyte with higher conductivity. A solid-state electrolyte based on the succinonitrile (SN) exhibited outstanding ion transport in a quasi-solid state because its melting point is 58°C (Chen et al., 2016). Solid-state electrolytes containing lithium salt and SN exhibit ionic conductivity over 10^{-3} S/cm, which is much higher than these of SPEs. Moreover, the SN is electrochemically stable and negligible flammable, which is suitable for lithium batteries. However, the mechanical property of SN is poor. For solid-state LIBs, available SSEs need high mechanical strength, wide electrochemical windows, and high ionic conductivity to satisfy the solid-state LIBs.

However, the SSEs are symmetric because of the preparation method. Inorganic SSEs usually are prepared by solid-state sintered technology. The polymer SSEs are often prepared by solution-casting. The symmetric SSEs are not compatible with the cathode and anode at once. The cathode is oxidative, and the anode is reductive. The PEO-based SSEs are compatible with lithium metal anode, but they can be oxidized by a high-voltage cathode. LATP has high ionic conductivity, and the titanium in LATP can be reduced from +4 to +3 when in direct contact with metallic lithium, meaning the symmetric SSEs cannot safely be used in solid-state lithium metal batteries.

The present study proposes a design for a flexible asymmetric organic-inorganic composite solid-state electrolyte for all solid-state LIBs. The composite SSE contains polyimide film, polymer, ceramic electrolyte, SN, and a lithium salt. Polyimide film has an aligned porous and high mechanical strength to guarantee the structural integrity and good flexibility of the electrolyte to prevent potential dendrite penetration. The aligned composite SSEs structures in a horizontal configuration could enhance the ionic conductivity. The polymer in the SSEs could reduce dendrite growth. PEO solid-state electrolytes are the highest ionic conductivity and are applied at the organic-inorganic composite solid-state electrolyte. Ceramic electrolyte benefits for the high electrolyte window and ionic conductivity. LLZTO are significant for ceramic electrolyte power because of their excellent stability, high ionic conductivity (higher than 10^{-3} S/cm), and mechanical strength. LLZTO was thus used in the organic-inorganic composite solid-state electrolyte. SN was chosen as the plasticizer because of its high ionic conductivity, electrochemically stability, and nonflammability. Moreover, the SN could acquire a good interfacial contact between SSEs and Li metal anode. The solid-state electrolyte solution can permeate the PI membrane to form the organic-inorganic composite solid-state electrolyte. Utilizing the organic-inorganic composite solid-state electrolyte, the solid-state Lithium batteries can stably cycle at room temperature, which is dramatically high. All in all, the design idea of the composite electrolyte in this work could provide some guidance and opportunities for the novel design of high-performance solid-state lithium metal batteries.

EXPERIMENTAL SECTION

Materials and Chemical Reagents

Poly (ethylene glycol) (PEO, Mw = 8,000) was bought from Aladdin. Actone (99.5%) was purchased by Merck. Succinonitrile (SN, 99.7%), LiTFSI (99.9%) were bought from Energy Chemical. PI membrane was bought from Aladdin. $Li_{6.4}La_3Zr_{1.4}Ta_{0.6}O_{12}$ (LLZTO, dia12*0.8 mm) was purchased from the Kejing company. All the materials were used directly without any treatment.

Preparation of the Composite Separator

Firstly, 400 mg PEO, 300 mg SN, and 300 mg LLZTO particles were added to a beaker. Then, some acetone was added into this beaker and stirred at room temperature for 12 h to get a homogenous solution. Next, the homogenous solution was coated on Teflon mold with a PI membrane on the bottom. Finally, this membrane was dried 24 h at room temperature to evaporate the solvent and create the flexible asymmetric organic-inorganic composite solid-state electrolyte.

Preparation of the $LiNi_{0.8}Co_{0.1}Mn_{0.1}O_2$ Cathode Electrode

$LiNi_{0.8}Co_{0.1}Mn_{0.1}O_2$, acetylene black, PVDF with a weight ratio of 8:1:1 was added in N-methylpyrrolidone (NMP) and stirred for 12 h to get homogenous slurry. Next, the obtained slurry was

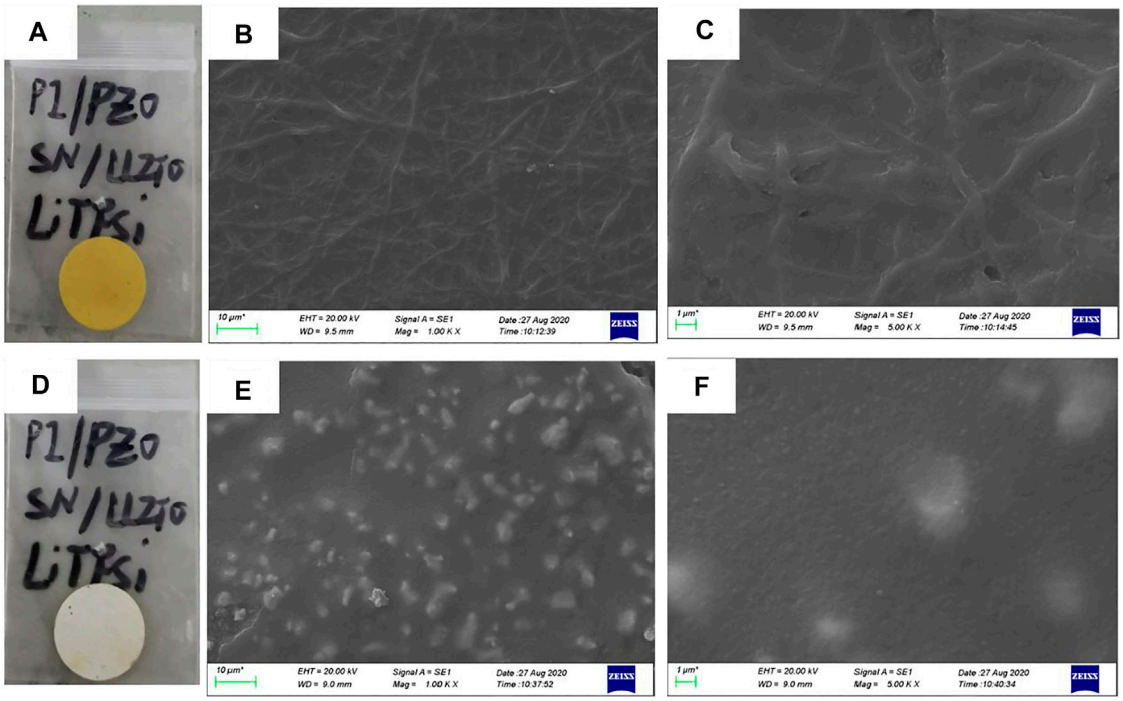

FIGURE 1 | Image and SEM image of asymmetric organic-inorganic composite solid-state electrolyte, **(A), (B), and (C)** are images of the bottom-surface, **(D), (E), and (F)** are the images of the top-surface.

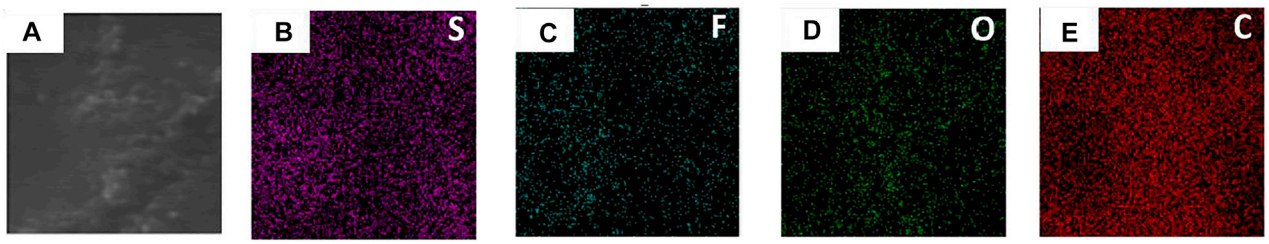

FIGURE 2 | SEM and EDS mapping of the bottom surface of the flexible asymmetric organic-inorganic composite solid-state electrolyte. **(A)** SEM image, **(B)** EDS mapping image of S, **(C)** F, **(D)** O, **(E)** C.

coated on aluminum current collectors by a doctor blade. Then the electrode was dried at 80°C for 12 h. The cathode electrode was dried at 100°C for 48 h in a vacuum. The active mass loading on the cathode foil was about 5.1 mg cm^{-2}.

Electrochemical Measurements

CHI 660E was used to test the ionic conductivity of the PVDF-HFP/LLZTO composite GPEs. The symmetric cell stainless steel (SS)/GPE/SS was used. The ionic conductivity of GPE was measured by A.C. impedance spectrum (EIS) at room temperature to 100°C with a frequency range from 1 Hz to 1M Hz. The ionic conductivity was calculated by **Eq. 1**:

$$\sigma = d/(S \times R_b) \tag{1}$$

σ represents the ionic conductivity, d is the thickness of the GPE, S is the area of polymer electrolyte. AC impedance and DC polarization methods were combined to measure the lithium transference number. The symmetric cell system Li/GPE/Li was used in this test. The lithium transference number was calculated by the following **Equation 2**

$$t_{Li^+} = \frac{I_s(\Delta V - I_0 R_0)}{I_0(\Delta V - I_0 R_0)} \tag{2}$$

I_0 represents the initial polarization currents; Is represents the steady-state polarization currents; R_0 represents the initial interfacial resistance; R_0 represents the steady-state interfacial resistance; and the voltage amplitude is set at 0.1 V.

SS/GPE/Li was used to tests the electrochemical window by linear sweep voltammetry. Voltage ranges from 0 to 5 V with a rate 0.1 mV/s.

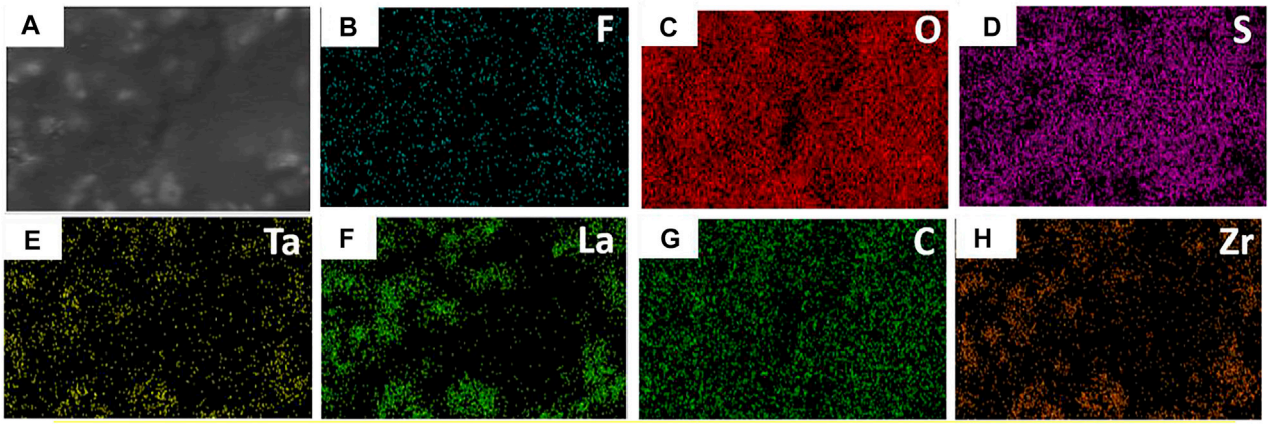

FIGURE 3 | SEM and EDS mapping of the top surface of the flexible asymmetric organic-inorganic composite solid-state electrolyte.**(A)** SEM image, **(B)** EDS mapping image of F, **(C)** O, **(D)** S, **(E)** Ta, **(F)** La, **(G)** C, **(H)** Zr.

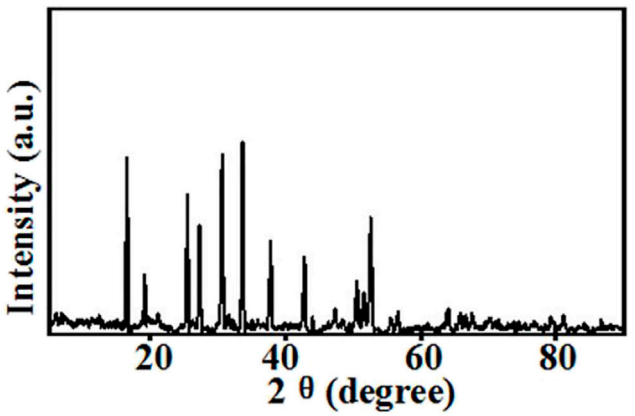

FIGURE 4 | XRD of flexible asymmetric organic-inorganic composite solid-state electrolyte.

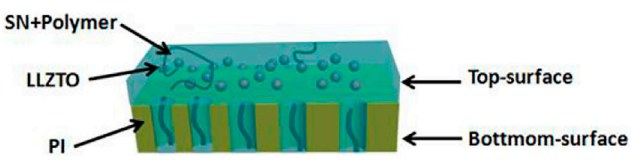

SCHEME 1 | The scheme of asymmetric organic-inorganic composite solid-state electrolyte.

FIGURE 5 | Flexible asymmetric organic-inorganic composite solid-state electrolyte is heated at 150°C for 10 min.

The compatibility of the GPE with Li metal was analyzed by plating/stripping cycling experiment of Li metal electrode in Li/GPE/Li cell. The cyclic voltammetry was performed by CHI 660E and ranged from 2.5 to 4.5 V with a scanning rate of 0.1 mV/s at room temperature.

The morphologies of the GPE membrane were characterized by scanning electron microscopy (EVO-18). The X-ray diffraction patterns of the polymer membranes were obtained with X-ray power diffraction (X pert3 Power) at a scanning rate of 4°/min in the 2θ range of 5–90°. The porosity of the polymer membrane was measured by gravimetry. The electrochemical properties of GPE were carried out using CHI660E.

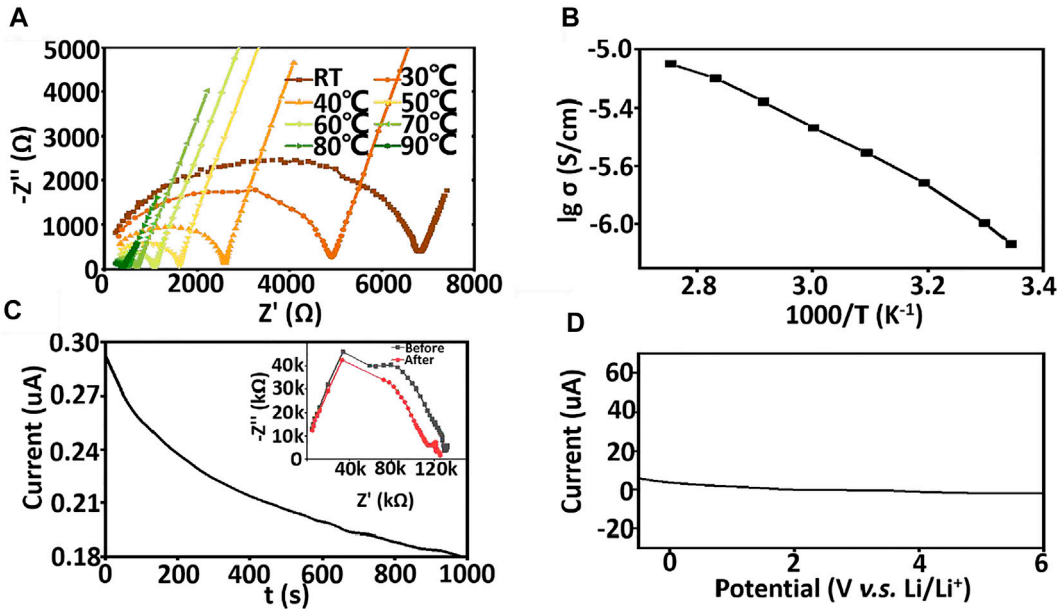

FIGURE 6 | (A) the A.C. impendence of asymmetric organic-inorganic composite solid-state electrolyte at different temperature **(B)** Arrhenius plots of asymmetric organic-inorganic composite solid-state electrolyte ranging room temperature to 90°C, **(C)** DC polarization curve for Li/ asymmetric organic-inorganic composite solid-state electrolyte/Li under a polarization voltage of 0.1 V. The insets show the EIS before and after the polarization. **(D)** LSV curve of asymmetric organic-inorganic composite solid-state electrolyte.

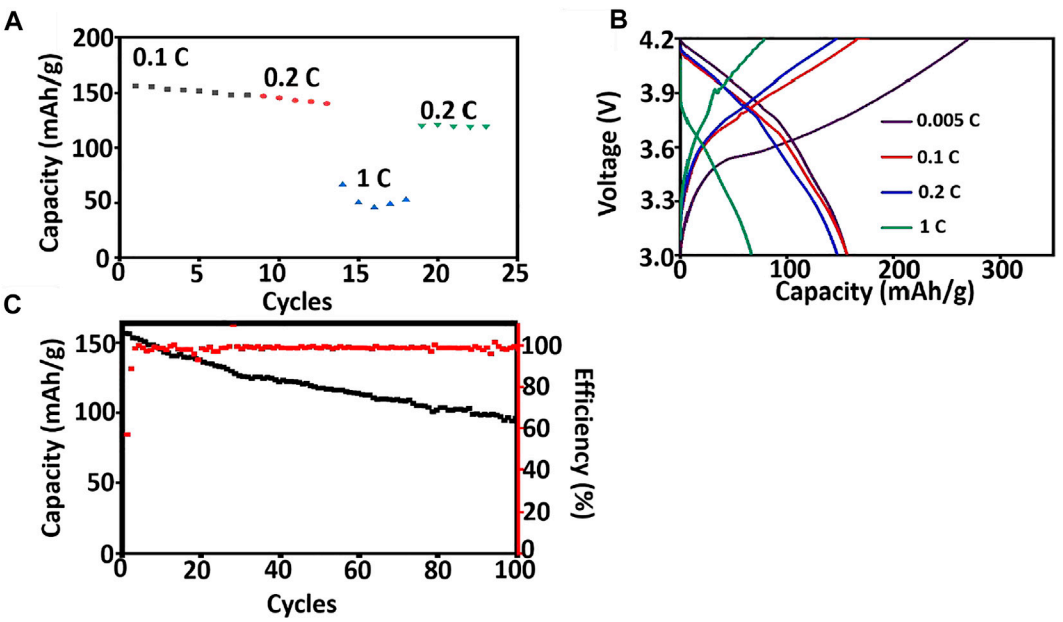

FIGURE 7 | Battery performance of NCM811/ asymmetric organic-inorganic composite solid-state electrolyte/Li at room temperature. **(A)** discharging capacity at different rates, **(B)** charging and discharging curves at different rates, **(C)** long term cycling performance at 0.2 C.

RESULTS AND DISCUSSION

The two sides of the asymmetric organic-inorganic composite solid-state electrolyte have different morphology, which can be seen in **Figure 1**. The bottom-surface is homogenous and nonporous, and the PI fiber can be seen from the SEM images (**Figures 1B,C**). The corresponding EDS mapping images show that S, F, O, and C are dispersed evenly in the electrolyte, as

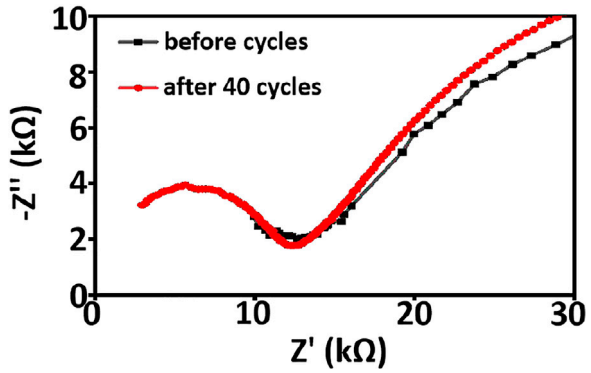

FIGURE 8 | EIS spectroscopy of NCM811/ asymmetric organic-inorganic composite solid-state electrolyte/Li cell before and after 40 cycles.

indicated in **Figure 2**. This demonstrates the PEO, SN, and PI are homogeneous on the bottom-surface, and that this side has no LLZTO nanoparticles.

The top-surface is very rough, which can be seen from **Figures 1E,F**. The original morphology of PI fiber is covered by polymer and nanoparticles, as shown in **Figure 3**. The corresponding EDS mapping images show that S, F, O, and C are homogenous on the top-surface, and Ti, La, and Zr are evenly distributed on the top-surface because the LLZTOs are nanoparticles. This demonstrates the PEO, SN, LLZTO, and PI are homogeneous on the bottom-surface. The two sides also contain different components. The PI is small, meaning that the LLZTO nanoparticles cannot permeate through to the bottom-surface. The two sides of asymmetric organic-inorganic composite solid-state electrolytes have different morphology, meaning this is a useful way of preparing the two sides of solid-state electrolytes that have different functions. For example, the LATP and LAGP have good ionic conductivity and high electrochemical windows, but they react with lithium metal anode, so they cannot be used in lithium metal batteries. In this way, we can prepare the solid-state electrolyte with two different sides as shown in **Scheme 1**, one side consists of polymer and lithium salt, so this side is compatible with the lithium metal anode. Another side is made up of nanoparticles, polymer, and lithium salt, so this side is compatible with the high-voltage cathode. Therefore, a solid-state electrolyte prepared in this way is compatible with the high-voltage cathode and a lithium anode. The XRD of the top-surface side is shown in **Figure 4**. Two board peaks at 18.9 and 20.1 are attributed to the crystal peaks of PEO (Zha et al., 2018). The peaks of garnet LLZTO can be seen from **Figure 4** and correspond to $Li_5La_5Nb_2O_{12}$, suggesting that cubic phase LLZTO exists on this side (Wei et al., 2020).

As the safety problems of batteries attract more and more attention, the thermal stability of the asymmetric organic-inorganic composite solid-state electrolyte was evaluated. As shown in **Figure 5**, the asymmetric organic-inorganic composite solid-state electrolyte showed excellent thermal stability at 150°C. The electrolyte membrane shows no significant change in size and color before and after treatment at 150°C. This is attributed to the high thermal stability of LLZTO (Lu et al., 2019) and PI (Munakata et al., 2008).

The electrochemical properties of the asymmetric organic-inorganic composite solid-state electrolyte are investigated in **Figure 6**. The ionic conductivity of the asymmetric organic-inorganic composite solid-state electrolyte is 7.3×10^{-7} S/cm, which is higher than PEO/LLZTO/LiTFSI solid-state electrolyte (**Figure 6A**). The polymers are aligned in the PI holes, the ionic diffusion along the aligned direction shows an even bigger difference to those in the other two directions (x and y) in the aligned PEO/LiTFSI system (Wan et al., 2019). Therefore, polymer-chain alignment is beneficial to ion diffusion in the alignment direction and the ionic conductivity of asymmetric organic-inorganic composite solid-state electrolyte increases with the increasing temperature. In **Figure 6B**, the activation energy was also calculated by Arrhenius theory and was 39.4 kJ/mol. The lithium transference number is characterized by AC impedance and the DC polarization method **Figure 6C**. The lithium transference number is 0.40. The LSV is used to characterize the electrochemical window. As

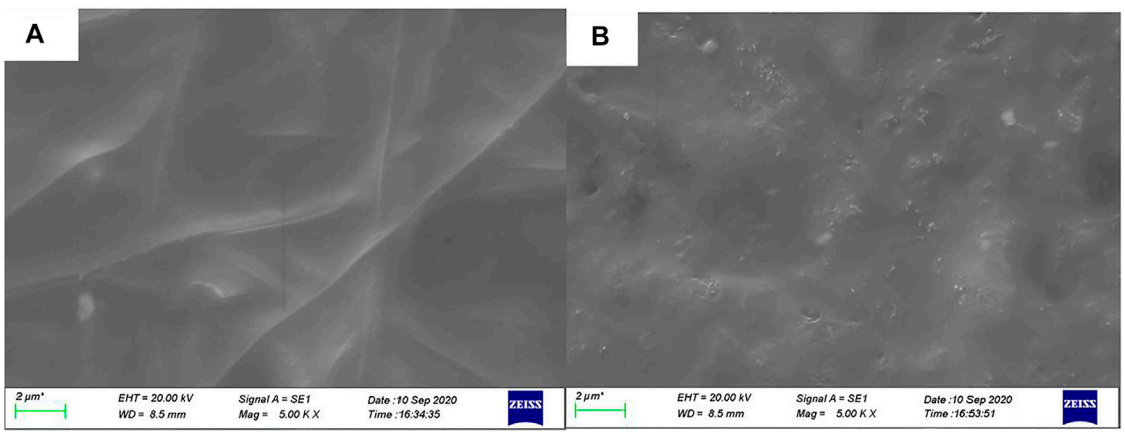

FIGURE 9 | (A) bottom-surface **(B)** top-surface SEM of the asymmetric organic-inorganic composite solid-state electrolyte after 40 cycles.

shown in **Figure 6D**, there is no oxide peak below 6 V, which is higher than the usual solid-state electrolyte because the SN and LLZTO are electrochemically stable. Therefore, the asymmetric organic-inorganic composite solid-state electrolyte is a satisfactory candidate for high-voltage lithium batteries.

Asymmetric organic-inorganic composite solid-state electrolytes are applied at NCM811/Li to evaluate the possible application in lithium metal batteries. The coin cell is charging and discharging at room temperature to monitor its rate and cycle performance and the results are shown in **Figure 7**. The specific discharge capacity of coin cells using Asymmetric organic-inorganic composite solid-state electrolytes is 156.56 mAh/g, 147.25 mAh/g, and 66.55 mAh/g at 0.1, 0.2, and 1C at room temperature. This is better than the solid-state lithium metal batteries using PEO/LLZTO composite solid-state electrolyte (Zhang et al., 2015; Zhao et al., 2017). After the discharging rate is changed to 0.2C, the specific discharge capacity is 120.45 mAh/g. Furthermore, the coin cell also exhibits good cycle performance. After 100 cycles, the reversible discharging capacity is 96.01 mAh/g, and Coulombic efficiency is 98%. The excellent cycle performance is attributed to the good interface performance between electrolyte and Li metal anode (Wang et al., 2017).

Electrochemical impedance spectroscopy and cyclic voltammetry are used to evaluate the stability of cells with asymmetric organic-inorganic composite solid-state electrolytes. In the EIS spectrum (**Figure 8**), we can see the interfacial resistance and charge transfer resistance of the cell do not change obviously before and after 40 cycles. This demonstrates that the electrolyte/electrode interface and passivation layer on the electrode is stable and the asymmetric organic-inorganic composite solid-state electrolyte is compatible with the cathode and anode at once. This result corresponds to the result in **Figure 9**. Illustrated in **Figure 9** are the SEM images of the bottom-surface and top-surface of the asymmetric organic-inorganic composite solid-state electrolyte after 40 cycles. Compared with the corresponding SEM images in **Figures 1B,C**, the bottom-surface is still homogenous and nonporous after 40 cycles. Moreover, the original morphology of PI fiber is still covered by polymer and nanoparticles on the top-surface of the asymmetric organic-inorganic composite solid-state electrolyte after 40 cycles. These findings confirm that the electrolyte/electrode interface and passivation layer on the electrode is stable and the two sides of the asymmetric organic-inorganic composite solid-state electrolyte contain different components.

According to the above analysis, the two sides of asymmetric organic-inorganic composite solid-state electrolytes have different morphology and functions. This is very useful in solid-state electrolytes. We can prepare the solid-state electrolyte with two different sides, one side consists of polymer and lithium salt, so this side is compatible with the lithium metal anode. The other side is made up of nanoparticles, polymer, and lithium salt, so this side is compatible with the high-voltage cathode. Therefore, the solid-state electrolyte prepared in this way is compatible with the high-voltage cathode and a lithium anode. Our designed flexible asymmetric organic-inorganic composite solid electrolyte undoubtedly provides more convenience for the next-generation solid-state batteries with high cycling stability. Furthermore, the design idea of the composite electrolyte in this work can provide some guidance and opportunities for the novel design of high-performance solid-state lithium metal batteries.

CONCLUSION

The flexible asymmetric organic-inorganic composite solid-state electrolyte consisting of PI membrane, succinonitrile (SN), LiLaZrTaO(LLZTO), PEO, and LiTFSI were prepared successfully. The flexible asymmetric composite solid-state electrolyte is compatible with the cathode and anode at once. The solid-state batteries assembled with this flexible asymmetric organic-inorganic composite solid electrolyte exhibit excellent performance at ambient temperature. The specific discharge capacity of coin cells using asymmetric organic-inorganic composite solid-state electrolytes is 156.56 mAh/g, 147.25 mAh/g, and 66.55 mAh/g at 0.1, 0.2, and 1 C at room temperature. After 100 cycles at 0.2 C, the reversible discharging capacity is 96.01 mAh/g, and Coulombic efficiency is 98%. Considering the good performance mentioned above, our designed flexible asymmetric organic-inorganic composite solid electrolyte is appropriate for the next-generation solid-state batteries with high cycling stability.

DATA AVAILABILITY STATEMENT

The original contributions presented in the study are included in the article/supplementary material, further inquiries can be directed to the corresponding authors.

AUTHOR CONTRIBUTIONS

RY, ZZ, QZ, SK, JS, and YF conducted the literature searches, summarized the pertinent references, and wrote the manuscript. All authors contributed to the article and approved the submitted version.

FUNDING

This work was supported by the Natural Science Foundation of the Jiangsu Higher Education Institutions of China (grant number 19KJB150037) and State Key Laboratory of Advanced Chemical Power Sources.

REFERENCES

Chen, B., Huang, Z., Chen, X., Zhao, Y., Xu, Q., Long, P., et al. (2016). A New Composite Solid Electrolyte PEO/$Li_{10}GeP_2S_{12}$/SN for All-Solid-State Lithium Battery. *Electrochim. Acta* 210, 905–914. doi:10.1016/j.electacta.2016.06.025

Chua, S., Fang, R., Sun, Z., Wu, M., Gu, Z., Wang, Y., et al. (2018). Hybrid Solid Polymer Electrolytes with Two-Dimensional Inorganic Nanofillers. *Chem. Eur. J.* 24, 18180–18203. doi:10.1002/chem.201804781

Dawson, J. A., Canepa, P., Famprikis, T., Masquelier, C., and Islam, M. S. (2017). Atomic-Scale Influence of Grain Boundaries on Li-Ion Conduction in Solid Electrolytes for All-Solid-State Batteries. *J. Am. Chem. Soc.* 140, 362–368. doi:10.1021/jacs.7b10593

Ding, W.-Q., Lv, F., Xu, N., Wu, M.-T., Liu, J., and Gao, X.-P. (2021). Polyethylene Oxide-Based Solid-State Composite Polymer Electrolytes for Rechargeable Lithium Batteries. *ACS Appl. Energ. Mater.* 4, 4581–4601. doi:10.1021/acsaem.1c00216

Eshetu, G. G., Grugeon, S., Laruelle, S., Boyanov, S., Lecocq, A., Bertrand, J.-P., et al. (2013). In-depth Safety-Focused Analysis of Solvents Used in Electrolytes for Large Scale Lithium Ion Batteries. *Phys. Chem. Chem. Phys.* 15, 9145–9155. doi:10.1039/c3cp51315g

Gai, J., Ma, F., Zhang, Z., Sun, D., Jin, Y., Guo, Y., et al. (2019). Flexible Organic-Inorganic Composite Solid Electrolyte with Asymmetric Structure for Room Temperature Solid-State Li-Ion Batteries. *ACS Sustain. Chem. Eng.* 7, 15896–15903. doi:10.1021/acssuschemeng.9b01869

Humana, R. M., Ortiz, M. G., Thomas, J. E., Real, S. G., Sedlarikova, M., Vondrak, J., et al. (2016). Characterization of Anodes for Lithium-Ion Batteries. *J. Solid State. Electrochem.* 20, 1053–1058. doi:10.1007/s10008-015-3004-7

Judez, X., Martinez-Ibañez, M., Santiago, A., Armand, M., Zhang, H., and Li, C. (2019). Quasi-solid-state Electrolytes for Lithium Sulfur Batteries: Advances and Perspectives. *J. Power Sourc.* 438, 226985. doi:10.1016/j.jpowsour.2019.226985

Jung, Y.-C., Park, M.-S., Doh, C.-H., and Kim, D.-W. (2016). Organic-inorganic Hybrid Solid Electrolytes for Solid-State Lithium Cells Operating at Room Temperature. *Electrochim. Acta* 218, 271–277. doi:10.1016/j.electacta.2016.09.141

Lian, P.-J., Zhao, B.-S., Zhang, L.-Q., Xu, N., Wu, M.-T., and Gao, X.-P. (2019). Inorganic Sulfide Solid Electrolytes for All-Solid-State Lithium Secondary Batteries. *J. Mater. Chem. A.* 7, 20540–20557. doi:10.1039/c9ta04555d

Liu, Y., Wang, Y., Wang, F., Lei, Z., Zhang, W., Pan, K., et al. (2019). Facile Synthesis of Antimony Tungstate Nanosheets as Anodes for Lithium-Ion Batteries. *Nanomaterials* 9, 1689. doi:10.3390/nano9121689

Lu, L., Han, X., Li, J., Hua, J., and Ouyang, M. (2013). A Review on the Key Issues for Lithium-Ion Battery Management in Electric Vehicles. *J. Power Sourc.* 226, 272–288. doi:10.1016/j.jpowsour.2012.10.060

Lu, J., Liu, Y., Yao, P., Ding, Z., Tang, Q., Wu, J., et al. (2019). Hybridizing Poly(vinylidene Fluoride-Co-Hexafluoropropylene) with $Li_{6.5}La_3Zr_{1.5}Ta_{0.5}O_{12}$ as a Lithium-Ion Electrolyte for Solid State Lithium Metal Batteries. *Chem. Eng. J.* 367, 230–238. doi:10.1016/j.cej.2019.02.148

Manthiram, A., Yu, X., and Wang, S. (2017). Lithium Battery Chemistries Enabled by Solid-State Electrolytes. *Nat. Rev. Mater.* 2, 16103. doi:10.1038/natrevmats.2016.103

Munakata, H., Yamamoto, D., and Kanamura, K. (2008). Three-dimensionally Ordered Macroporous Polyimide Composite Membrane with Controlled Pore Size for Direct Methanol Fuel Cells. *J. Power Sourc.* 178, 596–602. doi:10.1016/j.jpowsour.2007.08.060

Porz, L., Swamy, T., Sheldon, B. W., Rettenwander, D., Frömling, T., Thaman, H. L., et al. (2017). Mechanism of Lithium Metal Penetration through Inorganic Solid Electrolytes. *Adv. Energ. Mater.* 7, 1701003. doi:10.1002/aenm.201701003

Quartarone, E., and Mustarelli, P. (2011). Electrolytes for Solid-State Lithium Rechargeable Batteries: Recent Advances and Perspectives. *Chem. Soc. Rev.* 40, 2525–2540. doi:10.1039/c0cs00081g

Reddy, M. V., Julien, C. M., Mauger, A., and Zaghib, K. (2020). Sulfide and Oxide Inorganic Solid Electrolytes for All-Solid-State Li Batteries: A Review. *Nanomaterials* 10, 1606. doi:10.3390/nano10081606

Sen, S., Trevisanello, E., Niemöller, E., Shi, B.-X., Simon, F. J., and Richter, F. H. (2021). The Role of Polymers in Lithium Solid-State Batteries with Inorganic Solid Electrolytes. *J. Mater. Chem. A.* 9, 18701–18732. doi:10.1039/d1ta02796d

Sheng, J., Chen, T., Wang, R., Zhang, Z., Hua, F., and Yang, R. (2020). Ultra-light Cellulose Nanofibril Membrane for Lithium-Ion Batteries. *J. Membr. Sci.* 595, 117550. doi:10.1016/j.memsci.2019.117550

Soares, M. R. S., Costa, C. A. R., Lanzoni, E. M., Bettini, J., Ramirez, C. A. O., Souza, F. L., et al. (2019). Unraveling the Role of Sn Segregation in the Electronic Transport of Polycrystalline Hematite: Raising the Electronic Conductivity by Lowering the Grain-Boundary Blocking Effect. *Adv. Electron. Mater.* 5, 1900065. doi:10.1002/aelm.201900065

Wan, J., Xie, J., Kong, X., Liu, Z., Liu, K., Shi, F., et al. (2019). Ultrathin, Flexible, Solid Polymer Composite Electrolyte Enabled with Aligned Nanoporous Host for Lithium Batteries. *Nat. Nanotechnol.* 14, 705–711. doi:10.1038/s41565-019-0465-3

Wang, Q., Ping, P., Zhao, X., Chu, G., Sun, J., and Chen, C. (2012). Thermal Runaway Caused Fire and Explosion of Lithium Ion Battery. *J. Power Sourc.* 208, 210–224. doi:10.1016/j.jpowsour.2012.02.038

Wang, C., Yang, Y., Liu, X., Zhong, H., Xu, H., Xu, Z., et al. (2017). Suppression of Lithium Dendrite Formation by Using LAGP-PEO (LiTFSI) Composite Solid Electrolyte and Lithium Metal Anode Modified by PEO (LiTFSI) in All-Solid-State Lithium Batteries. *ACS Appl. Mater. Inter.* 9, 13694–13702. doi:10.1021/acsami.7b00336

Wang, T., Salvatierra, R. V., and Tour, J. M. (2019). Detecting Li Dendrites in a Two-Electrode Battery System. *Adv. Mater.* 31, 1807405. doi:10.1002/adma.201807405

Wei, T., Zhang, Z.-H., Wang, Z.-M., Zhang, Q., Ye, Y.-s., Lu, J.-H., et al. (2020). Ultrathin Solid Composite Electrolyte Based on Li6.4La3Zr1.4Ta0.6O12/PVDF-HFP/LiTFSI/Succinonitrile for High-Performance Solid-State Lithium Metal Batteries. *ACS Appl. Energ. Mater.* 3, 9428–9435. doi:10.1021/acsaem.0c01872

Xia, W., Zhao, Y., Zhao, F. P., Adair, K., Zhao, R., Li, S., et al. (2022). Antiperovskite Electrolytes for Solid-State Batteries. *Chem. Rev.* 122, 3763. doi:10.1021/acs.chemrev.1c00594

Xiao, Y., Wang, Y., Bo, S.-H., Kim, J. C., Miara, L. J., and Ceder, G. (2020). Understanding Interface Stability in Solid-State Batteries. *Nat. Rev. Mater.* 5, 105–126. doi:10.1038/s41578-019-0157-5

Xie, J., and Lu, Y.-C. (2020). A Retrospective on Lithium-Ion Batteries. *Nat. Commun.* 11, 2499. doi:10.1038/s41467-020-16259-9

Yu, W., Zhai, Y., Yang, G., Yao, J., Song, S., Li, S., et al. (2021). A Composite Electrolyte with Na3Zr2Si2PO12 Microtube for Solid-State Sodium-Metal Batteries. *Ceramics Int.* 47, 11156–11168. doi:10.1016/j.ceramint.2020.12.239

Yu, X., Liu, Y., Goodenough, J. B., and Manthiram, A. (2021). Rationally Designed PEGDA-LLZTO Composite Electrolyte for Solid-State Lithium Batteries. *ACS Appl. Mater. Inter.* 13, 30703–30711. doi:10.1021/acsami.1c07547

Zha, W., Chen, F., Yang, D., Shen, Q., and Zhang, L. (2018). High-performance $Li_{6.4}La_3Zr_{1.4}Ta_{0.6}O_{12}$/Poly(ethylene oxide)/Succinonitrile Composite Electrolyte for Solid-State Lithium Batteries. *J. Power Sourc.* 397, 87–94. doi:10.1016/j.jpowsour.2018.07.005

Zhang, J., Zhao, J., Yue, L., Wang, Q., Chai, J., Liu, Z., et al. (2015). Safety-Reinforced Poly(Propylene Carbonate)-Based All-Solid-State Polymer Electrolyte for Ambient-Temperature Solid Polymer Lithium Batteries. *Adv. Energ. Mater.* 5, 1501082. doi:10.1002/aenm.201501082

Zhang, J., Zhao, N., Zhang, M., Li, Y., Chu, P. K., Guo, X., et al. (2016). Flexible and Ion-Conducting Membrane Electrolytes for Solid-State Lithium Batteries: Dispersion of Garnet Nanoparticles in Insulating Polyethylene Oxide. *Nano Energy* 28, 447–454. doi:10.1016/j.nanoen.2016.09.002

Zhang, S. S. (2018). Problem, Status, and Possible Solutions for Lithium Metal Anode of Rechargeable Batteries. *ACS Appl. Energ. Mater.* 1, 910–920. doi:10.1021/acsaem.8b00055

Zhao, C.-Z., Zhang, X.-Q., Cheng, X.-B., Zhang, R., Xu, R., Chen, P.-Y., et al. (2017). An Anion-Immobilized Composite Electrolyte for Dendrite-free Lithium Metal Anodes. *Proc. Natl. Acad. Sci. USA* 114, 11069–11074. doi:10.1073/pnas.1708489114

Conflict of Interest: The authors declare that the research was conducted in the absence of any commercial or financial relationships that could be construed as a potential conflict of interest.

Publisher's Note: All claims expressed in this article are solely those of the authors and do not necessarily represent those of their affiliated organizations, or those of the publisher, the editors and the reviewers. Any product that may be evaluated in this article, or claim that may be made by its manufacturer, is not guaranteed or endorsed by the publisher.

frontiers | Frontiers in Chemistry

REVIEW
published: 19 May 2022
doi: 10.3389/fchem.2022.865281

Strategies to Improve the Thermoelectric Figure of Merit in Thermoelectric Functional Materials

Yan Sun[1,2†], *Yue Liu*[1†], *Ruichuan Li*[1], *Yanshuai Li*[1]* *and Shizheng Bai*[1]

[1]College of Material Science Engineer, Liaoning Technical University, Fuxin, China, [2]College of Material Science Engineer, Harbin Institute of Technology, Harbin, China

In recent years, thermoelectric functional materials have been widely concerned in temperature difference power generation, electric refrigeration and integrated circui, and so on. In this paper, the design and research progress of thermoelectric materials around lifting *ZT* value in recent years are reviewed. Optimizing the carrier concentration to improve the Seebeck coefficient, the steady improvement of carrier mobility and the influence of energy band engineering on thermoelectric performance are discussed. In addition, the impact of lattice thermal conductivity on *ZT* value is also significant. We discuss the general law that the synergistic effect of different dimensions, scales, and crystal structures can reduce lattice thermal conductivity, and introduce the new application of electro-acoustic decoupling in thermoelectric materials. Finally, the research of thermoelectric materials is summarized and prospected in the hope of providing practical ideas for expanding the application and scale industrialization of thermoelectric devices.

Keywords: thermoelectric materials, *ZT* value, seebeck coefficient, electrical conductivity, thermal conductivity

OPEN ACCESS

Edited by:
Choongho Yu,
Texas A&M University, United States

Reviewed by:
Huixia Luo,
Sun Yat-sen University, China
Siqi Lin,
Tongji University, China
Ahmad Ridwan Tresna Nugraha,
National Research and Innovation Agency (BRIN), Indonesia

***Correspondence:**
Yanshuai Li
yanshuaili666@163.com

†These authors have contributed equally to this work

Specialty section:
This article was submitted to Electrochemistry, a section of the journal Frontiers in Chemistry

Received: *29 January 2022*
Accepted: *02 May 2022*
Published: *19 May 2022*

Citation:
Sun Y, Liu Y, Li R, Li Y and Bai S (2022) Strategies to Improve the Thermoelectric Figure of Merit in Thermoelectric Functional Materials. Front. Chem. 10:865281. doi: 10.3389/fchem.2022.865281

INTRODUCTION

With the progress of society, energy and environmental issues have become the most severe challenges for humanity in the new era. Especially for fossil energy, the large amount of waste heat generated in the combustion process cannot be reused, and the energy utilization rate is meager (Vining, 2009). To solve this problem, the research of a thermoelectric functional material that directly converts heat energy and electric energy to each other has received extensive attention. With their small size, high reliability, long life, high temperature sensitivity, and environmental friendliness, thermoelectric materials (TE) have become a current research hotspot (**Figure 1**). It is now mainly used in crucial new energy directions such as space probes, industrial waste heat utilization, and solar composite power generation (Poudel et al., 2008; Suarez et al., 2016). Since the middle of the last century, the performance of TE materials has been dramatically improved, which is the key to improving the energy conversion efficiency of TE devices. Solid-state TE devices can not only use the Seebeck effect to convert heat into electricity but also the Peltier effect to provide cooling.

The energy conversion efficiency of TE material power generation equipment is defined as the output electric energy (P) divided by the provided thermal energy (Q) (Yang and Caillat, 2006):

$$\eta = \frac{P}{Q} = \frac{\Delta T}{T_H}\left(\frac{\sqrt{1+\overline{ZT}}-1}{\sqrt{1+\overline{ZT}}+\frac{T_C}{T_H}}\right) \quad (1)$$

Where T_H is hot end temperature, T_C is cold end temperature, and ΔT is temperature difference, respectively. ZT is the average value of thermoelectric properties, which can be used as a dimensionless parameter to measure the properties of TE materials:

$$ZT = \left(S^2\sigma/\kappa_e + \kappa_L\right)T \quad (2)$$

where S is the Seebeck coefficient, σ is the conductivity of the material, κ_e is electronic thermal conductivity, κ_L is lattice thermal conductivity, and T is the absolute temperature. Obviously, the larger the ZT value, the better the thermoelectric properties of the material. However, there is an intricate relationship between the Seebeck coefficient, electrical conductivity, and thermal conductivity, making it difficult for the thermoelectric figure of merit to be significantly improved for a long time (Bell, 2008; Snyder and Toberer, 2011). Therefore, our primary goal is to improve the electrical transmission performance ($S^2\sigma$) of the material and reduce its heat transmission performance (κ) through the coupling regulation of electrical transmission and heat transmission. According to Wiedemann-Franz law $\kappa_e = L\sigma T$, where L is the Lorentz constant. It can be seen that there is a positive correlation between electronic thermal conductivity and electrical conductivity. Therefore, as long as the thermal conductivity of the lattice with a small correlation is reduced, the thermoelectric figure of merit can be effectively optimized (Biswas et al., 2012; Zhao et al., 2014a; Kim et al., 2015; Li et al., 2017). **Figure 2** summarizes the ZT statistical results of some typical TE materials in recent years (Ioffe et al., 1959; Cutler et al., 1964; Hicks and Dresselhaus, 1993; Horbach et al., 2001; Yang et al., 2001; Dashevsky et al., 2002; Kuznetsov et al., 2002; Hsu et al., 2004; Shutoh and Sakurada, 2005; Heremans et al., 2008; Poudel et al., 2008; Wang et al., 2008; Yang et al., 2008; Zhao et al., 2008; Xie et al., 2009; Du et al., 2011; Levin et al., 2011; Pei et al., 2011; Li et al., 2012; Liu et al., 2012; Chen et al., 2013; Gelbstein et al., 2013; Sui et al., 2013; Yamini et al., 2013; Yan et al., 2013; Hu et al., 2014; Lee et al., 2014; Tan et al., 2014; Wu et al., 2014; Zhao et al., 2014a; Zhao et al., 2014b; Zhong et al., 2014; Kim et al., 2015; Kraemer et al., 2015; Tan et al., 2015a; Tang et al., 2015; Huang et al., 2016; Liu et al., 2016; Tan et al., 2016a; Liu et al., 2017; Roychowdhury et al., 2017; Zhang et al., 2017; Li et al., 2018; Ren et al., 2018; Zhou et al., 2018; Xiang et al., 2019; Chong et al., 2020; Feng et al., 2020; Qin et al., 2020; Yvenou et al., 2020; Selimefendigil et al., 2021; Su et al., 2022).

Figure 2 shows that the thermoelectric materials studied mainly include tellurides, layered chalcogenide compounds, oxides, clathrates, Half-Heusler, skutterudite, and copper chalcogenides. For example, telluride itself has good low thermal conductivity and is potential thermoelectric material. Kim et al. (2015) synthesized $Bi_{0.5}Sb_{1.5}Te_3$ by liquid-phase compression. The dense array of dislocations formed at the low-energy grain boundaries effectively scattered intermediate-frequency phonons, leading to a significant decrease in lattice thermal conductivity. The full-spectrum phonon scattering significantly increases the ZT to 1.86 at 320 K. Alkaline Earth oxides, such as cobalt compounds, have weak crystal symmetry and are also characterised by layered materials, which leads to a decrease in the lattice thermal conductivity of the material (Tang et al., 2015). The Cu_2Se of the copper chalcogenide has a layered monoclinic crystal structure at low temperatures, and its symmetry is also poor. At the same time, Cu ions can migrate freely in the sublattice like a liquid at high temperatures. The liquid-phase metal ions induce a specific deformation of the crystal structure and a significant increase in asymmetry, which facilitates the acquisition of solid anharmonicity and increases the phonon scattering ability, while having no effect on the electron mobility (Gelbstein et al., 2013). Zhong et al.

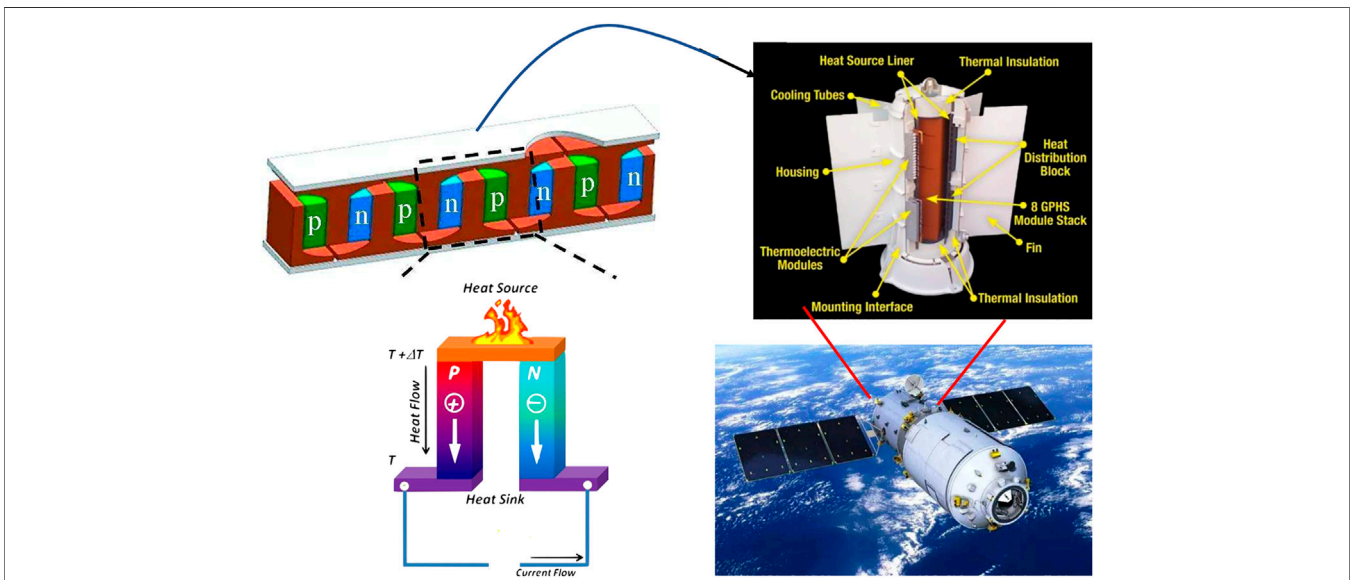

FIGURE 1 | Application and working mechanism of thermoelectric materials in aerospace.

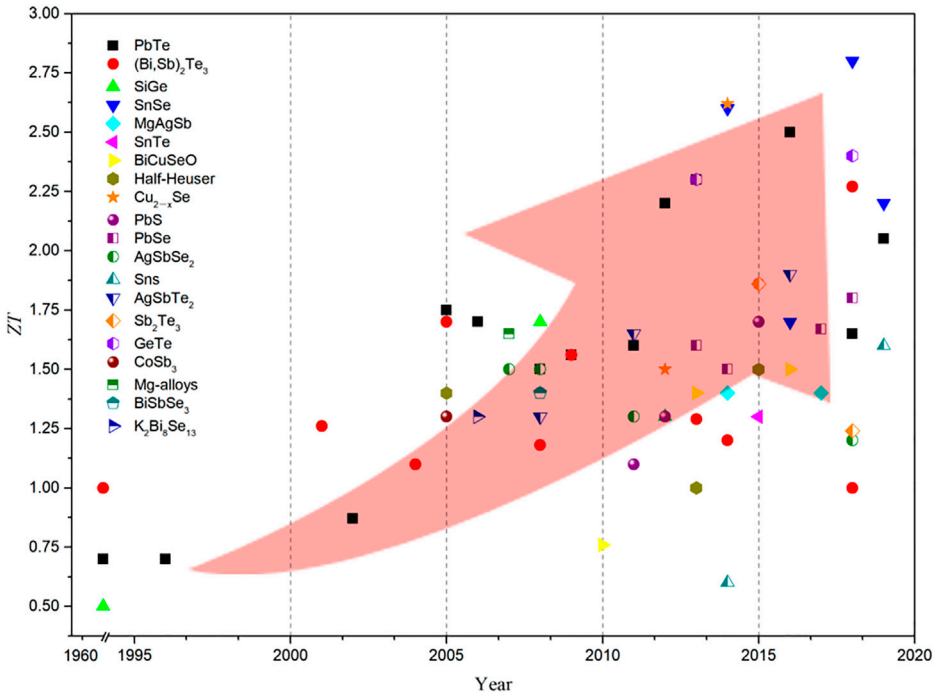

FIGURE 2 | The figure of merit of TE, thermoelectricity in recent years (Ioffe et al., 1959; Cutler et al., 1964; Hicks and Dresselhaus, 1993; Horbach et al., 2001; Yang et al., 2001; Dashevsky et al., 2002; Kuznetsov et al., 2002; Hsu et al., 2004; Shutoh and Sakurada, 2005; Heremans et al., 2008; Poudel et al., 2008; Wang et al., 2008; Yang et al., 2008; Zhao et al., 2008; Xie et al., 2009; Bergum et al., 2011; Du et al., 2011; Levin et al., 2011; Pei et al., 2011; Li et al., 2012; Liu et al., 2012; Chen et al., 2013; Gelbstein et al., 2013; Sui et al., 2013; Yamini et al., 2013; Yan et al., 2013; Hu et al., 2014; Lee et al., 2014; Tan et al., 2014; Wu et al., 2014; Zhao et al., 2014a; Zhao et al., 2014b; Zhong et al., 2014; Kim et al., 2015; Kraemer et al., 2015; Tan et al., 2015a; Tang et al., 2015; Liu et al., 2016; Tan et al., 2016a; Liu et al., 2017; Roychowdhury et al., 2017; Zhang et al., 2017; Chang et al., 2018; Li et al., 2018; Zhou et al., 2018; Xiang et al., 2019; Chong et al., 2020; Feng et al., 2020; Qin et al., 2020; Yvenou et al., 2020; Selimefendigil et al., 2021; Su et al., 2022).

(2014) used DC hot pressing process to prepare layered flake $Cu_{1.94}Al_{0.02}Se$, found that under the linkage of the disordered movement of the liquid phase of the Cu ion layer and the low symmetry, a maximum *ZT* value of 2.62 appeared. And SnSe, BiCuSeO, GeTe, and other materials have also found great thermoelectric figures of merit in recent studies (Gelbstein et al., 2013; Sui et al., 2013; Zhao et al., 2014a; Li et al., 2018; Qin et al., 2020). These materials are expected to further improve thermoelectric performance through methods, such as further parameter optimization, nanostructure design, and tape structure engineering.

For today's rapid development of modern technology, it is necessary to improve the *ZT* value of thermoelectric materials through different strategies. It has been shown that the strategy to improve the *ZT* value are mainly focused on the design of defect engineering. The first one is the energy band engineering design by adding atomic or second phase doping (Bell, 2008; Pei et al., 2011), which is done to optimize the carrier concentration and to increase the carrier mobility and thus obtain a more significant power factor. The doping process inevitably introduces lattice defects and distortions, which greatly affect the physical properties of the material. It is worth noting that the electric field, magnetic field, and light radiation can also stimulate and control the carrier concentration by cooperating with thermal energy transmission (Horbach et al., 2001; Du et al., 2011; Levin et al., 2011; Chen et al., 2013; Kraemer et al., 2015). The second is to rely on phonon engineering through nanostructures of different scales or mesoscale materials to reduce the lattice thermal conductivity κ_L through phonon scattering at the interface and crystal plane (Heremans et al., 2008; Biswas et al., 2012; Tan et al., 2014). Here we review recent advances in several aspects of thermoelectric materials, such as carrier concentration, carrier mobility, effective mass, lattice thermal conductivity and evidence of low thermal conductivity materials, and then summarise the effects of electro-acoustic decoupling effects on thermoelectric materials, finding commonalities in these materials through the above sections and refining rational design strategies for exploring materials with high thermoelectric efficiency.

ADJUSTMENTS OF CARRIER PARAMETERS TO IMPROVE *ZT*

Carrier Concentration

The fundamental challenge of high *ZT* thermoelectric material design stems from *S*, σ, and κ. Through the strong correlation of carrier concentration n, the energy level can generally be adjusted

by controlling the doping. Assuming that the dopant does not significantly change the scattering or band structure, the Seebeck coefficient can be derived from (Cutler et al., 1964):

$$S = \frac{8\pi^2 k_B^2}{3eh^2} m^* T \left(\frac{\pi}{3n}\right)^{2/3} \tag{3}$$

Among them, k_B is Boltzmann's constant, m^* is the effective carrier mass, h is Planck's constant, and n is the carrier concentration. In semiconductor thermoelectric materials, according to the Kane energy band theory, the Hall carrier concentration can be expressed as (Ioffe et al., 1959; Cutler et al., 1964):

$$n_H = \frac{1}{eR_H} = A^{-1} \frac{N_v \left(2m_b^* k_B T\right)^{3/2}}{3\pi^2 h^3} F_0^{3/2} \tag{4}$$

where N_v is the degree of degeneration, ${}^0F_0$ is the Fermi integral function, which is the reduced Planck constant. Although the carrier concentration n has an inverse relationship with the Seebeck coefficient, the increase of n has a positive effect on the energy band degeneration and the increase of effective mass. Therefore, the current strategy of optimizing carrier concentration usually adopts the increasing carrier Concentration method to improve thermoelectric performance (Dashevsky et al., 2002; Kuznetsov et al., 2002; Pei et al., 2011).

The main strategy for optimizing the carrier concentration is doping, such as modulation doping, uniform doping, and gradient doping (**Figure 3**). Feng et al. (2020) systematically revealed the theoretical origin of high average ZT in GeTe-based alloys uniformly doped with Pb through theoretical simulations and experimental tests on GeTe-based alloys. On the one hand, the intrinsic high hole carrier density is reduced to a rough optimal range, and then the carrier density is fine-tuned by Pb doping. The lead-doped energy band convergence can maintain a higher power factor. On the other hand, lead causes a decrease in carrier density and can significantly reduce κ, and the combination of the two is almost the same. PF results in a maximum ZT at the corresponding carrier density, so that the average ZT is about 1.5 in the 300–773 K range and the peak ZT is about 2.0 at 573 K, indicating that Pb doping can be used over a wide temperature range (e.g., 300–800 K), rather than only for TE applications at higher temperatures (e.g., T > 600 K) (Feng et al., 2020). In the case of uniform doping, the carrier concentration is generally independent of temperature, so the best thermoelectric performance cannot be guaranteed in the entire temperature range. One way to deal with this problem is to use gradient doping. By integrating two or more different segments, a common method of preparing this graded material is the so-called spark plasma sintering or hot-pressed powder layer. Each powder layer has different carrier concentration (Dashevsky et al., 2002; Selimefendigil et al., 2021). Zhao et al. (2014c) take advantage of the low thermal conductivity of layered materials in the out-layer direction. The migration of carriers between layers is improved in the out-layer direction by adjusting the symmetry of the crystal structure, thereby promoting electron tunneling in the inter-layer direction. At 600–800 K, SnSe has a continuous phase transition process from low-symmetry Pnma (L-Pnma) phase to high-symmetry Pnma (H-Pnma) phase, and then to high-temperature high-symmetry Cmcm phase. In addition to temperature, introducing stress into SnSe crystals by doping/solid solution can also adjust the symmetry of the crystal structure, thereby optimizing the thermoelectric properties of the material, as shown in **Figure 4** (Su et al., 2022).

However, with prolonged use, the initial carrier concentration gradient in the gradient material may decrease or disappear due to the homogenization effect induced by diffusion, thereby reducing the conversion efficiency. To solve this limitation, using the temperature dependence of the solubility of certain specific dopants (Yamini et al., 2013), a carrier concentration n is controlled only by temperature, and its gradient can be created in a single material. A well-known example is Cu, Ag, and excess Pb. They have negligible solubility in PbTe at room temperature but have high solubility at high temperatures (Bergum et al., 2011). Lidong Zhao et al. synthesized an n-type SnSe crystal with a two-dimensional layered structure using the temperature gradient method and bromine doping method. The electron doping promotes the hybridization of delocalized electrons and realizes the tunneling of electrons between the n-type SnSe layers. This "two-dimensional phonon/three-dimensional charge" transfer characteristic greatly improves the thermoelectric properties of n-type SnSe crystal materials, with a ZT as high as 2.8 (Chang et al., 2018). This temperature-dependent doping is reversible in the heating-cooling process and eliminates the diffusion problem of gradient doping, making it more suitable for practical applications. Polyatomic doping takes advantage of the synergistic effect to have a more significant change in carrier concentration (Zhu et al., 2002). Lixia Zhang et al. fabricated the Yb-filled $CoSb_3$ skutterudites with an ultra-high Yb filling fraction by melt-spinning methods, and they found a high ZT value of about 1.3 was achieved at 823 K for the nominal composition $Yb_{0.4}Co_4Sb_{12}$. An ultra-low lattice thermal conductivity approaching the glass limit was achieved due to the enhanced rattling effect from the ultra-high Yb filling fraction and extra phonon scattering from the ordered superstructures, nano-scale inhomogeneous Yb fillers, and high-density lattice strain caused by the ordered and modulated fillers (Ren et al., 2021). Shi et al. (2011) synthesized $CoSb_3$ with a variety of co-fillers such as Ba, La, and Yb. Finally, from single filling to double filling, and finally to multiple fillings to achieve continuous growth of ZT value, the maximum ZT at 850 K was increased to 1.7. Therefore, for thermoelectric material systems with different characteristics, it is particularly important to select a suitable doping method (the most current method is temperature-dependent doping) to optimize the carrier concentration in a broader temperature range.

Carrier Mobility

The improvement of carrier mobility is mainly through introducing impurity atoms in the intrinsic atomic vacancies. In most cases, the increase of m^* will lead to a decrease in carrier mobility, and it will reduce the conductivity (Ioffe et al., 1959):

$$\mu = \frac{e\tau}{m^*} \tag{5}$$

where τ is the relaxation time, so the improvement of carrier mobility also has a positive effect on the increase of ZT. Generally

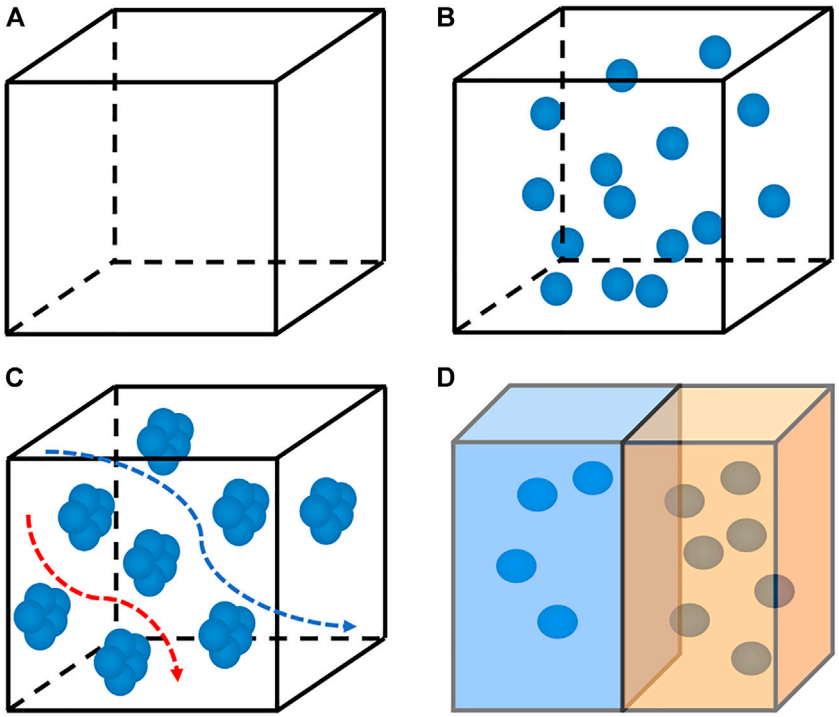

FIGURE 3 | The schematic diagram of changing the carrier concentration by different doping methods; **(A)** undoped; **(B)** uniform doping; **(C)** modulated doping; **(D)** gradient doping.

speaking, the smaller the electronegativity difference between the elements of the compound, the greater the mobility of the material, such as PbTe, Bi_2Se_3, etc. Lidong Zhao et al. further studied the effect of copper doping on n-type PbTe. The effective filling of Cu reduces the scattering of carriers in the gaps of Pb crystals, resulting in considerable carrier mobility and a high power factor (Xiao et al., 2017). The PbTe-2% Cu_2Te reaches a peak value of $ZT \sim 1.5$ at 723 K, and the $ZT_{ave} \sim 1.0$ of the n-type PbTe system achieves the highest value in history, as shown in **Figure 5**.

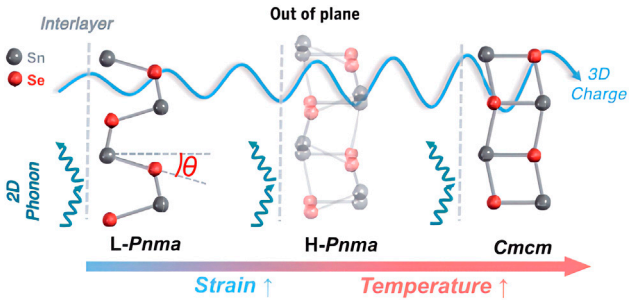

FIGURE 4 | 3D electron-2D phonon transport properties outside the n-type SnSe layer: Layered SnSe crystals use their layer structure to suppress (lattice vibration) phonon transport, but electrons different from phonons can tunnel through overlapping electron orbital transport (Su et al., 2022).

Studies have shown that to improve carrier mobility, three-dimensional modulation doping (mainly under low-temperature conditions) can effectively increase the ZT value of some important thermoelectric materials (Zebarjadi et al., 2011; Koirala et al., 2013; Pei et al., 2014). The modulated doped sample is a two-phase composite material composed of undoped and heavily doped. Undoped original samples have low carrier concentration but high carrier mobility, while uniformly doped and heavily doped samples have high carrier concentration but low carrier mobility. The Fermi level of undoped samples is usually in the middle of the energy gap, and the Fermi level of heavily doped samples goes deep into the conduction band (n-type doping) or valence band (p-type doping). With the energy imbalance between the undoped phase and the heavily doped phase, the carriers in the sample overflow from the heavily doped area to the undoped site, and this process enhances the carrier mobility (Valset et al., 2012).

In addition to modulating doping, the texture structure of the material can be used as another feasible way to improve carrier mobility, especially for some materials with anisotropic structures. In various heterostructures, the carrier mobility may only be higher in some specific crystal orientations (Zhao et al., 2014a). Li et al. (2018) proposed a method of high-efficiency thermoelectric materials that optimizes both electrical and heat transport performance. In $(Bi, Sb)_2Te_3$, the two-step sintering process with excess Te can increase mobility and reduce thermal conductivity at the same time. The two-step sintering process reduces the grain boundaries and defects that seriously hinder the

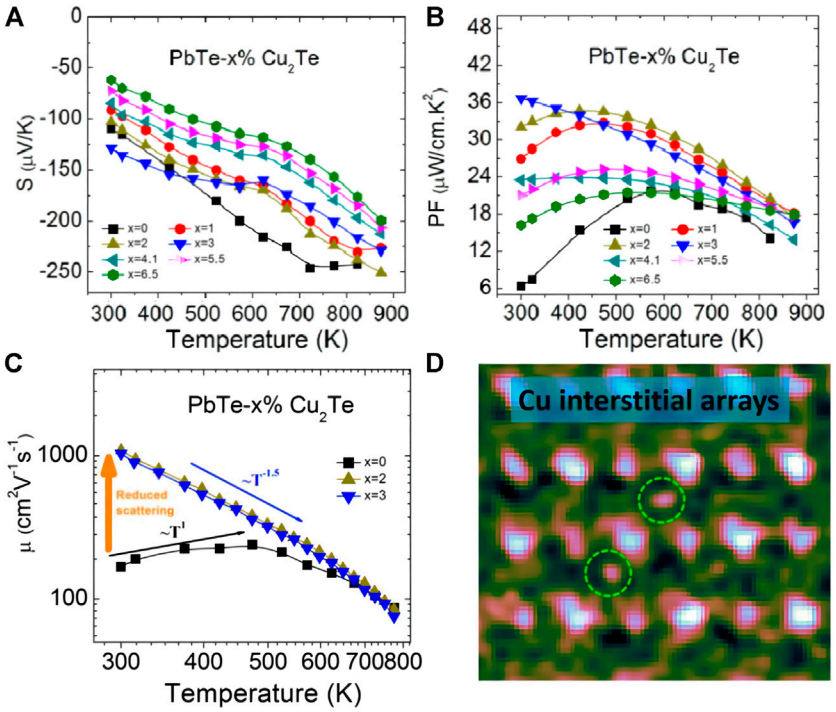

FIGURE 5 | (A) Elimination of lead vacancies can reduce carrier scattering and significantly increase carrier mobility; **(B)** PbTe-Cu_2Te electrical transport properties change with temperature; **(C)** PbTe-Cu_2Te power factor change with temperature; **(D)** High magnification STEM HAADF image of Cu gap array (enlarged) (Xiao et al., 2017).

transport of charge carriers, thereby increasing the mobility, and the maximum ZT of $Bi_{0.4}Sb_{1.6}Te_3$ can reach 1.3. Studies have shown that the two-step sintering technology is an effective method, which can control the existence and distribution of element inhomogeneity, so that the carrier transport and phonon transport have a special directionality. This has a specific guiding significance for other thermoelectric material systems with similar characteristics (Cha et al., 2019; Pan et al., 2019).

IMPROVEMENT OF EFFECTIVE QUALITY

The effect of the local increase of the density of states on the Seebeck coefficient is given by Mott's expression (Heremans et al., 2008). When semiconductors are doped or heavily doped with metals, according to the Mahan-Sofo theory, at a given carrier concentration, a high total density of states effective mass (m_d^*) will determine a high Seebeck coefficient (Pei et al., 2012a), and then increase the ZT value of the material. To increase local DOS in a narrow energy range, md^* can be effectively increased. Since the ZT value is related to the conductivity, the carrier concentration n cannot be too low. Most high-performance thermoelectric materials are heavily doped semiconductors, and the optimal carrier concentration n_{opt} varies with $(m^*T)^{3/2}$. Therefore, n_{opt} can also be achieved by tuning the effective quality m_d^* (Cha et al., 2019). According to $m_d^* = N_v^{2/3} m_b^*$, degeneracy (N_v) and effective mass (m_b^*) play a decisive role in m_d^*. In most cases, the increase in m_d^* is due to the increase in m_b^* (Pei et al., 2012b; Dutta et al., 2020), with the increase of the effective mass m_b^* will result in a decrease in the carrier mobility μ and a decrease in the material conductivity (Tan et al., 2016b). Energy band engineering causes the density of states distortion by doping or changing symmetry, using energy band degeneration, increasing resonance states, hybridizing the energy gap, and doping Kondo atoms to change its effective mass essentially (Suwardi et al., 2019).

High energy band degeneracy is of great significance in thermoelectric materials because it can produce higher m_d^* (as shown in **Figure 6A**), resulting in a more significant Seebeck coefficient, and has no deleterious effect on carrier mobility. N_v is closely related to the symmetry of the crystal structure. Low symmetry has very low κ_L and poor thermoelectric performance. The current superior TE materials usually have a high symmetry crystal structure and symmetry-related multi-valley carrier structure (Zhang et al., 2014). To obtain more equivalent degenerate valleys and peaks, the N_v and Seebeck coefficients can be increased. For example, Zhao's team found that due to the layered change of the crystal structure in the SnSe crystal structure, different N_v causes different m_b^* in different directions, and the ZT value changes (Zhao et al., 2016). Then, Jiawei Zhang designs a constrained cubic structure by coexisting a long-range cubic frame and a partial short-range cubic lattice distortion (Zhang et al., 2014). By controlling the crystal structure of diamond distortion (Li et al., 2018), achieves low symmetry with convergence, while reducing the lattice thermal conductivity and increasing ZT values, it is shown

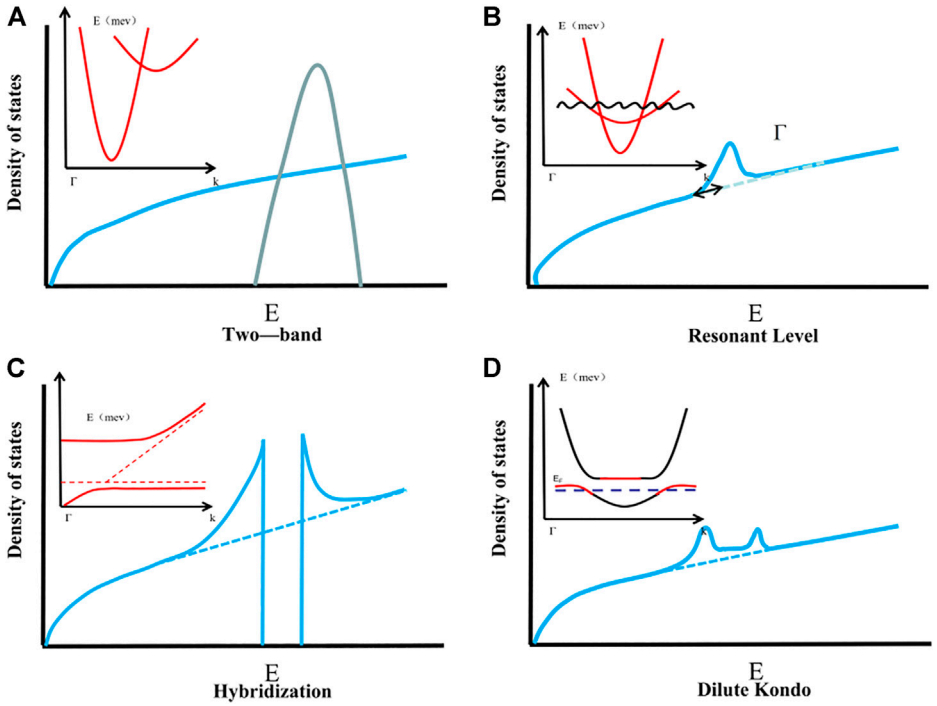

FIGURE 6 | Four ways to improve effective mass: **(A)** Degenerate energy band; **(B)** Increase resonance state; **(C)** Hybrid energy gap; **(D)** Doping Kondo atoms.

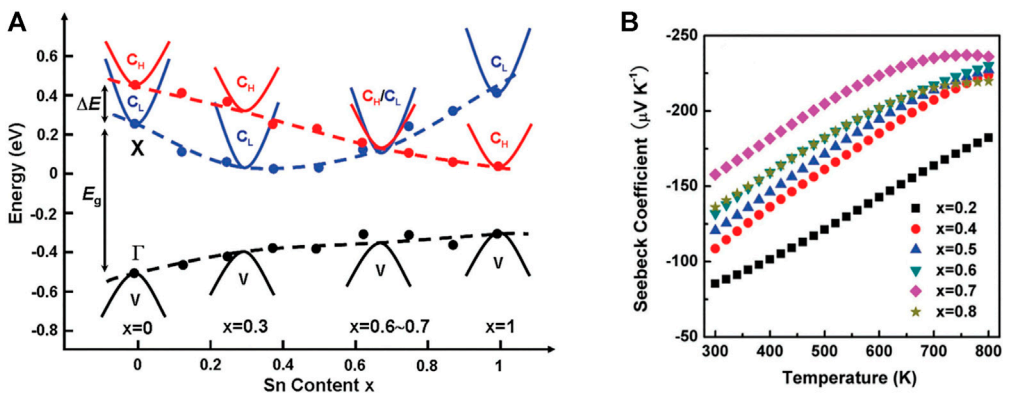

FIGURE 7 | (A) The relationship between the tin content in the $Mg_2Si_{1-x}Sn_x$ solid solution and the relative position of the weight and light transmission bands and the highest valence band; **(B)** the temperature dependence of the Seebeck coefficient of the n-type $Mg_2Si_{1-x}Sn_x$ solid solution (Su et al., 2017).

that the symmetry breaking with degeneracy is small, and the high simplification and low lattice thermal conductivity can be realized simultaneously. This method of reconstructing the approximate cubic structure to obtain a highly symmetrical crystal structure is considered to be a feasible approach to obtaining a larger N_v and a higher Seebeck coefficient.

Another effective method to improve N_v is to converge the different bands in the Brillouin region within the nk_BT of each other's energy. The valley number in the conduction band and the peak number in the valence band increase, so that the mobility is not affected by N_v. For example, Su et al. (2017) regulates N_V according to the formation of $Mg_2Si_{1-x}Sn_x$ in the solid solution, when the concentration of Sn is close to $x = 0.7$, the band edges of the two conduction bands are guaranteed to overlap, and the band convergence is realized, as shown in **Figure 7A**. Due to the increase of m_d^*, the Seebeck coefficient reaches its maximum value (as shown in **Figure 7B**), resulting in abnormally high TE performance at 700 K ($ZT = 1.3$). It is proved that by doping, the band structure with multiple extreme values can be formed at the top or bottom of the valence band, or the convergence of light band and heavy band can increase the degeneration of the band, so as to obtain better thermoelectric performance.

The introduction of the resonance state can cause the density of states to be distorted (as shown in **Figure 6B**). If the Fermi energy E_F falls near the center of the resonance band, the PbTe density of states is distorted in **Figure 6B**, resulting in a large increase in the Seebeck coefficient. It is mainly achieved by doping, usually because after the resonant impurity atoms are introduced into the complete periodic structure, the same energy level and different energy states are superimposed so that the energy band of the doped impurity falls below the edge of the valence band or the host above the edge. In general, the lower the resonance level, the greater the distortion of the electronic density of states, and the Seebeck coefficient will increase (Dutta et al., 2020). Heremans et al. (2008) used PbTe doping with Ti and found that the electron DOS was enhanced near the Fermi level. Later, Tan et al. (2016a) used Na atoms to replace vacancies and defects in PbTe, which once again proved that doping can actually increase the effective mass of the density of states and increase the *ZT* value. However, Pei et al. (2012b) improved the effective mass by doping La in PbTe. They found that the effective mass is temperature-dependent, and the increase in the effective mass leads to an increase in the Seebeck coefficient, but it actually increases the *ZT* value significantly in the lower temperature range (Pei et al., 2012b), slightly deviating from the previous rule. Therefore, the core law of changing the effective mass of the density of states through the introduction of the resonance state to increase the *ZT* value needs further exploration.

The hybrid energy gap is another way to increase the effective mass of the density of states, as shown in **Figure 6C**. However, this method has great limitations on the change of the density of states. It will cause the carrier mobility of the material to drop to zero in a certain energy interval, and make the effective mass return to zero, which is fatal to the thermoelectric performance. However, the hybrid energy gap in its vicinity can effectively increase the effective mass of its density of states, and enhance the thermoelectric performance. For example, Tan et al. (2019) introduced an internal axis nanostructure into n-type PbTe, and they performed CdTe alloying and Sb doping on it, which enhanced the effective mass of state density by expanding the band gap, and increased the Seebeck coefficient. Improving the thermoelectric performance is also an effective method to enhance the Seebeck coefficient.

The Kondo effect may be triggered in some thermoelectric systems doped with magnetic atoms. The study found that the electrical conductivity of the material is higher when the Kondo temperature is near. The coupling of these Kondo atoms with nearby electrons will form a larger-scale Kondo cloud, which has an enhancement effect on the density of states, as shown in **Figure 6D**. Lu et al. (2015) maintains the additional valence band of the conductive spin-split Ni state by adding Ni-doped tetrahedral $Cu_{12}Sb_4S_{13}$, electrons fill holes in the valence band, and the resulting Kondo effect increases the thermoelectric performance by more than 30%. Qiu et al. (2014) used Fe doped Cu_2S at 900 K, the maximum *ZT* reaches 1.2, because Fe atoms are randomly distributed on the substrate to form a Kondo cloud, which leads to higher stability than Cu_2S (Tan et al., 2019). However, the Kondo effect will also reduce the electrical conductivity of the material when the Kondo temperature is far away, or the Kondo cloud-scale is too large, which is not suitable for increasing the *ZT* value. Therefore, it is generally used to dope Kondo atoms, while ensuring that the system application range is at the Kondo temperature. In the vicinity, the *ZT* value is guaranteed to increase. However, the current interpretation of the Kondo effect is still in its infancy, and there is a wide range of design prospects in the later period.

There have been extensive studies on improving the Seebeck coefficient by adjusting the effective mass through energy band engineering, but the improvement of the effective mass also means the reduction of carrier mobility, so blindly improving the effective mass is not necessarily beneficial to increasing the *ZT* value, even Some scholars believe that reducing the effective mass of energy bands in some systems can increase the *ZT* value (Pei et al., 2012a). Therefore, how to balance the relationship between effective mass and carrier mobility to achieve the maximum *ZT* value still needs further investigation and verification.

REDUCTION OF LATTICE THERMAL CONDUCTIVITY

The lattice thermal conductivity κ_L is an independent influencing factor, and it is the most direct and effective means to optimize the thermal power figure.

According to the lattice thermal conductivity formula:

$$\kappa_L = \frac{1}{3} C_v V_g l = \frac{1}{3} C_v V_g^2 \tau \tag{6}$$

(where C_v is the constant volume heat capacity, V_g is the group velocity of the phonon vibration mode, l is the mean free path, and τ is the phonon relaxation time) affects the lattice thermal conductivity. The main factors of the rate are heat capacity, speed of sound, and relaxation time. Therefore, by reducing any parameter, the lattice thermal conductivity can be reduced. The atomic point defects formed by element substitution and the nanostructures formed by the nucleation and growth of the second phase can significantly scatter short-wave phonons and medium-wave phonons, respectively. It is precise because the new structure generates an increased probability of phonon collisions, reduces the mean free path of phonons and the relaxation time of phonons, and enhances phonon scattering. And when the size of the defect in the material is close to the mean free path of the phonon, it will have a greater scattering effect on the phonon (Zhao et al., 2014c). According to the thermal conductivity model proposed by Klemens and Callaway (Callaway, 1959; Klemens, 1960), the degree of scattering reduction can be written by the scattering parameter evaluation (Γ) as:

$$\Gamma = x(1-x)\left[\left(\frac{\Delta M}{M}\right)^2 + \varepsilon\left(\frac{a_{disorder} - a_{pure}}{a_{pure}}\right)^2\right] \tag{7}$$

where x is the doping fraction, $\Delta M/M$ is the rate of change of relative atomic mass, $\alpha_{disorder}$ and α_{pure} represent the lattice constants of disordered and pure alloys, and ε is an elasticity-related adjustment parameter. Here we can find that maximizing Γ will result in the lowest lattice thermal conductivity. Generally,

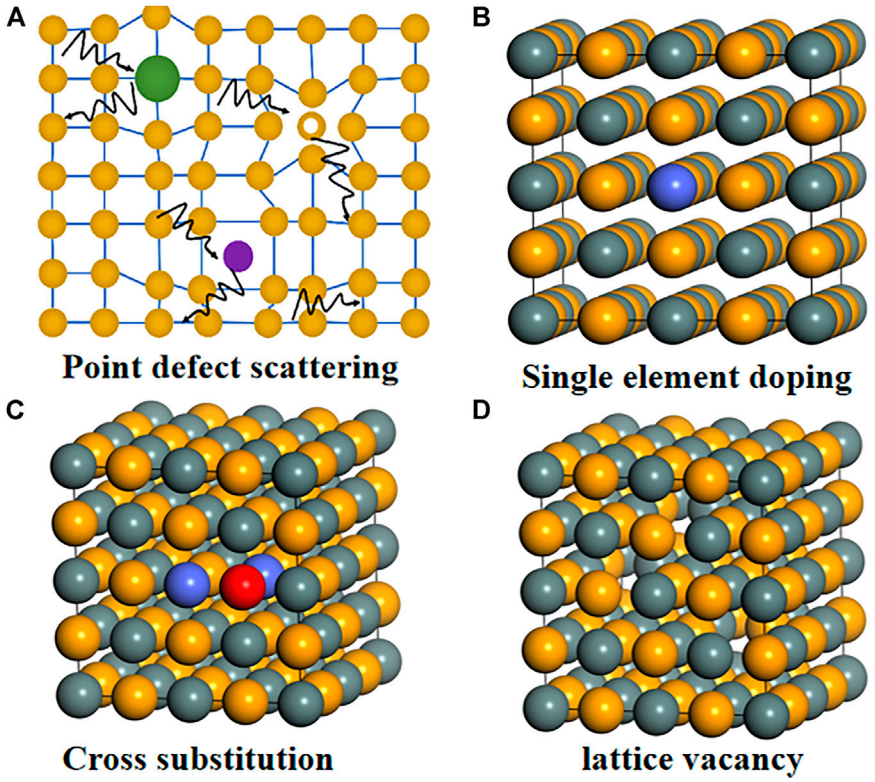

FIGURE 8 | Schematic diagram of point defect scattering and atomic-scale doping methods; **(A)** Schematic diagram of point defect scattering; **(B)** single-atom doping; **(C)** polyatomic doping; **(D)** lattice vacancy.

higher doping fractions, heavy element doping, and greater lattice mismatch can be used to reduce irritation. Next, we use several scattering mechanisms such as point defect scattering, dislocation scattering, interface scattering, and phonon resonance scattering to explain the influence of the above factors.

Point Defect Scattering

Introducing lattice point defects into the matrix lattice is an effective way to reduce the thermal conductivity of the lattice, as shown in **Figure 8A**. This is because phonons are more likely to be scattered by point defects rather than electrons, and thus have less impact on carrier mobility. **Figures 8B–D** show typical doping methods commonly used in thermoelectric materials research, namely single element doping, cross-substitution, and formation of lattice vacancies. In the case of single doping, the dopant can be the same valence as the main element, resulting in lattice disorder, or it can be heterovalent, so as to control the carrier concentration. However, this doping causes the system charge imbalance, which may hinder the reduction of κ_L if done alone.

To improve the solubility of different elements, cross-substitution is generally used. Cross-substitution refers to the pair-to-pair substitution of one or more main elements from other groups in the periodic table, while keeping the total number of valence electrons unchanged (Tan et al., 2013; Tan et al., 2015b).

Yu et al. (2018a) designed thermoelectric materials by isoelectronic substitution of the atom Ta for the atom Nb. By using isoelectronic substitution of atoms with similar size and chemical properties but the large mass difference, the lattice thermal conductivity of the alloy was greatly suppressed, but good electrical properties were maintained. As a result, the *ZT* reaches a peak of 1.6 at a Ta content of 0.4. It shows that the point defects caused by the substitute atoms will change the thermal conductivity of the lattice (Yu et al., 2018a). It is worth noting that the cross-substitution not only greatly affects the transport of phonons, but may also change the electronic structure (mainly the band gap), providing other ways to adjust the thermoelectric properties of the matrix material. Because only when these two heterogeneous elements exist together in a specific ratio, the amount of them entering the matrix will be greater. We call this effect synergistic alloying. In the $Pb_{0.98}Na_{0.02}Te$-8% SrTe sample, the *ZT* value is 2.5 at 923 K, and the average *ZT* value is 1.67 in the range of 300–900 K. It is further proved that by optimizing the Na concentration, a *ZT* of 2.5 can be obtained at a lower temperature of about 800 K (Xu et al., 2020a). Alloying is currently the most widely used method to enhance the scattering of point defects, in Bi_2Te_3 (Hu et al., 2014; Chen et al., 2015), Pb(Te, Se) (Pei et al., 2011), GeTe (Chen et al., 2020) and Half-Heusler (HH) alloys (Xue et al., 2016; Shen et al., 2018; Yu et al., 2018b) have applications.

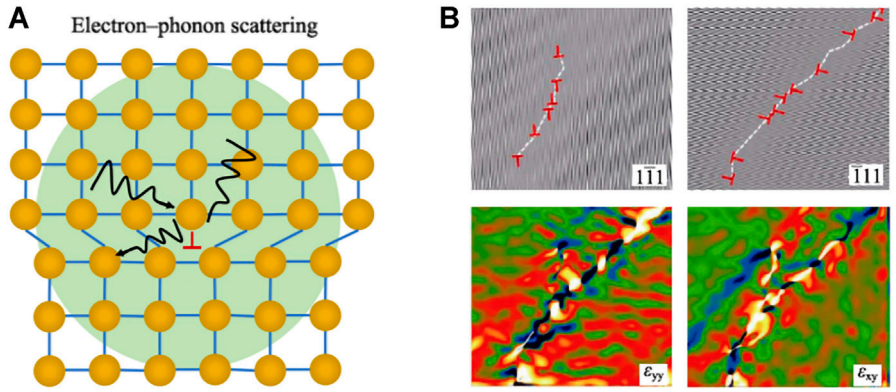

FIGURE 9 | (A) Schematic diagram of dislocation scattering; **(B)** IFFT diagram of dislocation in $Mg_2Si_{0.5}Sb_{0.5}$ and the corresponding stress scan diagram (Xin et al., 2017).

In addition to alloying, vacancies and interstitial atoms also belong to a relatively special point defect scattering mechanism (Xue et al., 2016). Jiaqing He introduced double-vacancy defects by doping BiI_3 (Xu et al., 2020b) to improve the thermoelectric performance of $Sb_2Te_3(GeTe)_{17}$. The maximum value of *ZT* is 2.2 at 723 K. There are nearly 20% intrinsic Nb vacancies in the HH alloy $Nb_{0.8}CoSb$, which makes the $Nb_{0.8}CoSb$ alloy have a relatively low lattice thermal conductivity (Xia et al., 2018). The same phenomenon exists in thermoelectric materials such as Cu_2SnSe_4 (Li et al., 2016). Like vacancies, interstitial atoms can also be generated by a solid solution method, but only compounds with a larger cation-anion ratio are applicable. The cations of such compounds need to have a smaller radius to fit the interstitial sites. Taking the solid solution $(SnTe)_{1-x}(Cu_2Te)_x$ as an example (Li et al., 2017; Zheng et al., 2017), its lattice thermal conductivity is as low as 0.5 $W\,m^{-1}\,K^{-1}$, which is close to the minimum lattice thermal conductivity limit of SnTe (About 0.4 $W\,m^{-1}\,K^{-1}$).

Dislocation Scattering

Dislocations are a typical line defect, especially in metal materials. Dislocations and strain fields will scatter mid-and high-frequency phonons, so dislocations can effectively reduce the free path of phonons (**Figure 9A**). Kim et al. (2015) reported that by forming a high-density dislocation array at the grain boundary by extrusion, the lattice thermal conductivity of the $Bi_{0.5}Sb_{1.5}Te_3$ material could be significantly reduced, which is a dense dislocation array pair. The result of phonon scattering. In addition, dislocations can also be introduced through the precipitation of the second phase, where dislocations can play a role in reconciling the lattice mismatch at the phase boundary (Hu et al., 2015).

In solid solution materials, due to the accumulation of vacancies, adjacent spaces collapse under external conditions to form vacancy dislocations. At the same time, vacancies will also spontaneously reduce energy. The released energy can promote dislocations to climb. The climbing motion of dislocations will increase the density of dislocations, and finally produce high-density and uniformly distributed dislocations in the crystal grain, thereby reducing κ_L. In $Mg_2Si_{1-x}Sb_x$ materials (Xin et al., 2017), high-dose alloying of Sb has a large number of Mg vacancies, making the vacancy concentration much higher than the equilibrium vacancy density, and the excess Mg vacancies spontaneously aggregate to form dislocations, as shown in **Figure 9B**. In $Mg_2Si_{0.5}Sb_{0.5}$, the dislocation density is as high as $2.8 \times 10^{16}\,m^{-2}$. Besides, similar phenomena were also observed in the $Na_yEu_{0.03}Pb_{0.97-y}Te$ system (Chen et al., 2017). Studies have shown that with the increase of Na doping, the main microscopic defects in the system gradually change from point defects to dislocations. Dislocation scattering reduces the lattice thermal conductivity of PbTe to below 0.4 $W\,m^{-1}\,K^{-1}$.

Interface Scattering

Because atomic defects and dislocation defects can effectively scatter low- and mid-wavelength phonons, there are still some long-wavelength phonons that are not scattered and affect the thermal conductivity of the lattice. In polycrystalline materials, grain boundaries or phase boundaries can effectively scatter low-frequency phonons, and the scattering rate is inversely proportional to the grain size. Therefore, the effective method to effectively scatter long-wavelength phonons is to introduce micro-nano structures (Girard et al., 2010). The mechanism of action is shown in **Figure 10A**. In particular, nanostructures have been proven to be an effective method to enhance *ZT* by placing suitable nano-scale precipitates in the matrix to reduce κ_L, such as $AgPb_mSbTe_{m+2}$ (Hsu et al., 2004), $NaPb_xSbTe_{2-x}$ (Poudeu et al., 2006) and PbTe-Ag_2Te (Zhao et al., 2013a). In addition, p-type $PbTe_{1-x}Se_x$ (Pei et al., 2011) and Tl-PbTe (Heremans et al., 2008) also have excellent thermoelectric properties, which come from the introduction of multiple valence bands and the density of states distortions in the valence band, respectively. Biswas et al. (2012), Liu et al. (2016), and others considered phonon scattering sources on all scales from the perspective of a layered approach, ranging from atomic-scale lattice disorder and nano-scale internal deposits to mesoscale crystals. The thermal conductivity of the crystal lattice is greatly reduced. Finally, the *ZT* of PbTe-SrTe is 2.2, and the *ZT* of

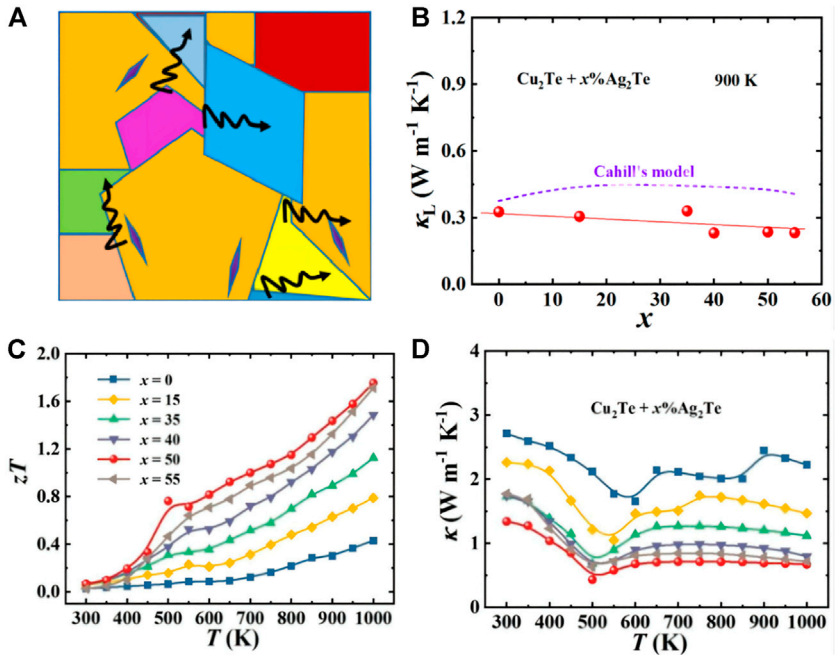

FIGURE 10 | (A) Schematic diagram of interface scattering; **(B)** lattice thermal conductivity κ_L at 900 K for all samples of $Cu_2Te + x\%$ Ag_2Te; **(C)** and **(D)** are $Cu_2Te + x\%$ Ag_2Te(x = 0, 15, 35, 40, 50, and 55) thermal conductivity (κ), thermoelectric figure of merit (*ZT*) varies with temperature (Zhao et al., 2019).

$Bi_{0.88}Ca_{0.06}Pb_{0.06}CuSeO$ is 1.5, which proves that the grain boundary scattering is important in reducing the thermal conductivity. Zhao et al. (2019) introduced the Ag_2Te phase into Cu_2Te. Due to multiple phase transitions, they show complex temperature dependence in the temperature range of 300–1000 K. As the Ag_2Te content increases, the interface scattering increases, and κ_L decreases significantly (as shown in **Figures 10B–D**). At the same time, its highest *ZT* value reaches 1.8. It shows ultra-low lattice thermal conductivity at 900 K, and its value is about 0.3 W m^{-1} K^{-1} (Zhao et al., 2019).

Commonly used methods to enhance grain boundary scattering include ball milling (Li et al., 2015) and plasma sintering (Xie et al., 2018), etc., to obtain finer or smaller grains from coarser-grained crystal powders to increase the grain boundary area. Li et al. (2015) prepared nanostructured $Na_{0.02}Pb_{0.98}Te$ samples with a grain size of 20–100 nm through high-energy ball milling and semi-solid powder processing. Through observation, they found that the interface between the particles can be clearly seen. The size (0.1–1 μm) of the pores, so there is stronger phonon scattering at the grain boundary, which reduces the lattice thermal conductivity κ_L to 0.74 W m^{-1} K^{-1} at 623 K. Similarly, Yu et al. (2017) combined melt spinning, ball milling and spark plasma sintering processes to construct a microstructure containing a large number of 60° twin grain boundaries in the $Bi_{0.5}Sb_{1.5}Te_3$ liquid alloy. The bilateral grain boundaries not only increase the current load mobility, and its scattering effect on phonons greatly reduces the thermal conductivity, so that $ZT = 1.42$ at 348 K (Yu et al., 2017).

In addition to the above methods, the process of separating the micro-nano phases to form twin crystals and dislocation network structures can also increase the grain boundary area, thereby enhancing phonon scattering and reducing thermal conductivity (Kim et al., 2015). Gelbstein et al. (2013) separated the p-type $Ge_{0.87}Pb_{0.13}Te$ into two phases of GeTe and PbTe through spark plasma sintering, thereby generating the characteristics of multiple interfaces, enhancing the phonon scattering at the crystal plane, and achieving a relatively highly stable TE Performance.

It can be seen that defects of different sizes prepared by doping in materials and related physical and chemical methods can effectively scatter phonons of different wavelengths and different free paths, thereby reducing the thermal conductivity of the lattice. Therefore, the changes in energy band and structure (mass ratio and degree of distortion) caused by the coordinated effect of point defect scattering, dislocation scattering, and interface scattering will enhance the scattering of phonons at different wavelength levels simultaneously (Li et al., 2018; Lee et al., 2019).

Resonance Scattering

Resonance scattering is generally used in thermoelectric materials with special crystal structures, such as cage compounds (Christensen et al., 2008; Beekman and VanderGraaff, 2017), skutterudite (Duan et al., 2016), and some thermoelectric materials with topological insulation (Wei et al., 2016; Zeugner et al., 2019). By adding filler atoms, a strong local vibration close to the vibration frequency is generated, and a resonance spectrum of a specific frequency (shown in **Figure 11**) is introduced, thereby reducing the thermal conductivity.

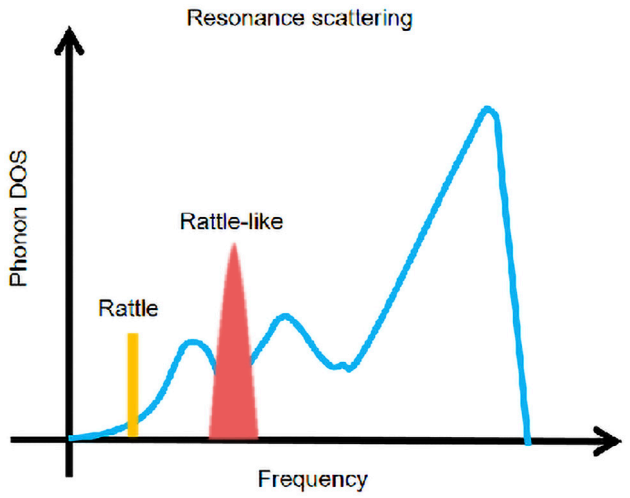

FIGURE 11 | Schematic spectrum of resonance scattering at a specific frequency.

Researchers fill $CoSb_3$ with S and Se as electronegative objects under equilibrium conditions. Because S and Se have unique localized "cluster vibrations," a section can be introduced in the phonon spectrum. The optical branch with lower frequency is coupled with the acoustic branch, which significantly affects the lattice dynamics, greatly reduces the thermal conductivity of the lattice, and obtains $S_{0.26}Co_4Sb_{11.11}Te_{0.73}$ with ZT = 1.5 at 850 K (Zeugner et al., 2019). In recent years, research on topological insulating thermoelectric materials has gradually increased, and many studies have also shown that some of them have resonance scattering. Samanta et al. (2018) reported a layered structure of n-type BiSe (Se-Bi-Se-Bi-Se), the study found that the local vibration generated by the Bi layer can cause some low-energy optical branches to inhibit the propagation of the acoustic branches (i.e., photoacoustic coupling), and the sound wave branch with low cut-off frequency and strong anharmonic vibration Phonon interaction further reduces the thermal conductivity, and finally κ_L = 0.3 W m^{-1} K^{-1} at 300 K. Similarly, Wei et al. (2016), Christensen et al. (2008) predicted the minimum thermal conductivity of bismuth-based stacked structures with topological insulation and found that the NI layer has a strong influence on Bi_2TeI lattice dynamics and impedes phonon propagation, with low-frequency photo-phonon and phonon interactions arising from local vibrations of the NI layer causing a high degree of lattice anharmonicity and producing extremely low thermal conductivity. Moreover, Ying et al. (2017) studied the cause and physical mechanism of the intrinsic low thermal conductivity of α-MgAgSb thermoelectric materials and predicted a class of thermoelectric material systems with low thermal conductivity. The study found that α-MgAgSb has weak chemical bonds in addition to layering. In addition to the low sound velocity, the half-Heusler-like twisted lattice makes it form a Mg-Ag-Sb triple-center bond structure (**Figures 12A,B**). The Ag atoms in the Mg-Ag-Sb tri-center bond can move reciprocally in the direction of the arrow to a greater extent, forming a low-frequency optical branch in the phonon spectrum (**Figure 12C**). These low-frequency optical branches can generate resonance scattering and effectively reduce the thermal conductivity of the lattice (Ying et al., 2017). It can be seen from the above that the research on reducing thermal conductivity through resonance scattering is becoming more mature.

THERMOELECTRIC MATERIALS WITH LOW THERMAL CONDUCTIVITY

The use of low-dimensional defects and nanocomposite structures to reduce multi-scale phonon scattering and reduction of existing TE materials κ_L does significantly increase the ZT value of thermoelectric materials, but existing methods at this stage will affect thermal stability and other issues. The search for thermoelectric materials with intrinsically low thermal conductivity is therefore also a necessary way to avoid the problems associated with reducing the thermal conductivity of existing materials. Most of the thermoelectric materials with an intrinsic low thermal conductivity that have been discovered so far have the characteristics of weak chemical bonding (Zhao et al., 2014a), strong anharmonic effects (Zhao et al., 2014d), liquid ionic properties (Liu et al., 2012), heavy molecular mass (Toberer et al., 2010), complex crystal structure (Kurosaki et al., 2005), etc. We will briefly describe the representative thermoelectric materials from the following five points.

Weak Chemical Bond

The lattice thermal conductivity is proportional to the speed of sound, so obtaining low sound speed performance often helps to improve the thermoelectric properties of the material. Materials with weak chemical bonds have a lower speed of sound, atoms have more space for movement near their equilibrium positions, and electron cloud distribution is more diffuse. In the phonon spectrum, weak chemical bonds often correspond to some low-frequency phonon models, which are easier to couple with the acoustic branch, thereby further reducing the contribution of the acoustic branch to the thermal conductivity.

SnSe is a typical simple thermoelectric material with weak chemical bonds and is very stable. SnSe has an orthogonal layer structure in the room temperature range. The Sn-Se bond in the bc direction is stronger and weaker in a direction. It is easy to cleave along the (100) plane and form a foldable projection in the b-axis direction. The structure contains a highly distorted $SnSe_7$ coordination polyhedron with three short Sn-Se bonds and four long Sn-Se bonds. Such a special structure makes it have strong non-resonance and high anisotropy, which essentially has ultra-low thermal conductivity. Lidong Zhao et al. prepared SnSe single crystal by the Briman method and found that the special crystal structure of SnSe (as shown in **Figure 13A**) made SnSe have a very low κ_L, and the room temperature thermal conductivity of SnSe in the direction of the axis a was about 0.47 W m^{-1} K^{-1}. With the increase of temperature, the thermal conductivity at 973 K decreased to about 0.23 W m^{-1} K^{-1} (as shown in **Figures 13A, C**), and a historic breakthrough was made at 923 K with a

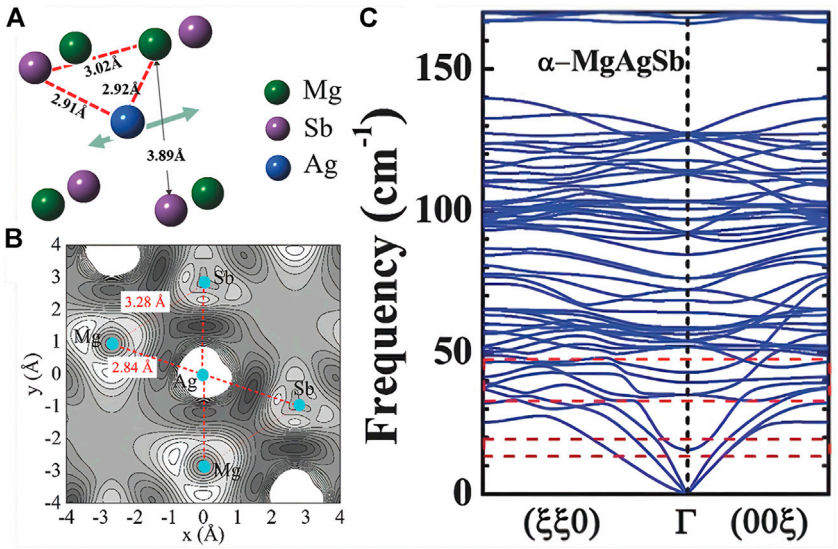

FIGURE 12 | (A) Schematic diagram of the three-center bond structure in α-MgAgSb; **(B)** α-MgAgSb charge distribution diagram; **(C)** α-MgAgSb phonon spectrum (Ying et al., 2017).

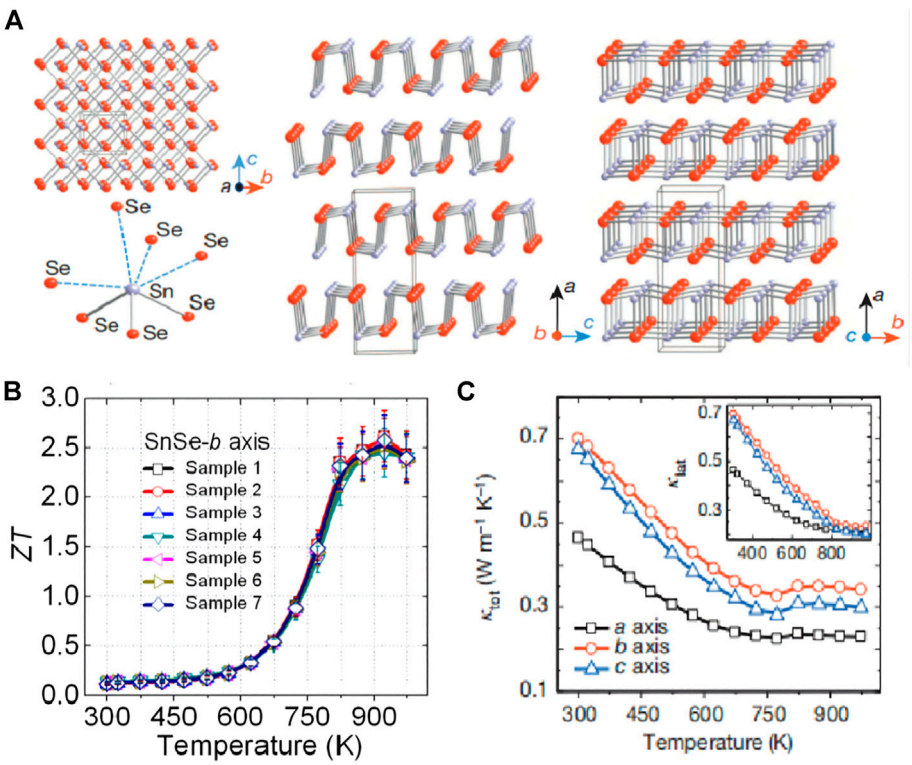

FIGURE 13 | (A) SnSe crystal structure along the a-axis: gray, tin atoms; red, selenium atoms; highly distorted $SnSe_7$ coordination polyhedron with three short and four long Sn-Se bonds; structure along the b-axis; Structure along the c axis; **(B)** SnSe along the b axis *ZT* value changes with temperature (T); **(C)** SnSe single crystal lattice thermal conductivity (κ_L) changes with temperature (T) in the a, b, and c directions (Zhao et al., 2014a).

ZT of 2.6 along the b-axis (as shown in **Figure 13B**) (Zhao et al., 2014a). Subsequently, Zhao et al. (2014a) synthesized an n-type SnSe crystal with a two-dimensional layered structure with *ZT* up to 2.8 (Chang et al., 2018). Similarly, based on the low thermal conductivity of SnSe, Qin et al. (2020) introduced $SnSe_2$ as an extrinsic defect dopant to increase the carrier concentration to 6.55×10^{19} cm^{-3} while increasing the effective Mass and Seebeck coefficient, obtained an unusually high power factor at room temperature (about 5.4×10^{-2} W m^{-1} K^{-2}), so that the maximum *ZT* value reached 2.2 and the average *ZT* value reached 1.7.

In addition to single crystals SnSe, polycrystalline SnSe has gradually been widely used in research due to its thermal conductivity comparable to that of single crystals SnSe. Although SnSe crystals have strong anisotropy, polycrystalline materials have more carrier migration than single crystals SnSe materials. The rate is much lower, and the conductivity is very low, but therefore, increasing the conductivity has become an important way to improve the thermoelectric properties of polycrystalline SnSe. Zhang et al. (2015) prepared n-type SnSe polycrystalline powder by using I doping and SnS solid solution, and processed it in a vacuum device, and found that the thermal conductivity of polycrystalline SnSe would decrease, approaching 0.30 W m^{-1} K^{-1} at 773 K, which makes $ZT = 1$ finally.

Perhaps because polycrystalline materials have many dislocations, vacancies, bond deformations, and other defects in the grain boundary during the powder metallurgy process, they are in a state of stress distortion, and the energy is high, which makes the material in an unstable state at high temperatures, resulting in relatively poor performance. There are many speculations about the reason for the low thermal conductivity of SnSe. For example, the spring-type crystal structure of SnSe has a great shock-absorbing and buffering effect on the transmission of phonons in it (Heremans, 2014). Therefore, the thermal conductivity of SnSe still needs further investigation and verification.

Non-Resonance Effect

The resonance effect refers to the balance of external forces experienced by phonons during the transmission process. The sound wave transmits uniformly forward in the form of a parabola, which is similar to the transmission in a perfect lattice, but when the transmission of phonons is affected by external factors, it will deviate from the equilibrium position and cause non-resonance effects. The strength of anharmonicity is mainly related to the symmetry of chemical bonds and atomic equilibrium positions. During the vibration of an atom, the greater the deviation of its symmetry center, the stronger the asymmetry. Materials with lone pairs of electrons are often due to the uneven distribution of the electron cloud, the crystal structure will be deformed to a certain extent, and the asymmetry is significantly enhanced, which is beneficial to obtain strong anharmonicity.

Because there are two isolated electrons in the outermost layer of the Sb nucleus. The two lone electrons in the outermost layer of the nucleus will make the transmission of phonons unbalanced, resulting in non-resonance effects, resulting in Sb compounds with low heat transport properties. In the same way, compounds with Bi atoms belonging to the same group as Sb atoms should also have anharmonic effects. Therefore, the common thermoelectric materials with intrinsic low thermal conductivity of this kind are $AgSbSe_2$, BiCuSeO, and so on. The room temperature thermal conductivity of $AgSbSe_2$ is 0.48 W m^{-1} K^{-1} (Nielsen et al., 2013), which is lower than most thermoelectric materials at room temperature. In recent years, some people have introduced $AgSbSe_2$ into GeTe to prepare $(GeTe)_{80}$ $(AgSbSe_2)_{20}$. The introduction of hierarchical nano/mesoporous structure inside the material causes large-scale scattering of phonons, which reduces the lattice thermal conductivity κ_L to 0.4 W m^{-1} K^{-1} at 300–700 K, which is close to the thermal conductivity of GeTe. The theoretical limit of the rate finally makes its ZT_{max} reach 1.9 at 660 K (Samanta et al., 2017). Later, Gao et al. (2018) used the method of mechanical alloying and rapid hot pressing to manufacture Ca doped $AgSbSe_2$ with the layered structure. Ca doping further optimized the carrier concentration and caused the point defect scattering of phonons, and obtained the ultra-low lattice thermal conductivity of 0.27 W m^{-1} K^{-1} at 673 K, thus increasing the *ZT* peak value to 1.2.

Since BiCuSeO was reported in 2010 (Zhao et al., 2010), BiCuSeO is considered to be one of the most promising oxygen-containing thermoelectric materials due to its special natural superlattice structure and corresponding ultra-low thermal conductivity. Later, researchers found that in BiCuSeO, modulating doping to increase carrier mobility can greatly improve thermoelectric performance. Modulating the heterostructure of the doped sample makes the carriers preferentially transport in the low carrier concentration region, which increases the carrier mobility by 2 times while maintaining the carrier concentration similar to the uniformly doped sample. The synergistic effect of the increased conductivity and the basically constant Seebeck coefficient results in a wide range of high power factors, about 5–10 $\times$ 10^{-2} W cm^{-1} K^{-2}. The combination of ultra-high power factor and extremely low thermal conductivity (about 0.25 W m^{-1} K^{-1}) enables BiCuSeO to obtain a high *ZT* $\approx$ 1.4 at 923 K (Pei et al., 2014).

Later, with the widespread acceptance of simulation calculations, Saha (2015) used first-principles density functional theory calculations to propose the atomic displacement map of the lowest frequency optical mode of BiCuSeO, and systematically studied the correlation of BiCuSeO (such as dielectric and Anharmonic) characteristics, and compared with LaCuSeO of the same structure, it is found that the reason for the ultra-low thermal conductivity κ of BiCuSeO is that the Bi atom exhibits a significant displacement during the action, which indicates that it has a higher anharmonic effect. Furthermore, the calculated out-of-plane thermal conductivity of BiCuSeO is approximately twice that of the in-plane thermal conductivity, which indicates that BiCuSeO has a greater anisotropy of heat flow between in-plane and out-of-plane.

Ionic Liquid Characteristics

In solid, $C_v = 3N_kB$, while in liquid, most transverse vibration waves cannot be transmitted, C_v decreases to 2–2.5N_kB, and N_k is the total atomic number. Therefore, materials with liquid properties often have relatively low thermal conductivity due to their small heat capacity. Ionic conductors introduce some ions with "liquid" characteristics into solid materials to form an ionic liquid-like semiconductor, thus reducing the lattice thermal conductivity to a level lower than that of glass, which can not only reduce the mean free path of phonons but also eliminate lattice vibration. $Cu_{2-x}Se$ compounds belong to this class of ion-electron composite conductors with special structures with two-phase structures at room temperature (transition from low-temperature α phase to high-temperature β phase at 400 K). The lattice network structure of $Cu_{2-x}Se$ face-centred cubic Se atoms provides a good electrical transport pathway for the randomly distributed free movement of Cu ions in the interstitial positions, which enhances the scattered lattice phonons while reducing some lattice vibrational modes, so that the lattice heat capacity of the material decreases with increasing temperature and ultimately low thermal conductivity properties can be obtained.

Skomorokhov et al. (2006) experimentally found the local migration of Cu atoms in Cu_2Se. Later, Liu et al. (2012) found that the abnormal "liquid-like" behavior of copper ions around the crystalline sublattice of Se in $Cu_{2-x}Se$ (**Figure 3** shows the simple Face-centered cubic structure of Se atoms in the High-temperature β phase) leads to essentially very low lattice thermal conductivity (0.4–0.6 W m^{-1} K^{-1}), thus achieving high ZT = 1.5 (T = 1,000 K) in this originally simple semiconductor. This unusual combination of properties resulted in ideal thermoelectric materials. The results show that exploring the network structure with electron conduction sublattices surrounded by liquid ions can provide new strategies and directions for High-efficiency thermoelectric materials.

Subsequently, Zhong et al. (2014) generated highly aligned wafers in the bulk $Cu_{1.94}Al_{0.02}Se$ by the direct current hot pressing process according to the alternating arrangement of single disordered layers of Se ions and double disordered layers of Cu ions. The superionic mechanism in $Cu_{1.94}Al_{0.02}Se$ was further enhanced by the enhancement of Cu ions and high crystal orientation. Finally, ZT = 2.62 was obtained at 756°C (Zhong et al., 2014). This study also provides a reliable way to use the superior mechanism. In the research process of $Cu_{2-x}Se$, the high fluidity of copper ions causes problems such as thermal stability during the preparation of $Cu_{2-x}Se$, which prevents the development of $Cu_{2-X}Se$. Therefore, it is also necessary to consider how to control such problems in the research process.

Molecular Weight

Heat capacity C_v is the important factor influencing the thermal conductivity and is proportional to the lattice thermal conductivity, based on the debye model for the heat capacity, the acoustic wave is the main source of contribution to the thermal conductivity, the assumption in a polyatomic system, the total number of the original cell of N, every cell in the atomic number is n, total system degrees of freedom to 3 nN, among them, the acoustic branch has 3N, optical 3(n−1)N, by the equipartition principle, the contribution of the acoustic branch heat capacity as the C/n, optical to C(n−1)/n (Toberer et al., 2011). Therefore, the total heat capacity remains unchanged. The more atoms in the primary cell, the less contribution of acoustic branches to the total heat capacity is, and the more conducive to obtaining low lattice thermal conductivity, which means that the thermoelectric materials with heavy molecular weight have certain advantages to obtain excellent thermoelectric properties. This has been demonstrated in many thermoelectric materials with complex crystal structures.

Zintl phase $Yb_{14}MnSb_{11}$ is a typical macromolecular mass material with a relative molecular weight of 3,783.088 g/mol, and its crystal structure is shown in **Figure 14C** (Wang Y. et al., 2018). Brown et al. (2006) found that electronic and thermal properties could be potentially modulated by doping at different locations in the $A_{14}MPn_{11}$ class of structures. Doped at cationic metal site A, the carrier concentration and phonon disordered scattering can be adjusted. Doped at cationic metal site A, the carrier concentration and phonon disordered scattering can be adjusted. Doping at a metal site M can adjust the electronic parameters, and for the first time by preparing Zintl phase $Yb_{14}MnSb_{11}$ to obtain the thermoelectric performance of the stability at high temperature, the thermal conductivity in about 0.7–0.9 W m^{-1} K^{-1} (400–1,300 K), the Seebeck coefficient reaches the maximum value of 185 μV/K at 1,275 K, and the ZT value reaches one at 1,223 K, which provides new guidance for the study of Zintl phase $Yb_{14}MnSb_{11}$.

Then, Cox et al. (2009) began to conduct Al doping on the metal sites of $Yb_{14}Mn_{1-x}Al_xSb_{11}$ structure to regulate electronic parameters. Studies have shown that within a certain range of heat capacity (300–1,100 K), as the aluminum content increases, the unit cell volume increases, and the bond distance changes less than 2%, which means that the increase in cell volume is related to the decrease in the deformation of the tetrahedron with the increase in Al content. When the ZT peak appears at 1,223 K, it deviates from the measurement range, indicating that the lattice thermal conductivity here is extremely low (about 0.3–0.4 W m^{-1} K^{-1}), as shown in **Figure 14A**. Subsequently, Uvarov et al. (2012) improved Seebeck's coefficient and reduced thermal conductivity by replacing Yb^{2+} with equivalent Ca^{2+} in $Yb_{14}MnSb_{11}$, thus increasing ZT and obtaining higher thermoelectric performance. Therefore, it can be seen that the thermoelectric materials with similar heavy molecular weight can be adjusted at different sites to obtain low lattice thermal conductivity and stable thermoelectric properties with great exploration value.

Complex Crystal Structure

It is well known that the main factors affecting the thermal conductivity of materials are heat capacity, sound velocity, and phonon relaxation time. The complex crystal structure not only reduces the contribution of the acoustic branches to the total heat capacity, but also reduces the group velocity of the acoustic branches.

Due to its complex crystal structure, Ag_9TlTe_5 has a heavy molecular mass, and the number of atoms in a single cell is 298.

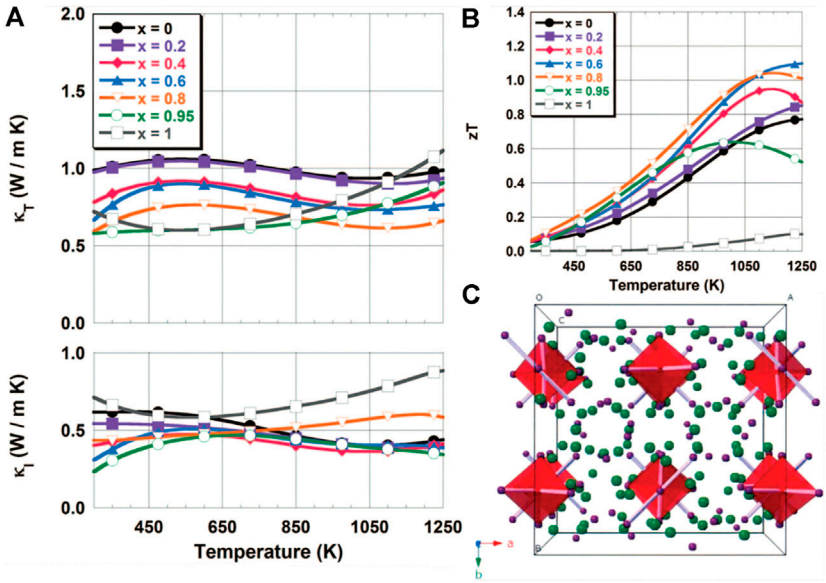

FIGURE 14 | (A) Variation of total thermal conductivity and lattice thermal conductivity of $Yb_{14}Mn_{1-x}Al_xSb_{11}$ with *x*; **(B)** The change of *ZT* with the temperature at different *x*; **(C)** The crystal structure of $Yb_{14}Mn_{1-x}Al_xSb_{11}$ (Cox et al., 2009).

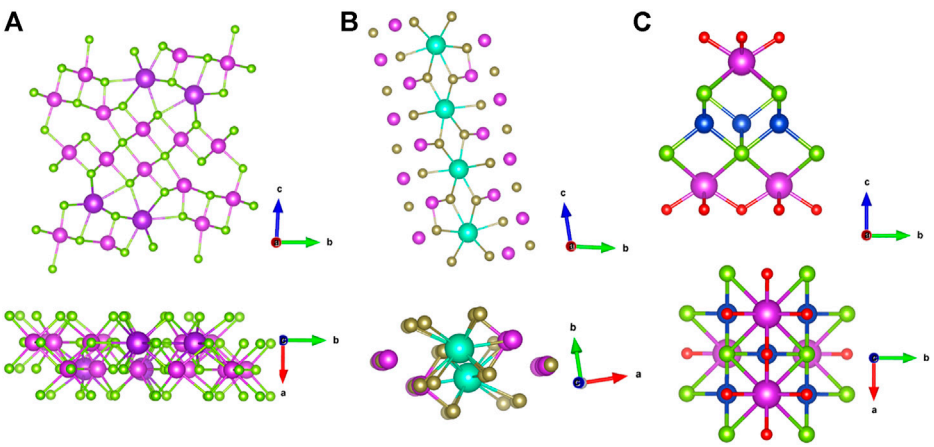

FIGURE 15 | Crystal structure of complex thermoelectric materials: **(A)** Crystal structure of β-$K_2Bi_8Se_{13}$; **(B)** Crystal structure of $CsBi_4Te_6$; **(C)** Crystal structure of BiCuSeO.

Meanwhile, the low elastic modulus indicates that the chemical bond of the material is weak. The thermal conductivity of Ag_9TlTe_5 remains about 0.25 W m^{-1} K^{-1} from room temperature to 650 K (Kurosaki et al., 2005), which makes the *ZT* of the material reach 1.25 at 673 K. The ternary alkali metal-bismuth-chalcogenides exhibit extremely low thermal conductivity due to their more complex crystal structure, such as β-$K_2Bi_8Se_{13}$ (**Figure 15A**), $CsBi_4Te_6$ (**Figure 15B**), etc. The low symmetry monoclinic crystal structure of β-$K_2Bi_8Se_{13}$ makes it highly anisotropic. β-$K_2Bi_8Se_{13}$ was first proposed by Meng et al. (2003), and its thermal conductivity is as low as 1.28 W m^{-1} K^{-1}. Afterwards, Kyratsi et al. (2011)prepared crystalline/amorphous β-$K_2Bi_8Se_{13}$ nanocomposites by ball milling the melt-synthesized polycrystalline β-$K_2Bi_8Se_{13}$ under an inert atmosphere. It was found that with the time of ball milling, the nanocrystalline phase gradually formed, the carrier concentration gradually decreased, the Seebeck coefficient gradually increased, and the thermal conductivity gradually decreased from the initial 1.28–0.3 W m^{-1} K^{-1}, which greatly improved the thermoelectric properties of β-$K_2Bi_8Se_{13}$, and provided a new and reliable idea for the follow-up research. In addition, there are many materials with complex crystal structures, such as Bicuseo (**Figure 15C**) and $Yb_{14}Mn_{1-x}Al_xSb_{11}$ mentioned above, all of which are more or less affected by their structures. Therefore,

given the many materials yet to be investigated, there is certainly much work ahead and promise for developing TE materials.

ELECTRON-PHONON DECOUPLING

In the above, we discussed that nanostructures in bulk materials greatly reduce thermal conductivity. However, due to the crystal mismatch or the electronic band of interface caused by the mismatch increased energy barrier, also can increase the carrier scattering, the carrier mobility and power factor have a negative effect, in other words, when doping material scale and the rise in the Numbers, thermal conductivity and electrical conductivity of coherence will increase, not conducive to improve the performance of thermoelectric (Zhao et al., 2013a). Therefore, ensuring high carrier mobility and wideband gap while fully regulating the thermal conductivity has become the key to the breakthrough of thermoelectric materials. The decoupling mode of electron and phonon transport is discussed below.

Slack proposed the concept of "Phonon glass and Electron Crystal" (PGEC), which can be used to guide the optimal design of thermoelectric materials. He believed that an ideal thermoelectric material should have phonon transport characteristics like glass and electron transport characteristics like crystal (Slack and Rowe, 1995). At present, the introduction of nano-sized precipitates can increase phonon scattering and produce very little electron scattering through interfacial interaction. When there is a coherent connection between the nano-precipitated phase and the matrix, but there is a certain tension around the interface (with nanostructure inside the tension), this interface is considered to promote the charge passing through, but strongly hinders the propagation of scattered phonons (Hsu et al., 2004; Cook et al., 2009). The coherent strain interface between the substrate and the nanometer precipitates results in strong phonon scattering, but the electron scattering is very small. Unfortunately, interfacial coherence can sometimes lead to asymmetry of energy band structure and generate potential barriers to hinder electron migration (Biswas et al., 2011). Although electron scattering can be minimized by improving the interfacial coherence of nanostructured materials, the energy barrier created by the asymmetry of electron bands hinders electron flow. Therefore, atomic fixation or nanometer phase minimization is generally used to increase electron migration. Huang et al. (2020) synthesized $CuGaTe_2$ + x wt.% CPS(x = 0, 0.3, 0.5, 1) composites. The results show that carbon particles (CPS) can be introduced into $CuGaTe_2$ matrix as electronic location center, and the conductivity and power factor of $CuGaTe_2$ matrix can be improved by adjusting its electrical transport performance. The results show that the introduction of CPS can be used as the local electron center, thus the hole concentration in the matrix is increased, and the electrical conductivity is increased by about 120% (300 K). Besides, the interface between carbon particles and matrix enhances the scattering of heat-carrying phonons and reduces the thermal conductivity of $CuGaTe_2$ + 0.5 wt.% CPS sample at 873 K, which significantly reduces the thermal conductivity of $CuGaTe_2$ sample by 37% compared with pure $CuGaTe_2$ (Huang et al., 2020).

To ensure the micro-transfer of energy bands and even form band alignment structure when embedded in nano-scale, the design of alloyed nano thermoelectric materials is also a good approach (Zhao et al., 2013b). The double alloying method of PbTe adopted by Sumanta Sarkar combines two different but identical structures, which can effectively improve the thermoelectric properties of PbTe from two aspects. First, in the presence of Bate, the solubility of Cate increases, leading to a widening of the band gap and a good convergence between L and $\sum$ bands, resulting in a record-high PF for the Seebeck coefficient. In addition, the point defects generated by alloying and the BaT-rich nanostructures contribute to the reduction of the lattice thermal conductivity of the system. This synergistic method generates a high ZT of 2.2 at 823 K (Sarkar et al., 2018). Makongo et al. (2011) proposed to obtain half-Heusler and Heusler nanocomposite phases *in situ* by atomic-scale regulation, which effectively improved the electrical conductivity and power factor of the material and reduced the lattice thermal conductivity of the material. At the same time, Jie Ma et al. studied the fundamental electron-phonon interaction using the chemical doping of ZrNis-based semi-Hessler materials as an example (Ren et al., 2020). This crossover between different major scattering mechanisms is achieved by shielding ionized impurities, grain boundary, and polarized phonon scattering, and enhanced phonon/alloy scattering. Based on the understanding of different carrier scattering, they derived the carrier scattering phase diagram, which can guide further improving the Te properties of semi-Hessler Te materials. This method can also be extended analogically to materials of different systems and may provide excellent guidance for electro-acoustic decoupling.

Organic materials would be a better choice purely from the direction of reducing thermal conductivity. However, the biggest disadvantage of organic materials is that their electrical properties are difficult to regulate, which greatly affects their thermoelectric properties. The thermal conductivity of organic thermoelectric materials is usually lower than 1 $W\,m^{-1}\,K^{-1}$, close to the lower limit of the thermal conductivity of inorganic thermoelectric materials (Huang et al., 2016). Moreover, the electronic structure of the organic (semi) conductor can be appropriately adjusted by molecular chemistry and doping treatment, so that electron transport is not affected (Ren et al., 2018). Wang L. et al. (2018) not only reduced the thermal conductivity through flexible organic-inorganic hybridizationbut also improved the electrical performance, effectively realizing electro-acoustic decoupling. Therefore, organic thermoelectric materials have great prospects in Low-temperature applications.

The above is mainly by suppressing phonon transmission to ensure electron transport to improve the thermoelectric performance. The difference is that Zhimei Sun et al. discussed the thermoelectric properties of two-dimensional Nb_2C through first-principles calculations. It is found that when the density of electron states near the Fermi level is high and the phonon frequency is high, the anomalous strong E-P scattering will be generated, and the thermal conductivity of the lattice will be greatly reduced, which also provides a new idea for

the design of two-dimensional metallic thermoelectric materials (Huang et al., 2019).

CONCLUSION

Although thermoelectric functional materials have a long history of research, from the discovery of narrow-band gap semiconductor materials to the vigorous development of wideband gap semiconductor thermoelectric materials, they still fail to achieve excellent ideal performance, so there is still a lot of room for exploration and improvement. This paper elaborates on the improvement of the thermoelectric optimal value *ZT* from the aspects of optimizing carrier concentration, improving carrier mobility, increasing effective mass, reducing lattice thermal conductivity, exploring intrinsic thermoelectric materials, and electro-acoustic decoupling, among which the relatively independent lattice thermal conductivity regulation has received extensive attention.

In energy band engineering, we can improve the effective mass by introducing resonant state density, increasing energy band degeneracy, controllable hybridization gap and doping Kondo atoms. However, increasing the Seebeck coefficient by increasing the effective mass tends to reduce carrier mobility. At the same time, the Seebeck coefficient can be improved by optimizing the carrier concentration and increasing carrier mobility by modulating doping and temperature-dependent gradient doping. In phonon engineering, the mechanism of point defect scattering, dislocation scattering, interface scattering and resonance scattering to reduce lattice thermal conductivity is summarized. It also reveals the structure-activity relationship of several influencing factors such as weak chemical bonding, strong anharmonic effects, liquid ionic properties, heavy molecular mass and complex crystal structure on the intrinsic low thermal conductivity thermoelectric materials. Finally, the electro-acoustic decoupling theory, such as how to block the transmission of electrons by phonons, is briefly explained.

It can be seen that further exploration of electro-acoustic synergy mechanism and design of intrinsic low thermal conductivity is still the mainstream research direction, but when making some breakthroughs, it is faced with challenges such as thermal dynamic stability and other issues. We can start with the following strategies: 1) new mechanism, new concept, and new theory of the synergy between band engineering and phonon engineering; 2) the influence mechanism of material defect engineering on thermoelectric properties; 3) the influence of synthesis methods, and characterization methods on the evolution of interface, and microstructure; 4) To design a comprehensive theoretical calculation module and establish a complete material genome database to screen new thermoelectric materials with high performance at a high speed and effectively. Although the influence conditions of thermoelectric performance are interlaced and complex, it is believed that breakthrough progress will be made under the rapid development of materials, physics, chemistry and computer science, and it is bound to play a role in the future reliable clean energy.

AUTHOR CONTRIBUTIONS

YS and RL organized the data analysis, YaL and SB is responsible for the essays written, and YuL, YS, and YaL organized the whole idea.

REFERENCES

Beekman, M., and VanderGraaff, A. (2017). High-temperature Thermal Conductivity of Thermoelectric Clathrates. *J. Appl. Phys.* 121 (20), 205105. doi:10.1063/1.4983817

Bell, L. E. (2008). Cooling, Heating, Generating Power, and Recovering Waste Heat with Thermoelectric Systems. *Science* 321 (5895), 1457–1461. doi:10.1126/science.1158899

Bergum, K., Ikeda, T., and Jeffrey Snyder, G. (2011). Solubility and Microstructure in the Pseudo-binary PbTe-Ag_2Te System. *J. Solid State Chem.* 184 (9), 2543–2552. doi:10.1016/j.jssc.2011.07.012

Biswas, K., He, J., Blum, I. D., Wu, C.-I., Hogan, T. P., Seidman, D. N., et al. (2012). High-performance Bulk Thermoelectrics with All-Scale Hierarchical Architectures. *Nature* 489 (7416), 414–418. doi:10.1038/nature11439

Biswas, K., He, J., Zhang, Q., Wang, G., Uher, C., Dravid, V. P., et al. (2011). Strained Endotaxial Nanostructures with High Thermoelectric Figure of Merit. *Nat. Chem.* 3 (2), 160–166. doi:10.1038/nchem.955

Brown, S. R., Kauzlarich, S. M., Gascoin, F., and Snyder, G. J. (2006). $Yb_{14}MnSb_{11}$: New High Efficiency Thermoelectric Material for Power Generation. *Chem. Mat.* 18 (7), 1873–1877. doi:10.1021/cm060261t

Callaway, J. (1959). Model for Lattice Thermal Conductivity at Low Temperatures. *Phys. Rev.* 113 (4), 1046–1051. doi:10.1103/physrev.113.1046

Cha, J., Zhou, C., Cho, S. P., Park, S. H., and Chung, I. (2019). Ultrahigh Power Factor and Electron Mobility in N-type $Bi_2Te_{3-x\%}Cu$ Stabilized under Excess Te Condition. *ACS Appl. Mater. interfaces* 11 (34), 30999. doi:10.1021/acsami.9b10394

Chang, C., Wu, M., He, D., Pei, Y., Wu, C.-F., Wu, X., et al. (2018). 3D Charge and 2D Phonon Transports Leading to High Out-Of-Plane ZT in N-type SnSe Crystals. *Science* 360 (6390), 778–783. doi:10.1126/science.aaq1479

Chen, S., Bai, H., Li, J., Pan, W., Jiang, X., Li, Z., et al. (2020). Vacancy-Based Defect Regulation for High Thermoelectric Performance in $Ge_9Sb_2Te_{12-X}$ Compounds. *ACS Appl. Mat. Interfaces* 12 (17), 19664–19673. doi:10.1021/acsami.0c02155

Chen, S., Logothetis, N., Ye, L., and Liu, J. (2015). A High Performance Ag Alloyed Nano-Scale N-type Bi_2Te_3 Based Thermoelectric Material. *Mater. Today Proc.* 2 (2), 610–619. doi:10.1016/j.matpr.2015.05.083

Chen, Z., Jian, Z., Li, W., Chang, Y., Ge, B., Hanus, R., et al. (2017). Lattice Dislocations Enhancing Thermoelectric PbTe in Addition to Band Convergence. *Adv. Mat.* 29 (23), 1606768. doi:10.1002/adma.201606768

Chen, Z., Yang, J., Liu, R., Xi, L., Zhang, W., and Yang, J. (2013). Theoretical Study on Structural Stability of Fully Filled P-type Skutterudites $RETM_4Sb_{12}$ (RE = Rare Earth; TM = Fe, Ru). *J. Elec Materi* 42 (8), 2492–2497. doi:10.1007/s11664-013-2594-z

Chong, X., Guan, P.-W., Wang, Y., Shang, S.-L., Soldan Palma, J. P., Drymiotis, F., et al. (2020). Correction to "Understanding the Intrinsic P-type Behavior and Phase Stability of Thermoelectric α-Mg_3Sb_2". *ACS Appl. Energy Mat.* 3 (1), 1249–1252. doi:10.1021/acsaem.9b02229

Christensen, M., Abrahamsen, A. B., Christensen, N. B., Juranyi, F., Andersen, N. H., Lefmann, K., et al. (2008). Avoided Crossing of Rattler Modes in Thermoelectric Materials. *Nat. Mater* 7 (10), 811–815. doi:10.1038/nmat2273

Cook, B. A., Kramer, M. J., Harringa, J. L., Han, M.-K., Chung, D.-Y., and Kanatzidis, M. G. (2009). Analysis of Nanostructuring in High Figure-Of-Merit Ag1-xPbmSbTe2^{+}mThermoelectric Materials. *Adv. Funct. Mat.* 19 (8), 1254–1259. doi:10.1002/adfm.200801284

Cox, C. A., Toberer, E. S., Levchenko, A. A., Brown, S. R., Snyder, G. J., Navrotsky, A., et al. (2009). Structure, Heat Capacity, and High-Temperature Thermal Properties of $Yb_{14}Mn_{1-x}Al_xSb_{11}$. *Chem. Mat.* 21 (7), 1354–1360. doi:10.1021/cm803252r

Cutler, M., Leavy, J. F., and Fitzpatrick, R. L. (1964). Electronic Transport in Semimetallic Cerium Sulfide. *Phys. Rev.* 133 (4A), A1143–A1152. doi:10.1103/physrev.133.a1143

Dashevsky, Z., Shusterman, S., Dariel, M. P., and Drabkin, I. (2002). Thermoelectric Efficiency in Graded Indium-Doped PbTe Crystals. *J. Appl. Phys.* 92 (3), 1425–1430. doi:10.1063/1.1490152

Du, B., Li, H., Xu, J., Tang, X., and Uher, C. (2011). Enhanced Thermoelectric Performance and Novel Nanopores in $AgSbTe_2$ Prepared by Melt Spinning. *J. Solid State Chem.* 184 (1), 109–114. doi:10.1016/j.jssc.2010.10.036

Duan, B., Yang, J., Salvador, J. R., He, Y., Zhao, B., Wang, S., et al. (2016). Electronegative Guests in $CoSb_3$. *Energy Environ. Sci.* 9 (6), 2090–2098. doi:10.1039/c6ee00322b

Dutta, M., Ghosh, T., and Biswas, K. (2020). Electronic Structure Modulation Strategies in High-Performance Thermoelectrics. *Apl. Mater.* 8 (4), 040910. doi:10.1063/5.0002129

Feng, Y., Li, J., Li, Y., Ding, T., Zhang, C., Hu, L., et al. (2020). Band Convergence and Carrier-Density Fine-Tuning as the Electronic Origin of High-Average Thermoelectric Performance in Pb-Doped GeTe-Based Alloys. *J. Mat. Chem. A* 8 (22), 11370–11380. doi:10.1039/d0ta02758h

Gao, W., Wang, Z., Huang, J., and Liu, Z. (2018). Extraordinary Thermoelectric Performance Realized in Hierarchically Structured $AgSbSe_2$ with Ultralow Thermal Conductivity. *ACS Appl. Mat. Interfaces* 10 (22), 18685–18692. doi:10.1021/acsami.8b03243

Gelbstein, Y., Davidow, J., Girard, S. N., Chung, D. Y., and Kanatzidis, M. (2013). Controlling Metallurgical Phase Separation Reactions of the $Ge_{0.87}Pb_{0.13}Te$ Alloy for High Thermoelectric Performance. *Adv. Energy Mat.* 3 (6), 815–820. doi:10.1002/aenm.201200970

Girard, S. N., He, J., Li, C., Moses, S., Wang, G., Uher, C., et al. (2010). *In Situ* nanostructure Generation and Evolution within a Bulk Thermoelectric Material to Reduce Lattice Thermal Conductivity. *Nano Lett.* 10 (8), 2825–2831. doi:10.1021/nl100743q

Heremans, J. P., Jovovic, V., Toberer, E. S., Saramat, A., Kurosaki, K., Charoenphakdee, A., et al. (2008). Enhancement of Thermoelectric Efficiency in PbTe by Distortion of the Electronic Density of States. *Science* 321 (5888), 554–557. doi:10.1126/science.1159725

Heremans, J. P. (2014). The Ugly Duckling. *Nature* 508 (7496), 327–328. doi:10.1038/508327a

Hicks, L. D., and Dresselhaus, M. S. (1993). *Use of Quantum-Well Superlattices to Obtain a High Figure of Merit from Nonconventional Thermoelectric Materials*. Cambridge: MRS Online Proceedings Library OPL, 326.

Horbach, J., Kob, W., and Binder, K. (2001). Structural and Dynamical Properties of Sodium Silicate Melts: an Investigation by Molecular Dynamics Computer Simulation. *Chem. Geol.* 174 (1-3), 87–101. doi:10.1016/s0009-2541(00)00309-0

Hsu, K. F., Loo, S., Guo, F., Chen, W., Dyck, J. S., and Uher, C. (2004). Cubic AgPb M SbTe 2^{+} M : Bulk Thermoelectric Materials with High Figure of Merit. *Science* 303 (5659), 818–821. doi:10.1126/science.1092963

Hu, L., Wu, H., Zhu, T., Fu, C., He, J., Ying, P., et al. (2015). Tuning Multiscale Microstructures to Enhance Thermoelectric Performance of N-type Bismuth-Telluride-Based Solid Solutions. *Adv. Energy Mat.* 5 (17), 1500411. doi:10.1002/aenm.201500411

Hu, L., Zhu, T., Liu, X., and Zhao, X. (2014). Point Defect Engineering of High-Performance Bismuth-Telluride-Based Thermoelectric Materials. *Adv. Funct. Mat.* 24 (33), 5211–5218. doi:10.1002/adfm.201400474

Huang, L., Zhang, J., Zhu, C., Ge, Z., Li, Y., Li, D., et al. (2020). Synergistically Optimized Electrical and Thermal Properties by Introducing Electron Localization and Phonon Scattering Centers in $CuGaTe_2$ with Enhanced Mechanical Properties. *J. Mat. Chem. C* 8 (22), 7534–7542. doi:10.1039/d0tc00795a

Huang, Y., Qiao, J., He, K., Bliznakov, S., Sutter, E., Chen, X., et al. (2016). Interaction of Black Phosphorus with Oxygen and Water. *Chem. Mat.* 28 (22), 8330–8339. doi:10.1021/acs.chemmater.6b03592

Huang, Y., Zhou, J., Wang, G., and Sun, Z. (2019). Abnormally Strong Electron-Phonon Scattering Induced Unprecedented Reduction in Lattice Thermal Conductivity of Two-Dimensional Nb_2C. *J. Am. Chem. Soc.* 141 (21), 8503–8508. doi:10.1021/jacs.9b01742

Ioffe, A. F., Stil'Bans, L. S., Iordanishvili, E. K., Stavitskaya, T. S., Gelbtuch, A., and Vineyard, G. (1959). Semiconductor Thermoelements and Thermoelectric Cooling. *Phys. Today* 12 (5), 42. doi:10.1063/1.3060810

Kim, S. I., Lee, K. H., Mun, H. A., Kim, H. S., Hwang, S. W., Roh, J. W., et al. (2015). Dense Dislocation Arrays Embedded in Grain Boundaries for High-Performance Bulk Thermoelectrics. *Science* 348 (6230), 109–114. doi:10.1126/science.aaa4166

Klemens, P. G. (1960). Thermal Resistance Due to Point Defects at High Temperatures. *Phys. Rev.* 119 (2), 507–509. doi:10.1103/physrev.119.507

Koirala, M., Zhao, H., Pokharel, M., Chen, S., Dahal, T., Opeil, C., et al. (2013). Thermoelectric Property Enhancement by Cu Nanoparticles in Nanostructured $FeSb_2$. *Appl. Phys. Lett.* 102 (21), 213111. doi:10.1063/1.4808094

Kraemer, D., Sui, J., McEnaney, K., Zhao, H., Jie, Q., Ren, Z. F., et al. (2015). High Thermoelectric Conversion Efficiency of MgAgSb-Based Material with Hot-Pressed Contacts. *Energy Environ. Sci.* 8 (4), 1299–1308. doi:10.1039/c4ee02813a

Kurosaki, K., Kosuga, A., Muta, H., Uno, M., and Yamanaka, S. (2005). $Ag_9T_1Te_5$: A High-Performance Thermoelectric Bulk Material with Extremely Low Thermal Conductivity. *Appl. Phys. Lett.* 87 (6), 061919. doi:10.1063/1.2009828

Kuznetsov, V. L., Kuznetsova, L. A., Kaliazin, A. E., and Rowe, D. M. (2002). High Performance Functionally Graded and Segmented Bi_2Te_3-Based Materials for Thermoelectric Power Generation. *J. Mater. Sci.* 37 (14), 2893–2897. doi:10.1023/a:1016092224833

Kyratsi, T., Hatzikraniotis, E., Ioannou, M., Chung, D. Y., and Tsiaoussis, I. (2011). Seebeck and Thermal Conductivity Analysis in Amorphous/crystallineβ-K2Bi8Se13nanocomposite Materials. *J. Appl. Phys.* 110 (3), 033713. doi:10.1063/1.3610393

Lee, S., Kim, K., Kang, D.-H., Meyyappan, M., and Baek, C.-K. (2019). Vertical Silicon Nanowire Thermoelectric Modules with Enhanced Thermoelectric Properties. *Nano Lett.* 19 (2), 747–755. doi:10.1021/acs.nanolett.8b03822

Lee, Y., Lo, S. H., Chen, C., Sun, H., Chung, D. Y., Chasapis, T. C., et al. (2014). Contrasting Role of Antimony and Bismuth Dopants on the Thermoelectric Performance of Lead Selenide. *Nat. Commun.* 5 (1), 3640–3711. doi:10.1038/ncomms4640

Levin, E. M., Cook, B. A., Harringa, J. L., Bud'ko, S. L., Venkatasubramanian, R., and Schmidt-Rohr, K. (2011). Analysis of Ce- and Yb-Doped TAGS-85 Materials with Enhanced Thermoelectric Figure of Merit. *Adv. Funct. Mat.* 21 (3), 441–447. doi:10.1002/adfm.201001307

Li, F., Li, J.-F., Zhao, L.-D., Xiang, K., Liu, Y., Zhang, B.-P., et al. (2012). Polycrystalline BiCuSeO Oxide as a Potential Thermoelectric Material. *Energy Environ. Sci.* 5 (5), 7188–7195. doi:10.1039/c2ee21274a

Li, J., Zhang, X., Chen, Z., Lin, S., Li, W., Shen, J., et al. (2018). Low-symmetry Rhombohedral GeTe Thermoelectrics. *Joule* 2 (5), 976–987. doi:10.1016/j.joule.2018.02.016

Li, W., Lin, S., Zhang, X., Chen, Z., Xu, X., and Pei, Y. (2016). Thermoelectric Properties of Cu2SnSe4 with Intrinsic Vacancy. *Chem. Mat.* 28 (17), 6227–6232. doi:10.1021/acs.chemmater.6b02416

Li, W., Zheng, L., Ge, B., Lin, S., Zhang, X., Chen, Z., et al. (2017). Promoting SnTe as an Eco-Friendly Solution for P-PbTe Thermoelectric via Band Convergence and Interstitial Defects. *Adv. Mat.* 29 (17), 1605887. doi:10.1002/adma.201605887

Li, Y., Mei, D., Wang, H., Yao, Z., Zhu, T., and Chen, S. (2015). Reduced Lattice Thermal Conductivity in Nanograined Na-Doped PbTe Alloys by Ball Milling and Semisolid Powder Processing. *Mater. Lett.* 140, 103–106. doi:10.1016/j.matlet.2014.11.015

Liu, H., Shi, X., Xu, F., Zhang, L., Zhang, W., Chen, L., et al. (2012). Copper Ion Liquid-like Thermoelectrics. *Nat. Mater* 11 (5), 422–425. doi:10.1038/nmat3273

Liu, Y., Zhao, L.-D., Zhu, Y., Liu, Y., Li, F., Yu, M., et al. (2016). Synergistically Optimizing Electrical and Thermal Transport Properties of BiCuSeO via a

Dual-Doping Approach. *Adv. Energy Mat.* 6 (9), 1502423. doi:10.1002/aenm.201502423

Liu, Z., Zhang, Y., Mao, J., Gao, W., Wang, Y., Shuai, J., et al. (2017). The Microscopic Origin of Low Thermal Conductivity for Enhanced Thermoelectric Performance of Yb Doped MgAgSb. *Acta Mater.* 128, 227–234. doi:10.1016/j.actamat.2017.02.015

Lu, X., Morelli, D. T., Xia, Y., and Ozolins, V. (2015). Increasing the Thermoelectric Figure of Merit of Tetrahedrites by Co-doping with Nickel and Zinc. *Chem. Mat.* 27 (2), 408–413. doi:10.1021/cm502570b

Makongo, J. P. A., Misra, D. K., Zhou, X., Pant, A., Shabetai, M. R., Su, X., et al. (2011). Simultaneous Large Enhancements in Thermopower and Electrical Conductivity of Bulk Nanostructured Half-Heusler Alloys. *J. Am. Chem. Soc.* 133 (46), 18843–18852. doi:10.1021/ja206491j

Meng, J. F., Chandra Shekar, N. V., Chung, D.-Y., Kanatzidis, M., and Badding, J. V. (2003). Improvement in the Thermoelectric Properties of Pressure-Tuned β-$K_2Bi_8Se_{13}$. *J. Appl. Phys.* 94 (7), 4485–4488. doi:10.1063/1.1599049

Nielsen, M. D., Ozolins, V., and Heremans, J. P. (2013). Lone Pair Electrons Minimize Lattice Thermal Conductivity. *Energy Environ. Sci.* 6 (2), 570–578. doi:10.1039/c2ee23391f

Pan, Y., Qiu, Y., Witting, I., Zhang, L., Fu, C., Li, J.-W., et al. (2019). Synergistic Modulation of Mobility and Thermal Conductivity in $(Bi,Sb)_2Te_3$ towards High Thermoelectric Performance. *Energy Environ. Sci.* 12 (2), 624–630. doi:10.1039/c8ee03225d

Pei, Y.-L., Wu, H., Wu, D., Zheng, F., and He, J. (2014). High Thermoelectric Performance Realized in a BiCuSeO System by Improving Carrier Mobility through 3D Modulation Doping. *J. Am. Chem. Soc.* 136 (39), 13902–13908. doi:10.1021/ja507945h

Pei, Y., LaLonde, A. D., Wang, H., and Snyder, G. J. (2012). Low Effective Mass Leading to High Thermoelectric Performance. *Energy Environ. Sci.* 5 (7), 7963–7969. doi:10.1039/c2ee21536e

Pei, Y., Shi, X., LaLonde, A., Wang, H., Chen, L., and Snyder, G. J. (2011). Convergence of Electronic Bands for High Performance Bulk Thermoelectrics. *Nature* 473 (7345), 66–69. doi:10.1038/nature09996

Pei, Y., Wang, H., and Snyder, G. J. (2012). Band Engineering of Thermoelectric Materials. *Adv. Mat.* 24 (46), 6125–6135. doi:10.1002/adma.201202919

Poudel, B., Hao, Q., Ma, Y., Lan, Y., Minnich, A., Yu, B., et al. (2008). High-thermoelectric Performance of Nanostructured Bismuth Antimony Telluride Bulk Alloys. *Science* 320 (5876), 634–638. doi:10.1126/science.1156446

Poudeu, P. F. P., D'Angelo, J., Downey, A. D., Short, J. L., Hogan, T. P., and Kanatzidis, M. G. (2006). High Thermoelectric Figure of Merit and Nanostructuring in Bulk P-type Na_{1-x}PbmSbyTem+2. *Angew. Chem.* 118 (23), 3919–3923. doi:10.1002/ange.200600865

Qin, B., Zhang, Y., Wang, D., Zhao, Q., Gu, B., Wu, H., et al. (2020). Ultrahigh Average ZT Realized in P-type SnSe Crystalline Thermoelectrics through Producing Extrinsic Vacancies. *J. Am. Chem. Soc.* 142 (12), 5901–5909. doi:10.1021/jacs.0c01726

Qiu, P., Zhang, T., Qiu, Y., Shi, X., and Chen, L. (2014). Sulfide Bornite Thermoelectric Material: a Natural Mineral with Ultralow Thermal Conductivity. *Energy Environ. Sci.* 7 (12), 4000–4006. doi:10.1039/c4ee02428a

Ren, Q., Fu, C., Qiu, Q., Dai, S., Liu, Z., Masuda, T., et al. (2020). Establishing the Carrier Scattering Phase Diagram for ZrNiSn-Based Half-Heusler Thermoelectric Materials. *Nat. Commun.* 11 (1), 3142–3149. doi:10.1038/s41467-020-16913-2

Ren, W., Sun, Y., Zhang, J., Xia, Y., Geng, H., and Zhang, L. (2021). Doping Distribution in Skutterudites with Ultra-high Filling Fractions for Achieving Ultra-low Thermal Conductivity. *Acta Mater.* 209, 116791. doi:10.1016/j.actamat.2021.116791

Ren, X., Yuan, L., Liang, Q., Xie, R., Geng, Z., Sun, Y., et al. (2018). Phase-Controlled Synthesis of High-Bi-Ratio Ternary Sulfide Nanocrystals of $Cu_{1.57}Bi_{4.57}S_8$ and $Cu_{2.93}Bi_{4.89}S_9$. *ChemPlusChem* 83 (8), 812–818. doi:10.1002/cplu.201800271

Roychowdhury, S., Panigrahi, R., Perumal, S., and Biswas, K. (2017). Ultrahigh Thermoelectric Figure of Merit and Enhanced Mechanical Stability of P-type $AgSb_{1-x}ZnxTe_2$. *ACS Energy Lett.* 2 (2), 349–356. doi:10.1021/acsenergylett.6b00639

Saha, S. K. (2015). Exploring the Origin of Ultralow Thermal Conductivity in Layered BiOCuSe. *Phys. Rev. B* 92 (4), 041202. doi:10.1103/physrevb.92.041202

Samanta, M., Pal, K., Pal, P., Waghmare, U. V., and Biswas, K. (2018). Localized Vibrations of Bi Bilayer Leading to Ultralow Lattice Thermal Conductivity and High Thermoelectric Performance in Weak Topological Insulator N-type BiSe. *J. Am. Chem. Soc.* 140 (17), 5866–5872. doi:10.1021/jacs.8b02691

Samanta, M., Roychowdhury, S., Ghatak, J., Perumal, S., and Biswas, K. (2017). Ultrahigh Average Thermoelectric Figure of Merit, Low Lattice Thermal Conductivity and Enhanced Microhardness in Nanostructured (GeTe) $x(AgSbSe_2)$100−x. *Chem. Eur. J.* 23 (31), 7438–7443. doi:10.1002/chem.201701480

Sarkar, S., Zhang, X., Hao, S., Hua, X., Bailey, T. P., Uher, C., et al. (2018). A Dual Alloying Strategy to Achieve High Thermoelectric Figure of Merit and Lattice Hardening in P-type Nanostructured PbTe. *ACS Energy Lett.* 3 (10), 2593–2601. doi:10.1021/acsenergylett.8b01684

Selimefendigil, F., Okulu, D., and Mamur, H. (2021). Numerical Analysis for Performance Enhancement of Thermoelectric Generator Modules by Using CNT-Water and Hybrid Ag/MgO-Water Nanofluids. *J. Therm. Anal. Calorim.* 143 (2), 1611–1621. doi:10.1007/s10973-020-09983-3

Shen, J., Fu, C., Liu, Y., Zhao, X., and Zhu, T. (2018). Enhancing Thermoelectric Performance of FeNbSb Half-Heusler Compound by Hf-Ti Dual-Doping. *Energy Storage Mater.* 10, 69–74. doi:10.1016/j.ensm.2017.07.014

Shi, X., Yang, J., Salvador, J. R., Chi, M., Cho, J. Y., Wang, H., et al. (2011). Multiple-filled Skutterudites: High Thermoelectric Figure of Merit through Separately Optimizing Electrical and Thermal Transports. *J. Am. Chem. Soc.* 133 (20), 7837–7846. doi:10.1021/ja111199y

Shutoh, N., and Sakurada, S. (2005). Thermoelectric Properties of the $Ti_x(Zr_{0.5}Hf_{0.5})_{1-\ x}$NiSn Half-Heusler Compounds. *J. alloys Compd.* 389 (1-2), 204–208. doi:10.1016/j.jallcom.2004.05.078

Skomorokhov, A. N., Trots, D. M., Knapp, M., Bickulova, N. N., and Fuess, H. (2006). Structural Behaviour of β-Cu_2-δ-Se (δ= 0, 0.15, 0.25) in Dependence on Temperature Studied by Synchrotron Powder Diffraction. *J. alloys Compd.* 421 (1-2), 64–71. doi:10.1016/j.jallcom.2005.10.079

Slack, G. A., and Rowe, D. M. (1995). *CRC Handbook of Thermoelectrics*. Boca Raton: CRC Press.

Snyder, G. J., and Toberer, E. S. (2011). *Complex Thermoelectric Materials*. London: Nature Publishing Group, 101.

Su, L., Wang, D., Wang, S., Qin, B., Wang, Y., Qin, Y., et al. (2022). High Thermoelectric Performance Realized through Manipulating Layered Phonon-Electron Decoupling. *Science* 375 (6587), 1385–1389. doi:10.1126/science.abn8997

Su, X., Wei, P., Li, H., Liu, W., Yan, Y., Li, P., et al. (2017). Multi-Scale Microstructural Thermoelectric Materials: Transport Behavior, Non-equilibrium Preparation, and Applications. *Adv. Mat.* 29 (20), 1602013. doi:10.1002/adma.201602013

Suarez, F., Nozariasbmarz, A., Vashaee, D., and Öztürk, M. C. (2016). Designing Thermoelectric Generators for Self-Powered Wearable Electronics. *Energy Environ. Sci.* 9 (6), 2099–2113. doi:10.1039/c6ee00456c

Sui, J., Li, J., He, J., Pei, Y.-L., Berardan, D., Wu, H., et al. (2013). Texturation Boosts the Thermoelectric Performance of BiCuSeO Oxyselenides. *Energy Environ. Sci.* 6 (10), 2916–2920. doi:10.1039/c3ee41859f

Suwardi, A., Bash, D., Ng, H. K., Gomez, J. R., Repaka, D. V. M., Kumar, P., et al. (2019). Inertial Effective Mass as an Effective Descriptor for Thermoelectrics via Data-Driven Evaluation. *J. Mat. Chem. A* 7 (41), 23762–23769. doi:10.1039/c9ta05967a

Tan, G., Shi, F., Hao, S., Zhao, L. D., Chi, H., Zhang, X., et al. (2016). Non-equilibrium Processing Leads to Record High Thermoelectric Figure of Merit in PbTe-SrTe. *Nat. Commun.* 7 (1), 12167–12169. doi:10.1038/ncomms12167

Tan, G., Chi, H., Liu, W., Zheng, Y., Tang, X., He, J., et al. (2015). Toward High Thermoelectric Performance P-type $FeSb_{2.2}Te_{0.8}$via *In Situ* Formation of InSb Nanoinclusions. *J. Mat. Chem. C* 3 (32), 8372–8380. doi:10.1039/c5tc01739d

Tan, G., Shi, F., Hao, S., Chi, H., Zhao, L.-D., Uher, C., et al. (2015). Codoping in SnTe: Enhancement of Thermoelectric Performance through Synergy of Resonance Levels and Band Convergence. *J. Am. Chem. Soc.* 137 (15), 5100–5112. doi:10.1021/jacs.5b00837

Tan, G., Wang, S., and Tang, X. (2013). High Thermoelectric Figure of Merit of P-type Ternary Unfilled Skutterudite $FeSb_2$ Te via Ge Doping. *Sci. Adv. Mat.* 5 (12), 1974–1982. doi:10.1166/sam.2013.1665

Tan, G., Zhang, X., Hao, S., Chi, H., Bailey, T. P., Su, X., et al. (2019). Enhanced Density-Of-States Effective Mass and Strained Endotaxial Nanostructures in

Sb-Doped $Pb_{0.97}Cd_{0.03}Te$ Thermoelectric Alloys. *ACS Appl. Mat. Interfaces* 11 (9), 9197–9204. doi:10.1021/acsami.8b21524

Tan, G., Zhao, L.-D., and Kanatzidis, M. G. (2016). Rationally Designing High-Performance Bulk Thermoelectric Materials. *Chem. Rev.* 116 (19), 12123–12149. doi:10.1021/acs.chemrev.6b00255

Tan, Q., Zhao, L.-D., Li, J.-F., Wu, C.-F., Wei, T.-R., Xing, Z.-B., et al. (2014). Thermoelectrics with Earth Abundant Elements: Low Thermal Conductivity and High Thermopower in Doped SnS. *J. Mat. Chem. A* 2 (41), 17302–17306. doi:10.1039/c4ta04462b

Tang, Y., Gibbs, Z. M., Agapito, L. A., Li, G., Kim, H.-S., Nardelli, M. B., .Curtarolo, S., and Snyder, G. J. (2015). Convergence of Multi-Valley Bands as the Electronic Origin of High Thermoelectric Performance in CoSb3 Skutterudites. *Nat. Mater* 14 (12), 1223–1228. doi:10.1038/nmat4430

Toberer, E. S., May, A. F., and Snyder, G. J. (2010). Zintl Chemistry for Designing High Efficiency Thermoelectric Materials. *Chem. Mat.* 22 (3), 624–634. doi:10.1021/cm901956r

Toberer, E. S., Zevalkink, A., and Snyder, G. J. (2011). Phonon Engineering through Crystal Chemistry. *J. Mat. Chem.* 21 (40), 15843–15852. doi:10.1039/c1jm11754h

Uvarov, C. A., Ortega-Alvarez, F., and Kauzlarich, S. M. (2012). Enhanced High-Temperature Thermoelectric Performance of $Yb_{14-x}CaxMnSb_{11}$. *Inorg. Chem.* 51 (14), 7617–7624. doi:10.1021/ic300567c

Valset, K., Böttger, P. H. M., Taftø, J., and Finstad, T. G. (2012). Thermoelectric Properties of Cu Doped ZnSb Containing Zn_3P_2 Particles. *J. Appl. Phys.* 111 (2), 023703. doi:10.1063/1.3675505

Vining, C. B. (2009). An Inconvenient Truth about Thermoelectrics. *Nat. Mater* 8 (2), 83–85. doi:10.1038/nmat2361

Wang, L., Zhang, Z., Liu, Y., Wang, B., Fang, L., Qiu, J., et al. (2018). Exceptional Thermoelectric Properties of Flexible Organic-Inorganic Hybrids with Monodispersed and Periodic Nanophase. *Nat. Commun.* 9 (1), 3817–3818. doi:10.1038/s41467-018-06251-9

Wang, X. W., Lee, H., Lan, Y. C., Zhu, G. H., Joshi, G., Wang, D. Z., et al. (2008). Enhanced Thermoelectric Figure of Merit in Nanostructured N-type Silicon Germanium Bulk Alloy. *Appl. Phys. Lett.* 93 (19), 193121. doi:10.1063/1.3027060

Wang, Y., Hu, Y.-J., Firdosy, S. A., Star, K. E., Fleurial, J.-P., Ravi, V. A., et al. (2018). First-principles Calculations of Lattice Dynamics and Thermodynamic Properties for $Yb_{14}MnSb_{11}$. *J. Appl. Phys.* 123 (4), 045102. doi:10.1063/1.5013601

Wei, P., Yang, J., Guo, L., Wang, S., Wu, L., Xu, X., et al. (2016). Minimum Thermal Conductivity in Weak Topological Insulators with Bismuth-Based Stack Structure. *Adv. Funct. Mat.* 26 (29), 5360–5367. doi:10.1002/adfm.201600718

Wu, H. J., Zhao, L. D., Zheng, F. S., Wu, D., Pei, Y. L., Tong, X., et al. (2014). Broad Temperature Plateau for Thermoelectric Figure of Merit ZT>2 in Phase-Separated $PbTe_{0.7}S_{0.3}$. *Nat. Commun.* 5 (1), 4515–4519. doi:10.1038/ncomms5515

Xia, K., Liu, Y., Anand, S., Snyder, G. J., Xin, J., Yu, J., et al. (2018). Enhanced Thermoelectric Performance in 18-Electron $Nb_{0.8}$ CoSb Half-Heusler Compound with Intrinsic Nb Vacancies. *Adv. Funct. Mat.* 28 (9), 1705845. doi:10.1002/adfm.201705845

Xiang, B., Liu, J., Yan, J., Xia, M., Zhang, Q., Chen, L., et al. (2019). Local Nanostructures Enhanced the Thermoelectric Performance of N-type PbTe. *J. Mat. Chem. A* 7 (31), 18458–18467. doi:10.1039/c9ta06247e

Xiao, Y., Wu, H., Li, W., Yin, M., Pei, Y., Zhang, Y., et al. (2017). Remarkable Roles of Cu to Synergistically Optimize Phonon and Carrier Transport in N-type PbTe-Cu_2Te. *J. Am. Chem. Soc.* 139 (51), 18732–18738. doi:10.1021/jacs.7b11662

Xie, J., Ohishi, Y., Ichikawa, S., Muta, H., Kurosaki, K., and Yamanaka, S. (2018). Naturally Decorated Dislocations Capable of Enhancing Multiple-Phonon Scattering in Si-Based Thermoelectric Composites. *J. Appl. Phys.* 123 (11), 115114. doi:10.1063/1.5019614

Xie, W., Tang, X., Yan, Y., Zhang, Q., and Tritt, T. M. (2009). Unique Nanostructures and Enhanced Thermoelectric Performance of Melt-Spun BiSbTe Alloys. *Appl. Phys. Lett.* 94 (10), 102111. doi:10.1063/1.3097026

Xin, J., Wu, H., Liu, X., Zhu, T., Yu, G., and Zhao, X. (2017). Mg Vacancy and Dislocation Strains as Strong Phonon Scatterers in $Mg_2Si_{1-x}Sb$ X Thermoelectric Materials. *Nano Energy* 34, 428–436. doi:10.1016/j.nanoen.2017.03.012

Xu, Q., Xu, S.-M., Tian, R., and Lu, C. (2020). Significantly Enhanced Thermoelectric Properties of Organic-Inorganic Hybrids with a Periodically Ordered Structure. *ACS Appl. Mat. Interfaces* 12 (11), 13371–13377. doi:10.1021/acsami.0c00949

Xu, X., Huang, Y., Xie, L., Wu, D., Ge, Z., and He, J. (2020). Realizing Improved Thermoelectric Performance in BiI_3-Doped $Sb_2Te_3(GeTe)_{17}$ via Introducing Dual Vacancy Defects. *Chem. Mat.* 32 (4), 1693–1701. doi:10.1021/acs.chemmater.0c00113

Xue, Q. Y., Liu, H. J., Fan, D. D., Cheng, L., Zhao, B. Y., and Shi, J. (2016). LaPtSb: a Half-Heusler Compound with High Thermoelectric Performance. *Phys. Chem. Chem. Phys.* 18 (27), 17912–17916. doi:10.1039/c6cp03211g

Yamini, S. A., Ikeda, T., Lalonde, A., Pei, Y., Dou, S. X., and Snyder, G. J. (2013). Rational Design of P-type Thermoelectric PbTe: Temperature Dependent Sodium Solubility. *J. Mat. Chem. A* 1 (31), 8725–8730. doi:10.1039/c3ta11654a

Yan, X., Liu, W., Chen, S., Wang, H., Zhang, Q., Chen, G., et al. (2013). Thermoelectric Property Study of Nanostructured P-type Half-Heuslers (Hf, Zr, Ti)$CoSb_{0.8}Sn_{0.2}$. *Adv. Energy Mat.* 3 (9), 1195–1200. doi:10.1002/aenm.201200973

Yang, J., and Caillat, T. (2006). Thermoelectric Materials for Space and Automotive Power Generation. *MRS Bull.* 31 (3), 224–229. doi:10.1557/mrs2006.49

Yang, J. Y., Aizawa, T., Yamamoto, A., and Ohta, T. (2001). Effects of Interface Layer on Thermoelectric Properties of a Pn Junction Prepared via the BMA-HP Method. *Mater. Sci. Eng. B* 85 (1), 34–37. doi:10.1016/s0921-5107(01)00630-4

Yang, S. H., Zhu, T. J., Sun, T., He, J., Zhang, S. N., and Zhao, X. B. (2008). Nanostructures in High-Performance (GeTe)x(AgSbTe$_2$)100−xthermoelectric Materials. *Nanotechnology* 19 (24), 245707. doi:10.1088/0957-4484/19/24/245707

Ying, P., Li, X., Wang, Y., Yang, J., Fu, C., Zhang, W., et al. (2017). Hierarchical Chemical Bonds Contributing to the Intrinsically Low Thermal Conductivity in α-MgAgSb Thermoelectric Materials. *Adv. Funct. Mat.* 27 (1), 1604145. doi:10.1002/adfm.201604145

Yu, J., Fu, C., Liu, Y., Xia, K., Aydemir, U., Chasapis, T. C., et al. (2018). Unique Role of Refractory Ta Alloying in Enhancing the Figure of Merit of NbFeSb Thermoelectric Materials. *Adv. Energy Mat.* 8 (1), 1701313. doi:10.1002/aenm.201701313

Yu, J., Xia, K., Zhao, X., and Zhu, T. (2018). High Performance P-type Half-Heusler Thermoelectric Materials. *J. Phys. D. Appl. Phys.* 51 (11), 113001. doi:10.1088/1361-6463/aaaa58

Yu, Y., He, D.-S., Zhang, S., Cojocaru-Mirédin, O., Schwarz, T., Stoffers, A., et al. (2017). Simultaneous Optimization of Electrical and Thermal Transport Properties of $Bi_{0.5}Sb_{1.5}Te_3$ Thermoelectric Alloy by Twin Boundary Engineering. *Nano Energy* 37, 203–213. doi:10.1016/j.nanoen.2017.05.031

Yvenou, E., Sandroni, M., Carella, A., Gueye, M. N., Faure-Vincent, J., Pouget, S., et al. (2020). Spray-coated PEDOT:OTf Films: Thermoelectric Properties and Integration into a Printed Thermoelectric Generator. *Mat. Chem. Front.* 4 (7), 2054–2063. doi:10.1039/d0qm00265h

Zebarjadi, M., Joshi, G., Zhu, G., Yu, B., Minnich, A., Lan, Y., et al. (2011). Power Factor Enhancement by Modulation Doping in Bulk Nanocomposites. *Nano Lett.* 11 (6), 2225–2230. doi:10.1021/nl201206d

Zeugner, A., Nietschke, F., Wolter, A. U. B., Gaß, S., Vidal, R. C., Peixoto, T. R. F., et al. (2019). Chemical Aspects of the Candidate Antiferromagnetic Topological Insulator $MnBi_2Te_4$. *Chem. Mat.* 31 (8), 2795–2806. doi:10.1021/acs.chemmater.8b05017

Zhang, J., Liu, R., Cheng, N., Zhang, Y., Yang, J., Uher, C., et al. (2014). High-Performance Pseudocubic Thermoelectric Materials from Non-cubic Chalcopyrite Compounds. *Adv. Mat.* 26 (23), 3848–3853. doi:10.1002/adma.201400058

Zhang, J., Song, L., Pedersen, S. H., Yin, H., Hung, L. T., and Iversen, B. B. (2017). Discovery of High-Performance Low-Cost N-type Mg_3Sb_2-Based Thermoelectric Materials with Multi-Valley Conduction Bands. *Nat. Commun.* 8 (1), 1–8. doi:10.1038/ncomms13901

Zhang, Q., Chere, E. K., Sun, J., Cao, F., Dahal, K., Chen, S., et al. (2015). Studies on Thermoelectric Properties of N-type Polycrystalline SnSe1-xSxby Iodine Doping. *Adv. Energy Mat.* 5 (12), 1500360. doi:10.1002/aenm.201500360

Zhao, H., Sui, J., Tang, Z., Lan, Y., Jie, Q., Kraemer, D., et al. (2014). High Thermoelectric Performance of MgAgSb-Based Materials. *Nano Energy* 7, 97–103. doi:10.1016/j.nanoen.2014.04.012

Zhao, K., Liu, K., Yue, Z., Wang, Y., Song, Q., Li, J., et al. (2019). Are Cu_2Te-Based Compounds Excellent Thermoelectric Materials? *Adv. Mat.* 31 (49), 1903480. doi:10.1002/adma.201903480

Zhao, L.-D., Dravid, V. P., and Kanatzidis, M. G. (2014). The Panoscopic Approach to High Performance Thermoelectrics. *Energy Environ. Sci.* 7 (1), 251–268. doi:10.1039/c3ee43099e

Zhao, L.-D., Hao, S., Lo, S.-H., Wu, C.-I., Zhou, X., and Lee, Y. (2013). High Thermoelectric Performance via Hierarchical Compositionally Alloyed Nanostructures. *J. Am. Chem. Soc.* 135 (19), 7364–7370. doi:10.1021/ja403134b

Zhao, L.-D., He, J., Berardan, D., Lin, Y., Li, J.-F., Nan, C.-W., et al. (2014). BiCuSeO Oxyselenides: New Promising Thermoelectric Materials. *Energy Environ. Sci.* 7 (9), 2900–2924. doi:10.1039/c4ee00997e

Zhao, L.-D., Lo, S.-H., Zhang, Y., Sun, H., Tan, G., Uher, C., et al. (2014). Ultralow Thermal Conductivity and High Thermoelectric Figure of Merit in SnSe Crystals. *Nature* 508 (7496), 373–377. doi:10.1038/nature13184

Zhao, L.-D., Tan, G., Hao, S., He, J., Pei, Y., Chi, H., et al. (2016). Ultrahigh Power Factor and Thermoelectric Performance in Hole-Doped Single-Crystal SnSe. *Science* 351 (6269), 141–144. doi:10.1126/science.aad3749

Zhao, L. D., Berardan, D., Pei, Y. L., Byl, C., Pinsard-Gaudart, L., and Dragoe, N. (2010). Bi1−xSrxCuSeO Oxyselenides as Promising Thermoelectric Materials. *Appl. Phys. Lett.* 97 (9), 092118. doi:10.1063/1.3485050

Zhao, L. D., Wu, H. J., Hao, S. Q., Wu, C. I., Zhou, X. Y., Biswas, K., et al. (2013). All-scale Hierarchical Thermoelectrics: MgTe in PbTe Facilitates Valence Band Convergence and Suppresses Bipolar Thermal Transport for High Performance. *Energy Environ. Sci.* 6 (11), 3346–3355. doi:10.1039/c3ee42187b

Zhao, L. D., Zhang, B.-P., Li, J.-F., Zhang, H. L., and Liu, W. S. (2008). Enhanced Thermoelectric and Mechanical Properties in Textured N-type Bi2Te3 Prepared by Spark Plasma Sintering. *Solid State Sci.* 10 (5), 651–658. doi:10.1016/j.solidstatesciences.2007.10.022

Zheng, L., Li, W., Lin, S., Li, J., Chen, Z., and Pei, Y. (2017). Interstitial Defects Improving Thermoelectric SnTe in Addition to Band Convergence. *ACS Energy Lett.* 2 (3), 563–568. doi:10.1021/acsenergylett.6b00671

Zhong, B., Zhang, Y., Li, W., Chen, Z., Cui, J., Li, W., et al. (2014). High Superionic Conduction Arising from Aligned Large Lamellae and Large Figure of Merit in Bulk Cu1.94Al0.02Se. *Appl. Phys. Lett.* 105 (12), 123902. doi:10.1063/1.4896520

Zhou, C., Yu, Y., Lee, Y. K., Cojocaru-Mirédin, O., Yoo, B., Cho, S.-P., et al. (2018). High-Performance N-type PbSe-Cu_2Se Thermoelectrics through Conduction Band Engineering and Phonon Softening. *J. Am. Chem. Soc.* 140 (45), 15535–15545. doi:10.1021/jacs.8b10448

Zhu, P. W., Jia, X., Chen, H. Y., Guo, W. L., Chen, L. X., Li, D. M., et al. (2002). A New Method of Synthesis for Thermoelectric Materials: HPHT. *Solid state Commun.* 123 (1-2), 43–47. doi:10.1016/s0038-1098(02)00182-5

Conflict of Interest: The authors declare that the research was conducted in the absence of any commercial or financial relationships that could be construed as a potential conflict of interest.

Publisher's Note: All claims expressed in this article are solely those of the authors and do not necessarily represent those of their affiliated organizations, or those of the publisher, the editors and the reviewers. Any product that may be evaluated in this article, or claim that may be made by its manufacturer, is not guaranteed or endorsed by the publisher.

frontiers | Frontiers in Chemistry

MINI REVIEW
published: 23 May 2022
doi: 10.3389/fchem.2022.903253

Progress of Dicyanomethylene-4H-Pyran Derivatives in Biological Sensing Based on ICT Effect

*Ting-Ting Hou[1], Yi Cai[1], Zhen-Yu Zhang[1], Cai-Yun Wang[1], Ying-Hao Tang[1], Ming-Qiang Zhu[2] and Ya-Long Wang[1,2,3]**

[1]Key Laboratory of Biomedical Engineering of Hainan Province, School of Biomedical Engineering, Hainan University, Haikou, China, [2]Wuhan National Laboratory for Optoelectronics, Huazhong University of Science and Technology, Wuhan, China, [3]One Health Institute, Hainan University, Haikou, China

As one of the typical fluorescent cores, dicyanomethylene-4H-pyran (DCM) derivatives exhibit excellent photophysical and photochemical properties, such as large Stokes shift, excellent light stability, and tunable near-infrared (NIR) emission. The luminescence mechanism of DCM probes mainly depends on the intramolecular charge transfer (ICT). Hence, by regulating the ICT process, the probes can specifically act on the target molecule. Accordingly, a series of NIR DCM probes have been constructed to detect the ions, reactive oxygen species (ROS), and biological macromolecules in cells. However, there is no relevant review to summarize it at present. This minireview mainly summarizes the NIR DCM probes based on ICT effect and their applications in biosensors and biological imaging in recent years. This will be beneficial to innovatively construct new DCM probes and actively promote their application in the future.

Keywords: dicyanomethylene-4H-pyran (DCM), intramolecular charge transfer, near-infrared probe, bioimaging, biosensor

OPEN ACCESS

Edited by:
Yue Liu,
Liaoning Technical University, China

Reviewed by:
Xu Qiu,
Shandong University of Science and Technology, China
Xiaohuan Sun,
Yangzhou University, China

****Correspondence:***
Ya-Long Wang
ylwang@hainanu.edu.cn

Specialty section:
This article was submitted to Electrochemistry, a section of the journal Frontiers in Chemistry

Received: *24 March 2022*
Accepted: *20 April 2022*
Published: *23 May 2022*

Citation:
Hou T-T, Cai Y, Zhang Z-Y, Wang C-Y, Tang Y-H, Zhu M-Q and Wang Y-L (2022) Progress of Dicyanomethylene-4H-Pyran Derivatives in Biological Sensing Based on ICT Effect. Front. Chem. 10:903253. doi: 10.3389/fchem.2022.903253

INTRODUCTION

Dicyanomethylene-4H-pyran (DCM) is a typical fluorophore, which shows excellent photophysical and photochemical properties, such as large Stokes shift, excellent light stability, and tunable near-infrared emission (Wang et al., 2016; Nabavi et al., 2018). Derivatives derived from DCM have been widely applied in nonlinear optical materials (Guo et al., 2012), logic gates, photovoltaic sensitization (Liu et al., 2009), sensing, and other fields. Compared with cyanine dyes, the excellent photophysical and photochemical properties of DCM derivatives are much conducive to the application in real-time evaluation, detection of analytes, and long-term tracking imaging (Chao et al., 2019). Moreover, the emission peaks of DCM derivatives are usually located at >600 nm, which makes the compounds easily excited by near-infrared (NIR) after simple modification. Dyes with NIR emission are beneficial for biological imaging due to their deep tissue penetration, weak background interference, and negligible cell damage (Guo et al., 2014). Furthermore, DCM dyes possess the merits of high quantum yield, two-photon absorption cross section (Nawimanage et al., 2017; Luo et al., 2021), and easy synthesis methods (Li et al., 2014; Li et al., 2018). Therefore, DCM probes are regarded as promising candidates for biosensors and biological imaging.

Generally, DCM molecules possess a D-π-A configuration, showing a typical ICT effect. ICT effect usually occurs in a molecule with a D-A structure. When the probe with the ICT effect is

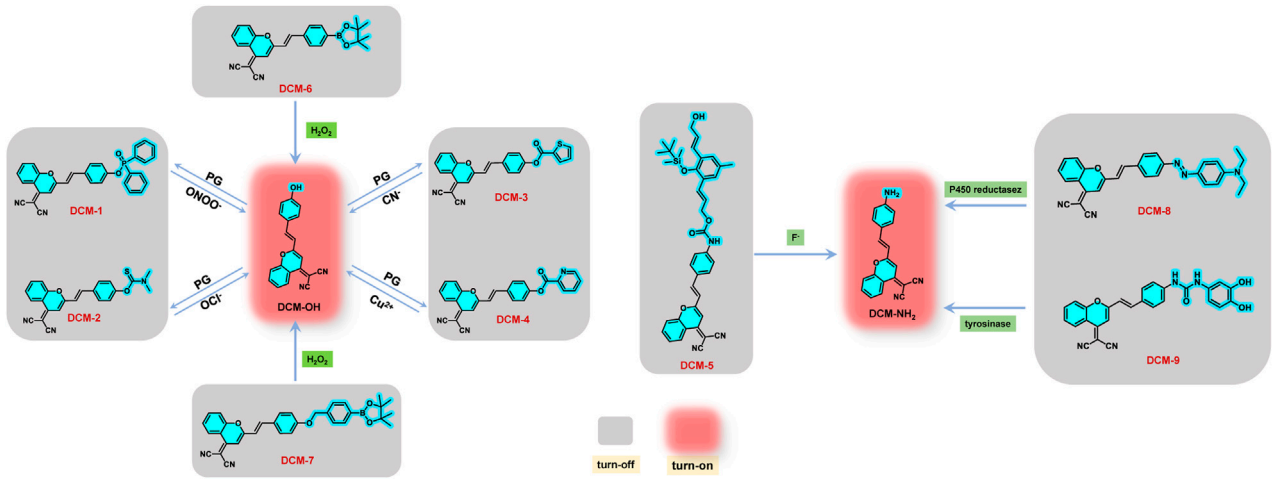

FIGURE 1 | Structure and mechanism of DCM-1~9 for detection of different substances.

activated, the charge is apt to flow from the donor (D) segment to the acceptor (A) segment, resulting in the variation of luminescence. Hence, the emission properties of DCM probes can be adjusted as required by tuning the molecular conjugation system or altering the electron donor group. In addition, DCM probes with an "off–on" function have been obtained successfully by introducing fluorescence-quenching groups as well as other active groups. When the probe contacts the target, the ICT mechanism of the DCM probe is reactivated due to the separation of the fluorescence-quenching group by reaction with the target (**Figure 1**). Thus, the probe lights up afresh. Based on this principle, a series of "off–on" DCM derivatives have been successfully constructed for the detection of ions, reactive oxygen species (ROS), and biological macromolecules in cells (Li et al., 2014; Wang et al., 2019; Yang et al., 2019; Dong et al., 2020; Ling et al., 2021). Although much attention has been paid on this kind of probes in recent years, a systematic overview is rarely reported. Recent advances in "off–on" DCM probes based on the ICT mechanism and their applications are highlighted. The current challenges for large-scale applications are discussed as well.

APPLICATIONS

DCM derivatives with "off–on" characteristics have been successfully applied in detection of ions, hydrogen peroxide, and enzymes. In this section, we will systematically and roundly discuss the current applications of "off–on"-type DCM derivatives with NIR emission based on the ICT mechanism.

Detection of Ions

Ions are closely related to life activities and play a vital role in the field of life (Gale et al., 2008). Therefore, it is of great significance to develop fluorescent probes with excellent recognition for ions. Based on DCM-OH, a series of NIR probes DCM-1~4 was designed and synthesized by introducing various ester-protecting groups (PG) as well as fluorescence-quenching groups (**Figure 1**). In the presence of specific ions, the PG is liable to detach, activating the ICT effect to emit fluorescence (**Figure 1**). Mulay et al. (2017) reported a NIR probe DCM-1 based on DCM, showing remarkable sensitivity to $ONOO^-$. The probe was prequenched skillfully with the diphenyl hypophosphite group, which was sensitive to $ONOO^-$ (**Figure 1**). The fluorescence of DCM-1 turned on again in the presence of $ONOO^-$ in a few minutes with emission enhancement of 120-fold, indicating high selectivity and sensitivity (**Figure 2A**). Moreover, DCM-1 can also track $ONOO^-$ in cells. By replacing the fluorescence-quenching group with dimethyl thiocarbamate (DMTC), Zhang et al. (2019) designed and synthesized an OCl^--targeting probe DCM-2 based on the DCM core (**Figure 1**). DCM-2 could rapidly generate fluorescence response to OCl^- ions within 3 s, with a low detection limit of 80 nM, behaving with high selectivity and sensitivity to OCl^- (**Figure 2B**). Furthermore, the probe was successfully applied in detecting endogenous/exogenous OCl^- in living cells. Those works provide inspirations for designing other ion sensors based on the DCM skeleton.

Recently, Wang et al. (2020) and Li et al. (2021) reported two DCM-type probes DCM-3 and DCM-4 by replacing the protecting group (PG) (**Figure 1**). DCM-3 exhibited remarkable selectivity and sensitivity to CN^-, with the detection limit of 1.44 μM (**Figure 2C**). DCM-4 emitted NIR fluorescence when Cu^{2+} traces were added, with the detection limit of 25.4 nM (**Figure 2D**). Further studies showed that DCM-4 was insensitive to other ions. Those results demonstrate that DCM-4 possesses satisfactory sensitivity and selectivity toward Cu^{2+}. Furthermore, the MTT assay showed that DCM-4 possesses low cytotoxicity and excellent biocompatibility. In addition, a probe DCM-5 sensitive to F^- was reported by Feng et al. (2019) based on the DCM derivative $DCM-NH_2$. A Si-O-connected detachable group was introduced as a fluorescence

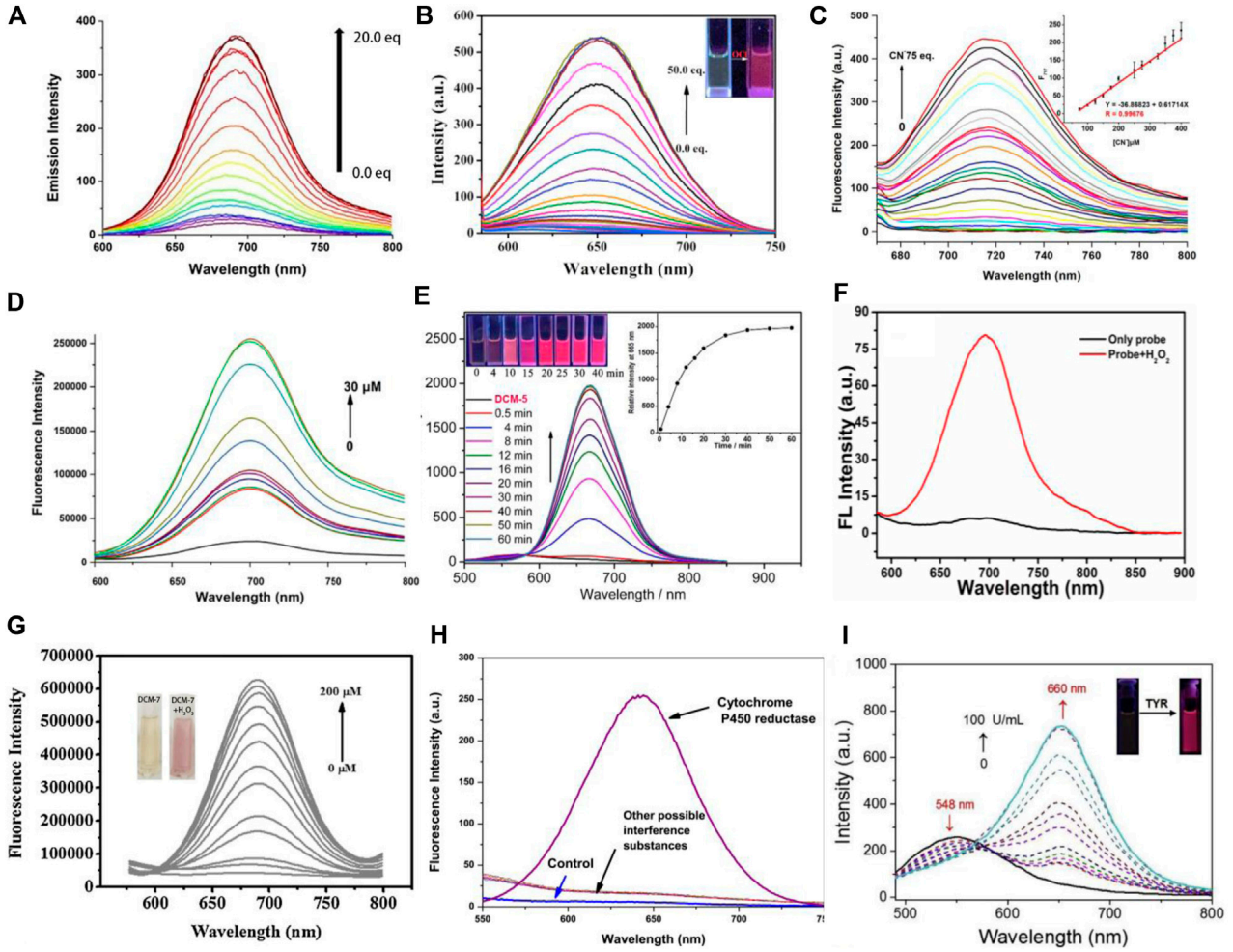

FIGURE 2 | (A) Fluorescence emission spectral changes of DCM-1 with various concentrations of $ONOO^-$ in solution. **(B)** Fluorescence emission spectra of DCM-2 upon gradual addition of OCl^- in EtOH: H_2O = 1:1 (v/v). **(C)** Fluorescence emission spectra of DCM-3 upon the addition of CN^-. **(D)** Fluorescence spectra of DCM-4 with different concentrations of Cu^{2+} in PBS solution. **(E)** Time-dependent emission spectra of DCM-5 with F^- in aqueous solution. **(F)** Fluorescence spectra of DCM-6 in the presence of H_2O_2 with excitation at 560 nm. **(G)** Fluorescence spectra measurement of DCM-7 in the presence of different concentrations of H_2O_2. **(H)** Specific detection of cytochrome P450 reductase among various reductants with DCM-8. **(I)** Emission spectra of DCM-9 with TYR in aqueous solution.

quenchant, and a specific fluoride trigger was elaborately designed (**Figure 2E**). The fluorescence was activated after the addition of F^- in several minutes with a detection limit as low as 157 nM, displaying high sensitivity and selectivity of F^-. Further studies showed that DCM-5 can be successfully applied to the quantitative detection of exogenous fluoride in HeLa cells and zebrafish embryos by fluorescence imaging. Those research studies not only expand the application of DCM-type probes but also provide strategies for the development of subsequent probes.

Detection of Hydrogen Peroxide

Hydrogen peroxide is a kind of reactive oxygen species (ROS), which plays a vital role in a variety of physiological processes. Studies have shown that the imbalance of H_2O_2 is associated with cardiovascular disease, neurodegenerative disease, Alzheimer's disease, cancer, and other serious diseases (Wang et al., 2015; Li et al., 2017; Zhou et al., 2019). Therefore, it is of great significance to develop probes to detect the concentration of hydrogen peroxide in cells.

By introducing borate ester groups sensitive to H_2O_2, DCM-6~7 was obtained with fluorescence quenching because the electron-donating effect of -OH was blocked (Wang et al., 2015; Li et al., 2017; Zhou et al., 2019). In the presence of H_2O_2, the fluorescence of DCM-6 and DCM-7 is turned on due to the restoration of the ICT effect *in vivo* and *in vitro*, showing excellent sensitivity and selectivity toward H_2O_2 (**Figures 2F, G**). It is worth mentioning that DCM-7 showed dual signal with colorimetry and fluorescence in response to H_2O_2 (**Figure 2G**), achieving more reliable detection results. The successful tracks of exogenous and endogenous H_2O_2 in living cells suggest great potential in bioassay.

Detection of Enzymes

The enzyme, a kind of biological macromolecule, is one of the indispensable substances in vital activities. Almost all kinds of reactions in organisms cannot be separated from the catalysis of enzymes. In addition, enzymes are closely related to the occurrence and development of some diseases. Therefore, effective labeling and detection of enzymes have aroused widespread concerns. Cui et al. (2017) and Li et al. (2019) designed and synthesized DCM-8 and DCM-9 based on DCM-NH_2, respectively (**Figure 1**). DCM-8, an off–on probe that is sensitive to cytochrome P450 reductase, was quenched with the azo group. After reacting with cytochrome P450 reductase, NIR fluorescence turned on due to the generation of DCM-NH_2 (**Figure 2H**). The fluorescence intensity was strengthened by more than 156 times after reacting with cytochrome P450 reductase and NADH system for 4 min. Moreover, the probe exhibited strong antiinterference ability and high sensitivity. Tyrosinase (TYR) is a significant biomarker of melanoma cancer and plays an important role in cellular biochemistry and etiology (Lin et al., 2016). Li et al. (2019) reported NIR probe DCM-9 for the detection of endogenous tyrosinase. In the presence of TYR, the tyrosinase trigger group escaped from the DCM core, generating NIR dye DCM-NH_2. DCM-9 possessed high sensitivity and selectivity toward TYR (**Figure 2I**). The MTT assay demonstrated that DCM-9 exhibits low cytotoxicity and good biocompatibility for B16 melanoma cells. Furthermore, the probe was successfully applied to the fluorescence imaging of endogenous TYR in B16 melanoma cells. Thus, the enzyme-activatable NIR probe based on DCM may be a powerful tool for investigating the important roles of enzymes in biological systems.

CONCLUSION

To sum up, DCM derivatives modified with fluorescence-quenching group have shown typical off–on characteristics. According to the different activated substances, the dyes are rationally divided into three sections in this minireview. They are potential candidates for biosensing due to their rich structures and conformations. DCM derivatives have broad prospects in biosensing and bioimaging due to their numerous merits. In the future, more DCM probes will be designed, and efforts focus on the following aspects: 1) design of new-type DCM derivatives with water-solubility, which exhibit great potential in detection of physiological environment, bioimaging, and disease detection drug carriers, etc., 2) developing more applications for DCM probes, such as new iron detection, detection of important active enzymes in the human body, disease screening, and visualization of latent fingerprints. In short, this mini minireview has summarized most of the excellent reports of off–on DCM probes with red emission in this field. It is anticipated that DCM probes with fluorescence activation features will attract more and more interest and greatly flourish.

AUTHOR CONTRIBUTIONS

T-TH. prepared the article. YC, C-YW, Y-HT, and Z-YZ participated in the work of data collection. Y-LW supervised the whole work. All authors discussed and commented on the manuscript.

FUNDING

This work was supported by the National Key R&D Program of China (2021ZD0201004), the National Natural Science Foundation of China (22165008 and 22077037), the Hainan Provincial Natural Science Foundation of China (521RC506), and the Open Project Program of Wuhan National Laboratory for Optoelectronics (No. 2020WNLOKF018).

REFERENCES

Chao, X.-J., Pan, Z.-Y., Sun, L.-L., Tang, M., Wang, K.-N., and Mao, Z.-W. (2019). A pH-Insensitive Near-Infrared Fluorescent Probe for Wash-Free Lysosome-Specific Tracking with Long Time during Physiological and Pathological Processes. *Sensors Actuators B Chem.* 285, 156–163. doi:10.1016/j.snb.2019.01.045

Cui, L., Shi, Y., Zhang, S., Yan, L., Zhang, H., Tian, Z., et al. (2017). A NIR Turn-On Fluorescent Probe Applied in Cytochrome P450 Reductase Detection and Hypoxia Imaging in Tumor Cells. *Dyes Pigments* 139, 587–592. doi:10.1016/j.dyepig.2016.12.062

Dong, L., Fu, M., Liu, L., Han, H. H., Zang, Y., Chen, G. R., et al. (2020). Supramolecular Assembly of TPE-Based Glycoclusters with Dicyanomethylene-4H-Pyran (DM) Fluorescent Probes Improve Their Properties for Peroxynitrite Sensing and Cell Imaging. *Chem. Eur. J.* 26, 14445–14452. doi:10.1002/chem.202002772

Feng, A., Jia, Y., Huang, L., Wang, L., Zhou, G., Wang, S., et al. (2019). 1,6-Elimination Reaction Induced Detection of Fluoride Ions *In Vitro* and *In Vivo* Based on a NIR Fluorescent Probe. *Spectrochimica Acta Part A Mol. Biomol. Spectrosc.* 220, 117108. doi:10.1016/j.saa.2019.05.013

Gale, P. A., García-Garrido, S. E., and Garric, J. (2008). Anion Receptors Based on Organic Frameworks: Highlights from 2005 and 2006. *Chem. Soc. Rev.* 37, 151–190. doi:10.1039/b715825d

Guo, Z., Park, S., Yoon, J., and Shin, I. (2014). Recent Progress in the Development of Near-Infrared Fluorescent Probes for Bioimaging Applications. *Chem. Soc. Rev.* 43, 16–29. doi:10.1039/c3cs60271k

Guo, Z., Zhu, W., and Tian, H. (2012). Dicyanomethylene-4H-Pyran Chromophores for OLED Emitters, Logic Gates and Optical Chemosensors. *Chem. Commun.* 48, 6073–6084. doi:10.1039/c2cc31581e

Li, H., Yao, Q., Fan, J., Du, J., Wang, J., and Peng, X. (2017). A Two-Photon NIR-to-NIR Fluorescent Probe for Imaging Hydrogen Peroxide in Living Cells. *Biosens. Bioelectron.* 94, 536–543. doi:10.1016/j.bios.2017.03.039

Li, K.-B., Chen, F.-Z., Yin, Q.-H., Zhang, S., Shi, W., and Han, D.-M. (2018). A Colorimetric and Near-Infrared Fluorescent Probe for Hydrogen Polysulfides and its Application in Living Cells. *Sens. Actuators B Chem.* 254, 222–226. doi:10.1016/j.snb.2017.07.079

Li, M., Wu, X., Wang, Y., Li, Y., Zhu, W., and James, T. D. (2014). A Near-Infrared Colorimetric Fluorescent Chemodosimeter for the Detection of Glutathione in Living Cells. *Chem. Commun.* 50, 1751–1753. doi:10.1039/c3cc48128j

Li, Q., Yan, C., Zhang, J., Guo, Z., and Zhu, W.-H. (2019). Ratiometric and Light-Up Near-Infrared Fluorescent DCM-Based Probe for Real-Time Monitoring

Endogenous Tyrosinase Activity. *Dyes Pigments* 162, 802–807. doi:10.1016/j.dyepig.2018.11.019

Li, Z., Xu, Y., Xu, H., Cui, M., Liu, T., Ren, X., et al. (2021). A Dicyanomethylene-4H-Pyran-Based Fluorescence Probe with High Selectivity and Sensitivity for Detecting Copper (II) and its Bioimaging in Living Cells and Tissue. *Spectrochimica Acta Part A Mol. Biomol. Spectrosc.* 244, 118819. doi:10.1016/j.saa.2020.118819

Lin, T.-E., Bondarenko, A., Lesch, A., Pick, H., Cortés-Salazar, F., and Girault, H. H. (2016). Monitoring Tyrosinase Expression in Non-Metastatic and Metastatic Melanoma Tissues by Scanning Electrochemical Microscopy. *Angew. Chem. Int. Ed.* 55, 3813–3816. doi:10.1002/anie.201509397

Ling, C., Liu, T., Li, R., Wang, S., Zhang, J., Li, S., et al. (2021). A Novel DCM-Based NIR Fluorescent Probe for Detecting Ozone and its Bioimaging in Live Cells. *Spectrochimica Acta Part A Mol. Biomol. Spectrosc.* 248, 119192. doi:10.1016/j.saa.2020.119192

Liu, B., Zhu, W., Zhang, Q., Wu, W., Xu, M., Ning, Z., et al. (2009). Conveniently Synthesized Isophorone Dyes for High Efficiency Dye-Sensitized Solar Cells: Tuning Photovoltaic Performance by Structural Modification of Donor Group in Donor-π-Acceptor System. *Chem. Commun.* 13, 1766–1768. doi:10.1039/b820964b

Luo, X., Cheng, Z., Wang, R., and Yu, F. (2021). Indication of Dynamic Peroxynitrite Fluctuations in the Rat Epilepsy Model with a Near-Infrared Two-Photon Fluorescent Probe. *Anal. Chem.* 93 (4), 2490–2499. doi:10.1021/acs.analchem.0c04529

Mulay, S. V., Kim, Y., Lee, K. J., Yudhistira, T., Park, H.-S., and Churchill, D. G. (2017). A Fluorogenic and Red-Shifted Diphenyl Phosphinate-Based Probe for Selective Peroxynitrite Detection as Demonstrated in Fixed Cells. *New J. Chem.* 41, 11934–11940. doi:10.1039/c7nj02530k

Nabavi, S. H., Khodabandeh, M. H., Golbabaee, M., Moshaii, A., and Davari, M. D. M. (2018). Excited States Study Reveals the Twisted Geometry Induced Large Stokes Shift in DCM Fluorescent Dye. *J. Photochem. Photobiol. A Chem.* 354, 127–138. doi:10.1016/j.jphotochem.2017.05.017

Nawimanage, R. R., Prasai, B., Hettiarachchi, S. U., and Mccarley, R. L. (2017). Cascade Reaction-Based, Near-Infrared Multiphoton Fluorescent Probe for the Selective Detection of Cysteine. *Anal. Chem.* 89 (12), 6886–6892. doi:10.1021/acs.analchem.7b01384

Wang, B.-B., Wang, Y., Wu, W.-N., Xu, Z.-H., Zhao, X.-L., Xu, Z.-Q., et al. (2020). A Near-Infrared Colorimetric and Fluorescent Dual-Channel Probe for Cyanide Detection Based on Dicyanomethylene-4H-Pyran. *Inorg. Chem. Commun.* 122, 108245. doi:10.1016/j.inoche.2020.108245

Wang, P., Wang, K., Chen, D., Mao, Y., and Gu, Y. (2015). A Novel Colorimetric and Near-Infrared Fluorescent Probe for Hydrogen Peroxide Imaging *In Vitro* and *In Vivo*. *RSC Adv.* 5, 85957–85963. doi:10.1039/c5ra16827a

Wang, T., Chai, Y., Chen, S., Yang, G., Lu, C., Nie, J., et al. (2019). Near-Infrared Fluorescent Probe for Imaging Nitroxyl in Living Cells and Zebrafish Model. *Dyes Pigments* 166, 260–265. doi:10.1016/j.dyepig.2019.03.013

Wang, X., Guo, Z., Zhu, S., Liu, Y., Shi, P., Tian, H., et al. (2016). Rational Design of Novel Near-Infrared Fluorescent DCM Derivatives and Their Application in Bioimaging. *J. Mat. Chem. B* 4, 4683–4689. doi:10.1039/c6tb01096b

Yang, Y., Wang, L., Xu, M., Chen, J., and Qu, Y. (2019). Triphenyl Phosphate End-Capped Dicyanomethylene-4H-Pyran as a Near Infrared Fluorescent Sensor for Lysozyme in Urine Sample. *Sensors Actuators B Chem.* 284, 553–561. doi:10.1016/j.snb.2019.01.001

Zhang, Y.-Y., Chen, X.-Z., Liu, X.-Y., Zhang, X.-Y., Gao, G., Hou, S.-C., et al. (2019). A Highly Selective and Ultrafast Near-Infrared Fluorescent Turn-On and Colorimetric Probe for Hypochlorite in Living Cells. *Anal. Chim. Acta* 1078, 135–141. doi:10.1016/j.aca.2019.06.014

Zhou, Z., Li, Y., Su, W., Gu, B., Xu, H., Wu, C., et al. (2019). A Dual-Signal Colorimetric and Near-Infrared Fluorescence Probe for the Detection of Exogenous and Endogenous Hydrogen Peroxide in Living Cells. *Sensors Actuators B Chem.* 280, 120–128. doi:10.1016/j.snb.2018.09.126

Conflict of Interest: The authors declare that the research was conducted in the absence of any commercial or financial relationships that could be construed as a potential conflict of interest.

Publisher's Note: All claims expressed in this article are solely those of the authors and do not necessarily represent those of their affiliated organizations, or those of the publisher, the editors, and the reviewers. Any product that may be evaluated in this article, or claim that may be made by its manufacturer, is not guaranteed or endorsed by the publisher.

frontiers | Frontiers in Chemistry

ORIGINAL RESEARCH
published: 26 May 2022
doi: 10.3389/fchem.2022.916860

Design of $Ni(OH)_2$/M-MMT Nanocomposite With Higher Charge Transport as a High Capacity Supercapacitor

G. M. Xu[1†], M. Wang[2,3†], H. L. Bao[2], P. F. Fang[2], Y. H. Zeng[2], L. Du[2] and X. L. Wang[2,3]*

[1]School of Mechanical Engineering, Liaoning Technical University, Fuxin, China, [2]School of Materials Science and Engineering, Liaoning Technical University, Fuxin, China, [3]Key Laboratory of Mineral High Value Conversion and Energy Storage Materials of Liaoning Province, Fuxin, China

OPEN ACCESS

Edited by:
Meng Zheng,
Qingdao Haiwan Science and Technology Industry Research Institute Co., Ltd., China

Reviewed by:
Yong Yan,
Beijing University of Technology, China
Huizhi Lu,
Qingdao University of Science and Technology, China
Xiao Lyu,
Shenyang Ligong University, China

***Correspondence:**
M. Wang
wangming@lntu.edu.cn

[†]These authors have contributed equally to this work

Specialty section:
This article was submitted to Electrochemistry, a section of the journal Frontiers in Chemistry

Received: 10 April 2022
Accepted: 27 April 2022
Published: 26 May 2022

Citation:
Xu GM, Wang M, Bao HL, Fang PF, Zeng YH, Du L and Wang XL (2022) Design of $Ni(OH)_2$/M-MMT Nanocomposite With Higher Charge Transport as a High Capacity Supercapacitor. Front. Chem. 10:916860. doi: 10.3389/fchem.2022.916860

Nano-petal nickel hydroxide was prepared on multilayered modified montmorillonite (M-MMT) using one-step hydrothermal method for the first time. This nano-petal multilayered nanostructure dominated the ion diffusion path to be shorted and the higher charge transport ability, which caused the higher specific capacitance. The results showed that in the three-electrode system, the specific capacitance of the nanocomposite with 4% M-MMT reached 1068 F/g at 1 A/g and the capacity retention rate was 70.2% after 1,000 cycles at 10 A/g, which was much higher than that of pure $Ni(OH)_2$ (824 F/g at 1 A/g), indicating that the $Ni(OH)_2$/M-MMT nanocomposite would be a new type of environmentally friendly energy storage supercapacitor.

Keywords: montmorillonite, $Ni(OH)_2$, charge transport, nano-petal multilayered nanostructure, electrochemical performance

INTRODUCTION

With the vigorous development of science and technology, there appear many problems, such as: energy crisis, environmental pollution, greenhouse effect, etc., (Shi et al., 2020; Delbari et al., 2021). It is now crucial to find new, low-cost and environmentally friendly energy conversion and storage systems (Liu et al., 2020). Until now, a great deal of research had been done on energy storage materials and systems (Duraković and Mešetović, 2019; Fleischmann et al., 2020; Dou et al., 2021; Yang et al., 2021; Caturwati et al., 2022; Lv et al., 2022).

Supercapacitors had been widely used in modern energy storage devices due to their higher power density, fast charging and discharging speed, and low impact on the ecological environment, which have become a hot research issue for many researchers (Wiston and Ashok, 2019; Ovhal et al., 2020; Wang et al., 2021a; Zhang et al., 2021). Supercapacitors can be classified into pseudocapacitor (PCs), electric double layer supercapacitors (EDLCs), and hybrid supercapacitors (HCs) according to different storage mechanisms. Carbon-based materials such as activated carbon (Wang et al., 2021b), graphene (Wan et al., 2020), carbon nanotubes (Saikia et al., 2020), etc., had been used for EDLC. On the other hand, transition metal oxides/hydroxides and conducting polymers were widely used in pseudocapacitors, which had higher power densities than EDLCs. Several metal oxides are used as electrode materials, such as RuO_2, NiO, CuO, MnO_2, TiO_2, etc., (Zheng et al., 2018). Metal hydroxides were an attractive alternative as electrode materials for higher-energy and higher-power supercapacitors because of the higher specific capacitance and the higher charge transport ability, which may

make the construction of higher-energy, higher-power supercapacitors more feasible (Soserov et al., 2018a).

Nickel hydroxide had the characteristics of being the cheapest, high specific capacity and good stability among electrode materials, and had become an important supercapacitor electrode material. The preparation and performance have become one of the current research hotspots (Xing et al., 2012; Liu et al., 2017; Wu et al., 2020; Yang et al., 2020). Due to its low specific surface area and poor electrical conductivity, the diffusion distance of the electrolyte during charging is very short, and often only the surface part of the active material exchanges charges, and a large amount of internal space does not participate in the electrochemical energy storage process (Singh et al., 2017). There appears Ni(OH)$_2$ aggregation formation during the preparation process, causing poor electrochemical performance (Soserov et al., 2018b). To solve the above problems, many scholars have loaded metal hydroxides on carbon materials with high specific surface area and high electrical conductivity or composited with metal oxides to improve the capacitance performance and cycle stability (Li et al., 2017; Liang et al., 2017; Chen et al., 2020; Li et al., 2020; Rawat et al., 2022). MMT was a layered substance composed of three parts, that is, two silicon-oxygen tetrahedra are located on the upper and lower sides of symmetry, and an aluminum-oxygen octahedron is sandwiched in the middle. These three parts constitute the 2:1 structural configuration of the entire montmorillonite crystal. MMT had a broad interlayer domain, which was very effective in storing and adsorbing water and organic matter, and also facilitated charge transport, so it was feasible to apply it in supercapacitors (Li et al., 2021a).

Many researchers on the utilization of montmorillonite were in the fields of environment, catalysis and biology, but very little in the field of supercapacitors (Numan et al., 2017). Therefore, in this paper, we designed of Ni(OH)$_2$/M-MMT nanocomposite with higher charge transport as a high capacity supercapacitor for the first time, and it is also the first time that the experiment and computational simulation of montmorillonite were combined. The electrode material was prepared by a simple hydrothermal process without using alkalis, organic solvents and chemical binders. Compared with pure Ni(OH)$_2$ nanomaterials, the prepared Ni(OH)$_2$/M-MMT nanocomposite would have higher capacitance and specific surface area and have great potential in the field of supercapacitors.

EXPERIMENT

Preparation of Modified Montmorillonite

5 g montmorillonite was dissolved in 50 ml deionized water and stirred for 30 min Na_2CO_3 powder was added, and then stirred to full reaction, the PH value of the solution was reached a weak alkaline with NaOH and HCl, continue to stir for 2 h, after the stirring is over, use deionized water for suction filtration, wash three times, put it in a drying box for 6 h, and finally grind the dried sample through a 300-mesh fine sieve. So far, the modified montmorillonite has been prepared.

Preparation of Ni(OH)$_2$/M-MMT Nanocomposite

8 mmoL $NiCl_2$·$6H_2O$ was dissolved in 30 ml deionized water. After $NiCl_2$·$6H_2O$ is completely dissolved in deionized water, modified montmorillonite with different contents (2, 4, 6, 8%) was added and stirred. After 1 h, 3 mmoL of hexamethylenetetramine was added, mixed and stirred for 30 min. The solution was added to the reaction kettle and reacted at 160°C for 1 h. After suction filtration, washing, drying, and finally grinding into powder. The whole experimental process was shown in **Figure 1**.

Material Characterization

The micro-morphology of the composite material was observed by SEM(JSM-7500F). The phase analysis and structural characterization of the Ni(OH)$_2$/M-MMT were carried out by XRD (SHIMADZU XRD-6100). The bonding condition of the nanocomposite was analyzed by XPS (SHIMADZU/KRATOS AXIS Ultra DLD). The specific surface area and pore distribution of the sample were measured by ASAP 2460 BET surface analyzer.

Electrochemical Properties Measurement

The electrochemical performance of the three-electrode system was tested in 1 mol/L KOH electrolyte with sample electrode as working electrode, mercuric oxide electrode as reference electrode and platinum sheet as counter electrode, using Shanghai Chenhua CHI660E electrochemical workstation.

Computational Method

First-principle calculation of Ni(OH)$_2$/MMT nanocomposite microstructure model was carried out by CASTEP module of Materials Studio calculation software. The interaction between adsorbates and different surfaces was accurately described using Perdew-Burke-Ernzerhof (PBE) function under generalized gradient approximation (GGA). During the whole calculation process, the number of plane wave basis functions was determined by the kinetic energy cut-off point Ecut, which was selected as 400 eV. The effects of various nuclei and inner electrons on outer electrons were described by ultra-soft pseudopotentials. 3 × 3 × 1 k-point grid was used for Brillouin zone integration. A single cell material model with 8 H atoms, 32 O atoms, 4 Al atoms, 8 Si atoms and 4 Ni atoms were constructed.

RESULTS AND DISCUSSION

The SEM images of the Ni(OH)$_2$/M-MMT nanocomposite with different content was shown in **Figure 2**, the inset image was locally enlarged. EDS pattern was showed in the (**Supplementary Figure S1**). From EDS analysis and the content of each element of the Ni(OH)$_2$/M-MMT nanocomposite, it can be seen that the contents of O, Ni, Al and Si were 65.4%, 34.4%, 0.05% and 0.15%, respectively. With the increase of M-MMT content, the nano-petal morphology

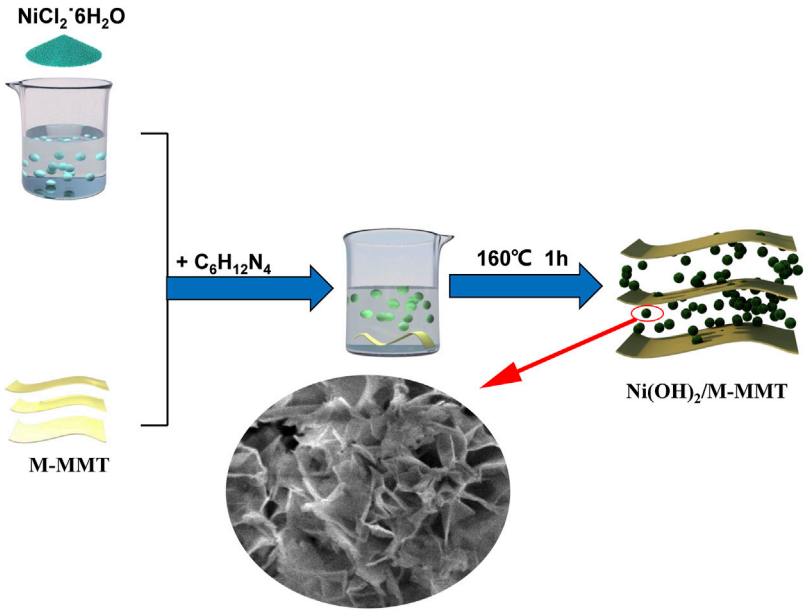

FIGURE 1 | The flow chart of the preparation of Ni(OH)$_2$/M-MMT nanocomposite.

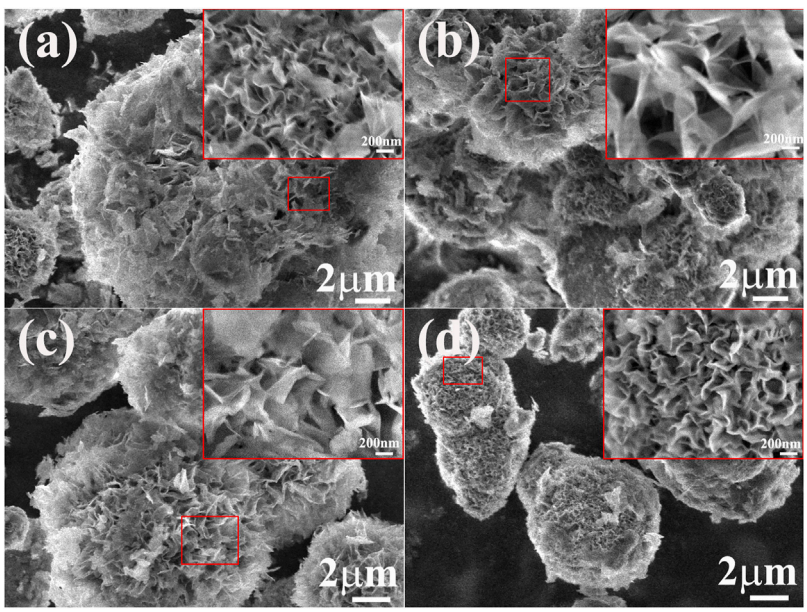

FIGURE 2 | SEM morphology of Ni(OH)$_2$/M-MMT nanocomposite with different M-MMT content. **(A)** M-MMT~2%, **(B)** M-MMT~4%, **(C)** M-MMT~6%, **(D)** M-MMT~8% (inset: locally enlarged image).

of the Ni(OH)$_2$/M-MMT nanocomposite persisted and was not destroyed due to the influence of the reaction conditions. At high magnification, it was obvious that the ultrathin nanoplates grown vertically or attached obliquely on M-MMT and were interlaced with each other to form a highly open nano-petals structure, in which the layered-space of nano-petals became wider as M-MMT content increased from 2 to 4% (see inset of **Figures 2A,B**), and the layer thickness and layer spacing of the nanocomposite with 4% M-MMT was about 23.0 and 68.30 nm respectively. The nano-petals of Ni(OH)$_2$/M-MMT nanocomposite appeared larger and became looser at the addition of 4%, which can increase specific surface area, provide more electroactive surface sites, and the more charge transport. The spacing of

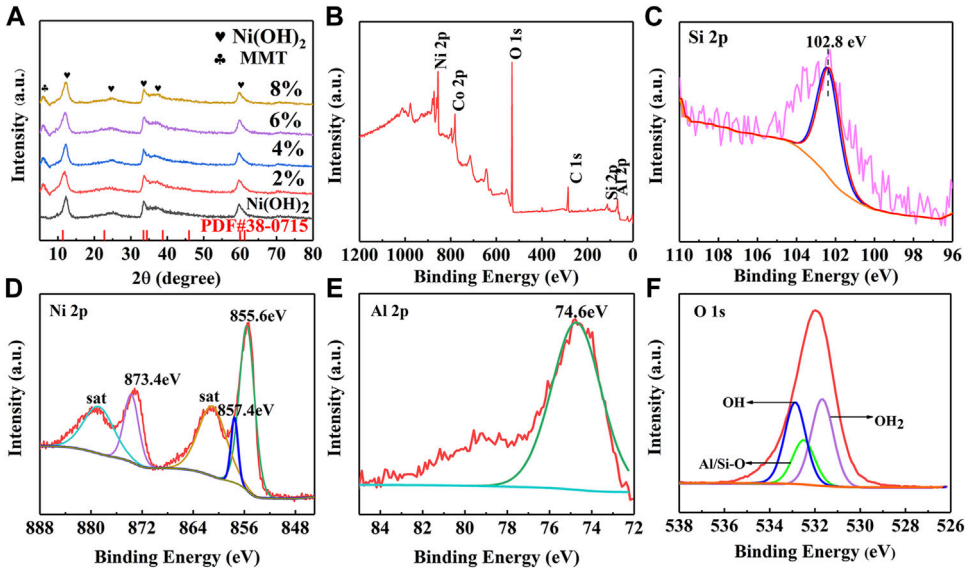

FIGURE 3 | (A) XRD patterns of pure Ni(OH)$_2$ and Ni(OH)$_2$/M-MMT nanocomposite with different content, **(B)** XPS full survey spectra of the Ni(OH)$_2$/M-MMT nanocomposite, XPS spectra of **(C)** Si 2p, **(D)** Ni 2p, **(E)** Al 2p and **(F)** O 1s for Ni(OH)$_2$/M-MMT nanocomposite.

the flowers is gradually reduced, and the vertically oriented nano-petals tend to cluster together to form micro-flowers. With increasing, the spacing of nano-petals of 4–8% nanocomposite gradually decreased. This was because when the Ni(OH)$_2$ entered the interlayer of the montmorillonite, with the increase of the M-MMT content, the nanoflowers "blooming" was inhibited, resulting in a decrease in the interlayer spacing of the Ni(OH)$_2$ nano-petals.

XRD patterns of Ni(OH)$_2$/M-MMT nanocomposite with different ratios was shown in **Figure 3A**. It was found that the diffraction peaks of M-MMT were located at 7.15°, 19.83°, 28.43°, 35.16°, and 61.76°, corresponding to (001) (100) (005) (110) and (300), respectively, which was consistent with the standard card of montmorillonite (JCPDS#12-0,204) (Ge et al., 2021). The diffraction peaks of Ni(OH)$_2$ located at 11.2°, 22.6°, 33.44°, 38°, 59.56°, and 61°. The peaks correspond to (003) (006) (101) (015) (110) and (113), respectively, which the XRD pattern matched the α-nickel hydroxide of JCPDS card number 38–0,715 (Zuo et al., 2020). The characteristic diffraction peaks of MMT and Ni(OH)$_2$ appeared in Ni(OH)$_2$/M-MMT, the diffraction peak of MMT was weaker than that of Ni(OH)$_2$. The broad and weak diffraction peaks of Ni(OH)$_2$/M-MMT nanocomposite indicate that the material was lower in crystallinity. However, the (003) diffraction peak of the Ni(OH)$_2$/M-MMT nanocomposite was slightly shifted to the high-angle direction. This may be because the atomic radius of Si element in MMT was smaller than that of Ni. Therefore, the lattice of α-Ni(OH)$_2$ shrank slightly after recombination. No peaks of other impurity phases could be found, indicating that the synthesized Ni(OH)$_2$/M-MMT had high purity.

The X-ray photoelectron spectroscopy (XPS) full survey spectra of the Ni(OH)$_2$/M-MMT nanocomposite was shown in **Figure 3B** and the corresponding deconvolution spectra of Si 2p, Ni 2p, Al 2p, O 1s was shown in **Figures 3C–F**, respectively. The peak at 102.8 eV in the energy spectrum of Si 2p in **Figure 3C** was characteristic of Si-O bonds in the montmorillonite structure (Payne et al., 2012; Biesinger et al., 2012; Cao et al., 2019). From **Figure 3D** Ni 2p scans depict spin-orbit peaks at 872.9 and 855.6 eV at chiral separation energy of 17.3 eV and two adjacent satellite vibrational peaks, assigned to Ni 2p$_{1/2}$ and Ni 2p$_{3/2}$ (He et al., 2022), indicating that Ni^{2+} existed in Ni(OH)$_2$/M-MMT nanocomposite (Jiang et al., 2019). It can be seen that the energy spectrum of the Al 2p in **Figure 3E** element exhibits a characteristic peak with a binding energy of 74.6 eV. The exfoliated structure can be attributed to Al_2O_3 or AlO(OH) (Qin et al., 2015; Zhou et al., 2019). The peak located at 531.7 eV was usually associated with the hydroxide species (Bai et al., 2015). The lattice oxygen in silicon/aluminum oxides (Si/Al-O) was found with a binding energy of 532.5 eV (Yao et al., 2020). The contribution at 532.9 eV corresponded to physically adsorbed and chemically ad-sorbed water on or near the surface (Tong et al., 2016).

In order to determine the specific surface area and pore size distribution of the prepared specimen, N_2 adsorption/desorption isotherms BET analysis of Ni(OH)$_2$ and Ni(OH)$_2$/MMT nanocomposite was shown in **Figure 4A**. It was seen that the specific surface area of Ni(OH)$_2$/M-MMT nanocomposite was 60 m^2/g, which was higher compared with pure Ni(OH)$_2$ (50 m^2/g). All samples exhibited type IV isotherms, which were typical features of mesoporous materials (Yin et al., 2016). According to the pore size distribution (**Figure 3B**), the mean pore sizes of pure Ni(OH)$_2$ and Ni(OH)$_2$/M-MMT was 12.18 and 15.06 nm, respectively. The large specific surface area and moderate pore size of Ni(OH)$_2$/M-MMT can expose more electroactive sites, provide more electroactive surface sites and the more charge transport.

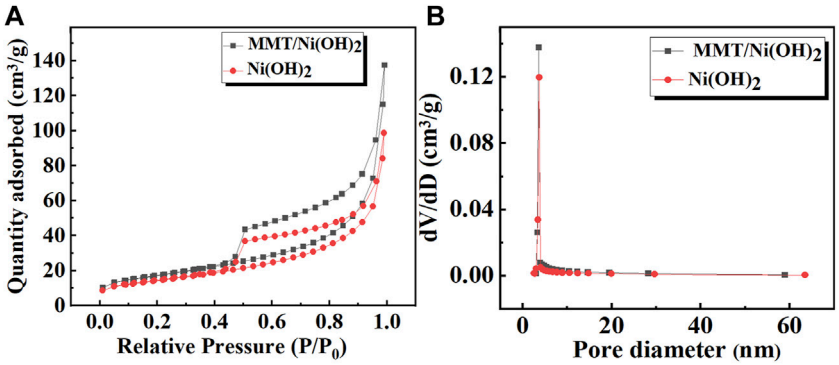

FIGURE 4 | (A) N_2 adsorption/desorption isotherms curves of pure $Ni(OH)_2$ and $Ni(OH)_2$/M-MMT nanocomposite, **(B)** Pore size distribution of pure $Ni(OH)_2$ and $Ni(OH)_2$/M-MMT nanocomposite.

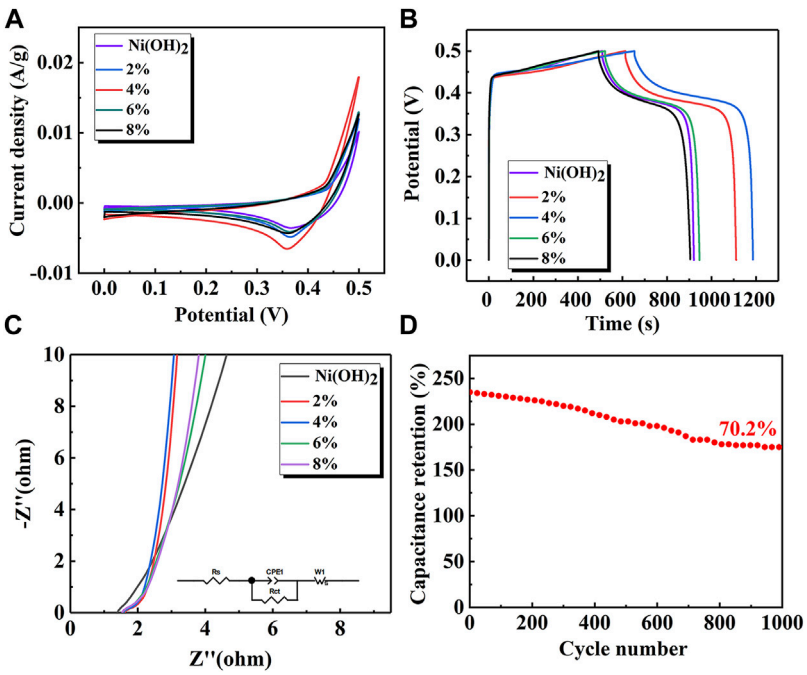

FIGURE 5 | Electrochemical performance curves of pure $Ni(OH)_2$ and $Ni(OH)_2$/M-MMT, **(A)** Cyclic voltammetry curve, **(B)** Galvanostatic discharge curve, **(C)** The EIS (AC impedance) diagram of $Ni(OH)_2$/M-MMT, **(D)** Long cycle curves of nanocomposite with M-MMT 4%.

The electrochemical performance of the $Ni(OH)_2$ and $Ni(OH)_2$/M-MMT nanocomposite with different M-MMT content was shown in **Figure 5**. **Figure 5A** showed the CV curves of $Ni(OH)_2$ and $Ni(OH)_2$/M-MMT nanocomposite with different M-MMT content. It can be seen that a pair of redox peaks caused by the redox reaction of Ni was generated and the pseudocapacitance characteristics was exhibited (Li et al., 2021b). The CV curve area of the $Ni(OH)_2$/M-MMT nanocomposite with the M-MMT content of 4% was the largest, which indicated the capacitance of $Ni(OH)_2$/M-MMT nanocomposite with the M-MMT content of 4% was larger than that of other M-MMT content, because the capacitance of the electrode was related to the integral CV curve area (Zheng et al., 2021).

The GCD curve of $Ni(OH)_2$ and $Ni(OH)_2$/M-MMT nanocomposite at 1 A/g was shown in **Figure 5B**. The platform indicated that this was a Faradaic reaction, in which the specific capacitance of pure $Ni(OH)_2$ was 824 F/g, the specific capacitance of pure M-MMT was only 1.4 F/g (**Supplementary Figure S2**), but the specific capacitance of $Ni(OH)_2$/M-MMT nanocomposite with different M-MMT content was 1000 F/g (2%), 1068 F/g (4%), 848 F/g (6%), 827.2 F/g (8%), respectively. It can be found that the specific capacitance of $Ni(OH)_2$/M-MMT with 4% $Ni(OH)_2$ had been improved with the addition of

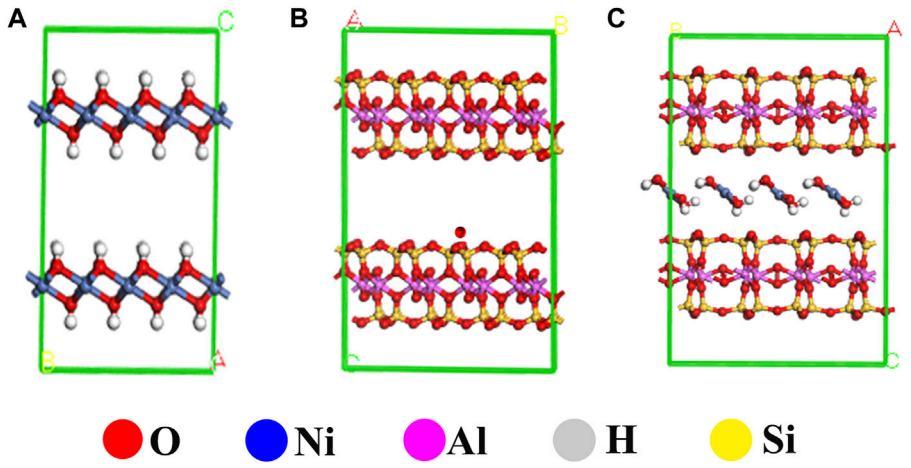

FIGURE 6 | The structural optimization diagrams of **(A)** MMT, **(B)** Ni(OH)$_2$ and **(C)** Ni(OH)$_2$/MMT.

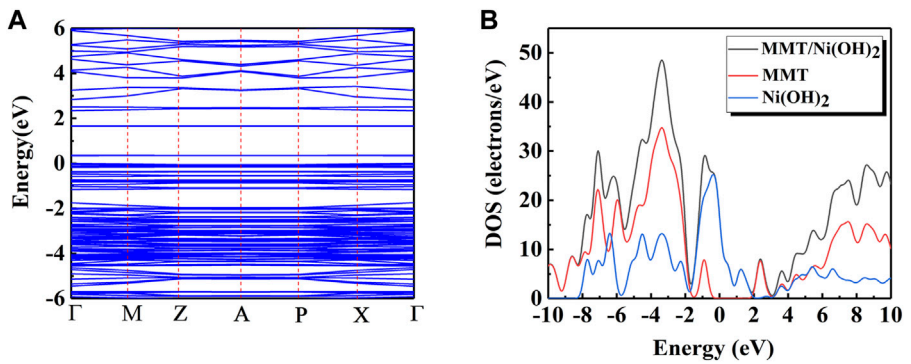

FIGURE 7 | (A) The energy band diagram of Ni(OH)$_2$/MMT; **(B)** The density of states of MMT, Ni(OH)$_2$ and Ni(OH)$_2$/MMT.

M-MMT. The specific capacitance of Ni(OH)$_2$/M-MMT nanocomposite with 4% was increased to 130% compared with that of pure Ni(OH)$_2$. This was because M-MMT had a multilayered "hamburger" structure, which provided greater ion exchange space, promoted ion diffusion path and increased the rate of charge transport. The nano-petals Ni(OH)$_2$ entered the M-MMT interlayer during hydrothermal synthesis. The nano-petals surface had grooves and gap, which improved the movement of electrolyte ions. The gap between the petals facilitated the insertion of electrolyte ions into the electrode surface (Jiang et al., 2021). This enhanced the electrochemical activity of Ni(OH)$_2$/M-MMT nanocomposite, resulting in a significant increase in the specific capacitance of the nanocomposite.

Figure 5C showed AC impedance curves of pure Ni(OH)$_2$ and Ni(OH)$_2$/M-MMT nanocomposite with different M-MMT content and the inset image was equivalent circuit diagram. The EIS data further validated the ion diffusion and conductance kinetics. The charge transfer resistance of the electrode material corresponds to the diameter of the semicircle in the high frequency range and lower resistance availed charge faster transport. The linear characteristic in the low frequency range represents the diffusion resistance of electrolyte ions on the surface. The smaller particle size and many interfaces of electrode material were beneficial to the diffusion of electrolytes (Ramesh et al., 2021). When the slope was closer to 90, the ion diffusion effect was stronger (Zou et al., 2020). From **Figure 5C**, the slope of Ni(OH)$_2$/M-MMT nanocomposite in the low frequency range was larger than that of pure Ni(OH)$_2$, and the slope of Ni(OH)$_2$/M-MMT nanocomposite with 4% M-MMT was the highest in the low frequency range. This was because the layer spacing of M-MMT was larger, which increased the space of ion transmission and enhanced the conductivity.

The long cycle performance of the Ni(OH)$_2$/M-MMT nanocomposite with 4% M-MMT at 10 A/g for 1,000 cycles was shown in **Figure 5D**. The specific capacitance was 175 F/g at 10 A/g after 1,000 cycles, and the capacitance retention rate reached 70.2%.

The structural model of MMT, Ni(OH)$_2$, and Ni(OH)$_2$/MMT was optimized based on the density functional theory (DFT) by Materials Studio (Boek et al., 1995; Tao et al., 2020; Han et al., 2021), as shown in **Figure 6**. **Figure 7** showed the energy bands and density

of states of $Ni(OH)_2$/MMT nanocomposite. From **Figure 7A**, $E_f = 0$ was considered as the Fermi level, and the integration path was Γ-M-Z-A-P-X-Γ. The top of the valence band was close to the Fermi level, and its band gap value was 0.335 eV, which was a typical semiconductor feature (Kong et al., 2021).

To obtain a further understanding of the interaction between $Ni(OH)_2$/MMT nanocomposite, the partial density of states (PDOS) and total density of states (TDOS) of $Ni(OH)_2$/MMT nanocomposite were calculated and compared with that of $Ni(OH)_2$ and MMT as shown in **Figure 7B**. In the $Ni(OH)_2$/MMT system, the atoms of the $Ni(OH)_2$/MMT nanocomposite material can gain more charges from $Ni(OH)_2$. Based on the above calculation results, it was shown that the addition of MMT leaded to the obvious charge transfer of Ni^{2+}, which increased the charge transport rate. At the Fermi level, the energy of the $Ni(OH)_2$/MMT nanocomposite was higher than that of pure $Ni(OH)_2$ and MMT, and the energy of $Ni(OH)_2$ was higher than that of MMT, indicating that the energy of the nanocomposite mainly from $Ni(OH)_2$ (Zhao et al., 2019). The state at the Fermi level was almost flat, indicating that the $Ni(OH)_2$/MMT nanocomposite was in a stable state, which was consistent with the previous experiments and achieved the expected effect.

CONCLUSION

1) The $Ni(OH)_2$ nano-petal was grown on the modified montmorillonite, and the nano-petal was uniformly distributed and had a large specific surface area.
2) The specific capacitance of $Ni(OH)_2$/M-MMT nanocomposite was 1086 F/g at 1 A/g under three electrodes, the capacitance retention rate of $Ni(OH)_2$/M-MMT nanocomposite can reach 70.2% at 10 A/g after 1,000 cycles.
3) According to the first-principles calculation, the band gap value of the $Ni(OH)_2$/MMT nanocomposite was 0.335 eV, and the state at the Fermi level was almost flat, indicating that the $Ni(OH)_2$/MMT nanocomposite was in a stable state and presented a semiconductor structure. The $Ni(OH)_2$/MMT nanocomposite could short the path of ion diffusion and improve the speed of charge transport.

DATA AVAILABILITY STATEMENT

The original contributions presented in the study are included in the article/**Supplementary Material**, further inquiries can be directed to the corresponding author.

AUTHOR CONTRIBUTIONS

MW: Resources, Writing-Review & Editing, Supervision, Project administration, Funding acquisition GX: Writing-Original draft HB: Designing and Completing experiments PF, YZ, and LD: Investigation, Writing-Review and Editing XW: Funding acquisition.

FUNDING

This work was financially supported by the National Natural Science Foundation of China. (51974152), General Project of Science Research Foundation of Liaoning Province (LJKZ0363), Central Government Guiding Local Project of Science and Technology Development Foundation (2022JH6/100100047) and Discipline Innovation Team Project of Liaoning Technical University (LNTU20TD-09 and LNTU20TD-16). Liaoning Research Project of Education Science and Technology (552001027155).

SUPPLEMENTARY MATERIAL

The Supplementary Material for this article can be found online at: https://www.frontiersin.org/articles/10.3389/fchem.2022.916860/full#supplementary-material

REFERENCES

Bai, Y., Wang, W., Wang, R., Sun, J., and Gao, L. (2015). Controllable Synthesis of 3D Binary Nickel-Cobalt Hydroxide/graphene/nickel Foam as a Binder-free Electrode for High-Performance Supercapacitors. *J. Mat. Chem. A* 3 (23), 12530–12538. doi:10.1039/c5ta01804h

Biesinger, M. C., Lau, L. W. M., Gerson, A. R., and Smart, R. S. C. (2012). The Role of the Auger Parameter in XPS Studies of Nickel Metal, Halides and Oxides. *Phys. Chem. Chem. Phys.* 14 (7), 2434–2442. doi:10.1039/c2cp22419d

Boek, E. S., Coveney, P. V., and Skipper, N. T. (1995). Molecular Modeling of Clay Hydration: A Study of Hysteresis Loops in the Swelling Curves of Sodium Montmorillonites. *Langmuir* 11 (12), 4629–4631. doi:10.1021/la00012a008

Cao, J., Mei, Q., Wu, R., and Wang, W. (2019). Flower-like Nickel-Cobalt Layered Hydroxide Nanostructures for Super Long-Life Asymmetrical Supercapacitors. *Electrochimica Acta* 321, 134711. doi:10.1016/j.electacta.2019.134711

Caturwati, N. K., Rosyadi, I., Yusuf, Y., and Saputra, E. T. (2022). Lauric Acid as an Energy Storage Material to Increase Distillation Solar Productivity in Indonesia. *Mater. Sci. Forum* 1057, 144–151. doi:10.4028/p-11m66k

Chen, G., Wan, H., Ma, W., Zhang, N., Cao, Y., Liu, X., et al. (2020). Layered Metal Hydroxides and Their Derivatives: Controllable Synthesis, Chemical Exfoliation, and Electrocatalytic Applications. *Adv. Energy Mat.* 10 (11), 1902535. doi:10.1002/aenm.201902535

Delbari, S. A., Ghadimi, L. S., Hadi, R., Farhoudian, S., Nedaei, M., Babapoor, A., et al. (2021). Transition Metal Oxide-Based Electrode Materials for Flexible Supercapacitors: A Review. *J. Alloys Compd.* 857, 158281. doi:10.1016/j.jallcom.2020.158281

Dou, Q., Wu, N., Yuan, H., Shin, K. H., Tang, Y., Mitlin, D., et al. (2021). Emerging Trends in Anion Storage Materials for the Capacitive and Hybrid Energy Storage and beyond. *Chem. Soc. Rev.* 50 (12), 6734–6789. doi:10.1039/d0cs00721h

Duraković, B., and Mešetović, S. (2019). Thermal Performances of Glazed Energy Storage Systems with Various Storage Materials: An Experimental Study. *Sustain. Cities Soc.* 45, 422–430.

Fleischmann, S., Mitchell, J. B., Wang, R., Zhan, C., Jiang, D.-e., Presser, V., et al. (2020). Pseudocapacitance: from Fundamental Understanding to High Power Energy Storage Materials. *Chem. Rev.* 120 (14), 6738–6782. doi:10.1021/acs.chemrev.0c00170

Ge, W., Ma, Q., Ai, Z., Wang, W., Jia, F., and Song, S. (2021). Three-dimensional Reduced Graphene Oxide/montmorillonite Nanosheet Aerogels as Electrode Material for Supercapacitor Application. *Appl. Clay Sci.* 206, 106022. doi:10.1016/j.clay.2021.106022

Han, Z., Cui, Y., Meng, Q., He, M., and Yan, X. (2021). The Effect of Inorganic Salt on the Mechanical Properties of Montmorillonite and its Mechanism: A Molecular Dynamics Study. *Chem. Phys. Lett.* 781, 138982. doi:10.1016/j.cplett.2021.138982

He, P., Xiong, Y., Chen, Y., Liu, M., Zhu, J., and Gan, M. (2022). One-step Synthesis of Natural Montmorillonite/hematite Composites with Enhanced Persulfate Catalytic Activity for Sulfamethoxazole Degradation: Efficiency, Kinetics, and Mechanism. *Environ. Res.* 204, 112326. doi:10.1016/j.envres.2021.112326

Jiang, D. B., Jing, C., Yuan, Y., Feng, L., Liu, X., Dong, F., et al. (2019). 2D-2D Growth of NiFe LDH Nanoflakes on Montmorillonite for Cationic and Anionic Dye Adsorption Performance. *J. colloid interface Sci.* 540, 398–409. doi:10.1016/j.jcis.2019.01.022

Jiang, D., Zheng, M., You, Y., Li, F., Yuan, H., Zhang, W., et al. (2021). β-Ni(OH)2/nickel-cobalt Layered Double Hydroxides Coupled with Fluorine-Modified Graphene as High-Capacitance Supercapacitor Electrodes with Improved Cycle Life. *J. Alloys Compd.* 875, 159929. doi:10.1016/j.jallcom.2021.159929

Kong, L., Tang, H., Wang, X., Lei, Y., Li, B., Chang, K., et al. (2021). Study on the *In Situ* Sulfidation and Electrochemical Performance of Spherical Nickel Hydroxide. *Int. J. Hydrogen Energy* 46 (58), 30079–30089. doi:10.1016/j.ijhydene.2021.06.124

Li, J., Qiao, J., and Lian, K. (2020). Hydroxide Ion Conducting Polymer Electrolytes and Their Applications in Solid Supercapacitors: A Review. *Energy Storage Mater.* 24, 6–21. doi:10.1016/j.ensm.2019.08.012

Li, S., Yu, C., Yang, J., Zhao, C., Zhang, M., Huang, H., et al. (2017). A Superhydrophilic "nanoglue" for Stabilizing Metal Hydroxides onto Carbon Materials for High-Energy and Ultralong-Life Asymmetric Supercapacitors. *Energy Environ. Sci.* 10 (9), 1958–1965. doi:10.1039/c7ee01040k

Li, X., Li, M., Huang, Z., Liang, G., Chen, Z., Yang, Q., et al. (2021). Activating the I0/I+ Redox Couple in an Aqueous I2-Zn Battery to Achieve a High Voltage Plateau. *Energy Environ. Sci.* 14 (1), 407–413. doi:10.1039/d0ee03086d

Li, Z., He, J., Ma, H., Zang, L., Li, D., Guo, S., et al. (2021). Preparation of Heterogeneous TiO2/g-C3n4 with a Layered Mosaic Stack Structure by Use of Montmorillonite as a Hard Template Approach: TC Degradation, Kinetic, Mechanism, Pathway and DFT Investigation. *Appl. Clay Sci.* 207, 106107. doi:10.1016/j.clay.2021.106107

Liang, C., Bao, J., Li, C., Huang, H., Chen, C., Lou, Y., et al. (2017). One-dimensional Hierarchically Porous Carbon from Biomass with High Capacitance as Supercapacitor Materials. *Microporous Mesoporous Mater.* 251, 77–82. doi:10.1016/j.micromeso.2017.05.044

Liu, J., Hu, R., Liu, H., and Ma, J. (2017). Chips Assembled Cuboid-like Nickel hydroxide/rGO Composite Material for High Performance Supercapacitors. *J. Alloys Compd.* 718, 349–355. doi:10.1016/j.jallcom.2017.05.198

Liu, S., Wei, L., and Wang, H. (2020). Review on Reliability of Supercapacitors in Energy Storage Applications. *Appl. Energy* 278, 115436. doi:10.1016/j.apenergy.2020.115436

Lv, J., Xie, J., Mohamed, A. G. A., Zhang, X., and Wang, Y. (2022). Photoelectrochemical Energy Storage Materials: Design Principles and Functional Devices towards Direct Solar to Electrochemical Energy Storage. *Chem. Soc. Rev.* 51, 1511. doi:10.1039/D1CS00859E

Numan, A., Duraisamy, N., Saiha Omar, F., Gopi, D., Ramesh, K., and Ramesh, S. (2017). Sonochemical Synthesis of Nanostructured Nickel Hydroxide as an Electrode Material for Improved Electrochemical Energy Storage Application. *Prog. Nat. Sci. Mater. Int.* 27 (4), 416–423. doi:10.1016/j.pnsc.2017.06.003

Ovhal, M. M., Kumar, N., Hong, S.-K., Lee, H.-W., and Kang, J.-W. (2020). Asymmetric Supercapacitor Featuring Carbon Nanotubes and Nickel Hydroxide Grown on Carbon Fabric: A Study of Self-Discharging Characteristics. *J. Alloys Compd.* 828, 154447. doi:10.1016/j.jallcom.2020.154447

Payne, B. P., Biesinger, M. C., and McIntyre, N. S. (2012). Use of Oxygen/nickel Ratios in the XPS Characterisation of Oxide Phases on Nickel Metal and Nickel Alloy Surfaces. *J. Electron Spectrosc. Relat. Phenom.* 185 (5-7), 159–166. doi:10.1016/j.elspec.2012.06.008

Qin, D., Niu, X., Qiao, M., Liu, G., Li, H., and Meng, Z. (2015). Adsorption of Ferrous Ions onto Montmorillonites. *Appl. Surf. Sci.* 333, 170–177. doi:10.1016/j.apsusc.2015.02.019

Ramesh, S., Karuppasamy, K., Haldorai, Y., Sivasamy, A., Kim, H.-S., and Kim, H. S. (2021). Hexagonal Nanostructured Cobalt Oxide @ Nitrogen Doped Multiwalled Carbon Nanotubes/polypyyrole Composite for Supercapacitor and Electrochemical Glucose Sensor. *Colloids Surfaces B Biointerfaces* 205, 111840. doi:10.1016/j.colsurfb.2021.111840

Rawat, S., Mishra, R. K., and Bhaskar, T. (2022). Biomass Derived Functional Carbon Materials for Supercapacitor Applications. *Chemosphere* 286, 131961. doi:10.1016/j.chemosphere.2021.131961

Saikia, B. K., Benoy, S. M., Bora, M., Tamuly, J., Pandey, M., and Bhattacharya, D. (2020). A Brief Review on Supercapacitor Energy Storage Devices and Utilization of Natural Carbon Resources as Their Electrode Materials. *Fuel* 282, 118796. doi:10.1016/j.fuel.2020.118796

Shi, J., Jiang, B., Li, C., Yan, F., Wang, D., Yang, C., et al. (2020). Review of Transition Metal Nitrides and Transition Metal Nitrides/carbon Nanocomposites for Supercapacitor Electrodes. *Mater. Chem. Phys.* 245, 122533. doi:10.1016/j.matchemphys.2019.122533

Singh, S., Shinde, N. M., Xia, Q. X., Gopi, C. V. V. M., Yun, J. M., Mane, R. S., et al. (2017). Tailoring the Morphology Followed by the Electrochemical Performance of NiMn-LDH Nanosheet Arrays through Controlled Co-doping for High-Energy and Power Asymmetric Supercapacitors. *Dalton Trans.* 46 (38), 12876–12883. doi:10.1039/c7dt01863k

Soserov, L., Stoyanova, A., Boyadzhieva, T., Koleva, V., Kalapsazova, M., and Stoyanova, R. (2018). Nickel-manganese Structured and Multiphase Composites as Electrodes for Hybrid Supercapacitors. *Electrochimica Acta* 283, 1063–1071. doi:10.1016/j.electacta.2018.06.191

Soserov, L., Stoyanova, A., Boyadzhieva, T., Koleva, V., Kalapsazova, M., and Stoyanova, R. (2018). Nickel-manganese Structured and Multiphase Composites as Electrodes for Hybrid Supercapacitors. *Electrochimica Acta* 283, 1063–1071. doi:10.1016/j.electacta.2018.06.191

Tao, E., Ma, D., Yang, S., and Hao, X. (2020). Graphene Oxide-Montmorillonite/sodium Alginate Aerogel Beads for Selective Adsorption of Methylene Blue in Wastewater. *J. Alloys Compd.* 832, 154833. doi:10.1016/j.jallcom.2020.154833

Tong, X., Chen, S., Guo, C., Xia, X., and Guo, X.-Y. (2016). Mesoporous NiCo2O4 Nanoplates on Three-Dimensional Graphene Foam as an Efficient Electrocatalyst for the Oxygen Reduction Reaction. *ACS Appl. Mat. Interfaces* 8 (42), 28274–28282. doi:10.1021/acsami.5b10044

Wan, L., Chen, D., Liu, J., Zhang, Y., Chen, J., Du, C., et al. (2020). Facile Preparation of Porous Carbons Derived from Orange Peel via Basic Copper Carbonate Activation for Supercapacitors. *J. Alloys Compd.* 823, 153747. doi:10.1016/j.jallcom.2020.153747

Wang, H., Wang, M., and Wang, J. (2021). Nickel Silicate Hydroxide on Hierarchically Porous Carbon Derived from Rice Husks as High-Performance Electrode Material for Supercapacitors. *Int. J. Hydrogen Energy* 46 (71), 35351–35364. doi:10.1016/j.ijhydene.2021.08.062

Wang, Y., Huang, H., and Choi, W. M. (2021). Polypyrrole Decorated Cobalt Carbonate Hydroxide on Carbon Cloth for High Performance Flexible Supercapacitor Electrodes. *J. Alloys Compd.* 886, 161171. doi:10.1016/j.jallcom.2021.161171

Wiston, B. R., and Ashok, M. (2019). Electrochemical Performance of Hydrothermally Synthesized Flower-like α-nickel Hydroxide. *Vacuum* 160, 12–17. doi:10.1016/j.vacuum.2018.11.014

Wu, Y., Yang, Y., Liu, B., Hu, M., Min, X., Wu, Y., et al. (2020). Self-assembled Three-Dimension Flower-like Nickel Hydroxide Synthesis with One-Pot Hydrothermal Method for Electrochemical Applications. *Mater. Lett.* 264, 127358. doi:10.1016/j.matlet.2020.127358

Xing, S., Wang, Q., Ma, Z., Wu, Y., and Gao, Y. (2012). Synthesis of Mesoporous α-Ni(OH)2 for High-Performance Supercapacitors. *Mater. Lett.* 78, 99–101. doi:10.1016/j.matlet.2012.03.023

Yang, L., Villalobos, U., Akhmetov, B., Gil, A., Khor, J. O., Palacios, A., et al. (2021). A Comprehensive Review on Sub-zero Temperature Cold Thermal Energy Storage Materials, Technologies, and Applications: State of the Art and Recent Developments. *Appl. Energy* 288, 116555. doi:10.1016/j.apenergy.2021.116555

Yang, S.-B., Tsai, Y.-C., and Wu, M.-S. (2020). Honeycomb-like Copper/cuprous Oxide with Supported Nickel Hydroxide Layer as an Electrode Material for

Electrochemical Oxidation of Urea. *J. Alloys Compd.* 836, 155533. doi:10.1016/j.jallcom.2020.155533

Yao, D., Shi, Y., Pan, H., Zhong, D., Hou, H., Wu, X., et al. (2020). Promotion Mechanism of Natural Clay Colloids in the Adsorption of Arsenite on Iron Oxide Particles in Water. *Chem. Eng. J.* 392, 123637. doi:10.1016/j.cej.2019.123637

Yin, X.-m., Xie, X.-m., Wu, X., and An, X. (2016). Catalytic Performance of Nickel Immobilized on Organically Modified Montmorillonite in the Steam Reforming of Ethanol for Hydrogen Production. *J. Fuel Chem. Technol.* 44 (6), 689–697. doi:10.1016/s1872-5813(16)30033-0

Zhang, M., Wang, Y., Guo, X., Li, R., Peng, Z., Zhang, W., et al. (2021). High-Performance Nickel Cobalt Hydroxide Nanosheets/Graphene/Ni Foam Composite Electrode for Supercapacitor Applications. *J. Electroanal. Chem.* 897, 115543. doi:10.1016/j.jelechem.2021.115543

Zhao, Q., Fu, L., Jiang, D., Ouyang, J., Hu, Y., Yang, H., et al. (2019). Nanoclay-modulated Oxygen Vacancies of Metal Oxide. *Commun. Chem.* 2 (1), 11. doi:10.1038/s42004-019-0112-9

Zheng, J., Lian, X., Wu, M., Zheng, F., Gao, Y., and Niu, H. (2021). One-step Preparation of Ni3S4 Quantum Dots Composite Graphene/carbon Nanotube Conductive Network for Asymmetric Supercapacitor. *J. Alloys Compd.* 859, 158247. doi:10.1016/j.jallcom.2020.158247

Zheng, M., Tang, H., Li, L., Hu, Q., Zhang, L., Xue, H., et al. (2018). Hierarchically Nanostructured Transition Metal Oxides for Lithium-Ion Batteries. *Adv. Sci.* 5 (3), 1700592. doi:10.1002/advs.201700592

Zhou, G., Wang, Y., Zhou, R., Wang, C., Jin, Y., Qiu, J., et al. (2019). Synthesis of Amino-Functionalized bentonite/CoFe2O4@MnO2 Magnetic Recoverable Nanoparticles for Aqueous Cd2+ Removal. *Sci. Total Environ.* 682, 505–513. doi:10.1016/j.scitotenv.2019.05.218

Zou, S., Liu, X., Xiao, Z., Xie, P., Liu, K., Lv, C., et al. (2020). Engineering the Interface for Promoting Ionic/electronic Transmission of Organic Flexible Supercapacitors with High Volumetric Energy Density. *J. Power Sources* 460, 228097. doi:10.1016/j.jpowsour.2020.228097

Zuo, H., Fu, W., Fan, R., Dastan, D., Wang, H., and Shi, Z. (2020). Bilayer Carbon Nanowires/nickel Cobalt Hydroxides Nanostructures for High-Performance Supercapacitors. *Mater. Lett.* 263, 127217. doi:10.1016/j.matlet.2019.127217

Conflict of Interest: The authors declare that the research was conducted in the absence of any commercial or financial relationships that could be construed as a potential conflict of interest.

Publisher's Note: All claims expressed in this article are solely those of the authors and do not necessarily represent those of their affiliated organizations, or those of the publisher, the editors and the reviewers. Any product that may be evaluated in this article, or claim that may be made by its manufacturer, is not guaranteed or endorsed by the publisher.

frontiers | Frontiers in Chemistry

PERSPECTIVE
published: 14 June 2022
doi: 10.3389/fchem.2022.933716

Flame Retardancy Properties and Rheological Behavior of PP/DiDOPO Conjugated Flame Retardant Composites

Daohai Zhang[1,2], Xiaoyu Shang[1], Jiyong Luo[2], Junzhuo Sun[1], Fang Tan[1], Dongmei Bao[1]* and Shuhao Qin[1,2]**

[1]School of Chemical Engineering of Guizhou Minzu University, Guiyang, China, [2]National Engineering Research Center for Compounding and Modification of Polymer Materials, Guiyang, China

OPEN ACCESS

Edited by:
Meng Zheng,
Qingdao Haiwan Science and Technology Industry Research Institute Co., Ltd., China

Reviewed by:
Zhifeng Deng,
Shaanxi University of Technology, China
Xuegang Chen,
Qingdao University of Science and Technology, China

***Correspondence:**
Daohai Zhang
zhangdaohai6235@163.com
Dongmei Bao
dongtian1314521@163.com
Shuhao Qin
qinshuhao@126.com

Specialty section:
This article was submitted to Electrochemistry, a section of the journal Frontiers in Chemistry

Received: 01 May 2022
Accepted: 30 May 2022
Published: 14 June 2022

Citation:
Zhang D, Shang X, Luo J, Sun J, Tan F, Bao D and Qin S (2022) Flame Retardancy Properties and Rheological Behavior of PP/DiDOPO Conjugated Flame Retardant Composites. Front. Chem. 10:933716. doi: 10.3389/fchem.2022.933716

A bridged 9,10-dihydro-9-oxa-10-phosphaphenanthrene-10-oxide derivative (DiDOPO) with conjugated structure was utilized as a novel conjugated flame retardant, Polypropylene(PP)/DiDOPO conjugated flame retardant composites were papered by being melt-extruding with a twin-screw extruder. The flame retardant efficiency of PP/DiDOPO conjugated flame retardant composites were investigated by cone calorimetry, limiting oxygen index (LOI), vertical burning test (UL-94). Besides, the rheological behavior of PP/DiDOPO conjugated flame retardant composites are measured by ARES rheometer. The results showed that when the content of DiDOPO with conjugated structure was 16 wt%, the LOI values of PP/DiDOPO conjugated flame retardant composites was 24%, and PP/DiDOPO conjugated flame retardant composites reaches V-0 grade. The heat release rate (HRR), total heat release rate (THR) and CO_2 of PP/DiDOPO conjugated flame retardant composites decreased, so PP/DiDOPO conjugated flame retardant composites had excellent flame retardant effect. Rheological analysis results indicated that DiDOPO with conjugated structure suppressed the melt dripping of PP/DiDOPO conjugated flame retardant composites by enhancing the melt stability. The results showed that the DiDOPO with conjugated structure can significantly enhance the flame retardancy effect of PP/DiDOPO conjugated flame retardant composites. In addition, the materials PP/DiDOPO might be with low conductivity and charge transport mobility.

Keywords: DiDOPO, conjugated structure, polypropylene, flame retardant efficiency, rheological behavior

INTRODUCTION

Polypropylene (PP) have widely been applied in electronic casings, building materials, automotive products, and furniture due to their desirable properties, such as cost-effective, ease processing, low density, and excellent mechanical properties (Wu et al., 2020; Park and Lee, 2021). Unfortunately, because of PP has poor flame retardancy properties, when using in some fields that requires flame resistance is limited. Recently, halogen-based flame retardant has caused great damage to the ecological environment, so the research and application of halogen-free flame retardant in PP composites is extremely urgent. At present, the halogen-free flame retardants are mainly in metal compounds and intumescent flame retardants. Among them, intumescent flame retardants for PP are the more effective. Intumescent flame retardants primarily composed of phosphorous, nitrogen and polyalcohols, but intumescent flame retardants is easy to absorb moisture, the dispersion of the

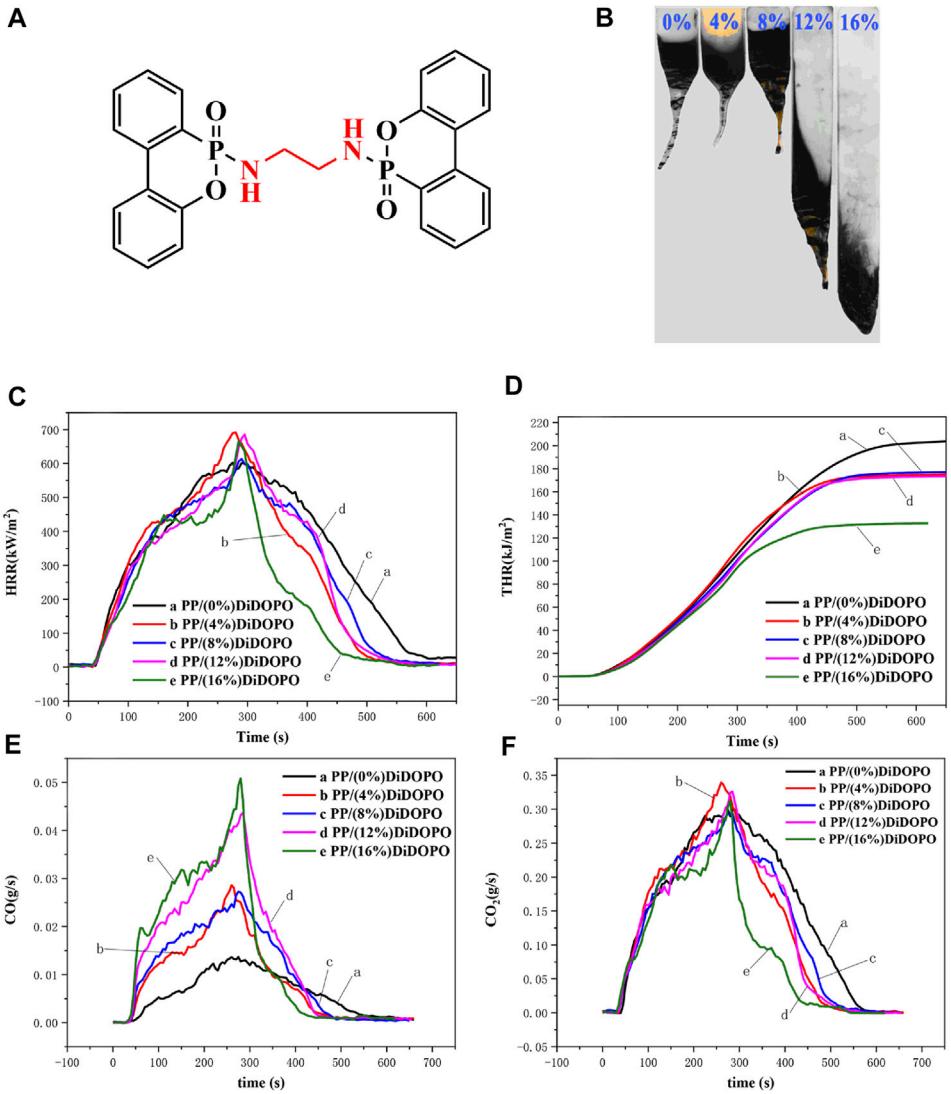

FIGURE 1 | the DiDOPO flame retardant with conjugated structure **(A)**, Photos of samples after UL-94 test **(B)** and HRR **(C)**, THR **(D)**, CO **(E)**, and CO_2 **(F)** yield curves of pure PP and each component PP/DiDOPO conjugated flame retardant composites.

intumescent flame retardants is uneven (Xia et al., 2018; Qi et al., 2020; Wang et al., 2021). Thus, to enhance the flame retardancy properties of PP, we exploring a new flame retardant systems that is DiDOPO with conjugated structure (**Figure 1A**). The DiDOPO with conjugated structure is a 9,10-dihydro-9-oxa-10-phosphaphenanthrene-10-oxide(DOPO) derivative, DOPO derivatives with conjugated structure have received extensive attention in the past few, which present low conductivity and poor charge transport mobility. In addition, these derivatives also exhibit excellent flame retardancy efficiency and environmental friendliness (Wang et al., 2011; Salmeia and Gaan, 2015). At present, DOPO derivatives with conjugated structure have been widely used in polymer such as polyester, polylactic acid, polyamide, epoxy resin and so on (Liu et al., 2013; Xie et al., 2013; Yang et al., 2015; Wang et al., 2016; Cai et al., 2017), but DOPO derivatives with conjugated structure are used less in PP.

In this study, PP/DiDOPO conjugated flame retardant composites were papered by a twin-screw extruder. The flame retardant properties and rheological behavior of PP/DiDOPO conjugated flame retardant composites were investigated by cone calorimetry, limiting oxygen index (LOI), vertical burning test (UL-94) and ARES rheometer.

MATERIALS AND METHODS

Materials

PP (commercial name: K9026) was supplied by SINOPEC Beijing Yanshan Petrochemical Co., Ltd. (China). The PP pellets were dried in flowing air at 60°C for 12 h before use. The bridged 9,10-dihydro-9-oxa-10-phosphaphenanthrene-10-oxide derivative (DiDOPO with conjugated structure, commercial name: HTP-6123)was

purchased by Guizhou Yuanyi Phosphorus Series New Material Co., Ltd. (China). All materials were used without any further purification.

Preparation of Flame Retardant PP Materials

PP, and dry DiDOPO (4, 8, 12, and 16 wt%) were first dry-mixed (shaken in a bag to combine), respectively, followed by being melt-extruding with a twin-screw extruder (CTE-20, Coperion Machinery Co., Ltd., China). The six heating zones were set to 190°C, 200°C, 205°C, 205°C, 210°C and 205°C, and the screw speed were set at 320 r/min. The purchased compound of DiDOPO were dried in a vacuum oven at 80°C for 12 h to remove any residual moisture, followed by molding on an injection molding machine (SE-130; DongHua Machinery Co., Ltd., China) at 240°C into various specimens for testing and characterization.

Characterization Methods

The combustion test was conducted on a cone calorimeter test using an FTT cone calorimeter (UK) in accordance with ISO 5660-1 standard. The specimens were prepared with sizes of 100*100*6 mm^3 and tested under a heat flux of 50 kW/m^2. Each measurement was performed twice, and the results were averaged.

Limiting oxygen index(LOI) measurements were performed on an oxygen index flammability gauge(HC-2C) according to ASTM D 2863-97 standard with a sample dimension of 100 mm*6.5 mm*3.2 mm^3.

The vertical burning test (UL-94) was carried out on a SH5300 type instrument (Guangzhou Xinhe Electronic Equipment Co., Ltd., China) was conducted with sample sizes of 130*10*3.2 mm^3 in accordance with the ASTM UL 94-2006.

The linear viscoelastic behavior of the PP/DiDOPO composites was analyzed by a dynamic oscillatory rheometer in the melt state. A rotation rheometer (ARES-G2, TA Instruments Corp., United States) equipped with 25 mm diameter parallel plates geometry was employed for the rheological tests. Samples were directly loaded and molded between the plates and rheological tests were carried out at 190°C with a gap distance of 0.8~1 mm. The linear viscoelasticity test has a strain setting of 0.1% and a scanning frequency range of 0.1 rad/s to 500 rad/s.

RESULTS AND DISCUSSION

The Flame Retardant Properties of PP/DiDOPO Conjugated Flame Retardant Composites

The effects of DiDOPO with conjugated structure on the flame retardancy properties of PP/DiDOPO conjugated flame retardant composites were investigated by vertical burning test (UL-94) and limiting oxygen index test (LOI). The results UL-94 and LOI for PP/DiDOPO conjugated flame retardant composites are shown in **Figure 1** and **Table 1**. As shown in **Table 1**, when the content of DiDOPO with conjugated structure was 16 wt%, the PP/DiDOPO conjugated flame retardant composites achieved the UL-94 V0 level.

TABLE 1 | UL-94 and LOI test results of PP/DiDOPO conjugated flame retardant composites.

Samples	LOI(%)	UL-94 (3.2 mm)			
		t_1/t_2[a](s)	Dripping	Ignition	Rating
PP/DiDOPO -0%	18.8	[b]BC	Yes	Yes	[c]NR
PP/DiDOPO -4%	19.6	—	Yes	Yes	—
PP/DiDOPO -8%	22	—	Yes	Yes	—
PP/DiDOPO -12%	23.2	3.65/0.28	Yes	Yes	V-1
PP/DiDOPO -16%	24	3.23/0.21	Yes	NO	V-0

[a]*Average combustion times after the first and second applications of the flame.*
[b]*BC, burns to clamp.*
[c]*NR, not rated.*

It can effectively inhibit the droplet drop phenomenon of PP for the addition of DiDOPO with conjugated structure. As shown in the **Figure 1B**, PP/DiDOPO conjugated flame retardant composites still have a droplet drop phenomenon, and the droplets of PP/DiDOPO conjugated flame retardant composites can take away heat and had a certain flame retardant effect. But the droplets of PP/DiDOPO conjugated flame retardant composites were weakened. What's more, the LOI value PP/DiDOPO conjugated flame retardant composites increased from 18.8% to 24.0%. It can be seen that the DiDOPO flame retardant with conjugated structure has high flame retardant efficiency for PP. This might be explained by that the conjugated materials DiDOPO present low conductivity and low charge transport mobility.

To further analyze the effect of DiDOPO with conjugated structure on the combustion behavior of PP/DiDOPO conjugated flame retardant composites, cone calorimeter test (CCT) of PP/DiDOPO conjugated flame retardant composites were performed. The test results are presented in **Figure 1** and **Table 2**. As shown in **Figure 1C**, the pure PP burned out after ignition, and a sharp heat release rate (HRR) peak of pure PP appeared. In the case of all other PP/DiDOPO conjugated flame retardant composites, it was observed that a reduction of time to ignition (TTI) happened, the time to the sharp HRR (PHRR) peak of PP/DiDOPO conjugated flame retardant composites was extended when added DiDOPO with conjugated structure into the PP/DiDOPO conjugated flame retardant composites (Schartel and Hull 2007), which was mainly caused by the decomposition of the DiDOPO with conjugated structure flame retardants. Because the thermal stability of DiDOPO with conjugated structure is relative lower than PP, and the addition of DiDOPO with conjugated structure reduces the thermal stability of the PP/DiDOPO conjugated flame retardant composites. The time peak HRR (t_p) of the PP/DiDOPO conjugated flame retardant composites increased with increasing the DiDOPO with conjugated structure content. This confirms that the DiDOPO with conjugated structure increases the thermal stability of PP/DiDOPO conjugated flame retardant composites. As shown in **Figure 1D**, the total heat release(THR) value PP/DiDOPO conjugated flame retardant composites were decreased, when the DiDOPO with conjugated structure was added into conjugated flame retardant composites. What's more, when the amount of DiDOPO with conjugated structure increased, the THR value of PP/DiDOPO conjugated flame retardant composites decreased. The THR value of PP/DiDOPO conjugated flame retardant composites

TABLE 2 | CCT data of PP/DiDOPO conjugated flame retardant composites.

Samples	TTI	PHRR (kW/m^2)	t $_p$ (s)	THR (MJ/m^2)	Av-HRR (KJ/m^2)	Av-EHC (MJ/Kg)	TSR (m^2/m^2)
PP/DiDOPO-0%	37	602.33	275	203.89	333.60	33.68	2272.82
PP/DiDOPO-4%	34	691.97	280	175.18	324.76	28.09	2933.40
PP/DiDOPO-8%	25	680.79	295	182.52	298.14	24.78	3397.75
PP/DiDOPO-12%	24	689.65	325	175.35	270.85	21.99	4119.14
PP/DiDOPO-16%	23	607.63	350	157.14	248.62	20.79	4040.19

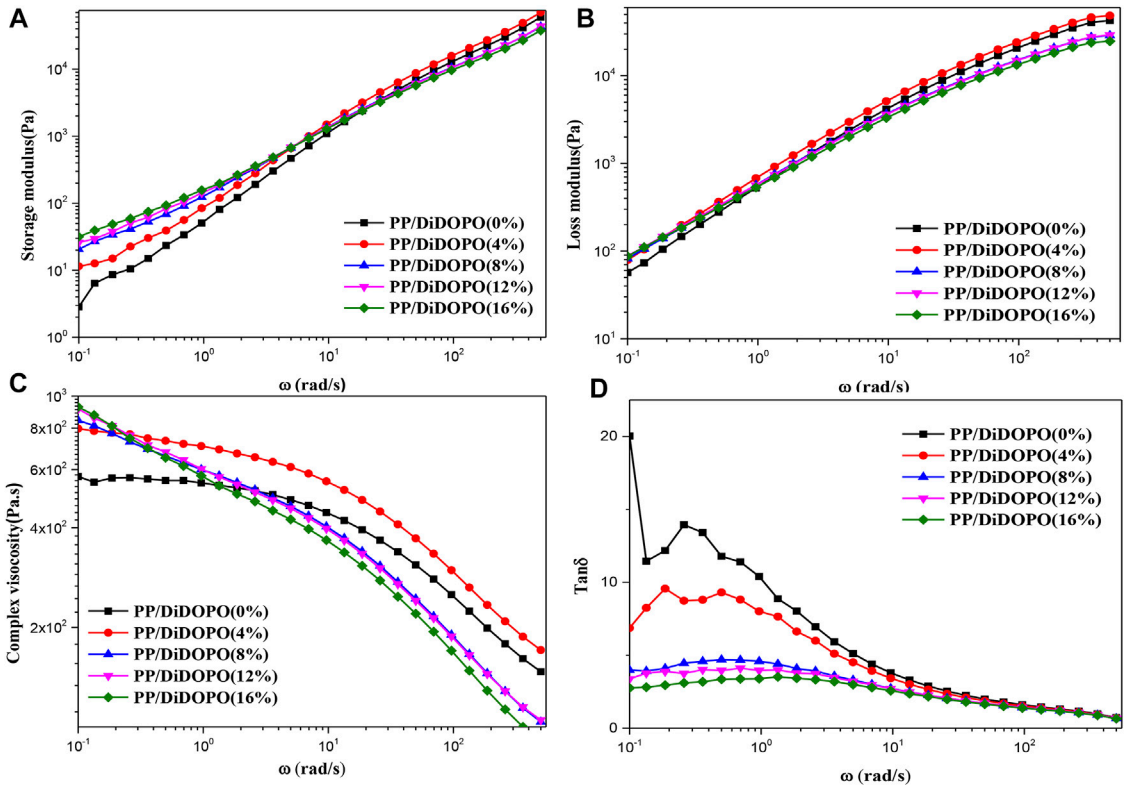

FIGURE 2 | Storage modulus (G′) **(A)**, Loss modulus (G″) **(B)**, Complex viscosity (η*) **(C)** and Tan δ**(D)** for the PP/DiDOPO conjugated flame retardant composites at 190°C.

decreased by 14.9%, when the DiDOPO with conjugated structure content was 15 wt%. In addition, the total smoke rate (TSR) value of the PP/DiDOPO conjugated flame retardant composites increased with increasing the DiDOPO with conjugated structure content (Zhao et al., 2013). This might be due to that the DiDOPO composite present low conductivities and charge transport mobility.

The toxic compounds and smoke were the harm in most cases during the course of a fire, in combination with the **Figures 1E,F**, the CO production rate of PP/DiDOPO conjugated flame retardant composites was improved, However, the CO_2 production rate of PP/DiDOPO conjugated flame retardant composites decreased. It is due to the phosphorus-containing compounds which the firing DiDOPO with conjugated structure content releases, and these compounds can inhibit flames and thereby increase the number of components that cause incomplete combustion (Wang et al., 2010). The effective heat of combustion (EHC) expresses the contribution of the active constituents of the material to the heat release in the gas phase during combustion (Qian et al., 2015). As the DiDOPO with conjugated structure content increased, av-EHC PP/DiDOPO conjugated flame retardant composites gradually decreased, that indicates that the content of effective combustion components in the gas phase component decreased. Therefore, the decrease of EHC and CO_2 production rate, and the increase of TSR and CO production for PP/DiDOPO conjugated flame retardant composites suggest that the quenching activity of DiDOPO with conjugated structure for PP/DiDOPO conjugated flame retardant composites mainly involves gas phase flame retardant effect. The gas phase flame retardant mechanism of PP/DiDOPO conjugated flame retardant composites is mainly due to the phosphorus-containing free radicals which released during the decomposition of DiDOPO

with conjugated structure, and these phosphorus-containing free radicals can capture free radicals such as H•, O• or HO• in the flame combustion region to suppress the flame (Fornes and Paul 2003; Cannillo et al., 2006; Buczko et al., 2014). Furthermore, PP/DiDOPO conjugated flame retardant composites produce more CO and less CO_2 than pure PP during combustion. Among the PP/DiDOPO conjugated flame retardant composites, with the increasing DiDOPO with conjugated structure content, the amount of CO generated increased and CO_2 generated decreased for PP/DiDOPO conjugated flame retardant composites. The addition of DiDOPO with conjugated structure flame retardant suppresses the combustion of PP/DiDOPO conjugated flame retardant composites, resulting in the flame retardant effect of incomplete combustion, thus increasing the release of CO in combustion fumes and gas phase, and also CO_2 generated goes down.

The Rheological Behavior of PP/DiDOPO Conjugated Flame Retardant Composites

The storage modulus (G′) of the melt represents the amount of recoverable energy stored in the melt, and loss modulus (G″) represents the magnitude of the non-recoverable energy released by the melt. Melt flow behavior for a material was usually studied by rheology, and the viscoelastic behaviors of the testing samples were investigated by rheology testing to further illustrate the flame mechanism of PP/DiDOPO conjugated flame retardant composites. **Figures 2A,B** shows the G′and G″of pure PP and PP/DiDOPO conjugated flame retardant composites as a function of the scanning frequency. It can be seen from the **Figure 2** that at a higher frequency, the G′ and G″ of PP/DiDOPO conjugated flame retardant composites decreased with the increase of the DiDOPO with conjugated structure content. However, at lower frequencies, the G′ and G″ of PP/DiDOPO conjugated flame retardant composites increased with the increase of the DiDOPO with conjugated structure content.

Complex viscosity η* is a measure of the total impedance of a material to dynamic shear, from storage viscosity (elastic component) and dynamic viscosity (viscous component) consists of two parts, which can be based on the G′ and G″ according to $\eta^* = (G'^2 + G''^2)^{1/2}/\omega$ is calculated, where η* is a complex viscosity. The relationship between the complex viscosity (η*) of PP/DiDOPO conjugated flame retardant composites and the frequency is shown in **Figure 2C**. The results indicated that η* for all the PP/DiDOPO conjugated flame retardant composites gradually decreased during the process. The η* of PP/DiDOPO conjugated flame retardant composites decrease in the entire frequency, which indicated that PP/DiDOPO conjugated flame retardant composites could form a continuous phase to enhance the melt stability, thus it suppress the melt dripping. The tan δ of PP/DiDOPO conjugated flame retardant composites were also significantly affected by the DiDOPO with conjugated structure incorporation, which can be based on the G′ and G″, according to tan δ= G″/G′ is calculated, where tan δ is a loss tangent. From **Figure 2D**, it can be seen that the tan δ values of the PP/DiDOPO conjugated flame retardant composites gradually shift to a lower with increasing DiDOPO with conjugated structure content. It is important to note that the DiDOPO with conjugated structure promotes the motions of the PP chain segments in the tan δ profile. All the PP/DiDOPO conjugated flame retardant composites had a lower G″ than G′ in the whole frequency region, which indicated a change in rheological behavior, the "solid-liquid" transformation. And that indicated thePP/DiDOPO conjugated flame retardant composites had a liquid behavior under the shear effect.

CONCLUSION

In this paper, PP/DiDOPO conjugated flame retardant composites were fabricated by a melt blending method. when the content of DiDOPO with conjugated structure was 16 wt%, the PP/DiDOPO conjugated flame retardant composites achieved the UL-94 V0 level. the LOI value PP/DiDOPO conjugated flame retardant composites increased from 18.8% to 24.0%. The time peak HRR (t_p) of the PP/DiDOPO conjugated flame retardant composites increased with increasing the DiDOPO with conjugated structure content. the amount of DiDOPO with conjugated structure increased, THR value of PP/DiDOPO conjugated flame retardant composites decreased. THR value of PP/DiDOPO conjugated flame retardant composites decreased by 14.9%, when the DiDOPO with conjugated structure content was 15 wt%. G′ and G″ of PP/DiDOPO conjugated flame retardant composites decreased with the increase of the DiDOPO with conjugated structure content. All the PP/DiDOPO conjugated flame retardant composites had a lower G″ than G′ in the whole frequency region, which indicated a change in rheological behavior, the "solid-liquid" transformation.

DATA AVAILABILITY STATEMENT

The original contributions presented in the study are included in the article/supplementary material, further inquiries can be directed to the corresponding authors.

AUTHOR CONTRIBUTIONS

DZ and XS prepared materials and carried out in experiments. JL and JS helped to analyze experimental data. FT and DB helped to characterize materials. SQ supervised the work. All authors contributed to revise the manuscript, approved the final version and agreed to be accountable for all aspects of this work.

ACKNOWLEDGMENTS

The authors would like to acknowledge the financial support from the Natural Science Foundation of China (Grants: 52163001, 51863004), Science and Technology Fund Project of Guizhou Province of China (No. [2020]1Y211), Guizhou Province Science and Technology Plan Projects (Grants CXTD [2021]005, [2018]1012, [2019]4022). Baiyun district Science and Technology Plan Projects (Grants: [2020]28, [2019]21), Polymer Composites Engineering Research Center of Guizhou Minzu University (Grants: GZMUGCZX [2021]01).

REFERENCES

Buczko, A., Stelzig, T., Bommer, L., Rentsch, D., Heneczkowski, M., and Gaan, S. (2014). Bridged DOPO Derivatives as Flame Retardants for PA6. *Polym. Degrad. Stab.* 107, 158–165. doi:10.1016/j.polymdegradstab.2014.05.017

Cai, J., Wirasaputra, A., Zhu, Y., Liu, S., Zhou, Y., Zhang, C., et al. (2017). The Flame Retardancy and Rheological Properties of PA6/MCA Modified by DOPO-Based Chain Extender. *RSC Adv.* 7, 19593–19603. doi:10.1039/c6ra28293h

Cannillo, V., Bondioli, F., Lusvarghi, L., Montorsi, M., Avella, M., Errico, M. E., et al. (2006). Modeling of Ceramic Particles Filled Polymer-Matrix Nanocomposites. *Compos. Sci. Technol.* 66, 1030–1037. doi:10.1016/j.compscitech.2005.07.030

Fornes, T. D., and Paul, D. R. (2003). Modeling Properties of Nylon 6/clay Nanocomposites Using Composite Theories. *Polymer.* 44, 4993–5013. doi:10.1016/s0032-3861(03)00471-3

Liu, P., Liu, M., Gao, C., Wang, F., Ding, Y., Wen, B., et al. (2013). Preparation, Characterization and Properties of a Halogen-free Phosphorous Flame-Retarded Poly(butylene Terephthalate) Composite Based on a DOPO Derivative. *J. Appl. Polym. Sci.* 130, 1301–1307. doi:10.1002/app.39318

Park, C., and Lee, J. (2021). Pyrolysis of Polypropylene for Production of Fuel-range Products: Effect of Molecular Weight of Polypropylene. *Int. J. Energy Res.* 45, 13088–13097. doi:10.1002/er.6635

Qi, H., Liu, S., Chen, X., Shen, C., and Gao, S. (2020). The Flame Retardant and Thermal Performances of Polypropylene with a Novel Intumescent Flame Retardant. *J. Appl. Polym. Sci.* 137, 49047–49057. doi:10.1002/app.49047

Qian, L., Qiu, Y., Wang, J., and Xi, W. (2015). High-performance Flame Retardancy by Char-Cage Hindering and Free Radical Quenching Effects in Epoxy Thermosets. *Polymer.* 68, 262–269. doi:10.1016/j.polymer.2015.05.031

Salmeia, K. A., and Gaan, S. (2015). An Overview of Some Recent Advances in DOPO-Derivatives: Chemistry and Flame Retardant Applications. *Polym. Degrad. Stab.* 113, 119–134. doi:10.1016/j.polymdegradstab.2014.12.014

Schartel, B., and Hull, T. R. (2007). Development of Fire-Retarded Materials-Interpretation of Cone Calorimeter Data. *Fire Mat.* 31, 327–354. doi:10.1002/fam.949

Wang, D.-Y., Song, Y.-P., Lin, L., Wang, X.-L., and Wang, Y.-Z. (2011). A Novel Phosphorus-Containing Poly(lactic Acid) toward its Flame Retardation. *Polymer.* 52, 233–238. doi:10.1016/j.polymer.2010.11.023

Wang, L., Wei, Y., Deng, H., Lyu, R., Zhu, J., and Yang, Y. (2021). Synergistic Flame Retardant Effect of Barium Phytate and Intumescent Flame Retardant for Epoxy Resin. *Polymers.* 13, 2900–2913. doi:10.3390/polym13172900

Wang, X., Hu, Y., Song, L., Xing, W., Lu, H., Lv, P., et al. (2010). Flame Retardancy and Thermal Degradation Mechanism of Epoxy Resin Composites Based on a DOPO Substituted Organophosphorus Oligomer. *Polymer.* 51, 2435–2445. doi:10.1016/j.polymer.2010.03.053

Wang, X., Qian, L. J., Qiu, Y., and Chen, Y. J. (2016). Flame-retardant Behavior of Bi-group Molecule Derived from Phosphaphenanthrene and Triazine Groups on Polylactic Acid. *Polym. Adv. Technol.* 27, 781–788.

Wu, M.-H., Wang, C.-C., and Chen, C.-Y. (2020). Preparation of High Melt Strength Polypropylene by Addition of an Ionically Modified Polypropylene. *Polymer.* 202, 122743–122777. doi:10.1016/j.polymer.2020.122743

Xia, S., Zhang, Z., Leng, Y., Li, B., and Xu, M. (2018). Synthesis of a Novel Mono-Component Intumescent Flame Retardant and its High Efficiency for Flame Retardant Polyethylene. *J. Anal. Appl. Pyrolysis.* 134, 632–640. doi:10.1016/j.jaap.2018.08.017

Xie, C., Zeng, B., Gao, H., Xu, Y., Luo, W., Liu, X., et al. (2013). Improving Thermal and Flame-Retardant Properties of Epoxy Resins by a Novel Reactive Phosphorous-Containing Curing Agent. *Polym. Eng. Sci.* 54, 1192–1200. doi:10.1002/pen.23642

Yang, S., Wang, J., Huo, S., Wang, M., and Cheng, L. (2015). Synthesis of a Phosphorus/Nitrogen-Containing Additive with Multifunctional Groups and Its Flame-Retardant Effect in Epoxy Resin. *Ind. Eng. Chem. Res.* 54, 7777–7786. doi:10.1021/acs.iecr.5b02026

Zhao, B., Chen, L., Long, J.-W., Chen, H.-B., and Wang, Y.-Z. (2013). Aluminum Hypophosphite versus Alkyl-Substituted Phosphinate in Polyamide 6: Flame Retardance, Thermal Degradation, and Pyrolysis Behavior. *Ind. Eng. Chem. Res.* 52, 2875–2886. doi:10.1021/ie303446s

Conflict of Interest: The authors declare that the research was conducted in the absence of any commercial or financial relationships that could be construed as a potential conflict of interest.

Publisher's Note: All claims expressed in this article are solely those of the authors and do not necessarily represent those of their affiliated organizations, or those of the publisher, the editors and the reviewers. Any product that may be evaluated in this article, or claim that may be made by its manufacturer, is not guaranteed or endorsed by the publisher.

frontiers | Frontiers in Chemistry

PERSPECTIVE
published: 16 June 2022
doi: 10.3389/fchem.2022.934203

Design, Synthesis, and Application in OFET of a Quinoxaline-Based D-A Conjugated Polymer

Zhicheng Dai[1], *Daohai Zhang*[2] *and Haichang Zhang*[1]*

[1]Key Laboratory of Rubber-Plastics of Ministry of Education/Shandong Province (QUST), School of Polymer Science and Engineering, Qingdao University of Science and Technology, Qingdao, China, [2]School of Chemical Engineering of Guizhou Minzu University, Guiyang, China

A novel alternating donor–acceptor polymer PQ1 is designed and synthesized by palladium-catalyzed Stille coupling between quinoxaline as an electron-deficient unit and indacenodithiophene (IDT) as electron-rich groups. Polymer PQ1 presents not only a strong intramolecular charge transfer effect, which is beneficial for the charge transport within single molecules but also a narrow electrochemical band gap and a high highest occupied molecular orbital (HOMO) energy level. In addition, the optical absorption study indicates that the PQ1 film exhibits good aggregation, which is an advantage for the charge transport between neighboring molecules. As a consequence, PQ1 presents p-type semiconductor properties with a high hole mobility of up to 0.12 cm^2 V^{-1} s^{-1}. This study reveals the great potential of quinoxaline-type chromophores in constructing novel organic semiconductors.

Keywords: organic field-effect transistor, conjugated polymers, quinoxaline, donor, acceptor

OPEN ACCESS

Edited by:
Yue Liu,
Liaoning Technical University, China

Reviewed by:
Xu Qiu,
Shandong University of Science and Technology, China
Detebg Zhang,
Qingdao University, China

***Correspondence:**
Haichang Zhang
haichangzhang@hotmail.com

Specialty section:
This article was submitted to Electrochemistry, a section of the journal Frontiers in Chemistry

Received: *02 May 2022*
Accepted: *10 May 2022*
Published: *16 June 2022*

Citation:
Dai Z, Zhang D and Zhang H (2022) Design, Synthesis, and Application in OFET of a Quinoxaline-Based D-A Conjugated Polymer. Front. Chem. 10:934203. doi: 10.3389/fchem.2022.934203

INTRODUCTION

Since the first organic field-effect transistor (OFET) was successfully prepared by Tsumura with polythiophene in 1987, organic semiconductors have received more and more attention from the academic society due to their multi-advantages and potential applications such as low cost, ease of fabrication, and compatibility with flexible substrates (Tsumura et al., 1986; Bogdanov and Mironov, 2021; Wang et al., 2020; Yoon et al., 2017; Zhang et al., 2018). In the past few years, OFETs have made significant achievements in charge carrier mobility, open-circuit voltage (V_{oc}), and current on/off ratio. Regarding semiconductor materials, most used are the organic π-conjugated small molecules and polymers (Cao et al., 2012; Donaghey et al., 2013; Zhang et al., 2020). Compared to small molecules, polymers are more popular and widely used as semiconductor layers in high-performance OFETs, since they are often present not only in high intracharge transport mobility but also in tunable chemical structures (Kettle et al., 2011; Sasikumar et al., 2016; Bhanuprakash et al., 2016; Bi et al., 2018). According to the composition of the polymer backbone, semiconductor polymers are usually classified into three types: A-A type (acceptor–acceptor), D-D type (donor–donor), and D-A type (donor–acceptor). Among them, the D-A type is the most popular and potential in high-performance OFETs due to its convenient molecular orbital modification capability and good intramolecular charge transfer (ICT) effect (Tomasz et al., 2013; Deng et al., 2018a). A suitable donor structure can modulate the highest occupied molecular orbital (HOMO), while a suitable acceptor group might adjust the lowest unoccupied molecular orbital (LUMO). This results in semiconductor materials with an appropriate Frontier molecular orbital level, which aligns with the working function of the electrode, in turn forming an Ohmic contact with it, and facilitates charge injection from the electrode into the semiconductor layer.

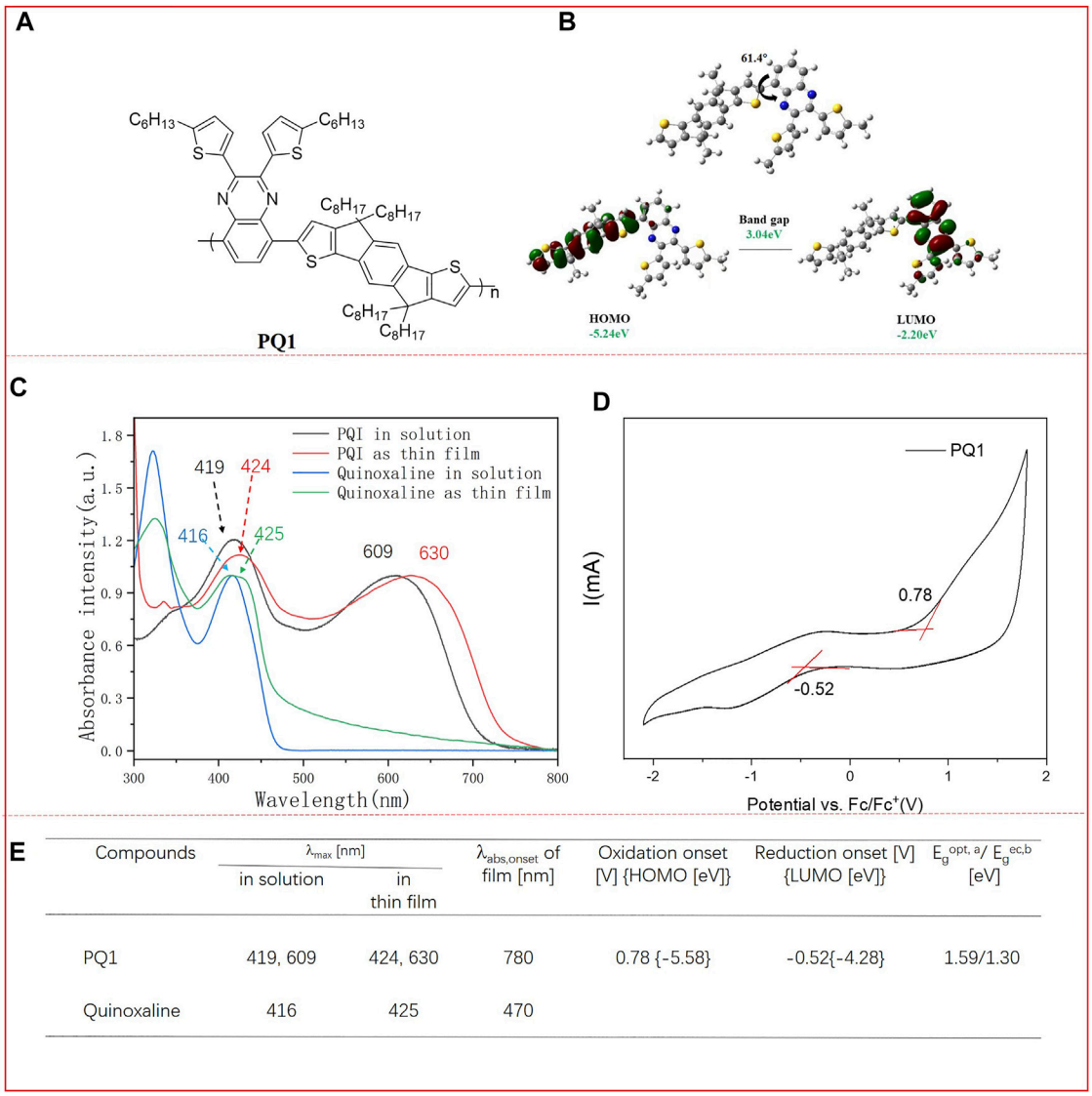

E

Compounds	λ_{max} [nm] in solution	λ_{max} [nm] in thin film	$\lambda_{abs,onset}$ of film [nm]	Oxidation onset [V] {HOMO [eV]}	Reduction onset [V] {LUMO [eV]}	$E_g^{opt,a}$/ $E_g^{ec,b}$ [eV]
PQ1	419, 609	424, 630	780	0.78 {-5.58}	-0.52{-4.28}	1.59/1.30
Quinoxaline	416	425	470			

FIGURE 1 | (A) Chemical structures of PQ1; **(B)** computational calculations of the simplified single repeat unit of the polymer obtained at the B3LYP/6-31G* level; **(C)** UV/vis absorption spectra of the monomer quinoxanline and polymer PQ1 in dichloromethane solution and the polymer thin film; **(D)** cyclic voltammograms of the polymer PQ1 as thin films deposited on ITO electrolyte: 0.1 M $TBAPF_6$/acetonitrile. Potential calculated versus ferrocene. Scan rate: 100 mV s^{-1}; T = 25°C. **(E)** Optical and electrochemical properties of the monomer and polymer PQ1. $^aE_{opt}$ (optical bandgap) was measured at the onset of absorption in the film (E_{opt} = 1,240/?$_{abs.\ onset}$ eV). $^bE_g^{ec}$ electrochemical bandgap. HOMO-LUMO gap was calculated according to the following equations: $E_{LUMO} = E_{onset\ (red)} + 4.8$ eV and $E_{HOMO} = E_{onset\ (ox)} + 4.8$ eV. $E_{onset\ (ox)}$ and $E_{onset\ (red)}$ are onset potentials for the oxidation and reduction processes *vs* Fc/Fc^+ couple, respectively.

Thiophene is a commonly used electron donor unit in π-conjugated polymers. Indacenodithiophene (IDT) belongs to a derivative of thiophene with conjugation system extension. With its excellent planar symmetric structure, it can effectively promote intermolecular charge transfer. Thus, the devices prepared by this structure usually have excellent charge carrier mobility (Cai et al., 2014; Zhai and Zhou, 2016). Recent research has reversed that IDT has become a widely used feeder structure for photovoltaic materials, especially in organic solar cells (OPV), which can provide an energy conversion efficiency of over 9.21% (Andrew et al., 2020). In addition, it is also used as donor units to construct D-A type semiconductors with good hole transport mobility. Apart from the donor unit, a suitable acceptor group also plays a crucial role in designing a high-performance semiconductor (Kettle et al., 2011). The derivatives of quinoxaline, an electron-deficient chromophore, play an important role as a good planar and rigid conjugated structure in organic light-emitting diodes (OLEDs), dyes, or as ligands in light-emitting materials, but are rarely used in the construction of semiconductors in OFETs (Liu et al., 2017; Park et al., 2019; Hee et al., 2020; Sagita, et al., 2021).

In this work, a novel polymer PQ1 is designed and synthesized by the Stille coupling reaction between IDT

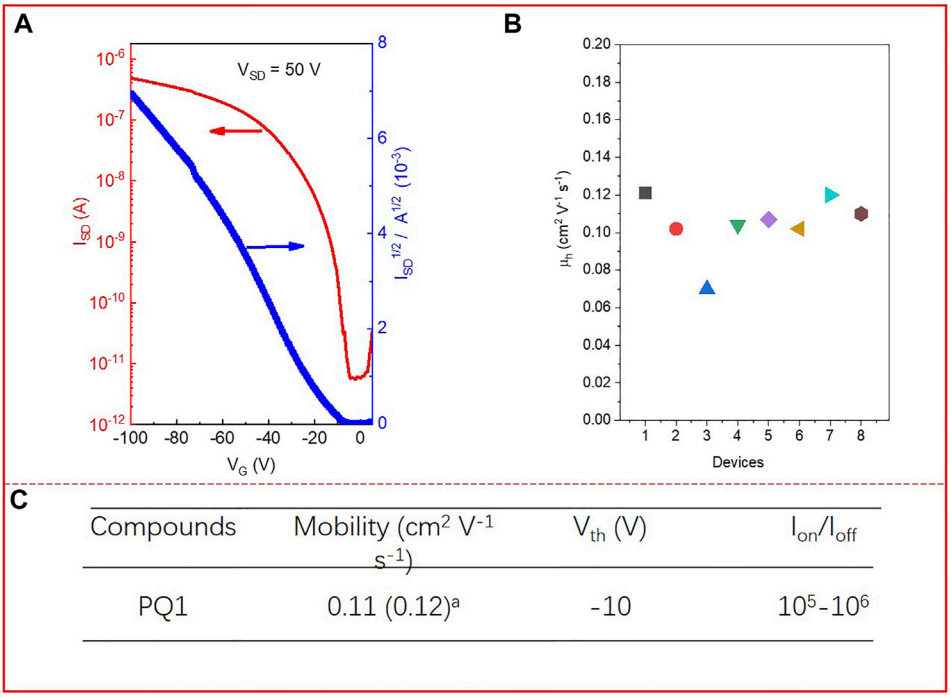

FIGURE 2 | (A) Characteristics of the OFET devices of PQ1; **(B)** hole transport mobility obtained eight different devices. **(C)** Hole mobilities (μ_h), threshold voltage (V_{Th}), and on/off ratios (I_{on}/I_{off}) of the PQ1-based FET device. The mobility was provided in average (highest)[a] form and the performance is based on eight different FETs. Mobility extracted by fitting the linear part of the plot of $I_{DS}^{1/2}$ versus V_G using the equation $I_{DS} = C_i\mu(V_G\text{-}V_{Th})^2W/2L$. [a] Hole mobility.

and thiophene-substituted quinoxaline (**Supplementary Scheme S1**) (Li et al., 2012; Deng et al., 2018b). In order to improve the solubility of the polymer, multiple large sized alky chains are introduced into the polymer. The optical and electrochemical properties of the polymer are investigated. In addition, the OFETs are constructed using PQ1 as the semiconductor layer, which presents a hole mobility of around 0.1 cm^2 V^{-1} s^{-1}.

RESULTS AND DISCUSSION

Computational Study

In order to investigate the Frontier molecular orbital features, backbone configuration, and the HOMO/LUMO energy levels of the two polymers, computational calculations were conducted by density-functional theory (DFT) at the B3LYP/6-31(d,p) level using the model compound containing a single repeating unit with a methyl group instead of an alky chain. As shown in **Figure 1A**, there is a 61.4 twisting angle between the donor units of IDT and the acceptor unit of quinoxaline. The electronic cloud distributions of LUMO are mainly located at the IDT part, while the LUMO electrons are localized on the quinoxaline groups. This indicates that once the polymer is excited, an electron transfer from the IDT part to the quinoxaline groups could take place, which means that the polymer has a stronger ICT effect. A good ICT effect is beneficial for the charge transport within the individual molecules. The calculated HOMO/LUMO level of PQ1 is -5.24 and -2.20 eV, resulting in a band gap of 3.04 eV.

Optical Properties

In order to evaluate the optical properties, UV/vis spectroscopy of the PQ1 polymer is performed in a chloroform solution and thin-film state. The corresponding optical data are summarized in **Supplementary Table S1**. In **Figure 1A**, the UV/Vis absorption spectra of quinoxaline and PQI in dichloromethane and in the thin-film state are shown. The polymer PQ1 presents dark blue color in both the solution and thin-film state. The absorption spectrum of the quinoxaline in dichloromethane exhibited a strong absorption maximum ($\lambda_{abs.max}$) at 416 nm with an extinction coefficient of 3.2×10^4 L mol^{-1} cm^{-1}, which was only blue-shifted around 9 nm compared to its thin-film state ($\lambda_{abs.max}$ = 425 nm). After polymerization, absorption of polymer PQ1 exhibited a large shift (around 193 nm) to a longer wavelength in the solutions compared to the monomer (from 416 to 609 nm). The red-shift could be due to the π-conjugation extension and the donor–acceptor interaction within the polymer backbones, which inevitably caused the intramolecular charge transfer (ICT) process to generate more delocalized intramolecular π-orbitals and thus increased the efficient conjugation lengths[23] Regarding the polymer film, a 21-nm red-shifted absorption was observed compared to their solution counterparts. In addition, in the long-wavelength

absorption range, the bathochromic shift appeared to be stronger (around 50 nm). These observations could be due to the aggregation, the π–π interaction, and the long-range ordered packing. From the onset of absorption, the optical band gap was calculated to be 1.59 eV.

Electrochemical Properties

The electrochemical properties of the polymer were investigated by cyclic voltammetry. The experimental details are described in the **Supporting Information**. Based on the onset reduction and oxidation potentials, the LUMO/HOMO energy levels of the monomer and polymers are estimated (Guo et al., 2014). As shown in **Figure 1D**, PQ1 presents quasi-reversible cathodic and anodic waves. The onset oxidation occurred at 0.78 V and reduction at -0.52 V, based on which the HOMO and LUMO energy levels were calculated to be -5.58 eV and -4.28 eV, respectively. The HOMO energy level of PQ1 is lower than the oxidation threshold of air, i.e., −5.27 eV, indicating the good stability of the materials in air. According to the HOMO/LUMO energy levels, the electrochemical band gap was calculated to be 1.3 eV. This value is smaller than the computation results, which is ascribed to the fact that the computation result is obtained using the single repeat unit, while the electrochemical band gap is obtained using the whole polymer. In addition, the electrochemical band gap is also 0.2 eV smaller than the optical band gap.

OFET Device

The charge transport properties of the PQ1 polymer are evaluated by fabricating the OFET devices of the materials with bottom-gate and bottom-contact (BGBC) configuration on a silicon wafer using a layer of 300 nm SiO_2 as the dielectric material. The devices with PQ1 IS were fabricated by direct spin-casting of the polymer solution in toluene onto the OTS-treated silicon wafer with prepatterned gold source and drain electrodes, and measured under vacuum conditions. The devices were measured after thermal annealing at 100°C for 30 min in an argon-filled glove box to remove the remaining solvent residues. The detailed fabrication and testing procedures are described in the **Supporting Information**. As shown in **Figure 2**, the PQ1 polymer presents a p-type charge transport behavior with a hole mobility (μ_h) estimated to be 0.11 cm^2 V^{-1} s^{-1} (average) for eight different devices. From the eight devices, the highest μ_h is 0.12 cm^2 V^{-1} s^{-1}. The high hole mobility could be ascribed to the strong ICT effect and the good aggregation (Du et al., 2018; Muhammad et al., 2020).

CONCLUSION

In conclusion, a D-A type polymer PQ1 is successfully designed and synthesized between quinoxaline as the electron-deficient unit and IDT as the electron-rich unit by the Stille coupling reaction. UV-vis spectra showed that after polymerization, there is a large red-shift from the monomer to the polymer, which indicates the strong ICT effect for D-A polymer PQ1. In addition, there is a 21-nm bathochromic shift from the solution to thin film for PQ1, which indicates that the PQ1 film presents good aggregation. The electrochemical study indicates that PQ1 exhibits a low band gap with a HOMO energy level of −5.48 eV, which is lower than the oxidation threshold of air, i.e., −5.27 eV, indicating the good stability of PQ1 in air. Using PQ1 as the semiconductor layer to construct OFET presents p-type behavior with a hole mobility of up to 0.12 cm^2 V^{-1} s^{-1}. This study demonstrated the great potential of quinoxaline-type chromophores in constructing novel organic semiconductors, and thus, further modification of quinoxaline structures is currently underway in our laboratory.

DATA AVAILABILITY STATEMENT

The datasets presented in this study can be found in online repositories. The names of the repository/repositories and accession number(s) can be found in the article/ **Supplementary Material**.

AUTHOR CONTRIBUTIONS

DZ helped design, synthesize, and characterize the polymers. In addition, part of the manuscript was written by him. ZD synthesized and characterized the materials. In addition, part of the manuscript was written by him. HZ designed the materials, helped discuss the whole characterization, and revised the whole manuscript.

ACKNOWLEDGMENTS

The authors acknowledge the support from Young Taishan Scholars under Grant 201909120, the Natural Science Foundation of China (Grant: 52163001), Guizhou Province Science and Technology Plan Projects (Grants: CXTD(2021) 005 and (2018)1012), Baiyun District Science and Technology Plan Projects (Grant: (2020)28), and Polymer Composites Engineering Research Center of Guizhou Minzu University (Grant: GZMUGCZX (2021)01).

SUPPLEMENTARY MATERIAL

The Supplementary Material for this article can be found online at: https://www.frontiersin.org/articles/10.3389/fchem.2022.934203/full#supplementary-material

REFERENCES

Andrew, W., Hu, C., Karl, T., Camila, C., Mark, N., Helen, B., et al. (2020). Modification of Indacenodithiophene-Based Polymers and its Impact on Charge Carrier Mobility in Organic Thin-Film Transistors. *J. Am. Chem. Soc.* 14, 2652–2664. doi:10.1021/jacs.9b09374

Arshad, M., Du, H., Javed, M. S., Maqsood, A., Ashraf, I., Hussain, S., et al. (2020). Fabrication, Structure, and Frequency-dependent Electrical and Dielectric Properties of Sr-Doped BaTiO3 Ceramics. *Ceram. Int.* 46, 2238–2246. doi:10.1016/j.ceramint.2019.09.208

Bi, S., Li, Y., He, Z., Ouyang, Z., Guo, Q., and Jiang, C. (2019). Self-assembly Diketopyrrolopyrrole-Based Materials and Polymer Blend with Enhanced Crystal Alignment and Property for Organic Field-Effect Transistors. *Org. Electron.* 65, 96–99. doi:10.1016/j.orgel.2018.11.008

Bogdanov, A. V., and Mironov, V. F. (2021). Recent Advances in the Application of Isoindigo Derivatives in Materials Chemistry. *Beilstein J. Org. Chem.* 17, 1533–1564. doi:10.3762/bjoc.17.111

Cai, Z., Luo, H., Chen, X., Zhang, G., Liu, Z., and Zhang, D. (2014). Extended Conjugated Donor-Acceptor Molecules withE-(1,2-Difluorovinyl) and Diketopyrrolopyrrole (DPP) Moieties toward High-Performance Ambipolar Organic Semiconductors. *Chem. Asian J.* 9, 1068–1075. doi:10.1002/asia.201301312

Cao, K., Sun, X., Zhang, Q., and Liu, Y. (2012). Synthesis and Characterization of a 2,4,6-Tri(2-Thienyl)pyridine-Based Conjugated Polymer for OFET Applications. *Macromol. Chem. Phys.* 213, 917–923. doi:10.1002/macp.201100660

Deng, Z., Li, L., Ai, T., Hao, X., and Bao, W. (2018a). Centrosymmetric Thiophenemethyleneoxindole-Based Donor-Acceptor Copolymers for Organic Field-Effect Transistors. *Macromol. Rapid Commun.* 39, 1800073. doi:10.1002/marc.201800073

Deng, Z., Yang, K., Li, L., Bao, W., Hao, X., Ai, T., et al. (2018b). Solution Processed Air-Stable P-Channel Organic Crystal Field-Effect Transistors of Aminobenzodifuranone. *Dyes Pigments* 151, 173–178. doi:10.1016/j.dyepig.2017.12.052

Donaghey, J. E., Sohn, E.-H., Ashraf, R. S., Anthopoulos, T. D., Watkins, S. E., Song, K., et al. (2013). Pyrroloindacenodithiophene Polymers: the Effect of Molecular Structure on OFET Performance. *Polym. Chem.* 4, 3537–3544. doi:10.1039/c3py00335c

Du, H., Ma, C., Ma, W., and Wang, H. (2018). Microstructure Evolution and Dielectric Properties of Ce-Doped SrBi4Ti4O15 Ceramics Synthesized via Glycine-Nitrate Process. *Pac* 12, 303–312. doi:10.2298/PAC1804303D

Guo, X., Facchetti, A., and Marks, T. J. (2014). Imide- and Amide-Functionalized Polymer Semiconductors. *Chem. Rev.* 114, 8943–9021. doi:10.1021/cr500225d

Kettle, J., Horie, M., Majewski, L. A., Saunders, B. R., Tuladhar, S., Nelson, J., et al. (2011). Optimisation of PCPDTBT Solar Cells Using Polymer Synthesis with Suzuki Coupling. *Sol. Energy Mater. Sol. Cells* 95, 2186–2193. doi:10.1016/j.solmat.2011.03.022

Kim, H. S., Rasool, S., Shin, W. S., Song, C. E., and Hwang, D.-H. (2020). Alkylated Indacenodithiophene-Based Non-fullerene Acceptors with Extended π-Conjugation for High-Performance Large-Area Organic Solar Cells. *ACS Appl. Mat. Interfaces* 12, 50638–50647. doi:10.1021/acsami.0c13277

Lee, Y. H., Jang, M., Lee, M. Y., Kweon, O. Y., and Oh, J. H. (2017). Flexible Field-Effect Transistor-type Sensors Based on Conjugated Molecules. *Chem* 3, 724–763. doi:10.1016/j.chempr.2017.10.005

Li, S., He, Z., Yu, J., Chen, S. a., Zhong, A., Wu, H., et al. (2012). 2,3-bis(5-Hexylthiophen-2-yl)-6,7-bis(octyloxy)-5,8-di(thiophen-2-yl) Quinoxaline: A Good Construction Block with Adjustable Role in the Donor-π-acceptor System for Bulk-heterojunction Solar Cells. *J. Polym. Sci. A Polym. Chem.* 50, 2819–2828. doi:10.1002/pola.26086

Liu, M., Gao, Y., Zhang, Y., Liu, Z., and Zhao, L. (2017). Quinoxaline-based Conjugated Polymers for Polymer Solar Cells. *Polym. Chem.* 8, 4613–4636. doi:10.1039/C7PY00850C

Marszalek, T., Wiatrowski, M., Dobruchowska, E., Jung, J., and Ulanski, J. (2013). One-step Technique for Production of Bi-functional Low Molecular Semiconductor-Polymer Composites for Flexible OFET Applications. *J. Mat. Chem. C* 1, 3190–3193. doi:10.1039/C3TC30163J

Park, J. M., Jung, C. Y., Wang, Y., Choi, H. D., Park, S. J., Ou, P., et al. (2019). Effect of Regioisomeric Substitution Patterns on the Performance of Quinoxaline-Based Dye-Sensitized Solar Cells. *Electrochimica Acta* 298, 650–662. doi:10.1016/j.electacta.2018.12.133

Sagita, C. P., Lee, J. H., Lee, S. W., Whang, D. R., Kim, J. H., and Chang, D. W. (2021). Enhanced Photovoltaic Performance of Quinoxaline-Based Donor-Acceptor Type Polymers with Monocyano Substituent. *J. Power Sources* 491, 229588. doi:10.1016/j.jpowsour.2021.229588

Sasikumar, M., Bharath, D., Kumar, G. S., Chereddy, N. R., Chithiravel, S., Krishnamoorthy, K., et al. (2016). Role of Acceptor Strength on OFET Properties of Small Molecular Organic Semiconducting Materials with D-A-D Architecture. *Synth. Met.* 220, 236–246. doi:10.1016/j.synthmet.2016.06.006

Tsumura, A., Koezuka, H., and Ando, T. (1986). Macromolecular Electronic Device: Field-effect Transistor with a Polythiophene Thin Film. *Appl. Phys. Lett.* 49, 1210–1212. doi:10.1063/1.97417

Wang, Y., Gong, Q., and Miao, Q. (2020). Structured and Functionalized Organic Semiconductors for Chemical and Biological Sensors Based on Organic Field Effect Transistors. *Mat. Chem. Front.* 4, 3505–3520. doi:10.1039/D0QM00202J

Zhai, W., and Zhou, E. (2016). Progress of Organic Photovoltaic Materials Based on Indacenodithiophene and its Derivatives. *Chin. J. Org. Chem.* 36, 2786–2812. doi:10.6023/cjoc201604052

Zhang, H., Li, R., Deng, Z., Cui, S., Wang, Y., Zheng, M., et al. (2020). π-Conjugated Oligomers Based on Aminobenzodifuranone and Diketopyrrolopyrrole. *Dyes Pigments* 181, 108552. doi:10.1016/j.dyepig.2020.108552

Zhang, H., Yang, K., Zhang, K., Zhang, Z., Sun, Q., and Yang, W. (2018). Thionating Iso-Diketopyrrolopyrrole-Based Polymers: from P-type to Ambipolar Field Effect Transistors with Enhanced Charge Mobility. *Polym. Chem.* 9, 1807–1814. doi:10.1039/C8PY00292D

Conflict of Interest: The authors declare that the research was conducted in the absence of any commercial or financial relationships that could be construed as a potential conflict of interest.

Publisher's Note: All claims expressed in this article are solely those of the authors and do not necessarily represent those of their affiliated organizations, or those of the publisher, the editors, and the reviewers. Any product that may be evaluated in this article, or claim that may be made by its manufacturer, is not guaranteed or endorsed by the publisher.

frontiers | Frontiers in Chemistry

ORIGINAL RESEARCH
published: 16 June 2022
doi: 10.3389/fchem.2022.917511

Adsorption Characteristics and Charge Transfer Kinetics of Fluoride in Water by Different Adsorbents

Jiaxi Tang[1,2]*, *Biao Xiang*[1], *Yu Li*[1], *Ting Tan*[1] and *Yongle Zhu*[1]

[1]College of Environmental Science and Engineering, Liaoning Technical University, Fuxin, China, [2]Liaoning Academy of Agricultural Sciences, Shenyang, China

Water containing high concentrations of fluoride is widely distributed and seriously harmful, largely because long-term exposure to fluoride exceeding the recommended level will lead to fluorosis of teeth and bones. Therefore, it is imperative to develop cost-effective and environmentally friendly adsorbents to remove fluoride from polluted water sources. In this study, diatomite (DA), calcium bentonite (CB), bamboo charcoal (BC), and rice husk biochar (RHB) were tested as adsorbents to adsorb fluoride (F^-) from water, and this process was characterized by scanning electron microscopy (FEI-SEM), X-ray diffraction (XRD), and Fourier-transform infrared spectroscopy (FT-IR). The effects of pH, dosage, and the initial mass concentration of each treatment solution upon adsorption of F^- were determined. Kinetic and thermodynamic models were applied to reveal the mechanism of defluoridation, and an orthogonal experiment was designed to obtain the optimal combination of conditions. The results show that the surfaces of CB, BC, and RHB have an irregular pore structure and rough surface, whereas DA has a rich pore structure, clear pores, large specific surface area, and high silica content. With regard to the adsorption process for F^-, DA has an adsorption complex electron interaction; that of CB, BC, and RHB occur mainly *via* ion exchange with positive and negative charges; and CB on F^- relies on chemical electron bonding adsorption. The maximum adsorption capacity of DA can reach 32.20 mg/g. When the mass concentration of fluoride is 100 mg/L, the pH value is 6.0 and the dosage is 4.0 g/L; the adsorption rate of F^- by DA can reach 91.8%. Therefore, we conclude that DA soil could be used as an efficient, inexpensive, and environmentally friendly adsorbent for fluoride removal, perhaps providing an empirical basis for improving the treatment of fluorine-containing water in the future.

Keywords: fluoride, electron binding, adsorption, kinetics, charge transfer

OPEN ACCESS

Edited by:
Meng Zheng,
Qingdao Haiwan Science and Technology Industry Research Institute Co., Ltd., China

Reviewed by:
Hui Wang,
Shenyang University, China
Liyu Du,
Shenyang Agricultural University, China

***Correspondence:**
Jiaxi Tang
tangjiaxi1986@163.com

Specialty section:
This article was submitted to Electrochemistry, a section of the journal Frontiers in Chemistry

Received: *11 April 2022*
Accepted: *04 May 2022*
Published: *16 June 2022*

Citation:
Tang J, Xiang B, Li Y, Tan T and Zhu Y (2022) Adsorption Characteristics and Charge Transfer Kinetics of Fluoride in Water by Different Adsorbents. Front. Chem. 10:917511. doi: 10.3389/fchem.2022.917511

1 INTRODUCTION

Fluoride is widely distributed in nature, being one of the abundant trace elements in the Earth's crust, where its content is 625 mg/g (Amini et al., 2008; Ozsvath, 2009). Fluoride, as a pollutant in water, is produced not only from natural geological resources but also from industries that use fluorine-containing compounds as raw materials (Xu et al., 2015). However, for the human body, fluorine is an essential micronutrient and one of the main components of human teeth and bones. Thus, an appropriate intake of fluorine can prevent dental caries and improve bone strength. However, excessive intake of fluoride will cause harmful health effects, such as tooth and bone fluorosis and

impaired fetal brain functioning (He X. et al., 2020). The concentration level of F^- in drinking water should be lower than the 1.5 mg/L, as stipulated by the World Health Organization (WHO) (Wang et al., 2013). Currently, endemic fluorosis has become a very serious health problem worldwide, and millions of people are affected by high concentrations of fluoridated drinking water. Therefore, it is necessary to develop fluoride-reduction technologies, especially those that are low-cost, efficient, and environmentally friendly.

Many experts and scholars in related fields have conducted extensive research on techniques for the removal and recovery of fluoride from water bodies. The common fluoride removal methods include chemical precipitation (Liu and Liu, 2016), reverse osmosis (Ndiaye et al., 2005), ion exchange (Pintar et al., 2001), nanofiltration (Shen and Schafer, 2014), and adsorption (Paudyal et al., 2011; Jagtap et al., 2012), among others, of which adsorption is most commonly used (He J. et al., 2020). Adsorption is the mass transfer process of adsorbing gas or solute onto the surface of a solid or liquid. When the molecules or atoms on the solid surface have residual surface energy due to force imbalance, the process of adsorption on the solid surface will occur to attract and maintain the colliding material (Ghosh et al., 2021). Currently, those adsorbents that can remove water pollutants mainly include carbon-based adsorbents, nanoadsorbents, metal oxides, hydroxide-based adsorbents, resins, and modified and composite adsorbents (Igwegbe et al., 2018). Yet, the application of many adsorption materials entails advantages and disadvantages. Nevertheless, their low cost and efficiency are seen as their chief advantages. Low-cost and widely used adsorbents include diatomite (Yitbarek et al., 2019), bentonite (Ortiz-Ramos et al., 2022), and biochar (Mei et al., 2020), all of which have great application value for fluoride's removal from water. Diatomite is a light-colored, soft, and lightweight sedimentary rock composed of amorphous silica (SiO_2-nH_2O), mainly derived from aquatic diatom plant skeletons. Due to its high porosity, large surface area, high permeability, low density, small particle size, heat resistance, and chemical stability (Hadjar et al., 2008; Zhang et al., 2013), it has been used for removing different pollutants in various water bodies. Xu et al. (2015) used natural diatomaceous earth for the purification of high fluoride wastewater and found that at a pH of 5 and a dosing rate of 50 g/L, 82% of fluoride was adsorbed. Similar to diatomite, bentonite is a clay mineral, whose main component is montmorillonite, which has a large surface area and strong adsorption capacity and is abundant in nature. Studies on the use of bentonite or modified bentonite for fluoride removal from water bodies have also been reported, for which good adsorption results are reported (Fang et al., 2016; Kalsido et al., 2021). Biochar is a typical carbon-based adsorbent obtained by high-temperature pyrolysis of waste biomass in an anaerobic environment. Biochar has a well-developed pore structure, a high specific surface area, excellent ion exchange properties, abundant surface functional groups, and good stability (Wang et al., 2019). Some studies have shown that biochar prepared using rice husk is capable of up to 72% adsorption of fluoride from water bodies (Pillai et al., 2020).

In summary, many studies have examined the use of adsorption materials to remove fluoride in water, but the adsorption capacity and action mechanism of different adsorption materials are likely to differ. Accordingly, in this study, diatomite (DA), calcium bentonite (CB), bamboo biochar (BC), and rice husk biochar (RHB) were selected to systematically study their adsorption properties for fluoride (F^-) in water and to screen for material's best enabling adsorption for fluoride. A second objective was to investigate the adsorption mechanism for fluoride in water in high-fluorine areas to provide a theoretical basis for the treatment of fluoride-containing water.

2 MATERIALS AND METHODS

2.1 Experimental Materials and Characterization

The DA used in the experiments was supplied from the Jiangsu Chengbo Environmental Protection Technology Co., Ltd., China, with an average particle size of 9.14 μm. BC and RHB were purchased from the Lize Environmental Technology Co., Ltd., Zhengzhou City, Henan Province, China, with average particle sizes of 6.71 and 10.43 μm, respectively. CB was purchased from Fuxin General Building Materials Factory, China, with an average particle size of 6.76 μm.

The microscopic morphology and surface characteristics of the four adsorbent materials were observed by ultra-high resolution field emission scanning electron microscopy (FEI-SEM, FEI-Verios 460L). Their crystal structures were characterized by X-ray diffraction (XRD, Ultima IV, Nippon Science), and their surface structural groups were analyzed by Fourier transform infrared spectroscopy (FT-IR, IS50, Thermofisher).

2.2 Experimental Reagents and Apparatus

Sodium fluoride (GR) was used (from the Tianjin FengChuan Chemical Reagent Technology Co., Ltd., China)to simulate aqueous fluoride (F^-). The experimental water was deionized; the buffer solutions used for the experiment were sodium citrate dihydrate and sodium nitrate (respectively from the Tianjin Guangfu Technology Development Co., Ltd. and Shenyang Huadong Reagent Factory, China). The instruments used in the experiment were a JA1003 electronic balance, a PHS-3C type pH meter, a BS-MS thermostatic oscillator, an L550 Xiang Yi centrifuge, a CM-230 laboratory pure water treatment system, a PXS-270 fluorometer, and a JB-10 magnetic stirrer.

2.3 Adsorption Experiments

2.3.1 Effect of the Initial Mass Concentration of F^- on the Adsorption Effect

The initial mass concentration gradient of F^- was adjusted to 0, 10, 20, 40, 60, 80, 100, and 150 mg/L, at pH 6.0, and 25 ml per concentration was measured in 50 ml centrifuge tubes. To these, 0.10 g of each of the four adsorbent materials was added (separately), and the adsorption experiment was carried out at 25°C for 120 min in a constant temperature shaker at 200 rpm.

After centrifugation at 4,000 r/min for 10 min, 10 ml of the supernatant was centrifuged through a 0.45 μm filter membrane, and the remaining F^- mass concentration in the solution was determined using a PXS-270 fluoride ion-selective electrode. Each adsorbent was tested for each F^- concentration in triplicate, and relative standard deviations of duplicate samples were less than 5.0%.

2.3.2 Adsorption Kinetics Experiments

The kinetic parameters of F^- (100 mg/L) sorption by each adsorbent (0.10 g) were determined with 25 ml solutions for 5, 10, 20, 40, 60, 120, 240, 360, 480, and 720 min at 25 °C in the solution at pH 6. After centrifugation at 4,000 r/min for 10 min, 10 ml of the supernatant was centrifuged through a 0.45 μm filter membrane, and the remaining F^- mass concentration in the solution was measured.

2.3.3 Effect of pH on the Adsorption Effect

, About 25 ml of an F^- solution (100 mg/L) was added into 50 ml centrifuge tubes, and its pH was adjusted to 3.0, 4.0, 5.0, 6.0, 7.0, or 8.0. To each tube, 0.10 g of DA was added, and all tubes were stored at 25°C. The adsorption experiment was the same as given in Section 2.3.1. After centrifugation, 10 ml of the supernatant was taken and passed through a 0.45 μm filter membrane to determine the remaining F^-mass concentration in the solution.

2.3.4 Effect of Dosage on the Adsorption Effect

The DA was weighed at 0.04, 0.08, 0.10, 0.15, 0.20, and 0.30 g in 50 ml centrifuge tubes, and 25 ml of a mass concentration of F^- (100 mg/L) in solution was added to each tube. The adsorption experiment was the same as given in Section 2.3.1. After centrifugation at 4,000 r/min for 10 min, 10 ml of the supernatant was centrifuged through a 0.45 μm filter membrane and then the remaining F^- mass concentration in the solution was measured.

2.3.5 Orthogonal Experiments

According to the design method of the orthogonal test, the factors selected for investigation were as follows: adsorption pH (A), the mass concentration of the F^- solution (B), and adsorbent dosage (C) on the adsorption of F^- in water. Three levels of each factor were selected for the three-factor, three-level orthogonal test of $L_9 3^4$.

2.4 Data Processing

The removal rate is calculated as:

$$R = \frac{(\rho_0 - \rho_e)}{\rho_0} \times 100\%. \quad (1)$$

where$\rho_0 - F^-$ is the initial mass concentration of the solution (mg/L), ρ_e is the mass concentration of F^- in solution at the adsorption equilibrium (mg/L), and$A$ is the adsorption rate.

The adsorption volume is calculated as follows:

$$q_e = \frac{[(\rho_0 - \rho_e) \times V]}{m}. \quad (2)$$

where $\rho_0 - F^-$ is the initial mass concentration of the solution (mg/L), ρ_e is the mass concentration of F^- in the solution at the adsorption equilibrium (mg/L), V is the volume of the solution (L), m is the material dosage (g/L), and q_e is the adsorption amount of F^- at the adsorption equilibrium (mg/g).

The two adsorption fitting models are as follows. The Langmuir model equation is

$$\frac{\rho_e}{q_e} = \frac{1}{Q_m K_L} + \frac{\rho_e}{Q_m}. \quad (3)$$

The Freundlich model equation is

$$log\, q_e = log\, K_f + \frac{1}{n} log\, \rho_e. \quad (4)$$

where $\rho_0 - F^-$ is the mass concentration of F^- in the solution at the adsorption equilibrium (mg/L), q_e is the adsorption amount of F^- at the adsorption equilibrium (mg/g), Q_m is the maximum saturation adsorption amount (mg/g), K_L is a constant in Langmuir's equation regarding the heat of adsorption, and $N$is a constant in the Freundlich equation related to the adsorption strength, preferential adsorption for $n > 1$, linear adsorption for $n = 1$, and non-preferential adsorption for $n < 1$.

The quasi-first-order kinetic equation is

$$ln(q_e - q_t) = lnq_e - K_1 t. \quad (5)$$

The quasi-second-order kinetic equation is

$$\frac{t}{q_t} = \frac{1}{K_2 q_e^2} + \frac{t}{q_e}. \quad (6)$$

where q_e is the equilibrium adsorption amount (mg/g), q_t is the adsorption amount at moment t (mg/g), t is the adsorption time (min), K_1 is the quasi-first-order kinetic adsorption rate constant (min-1), and K_2 is thequasi-second-order kinetic adsorption rate constant (min-1).

3 RESULTS AND DISCUSSION

3.1 Characterization of the Adsorbent Materials

3.1.1 FEI-SEM Analysis

Figure 1 shows the scanning electron micrographs of the four materials under a 10,000 × microscope. Evidently, the surface of DA has two types of pore structures with large and small pores and clear pores, indicating that DA has a unique multi-level pore structure. The DA's main component is silica, which has a large specific surface area and good thermal stability, and is a natural green material water treatment agent with a porous structure (Akafu et al., 2019); therefore, fluoride is likely to be adsorbed on DA. The surface of CB has an irregular pore structure but a rough surface; while for BC and RHB, they have relatively few pores, showing the presence of dispersed particulate matter as well as a plate-like structure. The granular material on their surface could be crystals formed by some mineral elements (Piri et al., 2020). Overall, DA has a relatively well-developed pore structure and a high specific surface area for better absorption.

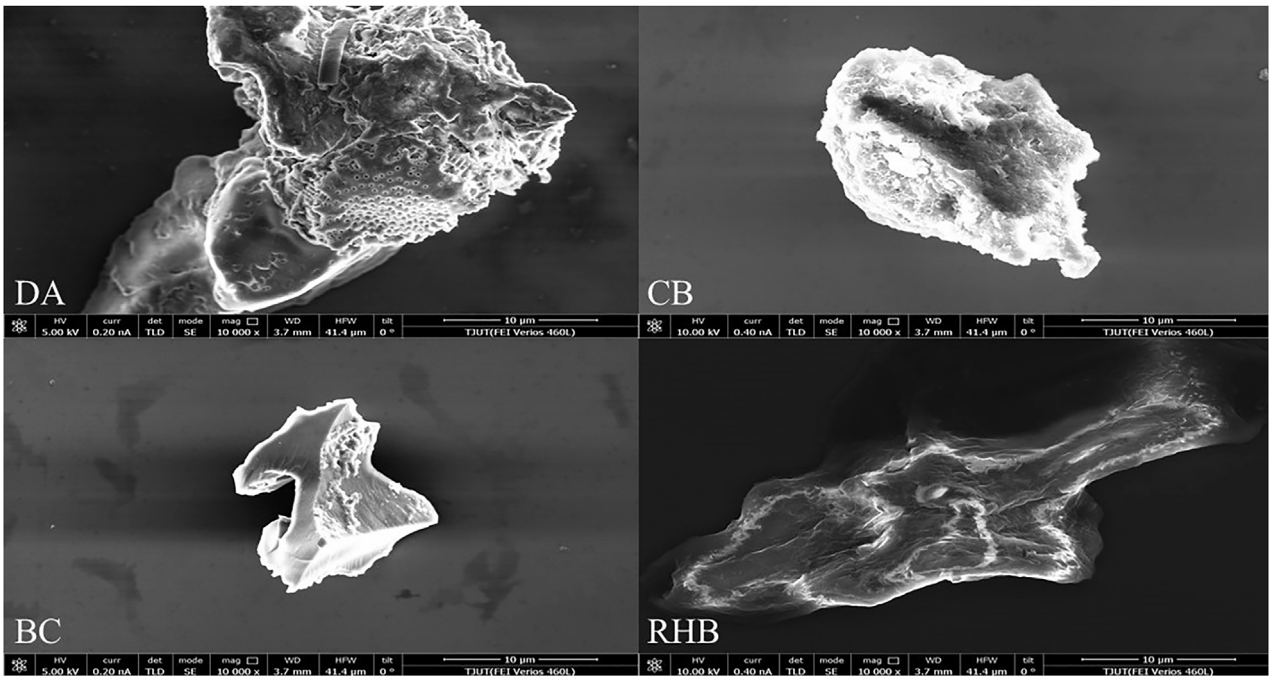

FIGURE 1 | FEI-SEM images of the four adsorbent materials.

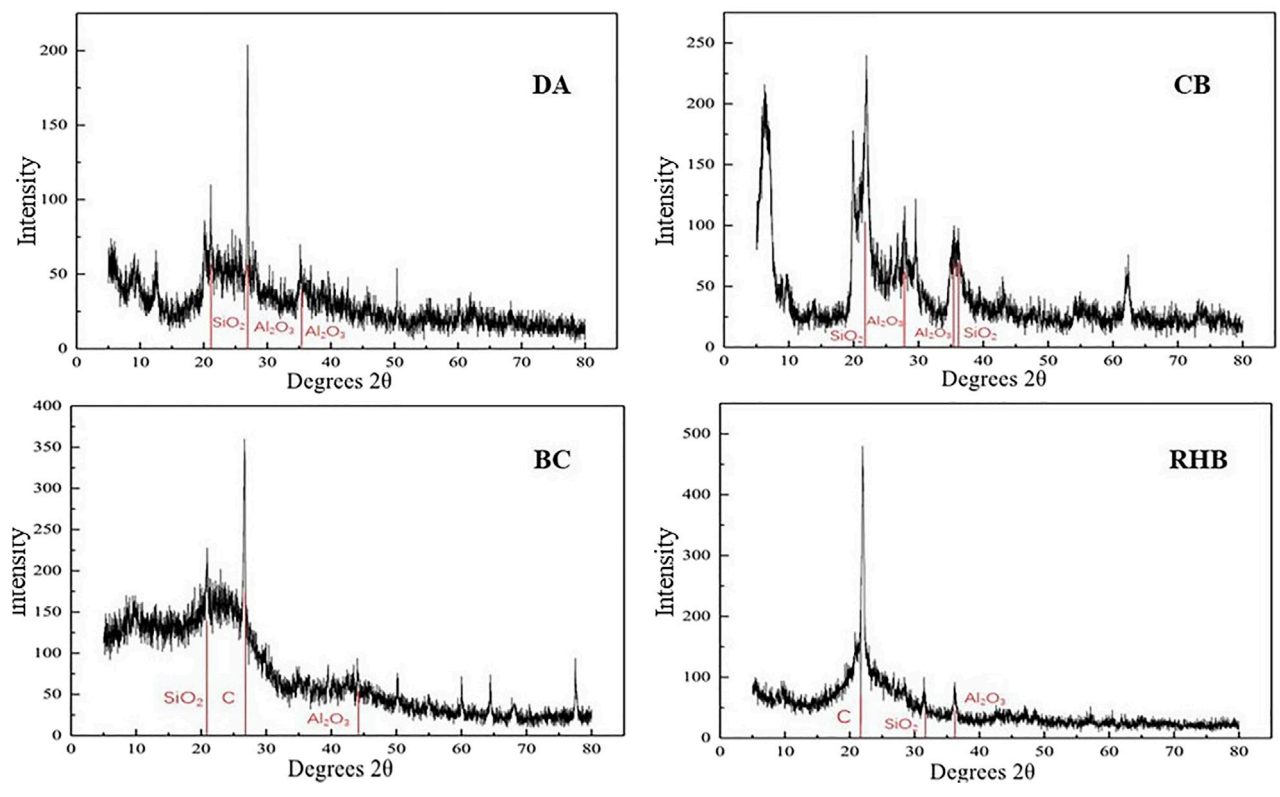

FIGURE 2 | XRD patterns of the four adsorbent materials.

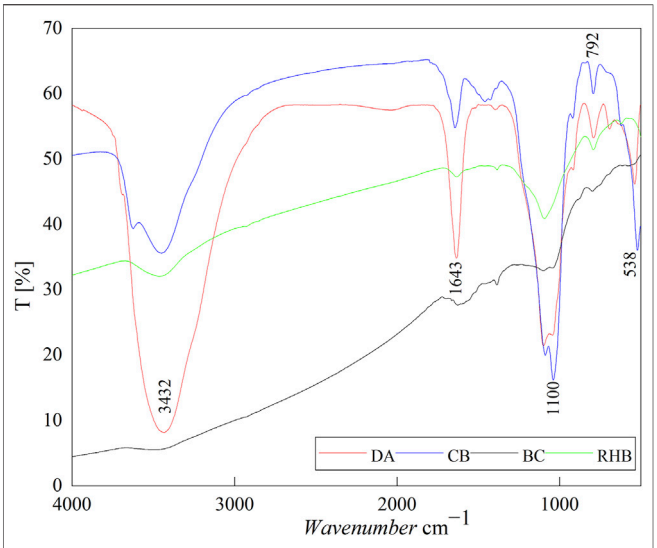

FIGURE 3 | Infrared spectra of the four adsorbent materials.

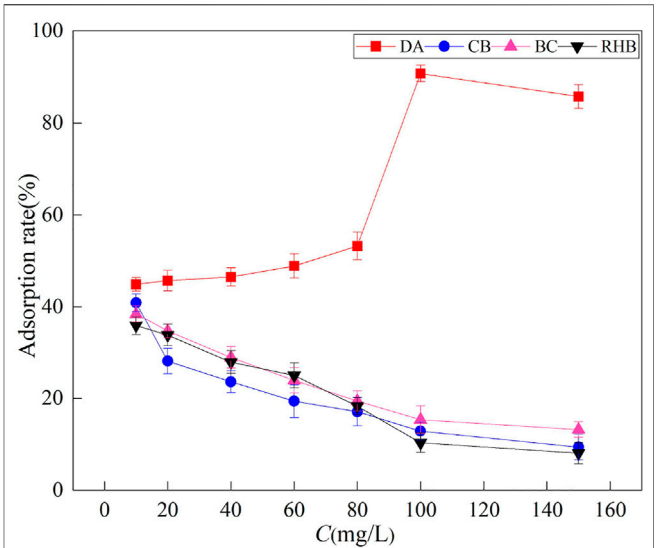

FIGURE 4 | Effects of four adsorbent materials on the adsorption of an F^- solution with different mass concentrations.

3.1.2 XRD Analysis

Figure 2 shows the XRD plots of the four materials. Evidently, DA and CB have wider diffraction peaks at around 22.0°, whose main composition corresponds to amorphous SiO_2. The sharp diffraction peaks at around 26° can be attributed to quartz impurities in the materials, while the wider diffraction peaks at around 35° correspond to amorphous Al_2O_3 (Xu et al., 2015). In terms of composition, DA and CB were polycrystalline. For BC and RHB, the main XRD diffraction peaks 2θ of the biochar crystals are at 25° and 27°, respectively (Yihuan et al., 2022). The relatively higher intensity of diffraction peaks for RHB than BC can arise from the better crystallization properties of carbon. In addition, all four materials contain SiO_2 and Al_2O_3, and these metal cations can adsorb F^-*via* electrostatic gravity, thus providing adsorption sites on the material surface (Teng et al., 2009). Moreover, the specific surface area and adsorption efficiency of these materials can be significantly increased because they are rich in surface-active functional groups (Cui et al., 2013).

3.1.3 FT-IR Analysis

The four adsorbents were identified in detail using their respective FTIR analysis data (**Figure 3**). The vibrations of DA, CB, and RHB of about 3,432 cm^{-1} are due to the stretching vibrations of the adsorbed water hydroxyl group (O-H) and the surface hydroxyl group. All four materials have vibrational peaks around 1,634 cm^{-1}, probably from the bound water or the surface hydroxyl group. The peaks of DA, CB, BC, and RHB located at 1,100 cm^{-1} and 538 cm^{-1} are of siloxane groups (Si-O-Si-), and the peak at 792 cm^{-1} is attributable to the Al-O absorption band (Akafu et al., 2019). These adsorbent materials are rich in oxygen-containing functional groups and thus can provide Π-electrons for surface complexation with F^-, resulting in stable structures (Datsko and Zelentsov, 2016). Additional studies have shown that silanol groups are very active and can react with many contaminants, including fluoride, through the formation of hydrogen bonds (Al-Ghouti et al., 2003). The formation of new bonding electronic structures by complexation with the F^- is one of the main mechanisms by which fluoride ions are adsorbed, as seen in the infrared spectra.

3.2 Effect of Different F^- Mass Concentrations on the Adsorption Effect

The adsorption rate of F^- by DA increased with an increasing initial mass concentration of F^- (**Figure 4**). The highest adsorption rate of 90.7% was achieved when the mass concentration was 100 mg/L. This is because at low concentrations, DA has a sufficient number of active sites, and therefore, most of the F^- interacts with the active sites on DA, leading to greater adsorption of F^- (Akafu et al., 2019). When the concentration reaches a certain value, the adsorption rate of F^- by DA begins to decline. This is because at higher concentrations, the active sites of the adsorbent are saturated and fluoride ions outnumber the adsorption sites, and at a constant mass of the adsorbent, the ratio of F^- to the available active surface sites is higher with an increasing initial F^- concentration, leading to a declining adsorption rate (Bhaumik et al., 2013). For the other three materials, their adsorption rates decreased with an increasing initial mass concentration of F^- because the adsorption sites of the three materials were saturated at this concentration; hence, the adsorption rate decreased as the concentration increased. The maximum adsorption rate of CB (41%) was higher than that of BC and RHB. It can be concluded that the magnitude of adsorption performance of the four materials is DA > CB > BC > RHB. Gomoro et al. (2012) showed that the efficiency of fluoride adsorption by adsorbents decreases as the initial mass concentration of fluoride increases and reaches a certain threshold value. This finding agrees with

TABLE 1 | Adsorption fitting parameters of four different tested materials.

Item	Freundlich model			Langmuir model		
	Log K_f	N	R^2	K_L	Q_m	R^2
DA	0.717	1.15	0.9930	0.00759	32.20	0.8867
CB	0.975	0.52	0.9483	0.0289	4.42	0.9841
BC	-0.549	1.70	0.9594	0.0177	6.58	0.9764
RHB	-0.384	2.20	0.7201	0.0701	3.42	0.9123

our results. Hence, the effectiveness of electron exchange at the active sites is the main factor determining the adsorption of fluoride ions.

The Freundlich and Langmuir models were used here to describe the adsorption of F^- processes of the four materials, and their fitted parameters are in **Table 1**. The Langmuir adsorption model describes the adsorption of a single molecular layer, the adsorption mechanism is mainly ion exchange, and the adsorption is mainly chemisorption, while the Freundlich adsorption model describes a non-homogeneous adsorption behavior, which refers to the adsorption process of multiple molecular layers occurring on the surface and spatially inhomogeneous distribution of the adsorbent, and the presumed adsorption mechanism is mainly adsorption--complexation interactions (Tang et al., 2020). As shown in **Table 1**, for DA the Freundlich model fits better than the Langmuir model, with R^2 values of up to 0.9930, indicating that the adsorption process of DA for F^- is an adsorption–complex electron interaction, surface adsorption, and multi-molecular layer adsorption. When applied to CB and BC, both models fit better, indicating that the adsorption process of F^- by CB and BC is unilamellar and multilamellar co-adsorption, mainly based on ion exchange involving positive and negative charges. For RHB, the Langmuir model fits better than the Freundlich model, with an R^2 value of 0.9128, indicating that the adsorption process of F^- by RHB is unilamellar. Its adsorption mechanism is mainly based on ion exchange involving positive and negative charges. Similar results were reported by Goswami and Kumar (2018), who studied the adsorption of fluoride using rice husk biochar.

3.3 Analysis of Adsorption Kinetics

Figure 5 shows the variation in the adsorption amount of F^- by the four materials over time. Clearly, the adsorption amount increased with the elapsed time, and the maximum adsorption amount was reached at around 120 min. The materials' adsorption amounts were ranked as follows: DA > CB > BC > RHB; the maximum adsorption amount of DA reached 22.300 mg/g, twice as much as that found for the other three materials. Beyond 120 min, the adsorption amount did not change and adsorption had reached equilibrium. Oladoja and Helmreich (2016) studied the adsorption of fluoride using calcium aluminate–diatomaceous earth composites and found that its adsorption reached equilibrium when the reaction time was 120 min, as found in our study. This is because at the initial stage of adsorption, there are more active sites on the adsorbent surface and so F^- rapidly occupies the active sites on the adsorbent's surface, and its adsorption capacity increases

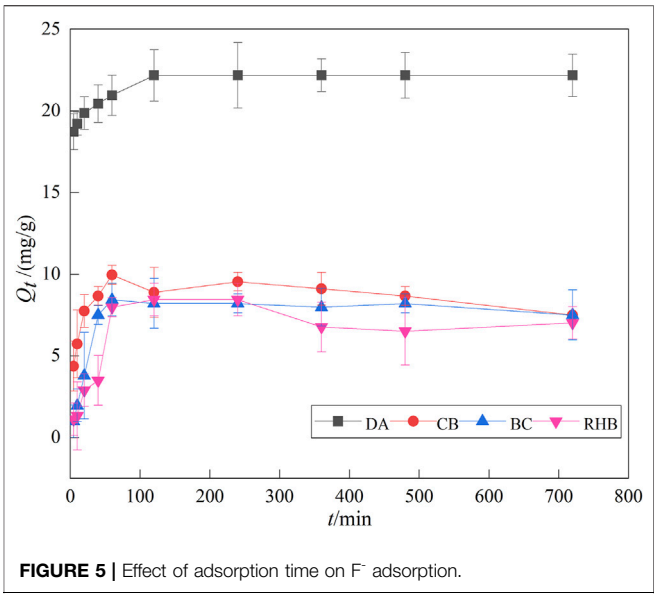

FIGURE 5 | Effect of adsorption time on F^- adsorption.

(Sadhu et al., 2021). But when prolonged, the available active sites on the adsorbent's surface decline significantly, and adsorption gradually spreads to the internal surface of the porous adsorbent, which strengthens its resistance and slows down adsorption such that the adsorption capacity no longer changes (Akafu et al., 2019).

Two kinetic models, quasi-first-order and quasi-second-order, were used to study the kinetic process of adsorption of F^- by the four adsorbents. The corresponding fitted parameters are shown in **Table 2**. For DA and CB, the fitting results were better for the quasi-second-order than the quasi-first-order kinetic models, with R^2 values of 0.9998 and 0.9461, respectively. This suggests that the adsorption process of DA and CB on F^- is dominated by chemisorption, with surface adsorption and physical adsorption acting in concert (Lu et al., 2012). The adsorption rate is mainly controlled by chemisorption, while the adsorption capacity shows a positive correlation with the number of active sites on the adsorbent surface, and the adsorption reaction chiefly occurs *via* the sharing of electrons and the gain and loss of electrons (Aboul-Kassim and Simoneit, 2001). Further, the theoretical adsorption amount obtained by fitting the quasi second-order kinetic equation of DA is closer to the experimental value, indicating that the adsorption of F^- by DA better conforms to quasi second-order kinetics. Oladoja and Helmreich (2014) also confirmed that the adsorption of fluorine by diatomaceous earth is better described by quasi-second-order kinetics. For RHB, in contrast, the fitted quasi-first-order kinetic model outperformed the second-order kinetic model, with an R^2 value of 0.9527. This indicates that the adsorption of F^- by RHB relies primarily on a physical process. Other studies have shown that due to excess sodium fluoride in the solution, the resulting aluminum fluoride binds NaF to form a $NaAlF_4$ intermediate compound, which is transformed into cryolite due to further adsorption of NaF (Datsko and Zelentsov, 2016). The reactions between fluoride ions and their adsorbent are as follows:

TABLE 2 | Kinetic fitting parameters of four different materials for F^- adsorption.

Item	Quasi-first-order kinetic model			Quasi-second-order kinetic model		
	q_e	K_1	R^2	q_e	K_2	R^2
DA	3.600	0.0182	0.9880	22.300	0.01990	0.9998
CB	0.988	0.0410	0.9234	1.142	0.1644	0.9461
BC	0.913	0.0450	0.7653	1.230	0.1991	0.8128
RHB	0.924	0.7620	0.9527	0.968	0.1756	0.7632

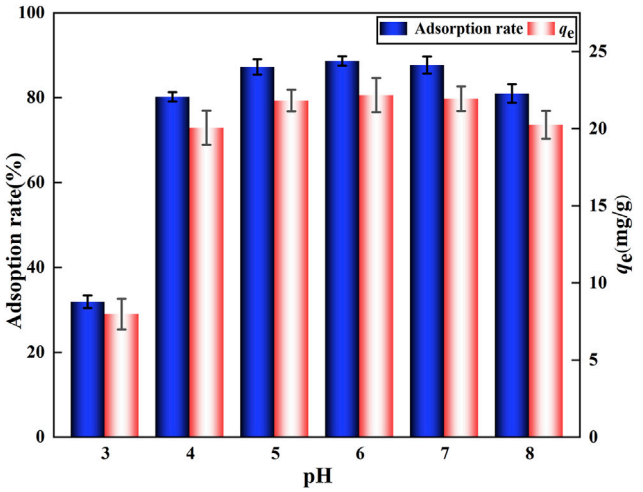

FIGURE 6 | Effect of DA on F^- adsorption at different pH levels.

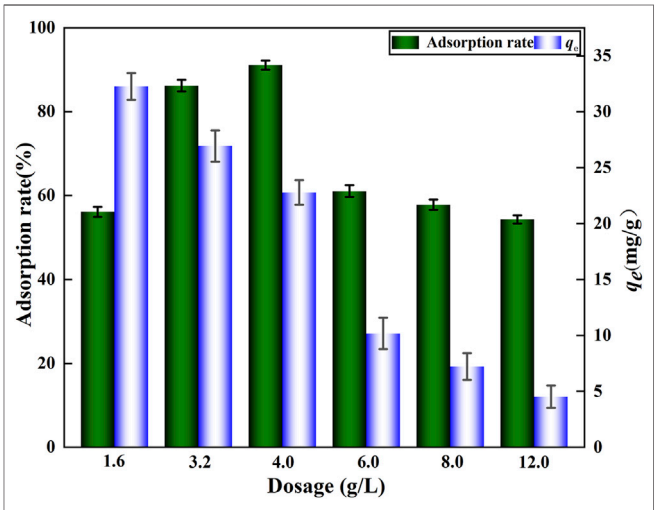

FIGURE 7 | Effects of different dosages of DA on F^- adsorption.

$$A1^{3+} + 3F^- \rightarrow A1F_3,$$
$$A1F_3 + NaF \rightarrow NaA1F_4,$$
$$NaA1F_4 + 2NaF \rightarrow Na_3A1F_6.$$

The aforementioned results showed that DA exhibited good adsorption performance for F^-; therefore, it was chosen to investigate how other conditions influence the adsorption of F^-.

3.4 Effects of Different Factors Influencing the Adsorption of F^-

3.4.1 Effect of pH

For the adsorption process, the solution pH is a critical factor that can change the pollutant's presence and morphology as well as the surface charge of the adsorbent (Zhao et al., 2020). The adsorption rate and adsorption capacity of F^- by DA increased with increasing pH, reaching a maximum at a pH of around 6.0 with an adsorption rate of 88.7% and an adsorption capacity of 22.2 mg/g (**Figure 6**); however, at a pH > 6.0, the adsorption rate and adsorption capacity of F^- by DA started to decrease, which can be attributed to the competition between hydroxyl ions and fluoride for active adsorption sites (Koilraj and Kannan, 2013). The surface charge of the adsorbent is related to the pH of the surrounding aqueous solution. Neutral or alkaline conditions generally result in a negative charge on the surface. Thus, under acidic conditions, the surface usually retains excess protons, resulting in a total positive charge (Cai et al., 2017). More H^+ on the adsorbent's surface leads to the electrostatic attraction between its positively charged surface and F^- under acidic conditions, and the exchange of hydroxyl groups with F^- is considered mainly responsible for the removal of fluoride at the interface with the adsorbent water (Yitbarek et al., 2019). At this time, the adsorption of F^- is favored. A higher pH means more negative charges on the adsorbent surface, which will lead to strong electrostatic repulsion between the adsorbent and F^- as well as a significantly diminished adsorption capacity (Wang et al., 2013). Therefore, weak acid solutions are favorable for DA-driven defluoridation and pH = 6.0 is the optimal adsorption condition for it.

3.4.2 Effect of DA Dosage

To determine the appropriate amount of DA, adsorption experiments were performed at different DA dosages fixed at pH 6. When the dosage was increased from 1.6 to 4.0 g/L, the F^- adsorption rate increased from 56.1 to 91.1% (**Figure 7**), but when the dosage was greater than 4.0 g/L, the adsorption rate started to decrease. The increase in adsorption efficiency with a larger adsorbent dose is due to the higher availability of fluoride bound to active surface sites at higher adsorbent doses (Fekadu et al., 2013). Evidently, the adsorption of F^- by DA eventually declines rather with higher dosing, and the weakened adsorption capacity is

TABLE 3 | Orthogonal experimental results for F^- adsorption on DA.

Items	A, dosage (g)	B, pH	C, *C* (mg/L)	Adsorption rate of F^- (%)
1	0.06	5.0	150	62.8
2	0.06	6.0	60	81.2
3	0.06	7.0	100	73.9
4	0.08	5.0	100	86.8
5	0.08	6.0	150	75.1
6	0.08	7.0	60	48.9
7	0.1	5.0	60	80.4
8	0.1	6.0	100	91.8
9	0.1	7.0	150	84.6
K_1	217	230	222	—
K_2	210	247	211	—
K_3	255	207	251	—
k_1	72.6	76.7	74.1	—
k_2	70.3	82.3	70.2	—
k_3	85.2	69.1	83.8	—
R	14.9	5.65	13.6	—

due to the greater fixed initial fluorine concentration and a solid dose of the fixed solute load, leading to the reduced availability of fluoride ions per unit mass of the adsorbent (Akafu et al., 2019). Given the porous structure of this DA material, it has more fine pores than the other tested adsorbents, likely increasing the specific surface area and contributing to the augmented adsorption capacity of this material. Based on the aforementioned analysis, the suitable amount of added DA should be 4.0 g/L to remove fluoride. Another study pointed out that DA is capable of regeneration after its adsorption of pollutants and that a K_2SO_4 solution is better for the regeneration of spent adsorbents (Gitari et al., 2017), thus enabling the recycling and re-use of the material.

3.5 Orthogonal Experiments

The DA material with the best effect was selected from orthogonal experiments. The results of the orthogonal experiments are presented in **Table 3**, namely the values of different influencing factors K_1, K_2, K_3, k_1, k_2, k_3, and their corresponding *R* values. By comparing the k_1, k_2, and k_3 values, the optimal level of each experimental influence factor can be determined, which in turn leads to the optimal combination of experimental conditions. By comparing the differences among *R*-values, the size of the influence of each factor on the experimental results can be determined; a larger *R*-value indicates that the factor has a greater effect on the adsorption process. As seen in **Table 3**, $R_A > R_C > R_B$, indicating that the effect size of each influencing factor is as follows: dosage > mass concentration > pH. Hence, the optimal combination derived from the experiments was a dosage of 4.0 g/L, pH of 6.0, and a mass concentration of 100 mg/L, under which the adsorption rate of F^- by DA could reach 91.8%.

4 CONCLUSION

This study focused on the mechanism of fluorine adsorption by the diatomite (DA) and biochar adsorbents. The characterization of four adsorbent materials was investigated by FEI-SEM, XRD, and FT-IR. The DA material has an excellent surface structure and is rich in oxygen-containing functional groups vis-à-vis the other three tested materials, conferring to it a strong adsorption force for F^-. The adsorption of DA for F^- better conforms to the Freundlich model, indicating that the process entails adsorption–complex electron interaction, surface adsorption, and multi-molecular layer adsorption, while the adsorption process of CB or BC for F^- occurs mainly *via* ion exchange with the participation of positive and negative charges, involving a unimolecular layer and multi-molecular layer co-adsorption process. The adsorption process of RHB on F^- follows the Langmuir model, mainly characterized by unimolecular layer adsorption with ion exchange. The quasi-second-order kinetic models fitted better to the dynamics of CB, indicating that their adsorption process was dominated by chemical electron bonding adsorption, whose adsorption rate was mainly controlled by chemisorption. By contrast, a quasi-first-order kinetic model yielded a better fit for RHB, indicating that its adsorption of F^- was dominated by physical adsorption. The adsorption capacity of the four materials was D > CB > BC > RHB in order of magnitude. The adsorption rate of F^- by DA was 91.8% at a fluoride mass concentration of 100 mg/L, a pH of 6.0, and a dose of 4.0 g/L. The factors influencing how DA's adsorption of fluoride in water was, in order of magnitude, dosing > mass concentration > pH. Taken together, these results reveal that DA can be recommended as an effective adsorbent to remove fluoride from contaminated water.

DATA AVAILABILITY STATEMENT

The raw data supporting the conclusion of this article will be made available by the authors, without undue reservation.

AUTHOR CONTRIBUTIONS

JT acquired the funding for the study, supervised the formation of the manuscript, wrote the manuscript, and designed the experiments. BX wrote the manuscript, collected samples, performed the experiments, and analyzed the data. YL conducted the experiments and processed the samples. TT provided assistance with the statistical analysis and graphing of figures. YZ proofread the manuscript and its modified format.

FUNDING

This research was funded by a Project sponsored by the "Liaoning BaiQianWan Talents Program" (2021921100). Shenyang Young and Middle-aged Science and Technology Innovation Talent Support Program (RC210377).

ACKNOWLEDGMENTS

The authors are grateful to Jiangsu Chengbo Environmental Protection Technology Co., Ltd., China, for giving them the diatomite sample used as an adsorbent for defluoridation.

REFERENCES

Aboul-Kassim, T., and Simoneit, B. (2001). Pollutant-Solid Phase Interactions Mechanisms, Chemistry and Modeling. *Handb. Environ. Chem.* 5, 172–377. doi:10.1007/10638318

Akafu, T., Chimdi, A., and Gomoro, K. (2019). Removal of Fluoride from Drinking Water by Sorption Using Diatomite Modified with Aluminum Hydroxide. *J. Anal. Methods Chem.* 2019, 1–11. doi:10.1155/2019/4831926

Al-Ghouti, M. A., Khraisheh, M. A. M., Allen, S. J., and Ahmad, M. N. (2003). The Removal of Dyes from Textile Wastewater: a Study of the Physical Characteristics and Adsorption Mechanisms of Diatomaceous Earth. *J. Environ. Manag.* 69, 229–238. doi:10.1016/j.jenvman.2003.09.005

Amini, M., Abbaspour, K. C., Berg, M., Winkel, L., Hug, S. J., Hoehn, E., et al. (2008). Statistical Modeling of Global Geogenic Arsenic Contamination in Groundwater. *Environ. Sci. Technol.* 42, 3669–3675. doi:10.1021/es702859e

Bhaumik, R., Mondal, N. K., Chattoraj, S., and Datta, J. K. (2013). Application of Response Surface Methodology for Optimization of Fluoride Removal Mechanism by Newely Developed Biomaterial. *Ajac* 04, 404–419. doi:10.4236/ajac.2013.48051

Cai, J., Zhao, X., Zhang, Y., Zhang, Q., and Pan, B. (2018). Enhanced Fluoride Removal by La-Doped Li/Al Layered Double Hydroxides. *J. Colloid Interface Sci.* 509, 353–359. doi:10.1016/j.jcis.2017.09.038

Cui, L., Meng, Q., Zheng, J., Wei, X., and Ye, Z. (2013). Adsorption of Cr(VI) on 1,2-Ethylenediamine-Aminated Macroporous Polystyrene Particles. *Vacuum* 89, 1–6. doi:10.1016/j.vacuum.2012.08.012

Datsko, T. Y., and Zelentsov, V. I. (2016). Fluorine Sorption by Aluminosilicate-Modified Diatomite from Highly Concentrated Fluorine Solutions: 1. Adsorption Equilibrium. *Surf. Engin. Appl.Electrochem.* 52, 300–311. doi:10.3103/S1068375516030042

Fang, D., Tian, H. J., Ye, X., He, C. L., Dan, Y. M., and Wei, S. Y. (2016). Adsorption Properties of Fluorine onto Fulvic Acid-Bentonite Complex. *Huan Jing Ke Xue* 37, 1023–1031. doi:10.13227/j.hjkx.2016.03.030

Fufa, F., Alemayehu, E., and Lennartz, B. (2013). Defluoridation of Groundwater Using Termite Mound. *Water Air Soil Pollut.* 224, 1152–1167. doi:10.1007/s11270-013-1552-y

Ghosh, S., Malloum, A., Igwegbe, C. A., Ighalo, J. O., Ahmadi, S., Dehghani, M. H., et al. (2022). New Generation Adsorbents for the Removal of Fluoride from Water and Wastewater: A Review. *J. Mol. Liq.* 346, 118257–118268. doi:10.1016/j.molliq.2021.118257

Gitari, W. M., Izuagie, A. A., and Gumbo, J. R. (2020). Synthesis, Characterization and Batch Assessment of Groundwater Fluoride Removal Capacity of Trimetal Mg/Ce/Mn Oxide-Modified Diatomaceous Earth. *Arabian J. Chem.* 13, 1–16. doi:10.1016/j.arabjc.2017.01.002

Gomoro, K., Zewge, F., Hundhammer, B., and Megersa, N. (2012). Fluoride Removal by Adsorption on Thermally Treated Lateritic Soils. *Bull. Chem. Soc. Eth.* 26, 361–372. doi:10.4314/bcse.v26i3.5

Goswami, R., and Kumar, M. (2018). Removal of Fluoride from Aqueous Solution Using Nanoscale Rice Husk Biochar. *Groundw. Sustain. Dev.* 7, 446–451. doi:10.1016/j.gsd.2017.12.010

Hadjar, H., Hamdi, B., Jaber, M., Brendlé, J., Kessaïssia, Z., Balard, H., et al. (2008). Elaboration and Characterisation of New Mesoporous Materials from Diatomite and Charcoal. *Microporous Mesoporous Mater.* 107, 219–226. doi:10.1016/j.micromeso.2007.01.053

He, J., Yang, Y., Wu, Z., Xie, C., Zhang, K., Kong, L., et al. (2020b). Review of Fluoride Removal from Water Environment by Adsorption. *J. Environ. Chem. Eng.* 8, 104516–104617. doi:10.1016/j.jece.2020.104516

He, X., Li, P., Ji, Y., Wang, Y., Su, Z., and Elumalai, V. (2020a). Groundwater Arsenic and Fluoride and Associated Arsenicosis and Fluorosis in China: Occurrence, Distribution and Management. *Expo. Health* 12, 355–368. doi:10.1007/s12403-020-00347-8

Igwegbe, C. A., Banach, A. M., and Ahmadi, S. (2018). Removal of Acid Blue 25 from Aqueous Media by Magnetic-SBA-15/CPAA Super Adsorbent: Adsorption Isotherm, Kinetic, and Thermodynamic Studies. *Pharma. Chem. J.* 5, 111–121. doi:10.1021/acs.jced.8b00474.s001

Jagtap, S., Yenkie, M. K., Labhsetwar, N., and Rayalu, S. (2012). Fluoride in Drinking Water and Defluoridation of Water. *Chem. Rev.* 112, 2454–2466. doi:10.1021/cr2002855

Kalsido, A. W., Meshesha, B. T., Behailu, B. M., and Alemayehu, E. (2021). Optimization of Fluoride Adsorption on Acid Modified Bentonite Clay Using Fixed-Bed Column by Response Surface Method. *Molecules* 26, 7112. doi:10.3390/molecules26237112

Koilraj, P., and Kannan, S. (2013). Aqueous Fluoride Removal Using ZnCr Layered Double Hydroxides and Their Polymeric Composites: Batch and Column Studies. *Chem. Eng. J.* 234, 406–415. doi:10.1016/j.cej.2013.08.101

Liu, C.-C., and Liu, J. C. (2016). Coupled Precipitation-Ultrafiltration for Treatment of High Fluoride-Content Wastewater. *J. Taiwan Inst. Chem. Eng.* 58, 259–263. doi:10.1016/j.jtice.2015.05.038

Liu, Y., Chen, Y., Li, Y., Chen, L., Jiang, H., Li, H., et al. (2022). Fabrication, Application, and Mechanism of Metal and Heteroatom Co-doped Biochar Composites (MHBCs) for the Removal of Contaminants in Water: A Review. *J. Hazard. Mater.* 431, 128584. doi:10.1016/j.jhazmat.2022.128584

Lu, H., Zhang, W., Yang, Y., Huang, X., Wang, S., and Qiu, R. (2012). Relative Distribution of Pb2+ Sorption Mechanisms by Sludge-Derived Biochar. *Water Res.* 46, 854–862. doi:10.1016/j.watres.2011.11.058

Mei, L., Qiao, H., Ke, F., Peng, C., Hou, R., Wan, X., et al. (2020). One-step Synthesis of Zirconium Dioxide-Biochar Derived from Camellia Oleifera Seed Shell with Enhanced Removal Capacity for Fluoride from Water. *Appl. Surf. Sci.* 509, 144685–144695. doi:10.1016/j.apsusc.2019.144685

Ndiaye, P. I., Moulin, P., Dominguez, L., Millet, J. C., and Charbit, F. (2005). Removal of Fluoride from Electronic Industrial Effluentby RO Membrane Separation. *Desalination* 173, 25–32. doi:10.1016/j.desal.2004.07.042

Oladoja, N. A., and Helmreich, B. (2014). Batch Defluoridation Appraisal of Aluminium Oxide Infused Diatomaceous Earth. *Chem. Eng. J.* 258, 51–61. doi:10.1016/j.cej.2014.07.070

Oladoja, N. A., and Helmreich, B. (2016). Calcium Aluminate-Diatomaceous Earth Composite as a Reactive Filter Material for Aqua Defluoridation. *J. Water Process Eng.* 9, 58–66. doi:10.1016/j.jwpe.2015.11.012

Ortiz-Ramos, U., Leyva-Ramos, R., Mendoza-Mendoza, E., and Aragón-Piña, A. (2022). Removal of Tetracycline from Aqueous Solutions by Adsorption on Raw Ca-Bentonite. Effect of Operating Conditions and Adsorption Mechanism. *Chem. Eng. J.* 432, 134428–134441. doi:10.1016/j.cej.2021.134428

Ozsvath, D. L. (2009). Fluoride and Environmental Health: A Review. *Rev. Environ. Sci. Biotechnol.* 8, 59–79. doi:10.1007/s11157-008-9136-9

Paudyal, H., Pangeni, B., Inoue, K., Kawakita, H., Ohto, K., Harada, H., et al. (2011). Adsorptive Removal of Fluoride from Aqueous Solution Using Orange Waste Loaded with Multi-Valent Metal Ions. *J. Hazard. Mater.* 192, 676–682. doi:10.1016/j.jhazmat.2011.05.070

Pillai, P., Dharaskar, S., Shah, M., and Sultania, R. (2020). Determination of Fluoride Removal Using Silica Nano Adsorbent Modified by Rice Husk from Water. *Groundw. Sustain. Dev.* 11, 100423–100430. doi:10.1016/j.gsd.2020.100423

Pintar, A., Batista, J., and Levec, J. (2001). Integrated Ion Exchange/Catalytic Process for Efficient Removal of Nitrates from Drinking Water. *Chem. Eng. Sci.* 56, 1551–1559. doi:10.1016/s0009-2509(00)00382-1

Piri, M., Sepehr, E., Samadi, A., Farhadi, K., and Alizadeh, M. (2020). Application of Diatomite for Sorption of Pb, Cu, Cd and Zn from Aqueous Solutions: Kinetic, Thermodynamic Studies and Application of Response Surface Methodology (RSM). *Water Environ. Res.* 93, 714–726. doi:10.1002/wer.1377

Sadhu, M., Bhattacharya, P., Vithanage, M., and Padmaja Sudhakar, P. (2021). Adsorptive Removal of Fluoride Using Biochar - A Potential Application in Drinking Water Treatment. *Sep. Purif. Technol.* 278, 119106–119117. doi:10.1016/j.seppur.2021.119106

Shen, J., and Schäfer, A. (2014). Removal of Fluoride and Uranium by Nanofiltration and Reverse Osmosis: A Review. *Chemosphere* 117, 679–691. doi:10.1016/j.chemosphere.2014.09.090

Tang, J. X., Zhu, Y. L., Li, M. X., Ma, S. L., Liu, Y., Wang, H. F., et al. (2020). Study on Adsorption Characteristics of Fluorine Ions in Water by Different Biochars. *Eco. Environ. Sci.* 29, 2270–2278. doi:10.16258/j.cnki.1674-5906.2020.11.015

Teng, S.-X., Wang, S.-G., Gong, W.-X., Liu, X.-W., and Gao, B.-Y. (2009). Removal of Fluoride by Hydrous Manganese Oxide-Coated Alumina: Performance and Mechanism. *J. Hazard. Mater.* 168, 1004–1011. doi:10.1016/j.jhazmat.2009.02.133

Wang, F., Wang, K., Muhammad, Y., Wei, Y., Shao, L., and Wang, X. (2019). Preparation of CeO2@SiO2 Microspheres by a Non-sintering Strategy for Highly Selective and Continuous Adsorption of Fluoride Ions from Wastewater. *ACS Sustain. Chem. Eng.* 7, 14716–14726. doi:10.1021/acssuschemeng.9b02643

Wang, J., Xu, W., Chen, L., Jia, Y., Wang, L., Huang, X.-J., et al. (2013). Excellent Fluoride Removal Performance by CeO2-ZrO2 Nanocages in Water Environment. *Chem. Eng. J.* 231, 198–205. doi:10.1016/j.cej.2013.07.022

Xu, L., Gao, X., Li, Z., and Gao, C. (2015). Removal of Fluoride by Nature Diatomite from High-Fluorine Water: An Appropriate Pretreatment for Nanofiltration Process. *Desalination* 369, 97–104. doi:10.1016/j.desal.2015.04.033

Yitbarek, M., Abdeta, K., Beyene, A., Astatkie, H., Dadi, D., Desalew, G., et al. (2019). Experimental Evaluation of Sorptive Removal of Fluoride from Drinking Water Using Natural and Brewery Waste Diatomite. *Process Saf. Environ. Prot.* 128, 95–106. doi:10.1016/j.psep.2019.05.052

Zhang, J., Ping, Q., Niu, M., Shi, H., and Li, N. (2013). Kinetics and Equilibrium Studies from the Methylene Blue Adsorption on Diatomite Treated with Sodium Hydroxide. *Appl. Clay Sci.* 83-84, 12–16. doi:10.1016/j.clay.2013.08.008

Zhao, N., Liu, K., Yan, B., Zhu, L., Zhao, C., Gao, J., et al. (2021). Chlortetracycline Hydrochloride Removal by Different Biochar/Fe Composites: A Comparative Study. *J. Hazard. Mater.* 403, 123889–123901. doi:10.1016/j.jhazmat.2020.123889

Conflict of Interest: The authors declare that the research was conducted in the absence of any commercial or financial relationships that could be construed as a potential conflict of interest.

frontiers | Frontiers in Chemistry

REVIEW
published: 21 June 2022
doi: 10.3389/fchem.2022.920676

Modelling Interfaces in Thin-Film Photovoltaic Devices

Michael D. K. Jones[1], *James A. Dawson*[2], *Stephen Campbell*[1], *Vincent Barrioz*[1], *Lucy D. Whalley*[1]* *and Yongtao Qu*[1]*

[1]Department of Mathematics, Physics and Electrical Engineering, Northumbria University, Newcastle Upon Tyne, United Kingdom, [2]Chemistry – School of Natural and Environmental Sciences, Newcastle University, Newcastle Upon Tyne, United Kingdom

Developing effective device architectures for energy technologies—such as solar cells, rechargeable batteries or fuel cells—does not only depend on the performance of a single material, but on the performance of multiple materials working together. A key part of this is understanding the behaviour at the interfaces between these materials. In the context of a solar cell, efficient charge transport across the interface is a pre-requisite for devices with high conversion efficiencies. There are several methods that can be used to simulate interfaces, each with an in-built set of approximations, limitations and length-scales. These methods range from those that consider only composition (e.g. data-driven approaches) to continuum device models (e.g. drift-diffusion models using the Poisson equation) and *ab-initio* atomistic models (developed using e.g. density functional theory). Here we present an introduction to interface models at various levels of theory, highlighting the capabilities and limitations of each. In addition, we discuss several of the various physical and chemical processes at a heterojunction interface, highlighting the complex nature of the problem and the challenges it presents for theory and simulation.

Keywords: kesterite Cu_2ZnSnS_4 thin films, CZTSSe, CZTS, interface, modelling, photovoltaic, thin-film, device

OPEN ACCESS

Edited by:
Syed Mubeen Jawahar Hussaini, The University of Iowa, United States

Reviewed by:
Malkeshkumar Patel, Incheon National University, South Korea
Jafar Iqbal Khan, King Abdullah University of Science and Technology, Saudi Arabia

***Correspondence:**
Lucy D. Whalley
l.whalley@northumbria.ac.uk
Yongtao Qu
y.qu@northumbria.ac.uk

Specialty section:
This article was submitted to Electrochemistry, a section of the journal Frontiers in Chemistry

Received: *14 April 2022*
Accepted: *27 May 2022*
Published: *21 June 2022*

Citation:
Jones MDK, Dawson JA, Campbell S, Barrioz V, Whalley LD and Qu Y (2022) Modelling Interfaces in Thin-Film Photovoltaic Devices. Front. Chem. 10:920676. doi: 10.3389/fchem.2022.920676

1 INTRODUCTION

Energy converters, such as solar cells, re-usable batteries and fuel cells, are a key ingredient for achieving the target of net-zero carbon by 2050. With less than 30 years until this deadline, there is a strong emphasis on accelerating the development of new materials and technologies with better performance (for example, batteries with higher energy densities) or allowing access to new markets (for example, product-integrated photovoltaics). Computational modelling can be used to predict device performance without synthesis, fabrication or characterisation, guiding experimental efforts to pursue only the most promising new designs and ultimately reducing the time from materials discovery to technology deployment. (Tabor et al., 2018).

Photovoltaic (PV) cells are generally semiconductor heterostructures consisting of multiple material components. In thin-film PV devices each component has a thickness ranging from a few nanometres to tens of micrometres—a typical example of a thin-film PV device structure is shown in **Figure 1**. Commercialised thin-film materials include CdTe, $CuIn_{1-x}Ga_xSe_2$ (CIGS), and amorphous thin-film silicon (a-Si), whilst perovskite-silicon tandem cells are targeted for commercial production by the end of 2022. There is also research activity around an array of materials with potential for commercialisation, including Cu_2ZnSnS_4 (CZTS), (Liu et al., 2020), Sb_2Se_3, (Liu et al., 2020), SnS, (Cho et al., 2020), Cu_2O, (Wei et al., 2012), and $AgBiS_2$. (Ju et al., 2020).

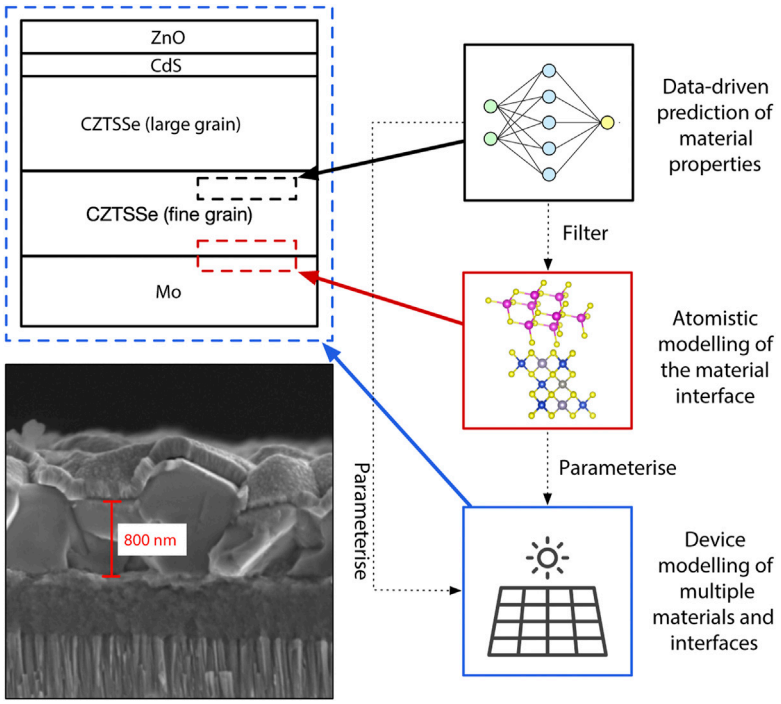

FIGURE 1 | Image and schematic outlining the multi-layered structure of a typical $Cu_2ZnSn(S,Se)_4$ (CZTSSe) solar cell and the various approaches to interface modelling. The bottom left image is a Scanning Electron Microscope (SEM) image of a CZTSSe thin film photovoltaic device fabricated from nanoparticle inks. The length scale is indicated in red. The top left is a schematic of the same device, shown for clarity. The three boxes on the right outline three complimentary approaches to interface modelling: 1) (black boxes) data-driven approaches for predicting the properties of a single interface material; 2) (red boxes) atomistic modelling of the interface between two materials; and 3) (blue boxes) continuum modelling of the complete device, including multiple materials and interfaces. The dotted arrows indicate how these models relate to one another: lower accuracy data-driven predictions can be used as a initial filtering step before higher accuracy atomistic models are applied, and both of these approaches can be used to parameterise device models. The solar cell icon is a resource downloaded with permission from Flaticon.com.

The interfaces in a PV device are particularly important as they determine the carrier dynamics and so the overall device performance. (Edward et al., 1992; Franciosi and Van de Walle, 1996; Fritsche et al., 2001; Fritsche et al., 2005; Jaegermann et al., 2009; Li and Jen, 2022). To understand why this is one must first have a basic understanding of the processes underlying PV performance. Consider, for example, a solar cell with a planar structure: 1) a photon is absorbed and an exciton is created; 2) the exciton separates into an electron and hole; 3) the electron and hole travel through the absorber material; and 4) the electron and hole are extracted through an interface to their respective contact materials. The contact materials may be a metal contact, a buffer layer, a window layer, or an electron/hole transport layer. In addition, for polycrystalline materials there are additional interfaces in the form of grain boundaries. Before successfully reaching an external circuit to do useful work a charge carrier will need to traverse multiple interfaces.

There are several examples where interface engineering has improved the light-to-electricity efficiency of a device. To take one example, consider the development of CdTe solar cells. Most devices used a CdS buffer layer between the absorber material and transparent conducting oxide (TCO) until it was demonstrated in 2016 that replacing this with $Mg_xZn_{1-x}O$ led to improved performance. (Kephart et al., 2016). The reason for this improved performance is threefold and demonstrates the variety of functions an interface material must fulfil: the electronic band alignment with the TCO can be optimised with the proportion of Mg content, $Mg_xZn_{1-x}O$ allows for a higher temperature deposition of the CdTe which results in larger grain sizes and improved charge transport, and $Mg_xZn_{1-x}O$ has a larger optical band gap for better ultraviolet light transmission. (Kephart et al., 2016).

The rate of charge transport across an interface is primarily dependant on the energy band alignment of the constituent materials and the defects existing at the interface, so these are key considerations when optimising device designs. However there are additional considerations including chemical compatibility, heat transfer, (Sutanto et al., 2020), the mechanical stability provided by the interface layer and the rate of intended, or unintended, ion transport. (Prabhakar and Jampana, 2011). Whilst accurate computational predictions of the properties and processes within a single bulk material are now well established, (Oba and Kumagai, 2018), capturing the complex physics and chemistry at the interface between two materials remains an on-going challenge for theory and computation. (van der Giessen et al., 2020). In particular, linking microscopic structures and processes with material function is an inherently multi-scale problem that requires a range of approaches (**Figure 1**).

For materials design and optimisation where the structure of a material (or materials) is unknown there are a growing number of

studies using the large amount of materials data that has already been generated and is readily available, or that can be generated using high-throughput-computing. For example, machine learning models have been used to predict thermodynamically stable quaternary oxides (Davies et al., 2019) and derive accurate force fields for molybdenum metal. (Chen et al., 2017). In the context of materials discovery, this data-driven approach can be used as a lower-cost filter before applying more expensive *ab-initio* models to the candidate interface material.

For modelling microscopic processes at the interface between two materials there are a range of atomistic simulation techniques based on either quantum chemical techniques or the equations of classical mechanics. These can also be used to calculate interface and bulk parameter values for device models. The typical size of unit cell used for interface simulations will depend on the process being modelled, the level of theory used and, unavoidably, the computer time that is available. The lower limit is on the order of hundreds of atoms, which has until recently restricted atomistic interface modelling to using classical potentials for describing the atom-atom interactions. However with recent research investment into high-performance-computing and the development of more computationally efficient codes, (Nakata et al., 2020; Prentice et al., 2020; Ratcliff et al., 2020), higher accuracy *ab-initio* quantum chemical predictions for systems with hundreds or thousands of atoms are now possible.

For predicting performance at the device level, continuum-scale models—most often Poisson-drift-diffusion simulations—are used. However capturing the full complexity of the processes at an interface in a numerical or analytical model at the device-level is not feasible. Instead it is most often assumed that the rate of charge transport is determined by the band offset energy between two materials and parameters (for example, the surface recombination velocity) which incorporate other microscopic physical effects. These values can be measured by experiment, calculated using atomistic simulations, or predicted using data-driven approaches, providing a straight-forward approach to multiscale modelling.

The focus of this review is interface modelling in thin-film PV devices. In particular, we are concerned with modelling planar interfaces between inorganic or hybrid organic-inorganic materials, rather than the bulk heterojunctions typically found in organic photovoltaic (OPV) devices or at grain boundaries. We do not consider mesoscale models that are designed to bridge between the micro- and macro-scale as although there are a limited number of applications in the context of hybrid perovskite photovoltaics, (Bahrami et al., 2021), these models have been most widely used within the OPV community where device performance is highly sensitive to the mesoscopic structuring of the bulk heterojunction.

We begin the review by introducing the key concepts underlying energy band alignment, which is the most important consideration for the design and optimisation of PV devices. We then go on to identify the other key features of an ideal PV interface material. In the second half of the review we introduce several approaches for modelling interfaces in PV devices: 1) data-driven methods for interface materials discovery and low-cost predictions of material performance; 2) atomistic interface models for a higher-accuracy understanding of processes at the microscale; and 3) continuum device models for understanding the combined effects of multiple interfaces at the device level.

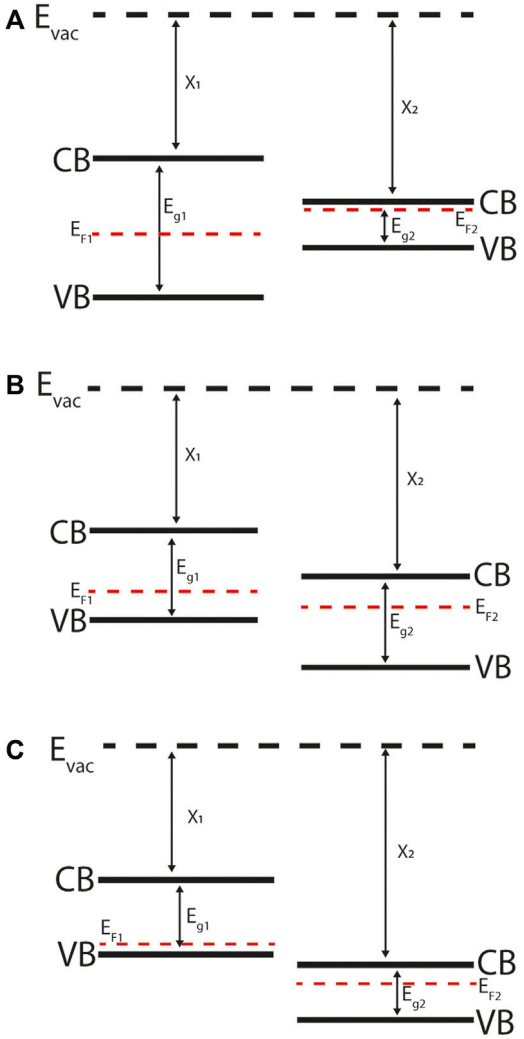

FIGURE 2 | Energy band diagrams of abrupt semiconductor-semiconductor heterojunctions: **(A)** Straddling gap (Type-I), **(B)** Staggered gap (Type-II), **(C)** Broken gap (Type-III). Note that the materials are not in contact or in equilibrium with one-another, as indicated by the mismatch between their Fermi levels (E_F). CB is the conduction band (minimum) and VB is the valence band (maximum) referenced to the vacuum level E_{vac}. For quantitative predictions of band alignment the electron affinity (χ) and band gap (E_g) are used in the Anderson rule, which assumes that the vacuum level is constant.

2 ENERGY BAND ALIGNMENT IN PHOTOVOLTAIC DEVICES

Electron energy level differences at an interface play a key role in a solar cell device. Their relative alignment describes built in electric fields that occur across material junctions, indicate the

preferred direction of drift currents and also suggest potential tunnelling mechanisms. This all gives a greater insight and understanding to the workings of a device and the role the interface plays.

Semiconductor-semiconductor interfaces can be characterised in two groups: homojunctions and heterojuctions. Homojunction describes an interface where the two neighbouring bulk materials are the same, though the materials are often differentiated through dopant species or densities. On the contrary heterojunctions are comprised of two different materials. The latter comprise the bulk of this review as they are the most well-studied interface type in thin-film PV devices. Later in this section a discussion relating to metal-semiconductor junctions, and their classification as Schottky or ohmic is presented.

Our understanding of the interfaces within a device is very often summarised as an energy band diagram. Constructing energy band diagrams allows the observer to represent band-edge electron or hole energy levels, electric fields and current flow in the dimensions of energy and one-dimensional space; **Figures 2**, **6** are examples of energy band diagrams that will be discussed in more detail later in the paper. Many of the interesting features in energy band diagrams are at the interface region between two materials. The relative alignment at the interfacial regions of these diagrams can represent a range of features that are of importance in the design and fabrication of semiconductor devices, including: charge separation characteristics, interface bonding dynamics, interface trap states and depletion region widths.

Differences in the conduction band minimum (CBM) and valence band maximum (VBM) of neighbouring materials at an abrupt semiconductor-semiconductor heterojunction interface lead to band offsets. The type of band discontinuity depends on the electronic structure of the materials and are commonly grouped as: straddling gap (also known as Type I, **Figure 2A**), staggered gap (Type II, **Figure 2B**), and broken gap (Type III, **Figure 2C**). (Kroemer, 2001) Straddling gap junctions have conduction and valence band offsets of opposite sign, so that the lower CBM and higher VBM occurs in the same material. This structure promotes two-carrier processes such as radiative recombination as it is energetically favourable for the electrons and holes to occur in the same material. Staggered gap junctions have conduction and valence band offsets of the same sign, so that the lower CBM occurs in one material and higher VBM occurs in the other material, with an energy separation between the two. This structure promotes separation of electrons and holes, and so is of particular relevance to PV devices where charge separation underlies voltage generation. In broken gap junctions the CBM in one material drops below the VBM in another material and there a direct tunnelling mechanism across the interface.

For quantitative estimates of band offsets at semiconductor junctions the electron affinity rule introduced by (Anderson, 1960) is commonly used. This simple rule allows the band offset of the conduction band minima (ΔE_c) and valence band minima (ΔE_v) to be calculated from the bulk properties (band gap E_g and electron affinity χ) of the neighbouring materials. For example, consider **Figure 2A** where there is a straddling gap junction. In this case the band offsets are given by:

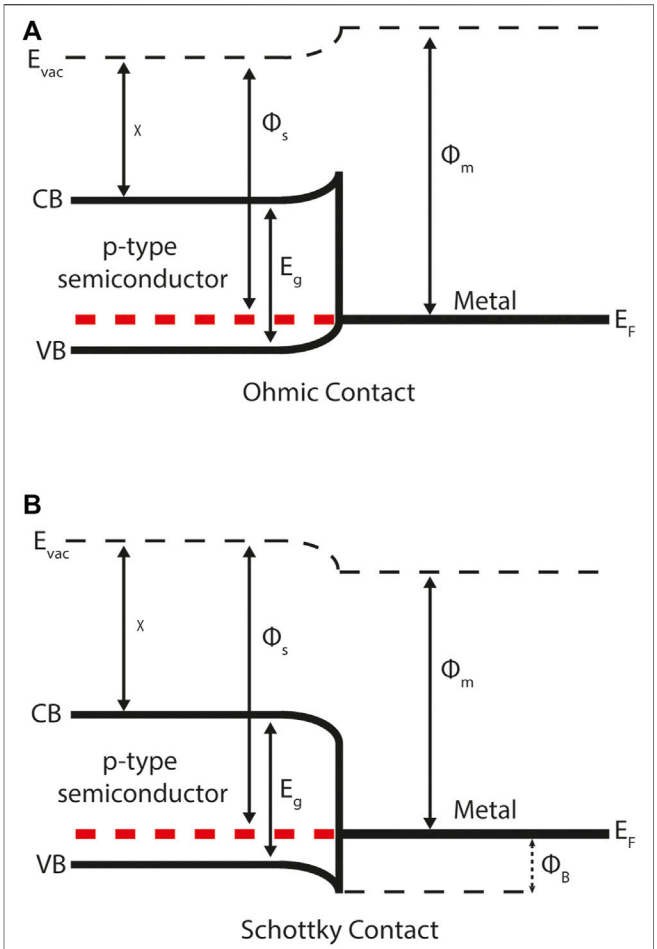

FIGURE 3 | Energy band diagrams for a semiconductor-metal contact demonstrating: **(A)** ohmic behaviour **(B)** Schottky behaviour. CB and VB represent the conduction band (minimum) and valance band (maximum) respectively. Φ_B describes the Schottky barrier height to majority carrier flow (in this case holes) across the junction. The Schottky-Mott rule can be used to calculate Φ_B from the metal work function Φ_m and semiconductor electron affinity χ (both defined relative to the vacuum level E_{vac}) and semiconductor band gap E_g. In equilibrium the Fermi-level E_f is constant across the semiconductor-metal interface.

$$\Delta E_c = \chi_1 - \chi_2 \tag{1}$$

$$\Delta E_v = \left(E_{g1} - E_{g2}\right) - \Delta E_c. \tag{2}$$

Anderson's model is based on the assumption that the vacuum level is consistent when forming junctions between two materials. This rule is often used to calculate the band offsets, followed by Poisson's rule to calculate the shape of the band bending that occurs upon carrier density equilibration across the heterojunction interface.

Semiconductor-metal interfaces are categorised differently given the absence of an electronic band gap in metals. They are classified as either Schottky or ohmic, depending on the difference between the semiconductor and metal work functions (**Figure 3**). For a p-type semiconductor with a work function greater than the metal, mobile charge will diffuse from the

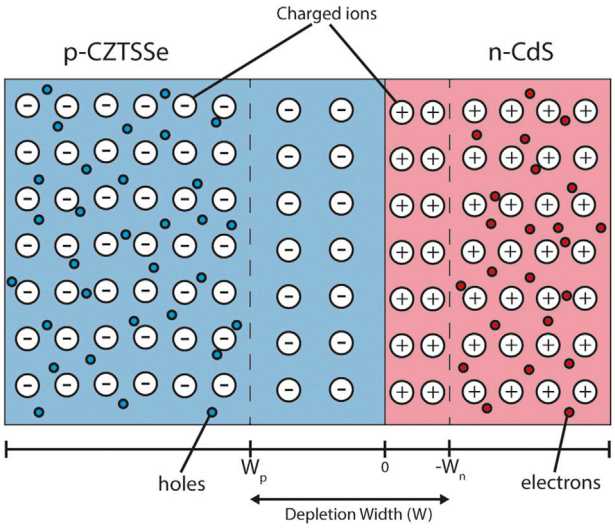

FIGURE 4 | Depletion region schematic of the CZTSSe/CdS junction. The blue and red colouring represent p-type CZTSSe and n-type CdS respectively. The static charged ions—responsible for material doping—are also drawn. The depletion region does not contain any mobile charges. The black bar below denotes the material interface point (0), p-type depletion width (W_p) and n-type depletion width (W_n).

semiconductor into the metal and a Schottky contact will form. The resulting electrostatic field impedes majority carrier flow across the junction. For a p-type semiconductor that has a work function less than the metal an ohmic contact will form. Ohmic contacts promote majority carriers over the junction and are thus the ideal scenario for majority carrier extraction at an electrical contact.

The Schottky-Mott rule for semiconductor-metal interfaces is used to estimate Schottky barrier height Φ_B from the metal work function Φ_m, semiconductor electron affinity χ and band gap E_g. (Francis Mott, 1939) For example, consider **Figure 3** where there is a p-type semiconductor in contact with a metal. In this case the Schottky barrier height is given by:

$$\Phi_B = \chi + E_g - \Phi_m. \tag{3}$$

It is important to note that both the electron affinity rule and Schottky-Mott rule can give only very rough estimates for band offsets as they ignore any chemical bonding, defect formation and electrical polarisation at the interface. These are highly idealised model that are only strictly valid in the limit of a large vacuum separation between the two materials.

For both semiconductor-semiconductor and semiconductor-metal contacts in thermodynamic equilibrium (where there is no illumination or external bias) the Fermi-level must be continuous across the interface. Physically this means that the electron or hole carriers will diffuse across the junction as a result of a concentration gradient. If the carriers were charge neutral this process would continue until there is a uniform distribution of carriers throughout the device. However, the carriers do carry charge and so they diffuse across the junction and leave behind charged ions. The charged ions form an electric field which eventually prevents further carrier diffusion. As a result of this process the conduction and valence bands exhibit band bending near the interface (**Figure 3**). There is no band bending in metals due to high concentrations of mobile charge carriers that can respond to the formation of an electric field.

For a semiconductor-semiconductor p-n junction in equilibrium the majority carriers (electrons in the n-type region and holes in the p-type region) diffuse across the junction as a result of their respective concentration gradients. This region at the interface is known as the depletion region (**Figure 4**) as it contains a built-in electric field which removes any free charge carriers. The width of the depletion region can be calculated using Poisson's equation and is primarily determined by the doping density and dielectric permittivity of the material.

3 WHAT MAKES THE IDEAL PHOTOVOLTAIC INTERFACE MATERIAL?

Any interface model should be designed towards capturing the physical and chemical processes relevant to the application in question. In this paper we are considering the operation of a solar cell, and in the previous section we have considered the band alignment that is required for the correct distribution of charges in a PV device. In addition to this there are a host of other features required for optimised performance at a PV device interface. We will use a hole-transporting material at the metal-CZTS interface as a motivating example, although the features identified will, in many cases, be transferable to a range of applications and energy harvesting materials and are not solely limited to CZTS. In line with the majority of the literature, we will use CZTS to denote any

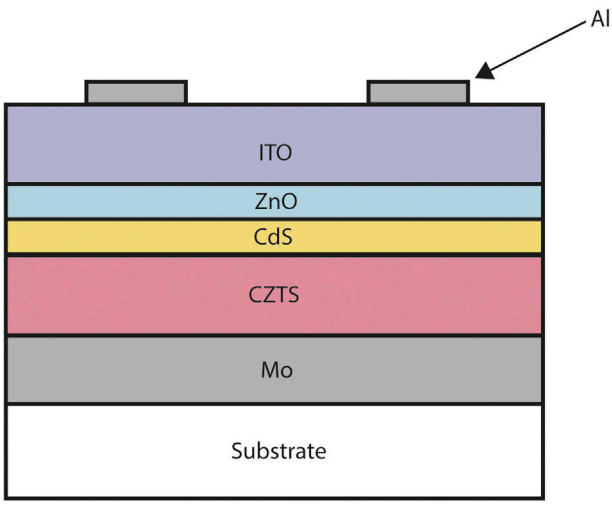

FIGURE 5 | Typical copper zinc tin sulfide (CZTS) solar cell cross-section. From top to bottom: nickel and aluminium front contact grid, indium tin oxide (ITO), intrinsic zinc oxide (ZnO), cadmium sulfate (CdS), copper zinc tin sulfide (CZTS), molybdenum (Mo), soda lime glass substrate. The layer widths are not to scale.

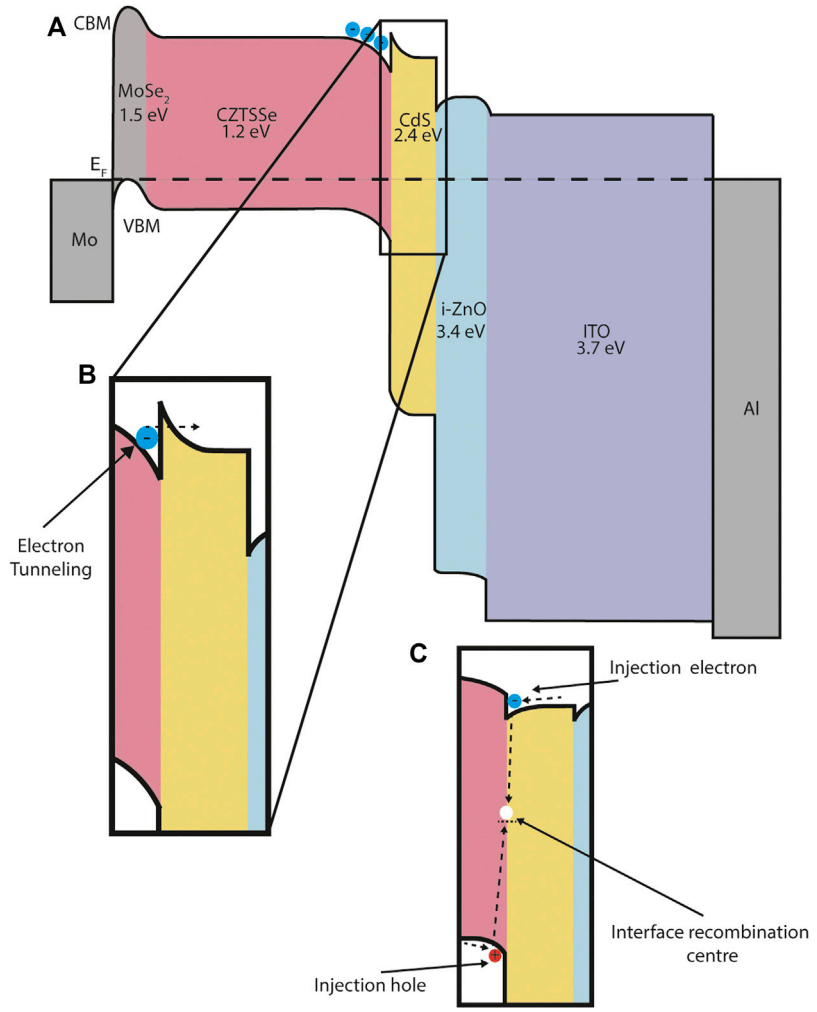

FIGURE 6 | CZTSSe energy band diagram schematic. **(A)** The main panel shows the band alignment across the device. CBM and VBM represent conduction band minimum and valence band maximum respectively. The Fermi-level E_F is denoted by a dashed line. The band gap for each material is given below each chemical formula. All material parameter data is taken from a previously published SCAPS simulation (Campbell et al., 2020). **(B)** Photocurrent resistance at a junction can produce a barrier to electron flow and reduce short circuit current, depending on the energy barrier height. For the CZTSSe/CdS interface a barrier less than 0.4 eV enables transport through a quantum tunnelling mechanism and is beneficial to device performance. **(C)** Alternative cliff-like band alignment at the CZTSSe/CdS interface. In this case injection electrons or holes (the diffusion current) are impeded by the large offset in available energy states and recombine at the interface. This causes a decrease in the reverse saturation current and a reduction in open-circuit voltage and fill factor.

compound of the form $Cu_2ZnSnS_xSe_{4-x}$ where x can take any value between 0 and 4.

CZTS thin film devices are based on the more established CIGS architecture in which the back contact material is molybdenum metal (**Figure 5**). As CZTS is a p-type material, the majority carriers are holes and it is these that must be extracted at the back contact. Molybdenum satisfies some qualities of a 'good' back contact: it maintains stability at high processing temperatures (Zoppi et al., 2011; Dai et al., 2014) and it has excellent adhesion with the substrate soda lime glass and CZTS absorber layer. However this picture is complicated through the sulfurization/selenisation process used to increase the efficiency of CZTS solar cells. During this process the Mo/CZTS structure is annealed on a substrate in a high temperature tube furnace (Qu et al., 2016a) and a barrier layer of $Mo(S,Se)_2$ develops. (Qu et al., 2016b; Xu et al., 2018). The impact of this unintended barrier layer on device performance is still under debate in the literature, with some studies indicating that the formation of $Mo(S,Se)_2$ can increase the ohmic nature of the back contact (**Figure 6**) and produce a contact with lower resistance (Salomé et al., 2010; Wu et al., 2012) providing the thickness of the $Mo(S,Se)_2$ is not too large.

3.1 Thermodynamic Stability

Thermodynamic stability against decomposition into competing phases is of primary importance, both in the design of bulk and interface materials. The key quantity here is the Gibbs free energy, as this is the value that is minimised for systems in

thermodynamic equilibrium. (Jackson and Walsh, 2014). For an accurate understanding of stability the Gibbs free energy for all competing reactions, and at temperatures and pressures relevant for synthesis and device operation, should be considered.

Molybdenum is a commonly used contact material as it can withstand the high temperatures (500–600°C) required for annealing and, as such, provides more flexibility for device design. In contrast, oxides such as MoO_x and NiO_x have several decomposition pathways at high temperature and so require deposition in a superstrate configuration after the high temperature anneal.

In addition to establishing the thermal stability of a single material, we must also consider competing reactions at the interface. These reactant and products formed at an interface can incorporate species from each of the contact materials, widening the chemical space to be considered. For example, Scragg *et al.* have described the decomposition of $Cu_2ZnSnS(e)_4$ at high temperatures, both without (Scragg et al., 2012a) (**Eq. 4**) and with (Scragg et al., 2012b) [**Eq. (5)**] the presence of molybdenum.

$$2Cu_2ZnSnS(e)_4 \rightarrow 2Cu_2S(e) + 2ZnS(e) + 2SnS(e) + 2S(e) \quad (4)$$

$$2Cu_2ZnSnS(e)_4 + Mo \rightarrow 2Cu_2S(e) + 2ZnS(e) + 2SnS(e) + MoS(e) \quad (5)$$

The free energy change of the reaction with molybdenum [**Eq. (5)**] is calculated as -100 kJ and -150 kJ at 550°C, for $Cu_2ZnSnSe_4$ and Cu_2ZnSnS_4 respectively. These large negative free energies indicate that, at this temperature, the decomposition of CZTS(e) is thermodynamically favourable and that the CZTS(e)/Mo interface is unstable. This demonstrates why molybdenum thin films as a back contact have demonstrated less favourable characteristics, compared to CIGS, when paired with CZTS. It also highlights the importance of the processing techniques used to synthesise high-quality thin-films; in this case high processing temperatures are needed for the improvement of CZTS crystalline structure.

3.2 Matched Lattice Parameters

Strain at the interface between two materials is a potential source of instability which can impact on the defect, electrical and optical properties of each material. (Wu et al., 2021). When the strain is below a particular threshold value the material can alleviate the strain through defect formation, which then provide potential sites for charge capture and recombination. Above this value the interface can become incoherent with weak chemical bonding across the boundary. (Butler et al., 2016). The interfacial strain originates primarily from two types of mismatch: mismatch between the lattice constant of each material, and mismatch between the thermal expansion coefficient (α) of each material.

Lattice mismatch and strain related defects have been of particular importance in the development of high-efficiency III-V multijunction solar cells. With conversion efficiencies now approaching 50%, these cells are fabricated using epitaxial growth and careful control of the atomic-scale structure. (Li et al., 2021). A pre-requisite for good performance is that each absorber layer is lattice-matched to its neighbours, which is the predominant reason that the absorber layers in the highest-efficiency multijunction devices consist of closely related materials from the III-V compounds, such as GaAs, GaInP and GaInAs.

Various models have been introduced to rationalise the strain formed at the boundary between two materials and to identify alternative contact materials. For materials with the same crystal structure (for example III-V compounds in the zincblende structure) a comparison of the lattice parameters will suffice, whilst for materials with different crystal structures the comparison requires more subtlety. In 1984 Zur and McGill developed a reduction scheme based on the primitive lattice vectors of each material, (Zur and McGill, 1984), which has been more recently applied to a screening study for hybrid perovskite contact layers, (Butler et al., 2016), and implemented in the ElectronicLatticeMatch code. (Butler, 2017). To account for chemical bonding, which is neglected in the Zur and McGill scheme, more advanced theories that account for the atomic species on each lattice site are required. (Park et al., 2018).

Matched thermal expansion coefficients are also important due to the high annealing temperatures often used to enhance crystallinity and reduce defects in thin film PV; for example, $CsPbI_3$ and CZTS are typically annealed at temperatures up to 330°C and 600°C respectively. These high temperatures result in a large temperature gradient during cooling to ambient temperatures. If combined with highly mismatched thermal expansion coefficients, a large thermally-induced strain results. (Wu et al., 2021).

In contrast to the lattice matching techniques introduced above, recent research has also harnessed the lattice mismatch between a material and substrate. This mismatch is used to facilitate a lift-off process, where the active material(s) are synthesised on a rigid substrate and then removed using physical, chemical or thermal methods. (Liu et al., 2021). For thermal lift-off processes the substrate is selected to have a different thermal expansion coefficient. When cooling a large stress field develops which is alleviated by the development of cracks parallel to the surface, and which eventually results in delamination of the active material. (Dross et al., 2007).

3.3 Energy Band Alignment

As already discussed, energy band alignment is also of critical importance, as this determines the rate of charge transport across an interface. At a metal-semiconductor junction the key quantity is the Schottky barrier height which relates to the difference in energy between the metal and semiconductor work functions. A contact is considered ohmic when the Schottky barrier height is non-existent or small enough to allow for unhindered transport of the electrons (for n-type materials) or holes (for p-type materials) across the interface.

At the CZTS back contact, there is evidence that the formation of a $MoS(e)_2$ layer creates an ohmic contact with the CZTS layer. However the overrall PV performance may be reduced due to increased recombination of electron and hole charge carriers at the $Mo/MoS(e)_2$ interface. The former observation is in line with research for closely related CIGS-based technologies, where it has

also been suggested that MoS_2 improves the ohmic nature of the Mo/CIGS back contact. (Wada et al., 2001; Polizzotti et al., 2013). However if the MoS_2 layer is too thick this will be detrimental to device performance, resulting in a reduction in V_{OC} and an increase in the series resistance. (Shin et al., 2012; Xu et al., 2019).

For CZTS an additional complication is the trade-off between thermodynamic stability of CZTS and the thickness of the $MoS(e)_2$ layer. To prevent the degradation of CZTS through the loss of 2S(e) during high-temperature annealing, over-pressures of S(e) are used. However these high gas pressures cause the formation of a thicker layer of $MoS(e)_2$ as a by-product.

Another important interface in CIGS and CZTS devices is the interface with the buffer layer, most commonly CdS. (Courel et al., 2014; Courel et al., 2015). There are two main types of conduction band offset (CBO) that occur at this interface: a positive, spike-like band alignment, where the buffer layer CB is higher than that of the absorber layer, and a negative, cliff-like, where the buffer layer conduction band (CB) is lower than that of the absorber layer (**Figure 6**).

In CIGS the most optimum CBO at the CIGS/CdS interface is, counter-intuitively, spike-like rather than cliff-like, providing that the barrier height is below 0.4 eV. This barrier allows electrons to tunnel through into the CdS, but does not produce a barrier to injection electrons under forward bias. The quantum tunnelling mechanism is described in more detail in **Section 6.1**. For cliff-like junctions, accumulated injection electrons under forward bias result in an increased recombination mechanism at the interface and a lower V_{OC}. A spike-like energy barrier greater than 0.4 eV forms a significant barrier to current flow resulting in a dramatic decrease of the short-circuit current. (Minemoto et al., 2001; Campbell et al., 2020).

3.4 Electrically Benign Defect Formation

The formation of material defects, whether in the bulk or at interfaces, cannot be avoided in most materials. (Walsh and Zunger, 2017).

Furthermore, these defects can have serious unwanted implications in a PV device. Of particular concern are electrically active defect states that can capture electrons and/or holes, as these can lead to a reduction in the open-circuit voltage (V_{OC}) and fill factor (FF), through processes such as Fermi-level pinning or non-radiative recombination.

The band bending model introduced in **Section 2** effectively breaks down when we start to introduce material imperfections at the semiconductor-metal interface (**Figure 6C**). There are two possibilities that can arise at a metal-semiconductor interface: metal-induced states and semiconductor-vacuum states. In both instances electrically-active defect levels can be created within the semiconductor band gap, but each are associated with a different mechanism. In the former the states are created upon contact with the metal and are induced, for example, by lattice strain or chemical bonding. The latter are present on the surface of the semiconductor interface without contact to other materials.

Defect states in the band gap can cause a phenomenon known as Fermi-level pinning. Fermi-level pinning occurs when the interface defect states trap charge carriers that diffuse from the metal into the semiconductor. This effectively isolates the semiconductor from the effects of the metal and the semiconductor bands are aligned (pinned) relative to the charge neutrality level (CNL) of the interface defect states. This process adjusts the potential and electrostatic field at the interface, which in turn adjusts carrier transport across the interface. (Dimoulas et al., 2006).

In Ge-metal contacts Fermi-level pinning is a strong limiting factor in depositing contact grids with ideal electrical behaviour. The charge neutrality level (CNL) in Ge is situated close to the valence band (0.09 eV above E_V), so that most acceptor states at the interface are filled at ambient temperature. (Dimoulas et al., 2006). As such, the Schottky barrier height that forms at this interface shows weak dependence on the particular metal used for contact to the electrical circuit. This is confirmed by a later study revealing that metal/*p*-Ge and metal/*n*-Ge junctions have ohmic and Schottky characteristics respectively, and both display a strong degree of Fermi-level pinning. (Nishimura et al., 2007).

Defects at the CZTS/CdS and $CZTS/MoS(e)_2$ interfaces are abundant due to the low formation energies required for exchanging ion species of the same type (in this case, sulfur or selenium) across an interface. In addition, Cu and Zn have comparable ionic radii resulting in low formation energies for Cu_{Zn} and Zn_{Cu} antisite defects in CZTS. This is compounded by the high annealing temperatures required for the growth of high-quality CZTS grains. (Chen et al., 2013). A large accumulation of antisite defects at the interface results in insufficient type inversion (the majority carrier being the opposite of its host layer) and weak band bending as an effect of Fermi-level pinning, whereby the Fermi-level is pinned close to the valence band at the interface. (Yuan et al., 2015). Cu-Zn disorder is also associated with band-tailing, where the measured band gap is less than that expected for the perfect bulk material. This fluctuation is dependent on the chemical purity of the precursor used to synthesise CZTS, and so the density of defects that are expected to be present. (Campbell et al., 2019).

Most studies of interfacial defects in CZTS solar cell devices focus on the CZTS/CdS or $CZTS/MoS(e)_2$/Mo interfaces. (Kaur et al., 2017; Qi et al., 2017; Suryawanshi et al., 2017; Campbell et al., 2018; Kim J et al., 2020). Defects that are particularly detrimental to performance are observed at the CZTS/CdS interface, where a high concentration of defects results in cliff-like band alignment and high non-radiative electron-hole recombination rates. This is also observed at the CIGS/CdS interface. (Kaur et al., 2017).

In addition to defect formation at semiconductor-semiconductor and semiconductor-metal heterojunctions, CZTS, CIGS and halide perovskite thin films are particularly prone to the development of grain boundary (GB) defects. (Yan et al., 2007; Li et al., 2011; Park et al., 2019). Not all GB defect formation is problematic; for example there is evidence that GBs in CIS-based materials are beneficial to device performance. (Yan et al., 2007). In contrast, the defect states associated with GBs in CZTSe are located in the band gap and as such provide sites for charge trapping and recombination. (Li et al., 2011). Similarly, the GBs in halide perovskite materials are detrimental to device performance in that they provide energetically favourable sites

for the formation of iodine interstitial defects, which in turn act as a site for charge trapping and recombination. (Park et al., 2019).

3.5 Favourable Ion Transport

Ion transport, when compared to electronic transport, is not as central to the functioning of a solar cell. However it can still influence the performance of a device through material doping and charge accumulation. For some materials, such as CZTS and CIGS, ion diffusion can increase the cell performance. In others, such as the halide perovskites, ion migration can lead to decreased performance. Examples for both extremes will be given in this section.

CZTS based solar cells are often fabricated on a soda lime glass (SLG) substrate, which primarily provides mechanical support to the cell. This results in sodium from the SLG also diffusing through the device into the $MoSe_2$, Mo and CZTS layers, leading to a notable improvement in the conductivity of the CZTS layer. (Prabhakar and Jampana, 2011). In a study comparing SLG to other substrates, the carrier concentration in CZTS increases by an order of magnitude (6.1×10^{16} to $35.4 \times 10^{16} cm^{-3}$), leading to a significant increase in conductivity (from 41.2 to 58.4 Ωcm^{-1}). (Prabhakar and Jampana, 2011). The underlying reasons for this increased carrier concentration has been examined using first-principles calculations. Wei and Zunger determined that sodium on a copper site (Na_{Cu}) results in an injection of holes into the system, increasing the hole density and thus the conduction of the CZTS p-type absorber layer. Sodium intercalation has also been associated with an increase in crystallite size, reducing the grain boundary area which in turn reduces the number of locations for non-radiative carrier recombination. (Prabhakar and Jampana, 2011). This same relationship has been observed in CIGS films fabricated on soda lime glass substrates. (Contreras et al., 1998).

Another source of beneficial ions in a CZTS cell is at the molybdenum rear contact. During the sulfurisation/selenisation process molybdenum is exposed to temperatures between 500–600°C, at which the molybdenum crystal structure should be relatively unchanged. However there is a clear temperature-dependent diffusion of molybdenum into the CZTS layer, with sulfurisation at 600°C leading to a more Mo-rich CZTS interfacial layer and PV efficiencies five times greater than materials formed *via* sulfurisation at 500°C. These studies demonstrate the importance of contact materials being able to maintain a stable crystal structure whilst still allowing beneficial ion diffusion throughout the device.

On the other hand, ion diffusion in perovskite-based PV negatively affects stability, performance, and effective working lifetime. Hybrid halide perovskites (ABX_3) are categorised as mixed conductors meaning they possess both electronic (Leijtens et al., 2015a) and ionic conductivity, (Eames et al., 2015; Egger et al., 2015; Yang et al., 2015), a phenomenon which has been extensively studied in recent years. (Xiao et al., 2015; Xu et al., 2015; Thomas et al., 2016). Ion transport in these materials is the primary contributing mechanism for I-V hysteresis (Meloni et al., 2016) and poor thermal stability, (Leijtens et al., 2015b; Zhao et al., 2016), leading to performance degradation over time. (Leijtens et al., 2015c). These materials also display a coupling between electrical and ionic behaviours, with increasing light intensity causing a reduction in the activation energy for ion migration. (Zhao et al., 2017).

In this section we have outlined several properties and processes at the interface that impact on device performance. We note here that this is a challenge not only for materials design, but also for materials process engineering. For example, to reduce the concentration of electrically active point defects various strategies have been developed: selecting high-quality precursors for materials synthesis, (Campbell et al., 2019), incorporating additional dielectric passivation layers, (Kim et al., 2017), or using post-deposition annealing. (Fritsche et al., 2005; Jaegermann et al., 2009).

We also note that our 'wish-list' for an ideal PV material is somewhat incomplete and could be extended to include other factors we do not mention here. This includes thermal transport properties (the rate of heat transfer), mechanical properties (elastic modulus and deformation) and optical properties (band gap and absorption coefficients). On the prior point we draw the readers attention briefly to **Figure 6**, which shows a series semiconductor materials with increasing band gap as we move between the back metal contact (Mo) and the front metal contact (Al). Increased optical band gaps result in increased ultraviolet light transmission and more light energy available for conversion within the absorber material.

In the next three sections we review methods for modelling the interface between two materials. We begin with a short section on chemical heuristics—using simple chemical rules to reduce the vast compositional space of possible interface materials. We then review atomistic methods for understanding at an atomistic level the complex physical and chemical processes at an interface. Finally, we outline the theory and techniques for modelling interfaces at the device level.

4 DATA-DRIVEN APPROACHES TO INTERFACE MATERIALS MODELLING

A common approach when developing a photvoltaic absorber material is to integrate the new material into the existing device architecture for a related compound. For example, CZTS in the kesterite structure is derived from CIGS in the chalcopyrite structure. As a result of this relation, CZTS thin film devices are based on the CIGS architecture with a CdS window layer and molybdenum back contact. However this transfer between technologies is unlikely to lead to a optimal material pairing because, as we have discussed above, processes at an interface are highly sensitive to the specific structural, electronic and defect properties of a material.

The opposite data-driven approach is to widen the search space to include all possible interface materials, and then apply a sequence of computational filters to identify those with a set of pre-defined target properties. The initial filters may include low-cost chemical rules (also known as chemical heuristics) to reduce the search space. For example, if searching for a binary material we might enforce the first Pauling rule, requiring that the ratio of the anion and cation ionic radii falls within a certain range.

(Pauling, 1929). Alternatively, the filters may not derive from chemical knowledge but from statistical (e.g machine learning) models built on a large dataset of material properties. An advantage of the screening approach is that additional constraints can be implemented in the workflow. For example, the Herfindahl Hirschman index can be applied to select for compounds which contain abundantly available elements, (Mansouri Tehrani et al., 2017), or compounds containing toxic elements can be removed at an early stage.

When an atomic-scale structure is yet to be determined the computational model must be able to make predictions based on elemental composition only. In the context of interfaces in solar cell devices we are particularly interested in predicting the electronic properties of materials, such as the CBM and VBM referenced to the vacuum level, and the electronic band gap. Chemical rules connecting elemental composition with electronic structure have a long history starting with the work of Mulliken who developed an absolute scale of atomic electronegativity (defined as the mid-point in a semiconductor band gap) in 1934. More recently, Pelatt *et al.* proposed the Atomic Solid State Energy (SSE) scale as an alternative approach to electronegativity. (Pelatt et al., 2011). This is derived from data for the ionisation potentials and electron affinities of 69 binary semiconductors containing 40 different elements. By considering the energy difference between the most negative cation SSE and the least negative anion SSE, this method provides estimates for the absolute CBM, VBM and band gap in any compound. The SSE scale has been used as a filter in a high-throughput search for photoactive chalcohalide semiconductors, identifying two new compounds with band gaps in the visible spectrum, (Davies et al., 2018), and to rationalise the measured hole concentrations in Cu-based chalcogenide PV absorber materials. (Itthibenchapong et al., 2013).

The SSE scale is based on a linear trend between the electron affinity and ionisation potential versus band gap. However for many properties of interest the trend is not so readily recognisable as there may be a higher number of dependent parameters and/or more complex non-linear relationships. In this case machine learning (ML) can be used to identify relationships in the data and develop predictive models.

The number of studies based on ML applied to materials science is growing quickly. This is driven by investment into high-performance computing, freely available materials databases [for example the Materials Project (Jain et al., 2013) or OQMD (Kirklin et al., 2015)] and open-source machine learning libraries. A common approach is to use well-known chemical concepts, such as ionic radii or electronegativity of the constituent elements, as features for supervised machine learning. This approach has been used in a number of studies to predict the electronic band gap across a range of potential materials for solar applications, including: double chalcogenide perovskites, (Agiorgousis et al., 2019), orthorhombic lead-free perovskites, (Lu et al., 2018), wurtzite nitride semiconductors (Huang et al., 2019) and kesterite materials. (Weston and Stampfl, 2018). The predictive power of the machine learning model depends on there being a training database of suitable size, hence the reliance on either existing materials data or high-throughput computing resources.

ML has also been used in the development of interatomic potentials. Here the ML model is trained to predict energies and forces from first-principles calculations of small systems (tens or hundreds of atoms). The ML-based potential (MLP) is then used to model large systems (thousands of atoms) that are intractable for first-principles simulation. This approach has particular relevance to interface materials where amorphous and nano-structured phases can be formed which require large periodic unit cells for building accurate models. For example, a MLP for molybdenum has been developed that achieves close to DFT accuracy for a broad range of properties including elastic constants, phonon spectra and surface energies. (Chen et al., 2017). This MLP is based on the spectral neighbor analysis potential (SNAP) developed by (Thompson et al., 2016) It also incorporates well-established, domain-agnostic machine learning techniques: principal component analysis for the structural selection process, and a differential evolution algorithm for optimizing the model hyperparameters.

The studies introduced so far in this section have been used to predict the properties of a single material. There are also a small number of studies that use ML to predict the chemical and structural changes that occur when two materials join to form an interface. For example, ML has been used to predict the structures formed at epitaxial inorganic interfaces typical of high-efficiency III-V PV materials. This technique uses surface matching accelerated with Bayesian optimisation to predict the interfacial distance and potential energy surface at a fraction of the computational cost required by the equivalent DFT calculations. (Moayedpour et al., 2021). It is also possible to use a MLP to describe interface bonding if a suitable training set is used. There are various cases in which this approach has been used to describe systems where the interface region is small, such as in supported nanoclusters. (Artrith, 2019). Modelling the interface between two extended crystalline materials is more challenging as this typically requires larger simulation cells to generate the training data. The grain boundaries in aluminium have been modelled using a MLP which was trained using structures optimised using conventional interatomic potentials and density functional theory. (Tamura et al., 2017). This allowed the prediction of minimum energy structures for extended grain boundary structures that would not have been accessible using DFT alone. There is not yet, to our knowledge, extension of this approach to other materials or heterogeneous interfaces.

The on-going challenge for materials simulation is the trade-off between accuracy and computer time. The common theme across all of the ML-based studies introduced in this section is that they aim to provide predictions with the accuracy of ab-initio quantum chemical simulations but at lower cost. Although this computational efficiency has been established for accurately predicting the properties of a single material, there has been minimal data-driven research which explicitly considers the bonding and structural changes at a PV interface. For these research problems the most commonly used approach is classical or quantum atomistic simulation, which is the subject of the following section.

5 ATOMISTIC MODELLING OF PHOTOVOLTAIC INTERFACES

Given that materials interfaces represent major bottlenecks to the performance and stability of PV devices, their accurate simulation and understanding at the atomistic scale are becoming ever more important. However, compared to the modelling of bulk crystalline materials, the methods for modelling interfaces in PV materials (and indeed other energy materials) are far less developed and often do not present the same reliability and computational efficiency. While bulk crystalline materials are modelled atomistically as infinite lattices using three-dimensional periodic boundary conditions, simulations of the heterogenous interfaces in PV devices require the preparation of surface slabs that are placed in direct contact with each other. The development of such interfacial models is challenging and careful consideration must be given to their scale, alignment, chemical composition, stability, disorder/defects and thermal and mechanical damage to ensure that they are reliable and representative of real interfaces. Nevertheless, despite the challenges they present, the atomistic modelling of interfaces can offer a wealth of valuable information regarding the performance of PV materials and devices at an atomic resolution, as well as the potential for the discovery of unique behaviour and properties not exhibited in bulk materials.

Thermodynamic stability is one of the most fundamental properties for defining the pertinency of a given interface. The first factors to consider when creating an interfacial model are surface formation and the energy it requires, i.e., the surface free energy ($\gamma_{surface}$, $J\,m^{-2}$). $\gamma_{surface}$ defines the energy required to cleave a bulk material and form a surface with a particular Miller index and can be calculated using both forcefield or electronic structure methods, as exemplified in many atomistic modelling studies of PV materials. (Raymand et al., 2008; Wang et al., 2015; Nicholson et al., 2020). Such a surface can then be modelled as a slab consisting of a number of atomic layers converged with respect to the calculated internal energies from DFT or a forcefield approach. Several approaches have been proposed to reduce the computational expense of converging the slab thicknesses, including orientating the reference bulk material with the Miller index of the surface of interest (Sun and Ceder, 2013) and saturating any dangling bonds with pseudo-hydrogens based on fractional core and electronic charges. (Sai et al., 2018). By combining the $\gamma_{surface}$ values for a selection of Miller index planes, the Wulff construction, which minimises the surface energy for a given enclosed volume, can be used to predict the equilibrium particle morphologies of PV materials. (Barnard and Curtiss, 2005; Wilson et al., 2016).

The energy of an interface ($\gamma_{interface}$) can also be obtained using a similar method to that for $\gamma_{surface}$ using the computed total energies of the interface and its corresponding bulk materials. Like $\gamma_{surface}$, $\gamma_{interface}$ must also be converged with regards to system size, which can represent a substantial computational cost, particularly for quantum mechanical simulations. The sign of $\gamma_{interface}$ signifies whether the interface is more (negative value) or less (positive value) stable than the respective bulk materials in isolation. This method has been used to provide significant insights into the stability of the interfaces of PV materials, for example CZTS/CdS (Rondiya et al., 2019; Rondiya et al., 2020), CCTS/CdS (Rondiya et al., 2020) and TiO_2/hybrid perovskites. (Mosconi et al., 2014). In addition to heterogenous interfaces, $\gamma_{interface}$ is equally applicable to homogenous interfaces and has been widely applied to investigate the stability and formation of grain boundaries in various PV materials. (Park and Walsh, 2021).

As discussed earlier in the review, the alignment of bands between different materials is critical to the performance of devices with semiconductor heterojunctions. Quantum mechanical simulations play an important role in predicting and optimising band alignment and the most used approach to provide a comparison with experiment is the use of slab models. (Singh-Miller and Marzari, 2009; Peng et al., 2013). In this approach, the electrostatic potential in the vacuum provides a reference so that the ionisation potential can be calculated using the valence band maximum of the slab model. One issue that can arise from the use of slab models based on ideal surface cuts in calculating the ionisation potential is the presence of dangling bonds. Although these surface states mean that the ionisation potential from a single slab does not represent the true ionisation potential from the bulk material, their effect can be corrected for by using the calculated valence band maximum of the bulk material and surface dipole of the slab. (Peressi et al., 1998). It is also important to bear in mind that the use of idealised surface models does not take into account the effect of impurities (either added intentionally or otherwise), which can have a dramatic effect on the electronic properties of the interface. (Davis et al., 1980; Ming et al., 2018; Borchert et al., 2019).

In addition to the use of explicit interfacial models, two alternative approaches have been utilised for the calculation of band alignment *via* atomistic modelling. The first is the natural band alignment approach, where the band offsets are obtained by explicitly calculating the heterojunctions of the semiconductors of interest. While this approach has the advantage of allowing for facile comparison with spectroscopic analyses, it is only appropriate for materials with similar structures and compositions due to the assumption of transitivity for the band offsets. (Butler et al., 2019).

This method has been successfully applied to investigate band alignment in a wide variety of PV materials, including II–VI and III–V semiconductors (Wei and Zunger, 1998) and hybrid perovskites. (Butler et al., 2015). The second technique utilises the branch-point energy, which is defined as a level at which defect states in the band gap change from donor-like to acceptor-like states, to align bands across bulk semiconductors. This can be achieved by calculating the band gap centre, which represents the average of the VBM and CBM across the Brillouin zone (Toroker et al., 2011). Although this approach is relatively straightforward, computationally inexpensive and has been applied to a large selection of oxide and nitride PV materials, (Schleife et al., 2009), it is highly sensitive to the choice of computational parameters. (Alidoust et al., 2014). In-depth reviews of these methods and their application to PV interfaces are available elsewhere. (De Angelis, 2014; Even et al., 2014; Park and Walsh, 2021).

It is also noteworthy that atomistic modelling can also potentially be used to assess a variety of other important properties that govern the performance of PV interfaces beyond thermodynamic stability, electronic structure and band alignment, such as ion transport, defects and degradation mechanisms. However, despite the importance of these properties and the fact they have been routinely simulated in individual PV materials (Oba et al., 2008; Eames et al., 2015; Lanzetta et al., 2021) and grain boundaries (Park and Walsh, 2021) using both classical and quantum methods, studies of their effect on PV heterointerfaces are at best scarce. This is primarily because of the inherent challenges in modelling interfaces discussed throughout this review.

Due to their own unique advantages and disadvantages, the application of both forcefield and electronic structure calculations is vital in closing the current gap between bulk and interfacial modelling in terms of practicality, efficiency and accuracy. The need for larger atomistic models that can be simulated for longer timescales is one of the most critical challenges currently facing the modelling of interfaces and this is where classical techniques, such as molecular dynamics, have a distinct advantage. Such models can also be parameterised using DFT and ML calculations to improve their accuracy and reliability. In contrast, there are clearly many properties, e.g., band alignment and charge transfer, where the electronic structure of the interface must be considered explicitly and the use of classical forcefields is not appropriate. The understanding of the interfaces in PV devices is inherently a multi-scale problem and therefore require multi-scale approaches to solve it.

6 CONTINUUM SCALE MODELS OF PHOTOVOLTAIC DEVICES

The simulation of a complete solar energy conversion system is a macro-scale problem that requires us to consider several material interfaces. In previous sections we have discussed modelling material structure and composition both in a bulk interface material, and at the interface itself. Here we consider models at the device level, which can incorporate several material interfaces, and include simulations up to the scale of module installations.

There are several approaches for calculating the electronic properties of a device. At the simplest level there is the detailed balance approach, which in some formalisms only requires the energy and absorptivity of the absorption edge. For increased accuracy, but where a detailed knowledge of the device structure is unknown, a diode model can be used. In this case, the various transport and recombination mechanisms can be modelled using electrical components. However the most fundamental and accurate method for predicting electronic behaviour is Poisson-drift-diffusion (PDD). This underlies the large majority of software tools used for modelling PV devices, and is the focus of the following section. Following this we summarise and discuss some of the key software packages used for device modelling and identify opportunities for accelerating our ability to model interfaces in a increasingly diverse array of PV devices.

6.1 Equations Governing Device Level Behaviour

The most fundamental equation for predicting electronic behaviour in semiconductor devices is the Poisson equation, which relates the electrical charges in the structure to the electrostatic potential ϕ. In a semiconductor the charge is typically split onto four density domains: electron density n, hole density p, acceptor atom density N_A^- and donor atom density $N_D{}^+$. The Poisson equation in one dimension is given by:

$$\frac{d}{dx}\left(\epsilon\frac{d\phi}{dx}\right) = -q\left(p(x) - n(x) - N_A^- + N_D^+\right), \tag{6}$$

where ϵ is the dielectric permittivity of the material. The continuity equations are used in conjunction with Poisson statistics. The continuity equations are book-keeping equations in that they ensure conservation of charge, balancing the carriers that enter and leave different parts of the model. The continuity equations for free electrons in the conduction band and holes in the valence band are given by the following two equations:

$$\frac{1}{q}\frac{dJ_n}{dx} = U(x) - G(x) \tag{7}$$

$$\frac{1}{q}\frac{dJ_p}{dx} = -U(x) + G(x)), \tag{8}$$

where J_n is the electron current density, J_p is the hole current density, $G(x)$ is the generation rate (for a solar cell this will be generation from illumination) and $U(x)$ is the net recombination rate. The recombination rate may incorporate several mechanisms including radiative band-to-band recombination, defect mediated Shockley-Reed-Hall recombination, Auger recombination and surface recombination at the interface between materials. The equations describe a steady-state system where the change in current is exactly balanced by charge generation and recombination.

The transport equations describe the dynamics of the carriers and therefore also the current in a solar cell. Current in a solar cell can be broken down into two parts: a drift component due to the electric field $E = -\frac{d\phi}{dx}$ and a diffusion component due to the carrier concentration gradient. This can be seen in the transport equations, where the first term correlates to drift current and the second term to diffusion current:

$$\frac{1}{q}J_n = -\mu_n n\frac{d\phi}{dx} + D_n\frac{dn}{dx} \tag{9}$$

$$\frac{1}{q}J_p = -\mu_p p\frac{d\phi}{dx} + D_p\frac{dp}{dx}, \tag{10}$$

where the as-yet undefined constants are material-specific transport parameters: μ_n is the electron mobility, μ_p is the hole mobility, D_n is the electron diffusivity and D_p is the hole diffusivity.

The above equations are well-established equations for semiconductors that are derived and expanded on in many semiconductor textbooks [for example, Reference (Nelson, 2003)]. They form a coupled system of nonlinear partial

differential equations which do not, in general, admit analytical solutions for systems of interest. Instead, numerical techniques are used to model the behaviour or these systems for given material types and geometries. These numerical techniques are all based on the discretisation of a device in both space and time yet can be approached in a variety of ways, such as the well-established and robust finite difference method, or the finite element method which is more flexible in terms of problem geometry. In addition, there are various alogrithms which implement each method. For example, the finite element method can be implemented using the Gummel method for fast convergence, or the Newton method when there are high recombination rates leading to strong coupling of the continuity and Poisson equations. (Liu et al., 2011). Once solved, the equations describe the movement of charge carriers and their relationship with current and electric field strength.

In addition to the classical physics introduced above, quantum tunnelling should be considered for the accurate prediction of charge transport behaviour across heterojunctions where either the material layer or depletion layer is thin (typically less than 15 nm). Quantum tunnelling can affect the calculated current as it results in the transport of electrons across a potential barrier even if the electron energy is less than the barrier height—transport that is forbidden in the classical regime. Experimental measurements demonstrate that quantum tunnelling mechanisms can dominate the charge transport current behaviour in a cell and can significantly impact the PV performance when there is a spike-like barrier at the interface. (Verschraegen and Burgelman, 2007). For a full description of quantum tunnelling, electrons with an energy below the potential barrier can be represented by the Schrödinger equation and solved to give wave vectors and a tunnelling probability. This however requires computational resources beyond that typically used for device level simulations, and so analytical approaches such as the WKB method are commonly used to give approximate corrections to the calculated current. (Burstein and Lundqvist, 1969; Gundlach and Simmons, 1969; Verschraegen and Burgelman, 2007).

There are also multi-scale device models that incorporate methods for solving the Schrödinger equation directly. These models are motivated by the increasing amount of research and development into solar cell devices based on nano-structured materials, such as quantum dot, nanowire or quantum well structures. These materials consist of multiple nanometre thin layers which can, as a result of being ultra-thin, accommodate large amount of strain at the interface. (Kroemer, 2001). Research interest is driven by their potential for increased conversion efficiencies over single-junction cells without the complexity of multi-junction designs. In several software packages (Birner et al., 2007; Alonso-Álvarez et al., 2018) the quantum properties of the nanostructures are calculated by solving the one-dimensional Schrödinger equation to give the eigenvalues and eigenvectors associated a given potential. To include local strain fields that develop as a result of lattice deformation the electron mass can be modified. (Birner et al., 2007; Alonso-Álvarez et al., 2018). It is also possible to repeatedly iterate through the Schrodinger and Poisson equations until a self-consistent solution that takes into account the classical and quantum mechanical charge densities has been found. (Birner et al., 2007).

As discussed further in the following section, these classical and quantum techniques are implemented in several software packages which are designed to output useful semiconductor characterisation data that can be directly compared to experimental results. Notable examples relevant for PV research include current-voltage (J-V) characteristics, internal quantum efficiency (IQE) and external quantum efficiency (EQE) and there are also software packages that can make predictions for more advanced characterisation techniques such as capacity-voltage and photoluminescence. (Froitzheim et al., 2003).

6.2 Solar Cell Modelling Packages

There are numerous packages to simulate crystalline, polycrystalline and nano-engineered PV cells. Many of these are well documented and have yielded significant insights whether paired with experimental results (Karthick et al., 2020; Houimi et al., 2021) or as stand-alone simulations. (Verschraegen and Burgelman, 2007; Feng et al., 2013; Mostefaoui et al., 2015). Whilst these packages tend to simulate the same sets of solar cell characterisation data (for example, current-voltage curves) they are differentiated by both the approach they use and the applications they are tailored towards. For example, nextnano (Birner et al., 2007) uses the finite element method and is particularly suited to the diverse geometries of nano-engineered materials. In contrast, PC3D uses a fourier transform solution to the drift-diffusion equations which is computationally efficient but more restricted in its applications. (Basore, 2020).

Table 1 summarises some of the other notable software packages for PV device simulation. The packages listed are capable of exploring several aspects of solar cell device behaviour, with the primary focus being on semiconductor physics. In addition to those listed in the table there are packages tailored towards simulating other sub-sets of the PV energy generation process, including SMARTS to calculate the solar spectrum as a function of atmospheric conditions, (Gueymard, 1995), OPTOS for light absorption at the module level (Tucher et al., 2016) and PVlib for module and systems level modelling. (Holmgren et al., 2018a).

The availability of each code is also listed in **Table 1**. The general purpose device simulators, capable of modelling a whole host of semiconductor devices including memory devices and power electronics, are proprietary and require a paid license. Of those listed that are freely available, only Solcore is distributed with an open source license (GNU LGPL, gnu. org/licenses/lgpl-3.0) although the source code for PC3D and wxAmps is openly available. Two of the software packages listed, Quokka3 and PC3D, are heavily geared towards silicon devices, and are the only freely available packages listed for simulations in three dimensions. The user interfaces come in a variety of forms: Solcore provides a library of tools which are called directly in a Python script, PC3D uses an excel-based user interface, whilst others (including SCAPS, wxAmps and AFORS-HET) provide a graphical user interface.

TABLE 1 | A non-exhaustive list of solar cell device simulation tools. The table allows a comparison of the key features and availability. Unless otherwise stated, the simulations are one-dimensional and a graphical user interface is available. 'Open source' indicates that the source code is available for free download. 'Freely available' indicates that the compiled software is available for free download. Note that Solcore is free to use and is distributed with an open source license, GNU LGPL (gnu.org/licenses/lgpl-3.0). We also include signposts for further information: a project web address and a reference in the academic literature. Finally we list selected publications in which the software has been applied.

Name	Features	Availability	Web Address	Reference	Applications
SCAPS	• widely used in academica • intra-band, band-to-band and interface defect tunnelling implemented	freely available	scaps.elis.ugent.be	Burgelman et al. (2000)	Verschraegen and Burgelman, (2007), Karthick et al. (2020), Houimi et al. (2021), Mostefaoui et al. (2015), Simya et al. (2015), AlZoubi and Moustafa, (2019), Jannat et al. (2021)
Solcore	• modular and extendable • no graphical user interface • Schrodinger solver for quantum mechanical properties	GNU LGPL	solcore.solar	Alonso-Álvarez et al. (2018)	Führer et al. (2013), Nikander et al. (2020)
PC3D	• for silicon solar cells only • simulations in 3D • Excel-based user interface	open source	pc3d.info	Basore, (2020), Basore, (2018)	Balaji et al. (2020)
wxAmps	• based on the AMPS code • Newton and Gummel methods for faster convergence	open source	github.com/wxAMPS	Liu et al. (2012a) and Liu et al. (2012b)	Yaşar et al. (2016), Chen et al. (2016)
Victory Device	• general purpose device simulator • simulations in 2D and 3D • electrical, optical and thermal properties	paid license	silvaco.com	Michael et al. (2005), Michael, (2005)	Elbar and Tobbeche, (2015)
Sentaurus	• general purpose device simulator • simulations in 2D and 3D • electrical, optical and thermal properties	paid license	synopsys.com	Wu and Jhan, (2018)	Passeri et al. (2016), Limpert et al. (2014)
Quokka3	• optimised for silicon cells • simulations in 1D, 2D and 3D	free and paid licenses	quokka3.com	Fell, (2012)	Fell and Altermatt, (2018), Richter et al. (2017)
AFORS-HET	• includes advanced characterisation techniques such as capacity-voltage and photoluminescence	freely available	helmholtz-berlin.de	Froitzheim et al. (2003), Rolf et al. (2006)	Yao et al. (2018), Wang et al. (2011)
nextnano	• optoelectronic device simulator • Schrodinger solver for quantum mechanical properties	paid software	nextnano.de	Birner et al. (2007)	Refaei, (2017)

The list of simulation codes in **Table 1** is not exhaustive. Several groups develop their own in-house codes tailored towards particular research problems, some of which have been developed and published in public code repositories. (Holmgren et al., 2018b; Juan, 2022; Koopmans and Vincent, 2022). These codes generally provide command line interface (CLI) or application programming interface (API) to underlying routines, and as such require a basic familiarity with programming. Script-based simulation tools are also more suitable for problems that use high-performance-computing or cloud computing on remote machines.

In the following sections we compare the simulation capabilities and use cases of SCAPS-1D and Solcore. These have been chosen for greater discussion as they provide contrasting approaches: SCAPS-1D is a well-established device level simulation package that is widely used in the experimental community, whilst Solcore is a highly modular, Python-based extensible open-source package that aims to provide flexibility for those who wish to develop and extend the code for their own research purposes.

6.3 Solar Cell Capacitance Simulator-1D

SCAPS (Burgelman et al., 2000) (a Solar Cell Capacitance Simulator) is one of the most widely used software tools for simulating solar cell device characteristics. (Verschraegen and Burgelman, 2007; Mostefaoui et al., 2015; Simya et al., 2015; AlZoubi and Moustafa, 2019; Karthick et al., 2020; Houimi et al., 2021; Jannat et al., 2021).

It was originally developed at the turn of the millenium for polycrystalline cell structures of the CIGS and CdTe family of materials, and is maintained by researchers based at the Department of Electronics and Information Systems (ELIS) of the University of Gent, Belgium. (Burgelman et al., 2000). It is designed to accommodate multiple thin films and interfaces, and has evolved over the years to include additional mechanisms for recombination (for example, Auger recombination) and tunnelling (for example, tunnelling at interface defects). As is common with the other software packages listed in **Table 1**, SCAPS-1D solves Poisson's equation along with the continuity equations to describe carrier transport physics and calculate quantum efficiency (QE) and J-V characteristics. It can be used to describe imperfect materials through the specification of various parameters including recombination and capture rates at defect centres, and defect densities. This provides quantative predictions for the recombination current and points to which recombination mechanisms in a device a particularly limiting to device performance.

The primary advantage of SCAPS-1D is in terms of accessibility. SCAPS-1D is fully self-contained and free to download, is straight-forward to install on a modern operating system and is distributed with a graphical user interface so that those without any familiarity with programming can use it with ease. The lightweight (in terms of computational expense) and accessible nature of the programme, yet ability to model multiple thin-film layers and interfaces, has led to it being applied in several studies of potential interface materials. For example, Campbell *et al.*(Campbell et al., 2020) use SCAPS to compare CdS and In_2S_3 as the buffer layer in a CZTSSe cell. Combined with optical and electronic characterisation techniques they establish that although In_2S_3 has the more favourable band alignment, the presence of interfacial defect states results in a lower overall V_{OC}.

6.4 Solcore

Solcore is a complete semiconductor solver written in Python 3 and developed by researchers at Imperial College London. (Führer et al., 2013; Alonso-Álvarez et al., 2018; Nikander et al., 2020).

The packages are arranged in a modular manner, with modules dedicated to materials science (including a material parameters database and quantum solver), optical methods, light sources, solar cell calculators and a large-circuit solver. Together these modules provide optical and electronic solving capabilities for a wide range of solar cell materials, with specific attention placed on III-IV devices, such as GaAs, and semiconductor nanostructures where quantum confinement effects are dominant. As such, Solcore is a multi-scale tools that extends from the micron length scales of light propagation to module-scale performance characteristics.

Device characteristics in Solcore can be predicted using a range of techniques (detailed balance and the diode equation), the most accurate being PDD as introduced above. A key advantage of Solcore is that it is designed for integration with external libraries. One such library is SMARTS (Gueymard, 1995) which incorporates a model of the atmospheric transfer of radiative sunshine. This allows for an accurate description of the solar irradiance depending on atmospheric conditions (such as water vapour, nitrogen dioxide, ozone or uniformly mixed gas absorption) along with other modelling capabilities such as Raleigh scattering, light diffusivity and back scattered light rays. Solcore is somewhat unique in that it has been designed with user extension and adaptation in mind: code development takes place in a public facing Github repository, the code has a modular structure, and Solcore 'bootcamps' have been organised for training and community building purposes. This is in contrast to the majority of simulation packages that are often high level, self-contained and do not invite extensive customisation.

Solcore has been applied to a number of research problems that incorporate multi-junction, quantum well and light-trapping technologies. For example, Pearce *et al.* use Solcore for the development of a perovskite on silicon tandem cell, where the perovskite top cell is deposited conformally onto the pyramidal surface of a silicon cell. (Pearce and Ekins-Daukes, 2019). Solcore has also been used in the development of ultra-thin GaAs cells for space applications. Here the challenge is to develop cells which are both physically thin (for radiation resistance) yet optically thick (for strong light absorption). Sayre *et al.* used the Solcore optical and solar cell modules to model and optimise these novel structures. (Sayre et al., 2022).

These examples demonstrate some important points about the role software design plays in enabling science. In the study from Pearce *et al.* the Rayflare software package used Solcore's light source module and Structure class to calculate light absorption in a challenging geometry. This was made possible through the interoperability of each code, a feature which will become increasingly important in the quickly growing ecosystem of open-source tools for PV. (Holmgren et al., 2018c; Ayala Pelaez and Deline, 2020; Kim S et al., 2020; Silva et al., 2022). In addition, the development of PV devices for niche applications, such as high-efficiency and radiation-resistance solar cells for space, highlights the importance of code extensibility and adaptability. For example, researchers in the field of space PV may wish to extend a code to include physical models particularly relevant at ultra-thin length scales, such as carrier recombination at radiation induced defect sites.

Within both Solcore and SCAPS-1D there are assumptions that are made about the device so that the Poisson statistics and continuity equations can be used. For example, the solver in Solcore uses the Boltzmann approximation for carrier distribution with the assumptions that carrier concentrations are not highly doped, all carrier populations are in quasi-thermal equilibrium, and that the mobility of carriers are completely independent of the electric field. As a direct result of this latter assumption the Poisson drift diffusion model is only valid in weak electric fields. The various assumptions and model limitations inherent in all device modelling highlights the need for clear software documentation and on-going communication channels between software developers and users.

The accuracy of predictions made at the device level are always limited by the complexity of the atomic-scale interactions at the interface. For example, device models commonly assume that the work functions and electron affinity of the bulk materials govern the band bending observed on energy diagrams. However, as we have discussed earlier in this review, heterojunctions experience interface-specific bond formation, and this is especially true for polycrystalline materials that are prone to defect state formation at interfaces. (Raymond and Kronik, 2018). When the specifics of material-material interaction are not accounted for in device level models there will always be an inherent limitation to the accuracy of any predictions made.

7 CONCLUSION

As Herbert Kroemer famously wrote in his Nobel lecture, 'The interface is the device'. (Kroemer, 2001). For solar cells, where charge transport across several heterojunction interfaces is a pre-requisite for working devices, this quote is particularly pertinent. However, despite material interfaces representing a bottleneck to the performance and stability of PV devices, their accurate simulation is less developed compared to bulk materials, and do not present the same accuracy, reliability or computational efficiency.

The main challenge for interface modelling is the inherent multi-scale nature of the problem. There is now the theoretical framework and computer power required to both build atomic scale structural interface models and predict the associated electronic properties. However, as explored towards the start of this review, the processes at an interface are often complex and intertwined, involving descriptions of chemical, thermal, electronic and thermodynamic behaviours. In this review we have discussed several approaches for modelling interface processes at various length and timescales, and have split these into three broad sections: data-driven approaches for high-throughput screening or lower-cost predictions of atomic-scale properties, atomistic approaches for high-accuracy predictions and explicit modelling of the structural and electronic changes at an interface, and continuum level models for predictions of device behaviour. We have outlined cases where these approaches have enabled a better understanding of material or device performance, alongside their key limitations.

In response to the challenges facing interface modelling, there are an abundance of opportunities for the future. In particular, we see opportunities for the data-driven approaches developed for bulk materials to be extended to consider the interactions at the interface between two material. We also see opportunities for the increased development and use of software programmes that embrace the multi-scale nature of semiconductor device simulation, and that combine quantum solvers alongside optical modelling, electrical modelling and large circuit solvers. Finally, we note that the majority of the most popular device-level simulation tools are self-contained applications which are not designed for user extension to new models. Given the fast-paced and increasingly diverse nature of photovoltaic research and development, we believe continued investment into open-source multi-scale software tools that are accessible, adaptable and extensible by members of the research community will accelerate both our understanding of materials interfaces and, as a consequence, the design of high-performing photovoltaic technologies.

DATA AVAILABILITY STATEMENT

No datasets were generated in this study.

AUTHOR CONTRIBUTIONS

MJ was primary author for the document along with coauthors JD, SC, VB, LW, and YQ. LW, YQ, and VB are supervisors of the primary author and contributed to the writing. JD provided written input to the atomistic modelling section.

FUNDING

MJ acknowledges support from the United Kingdom Engineering and Physical Sciences Research Council (EPSRC) CDT in Renewable Energy Northeast Uni-versities (ReNU) for funding through EPSRC grant EP/S023836/1. This work was supported by the British Council Newton fund institutional links grant No. 623804307.

ACKNOWLEDGMENTS

The authors acknowledge the EPSRC Centre for Doctoral Training in Renewable Energy Northeast Universities (ReNU) for funding through grant EP/S023836/1. The authors also appreciate the support from British Council Newton Fund Institutional Links Grant in Ultralight Absorber for Remote Energy Source (U-AREs, No. 623804307). JD gratefully acknowledges Newcastle University for funding through a Newcastle Academic Track (NUAcT) Fellowship. LW gratefully acknowledges Northumbria University for funding through a Vice-Chancellor's Fellowship.

REFERENCES

Alidoust, N., Toroker, M. C., Keith, J. A., and Carter, E. A. (2014). Significant Reduction in NiO Band Gap upon Formation of Li_x Ni_{1-X} O Alloys: Applications to Solar Energy Conversion. *ChemSusChem* 7 (1), 195–201. doi:10.1002/cssc.201300595

Alonso-Álvarez, D., Wilson, T., Pearce, P., Führer, M., Farrell, D., and Ekins-Daukes, N. (2018). Solcore: a Multi-Scale, Python-Based Library for Modelling Solar Cells and Semiconductor Materials. *J. Comput. Electron* 17 (3), 1099–1123. doi:10.1007/s10825-018-1171-3

AlZoubi, T., and Moustafa, M. (2019). Numerical Optimization of Absorber and CdS Buffer Layers in CIGS Solar Cells Using Scaps. *Sgce* 8, 291–298. doi:10.12720/sgce.8.3.291-298

Anderson, R. L. (1960). Germanium-Gallium Arsenide Heterojunctions [Letter to the Editor]. *IBM J. Res. Dev.* 4 (3), 283–287. doi:10.1147/rd.43.0283

Artrith, N. (2019). Machine Learning for the Modeling of Interfaces in Energy Storage and Conversion Materials. *J. Phys. Energy* 1 (3), 032002. doi:10.1088/2515-7655/ab2060

Ayala Pelaez, S., and Deline, C. (2020). Bifacial_Radiance: a Python Package for Modeling Bifacial Solar Photovoltaic Systems. *J. Open Source Softw.* 5 (50), 1865. doi:10.21105/joss.01865

Agiorgousis, M., Sun, Y. Y., Choe, D. H., West, D., and Zhang, S. (2019). Machine Learning Augmented Discovery of Chalcogenide Double Perovskites for Photovoltaics. *Adv. Theory Simul.* 2 (5), 1800173. doi:10.1002/adts.201800173

Bahrami, B., Mabrouk, S., Gurung, A., Reza, K. M., Elbohy, H., Pathak, R., et al. (2021). Kinetic Monte Carlo Simulation of Perovskite Solar Cells to Probe Film Coverage and Thickness. *Adv. Energy Sustain Res.* 2 (3), 2000068. doi:10.1002/aesr.202000068

Balaji, P., Bowden, S., and Augusto, A. (2020). "Studying Edge Losses in Silicon Heterojunction Solar Cells," in 2020 47th IEEE Photovoltaic Specialists Conference (PVSC) (IEEE), 2203–2206. doi:10.1109/pvsc45281.2020.9300984

Barnard, A. S., and Curtiss, L. A. (2005). Prediction of TiO2 Nanoparticle Phase and Shape Transitions Controlled by Surface Chemistry. *Nano Lett.* 5 (7), 1261–1266. doi:10.1021/nl050355m

Basore, P. A. (2020). Multidimensional Fourier-Series Solution of the Quasi-Neutral Drift-Diffusion Equations. *IEEE J. Photovoltaics* 10 (3), 905–911. doi:10.1109/jphotov.2020.2966831

Basore, P. A. (2018). Efficient Computation of Multidimensional Lambertian Optical Absorption. *IEEE J. Photovoltaics* 9 (1), 106–111. doi:10.1109/JPHOTOV.2018.2882180

Birner, S., Zibold, T., Andlauer, T., Kubis, T., Sabathil, M., Trellakis, A., et al. (2007). Nextnano: General Purpose 3-d Simulations. *IEEE Trans. Electron Devices* 54 (9), 2137–2142. doi:10.1109/TED.2007.902871

Borchert, J., Levchuk, I., Snoek, L. C., Rothmann, M. U., Haver, R., Snaith, H. J., et al. (2019). Impurity Tracking Enables Enhanced Control and Reproducibility of Hybrid Perovskite Vapor Deposition. *ACS Appl. Mat. Interfaces* 11 (32), 28851–28857. doi:10.1021/acsami.9b07619

Burgelman, M., Nollet, P., and Degrave, S. (2000). Modelling Polycrystalline Semiconductor Solar Cells. *Thin solid films* 361-362, 527–532. doi:10.1016/s0040-6090(99)00825-1

Burstein, E., and Lundqvist, S. (1969). *Tunneling Phenomena in Solids*. New York, NY: Springer.

Butler, K. (2017). Electroniclatticematch: Heteroepitaxial Lattice Matching for Electronic Applications. Available at https://github.com/keeeto/ElectronicLatticeMatch.

Butler, K. T., Frost, J. M., and Walsh, A. (2015). Band Alignment of the Hybrid Halide Perovskites $CH_3NH_3PbCl_3$, $CH_3NH_3PbBr_3$and $CH_3NH_3PbI_3$. *Mat. Horiz.* 2, 228–231. doi:10.1039/C4MH00174E

Butler, K. T., Sai, G., and Canepa, P. (2019). Designing Interfaces in Energy Materials Applications with First-Principles Calculations. *npj Comput. Mater* 5, 19. doi:10.1038/s41524-019-0160-9

Butler, K. T., Kumagai, Y., Oba, F., and Walsh, A. (2016). Screening Procedure for Structurally and Electronically Matched Contact Layers for High-Performance Solar Cells: Hybrid Perovskites. *J. Mat. Chem. C* 4, 1149–1158. doi:10.1039/C5TC04091D

Campbell, S., Qu, Y., Bowen, L., Chapon, P., Barrioz, V., Beattie, N. S., et al. (2018). Influence of OLA and FA Ligands on the Optical and Electronic Properties of $Cu_2ZnSn(S, Se)_4$ Thin Films and Solar Cells Prepared from Nanoparticle Inks. *Sol. Energy* 175, 101–109. doi:10.1016/j.solener.2018.03.065

Campbell, S., Qu, Y., Gibbon, J., Edwards, H. J., Dhanak, V. R., Tiwari, D., et al. (2020). Defect Limitations in $Cu_2ZnSn(S, Se)_4$ Solar Cells Utilizing an In_2S_3 Buffer Layer. *J. Appl. Phys.* 127 (20), 205305. doi:10.1063/5.0002372

Campbell, S., Qu, Y., Major, J. D., Lagarde, D., Labbé, C., Maiello, P., et al. (2019). Direct Evidence of Causality between Chemical Purity and Band-Edge Potential Fluctuations in Nanoparticle Ink-Based $Cu_2ZnSn(S,Se)_4$ Solar Cells. *J. Phys. D. Appl. Phys.* 52 (13), 135102. doi:10.1088/1361-6463/aafe60

Chen, C., Deng, Z., Tran, R., Tang, H., Chu, I.-H., and Ong, S. P. (2017). Accurate Force Field for Molybdenum by Machine Learning Large Materials Data. *Phys. Rev. Mater.* 1, 043603. doi:10.1103/PhysRevMaterials.1.043603

Chen, S., Walsh, A., Gong, X. G., and Wei, S. H. (2013). Classification of Lattice Defects in the Kesterite Cu_2ZnSnS_4 and $Cu_2ZnSnSe_4$ Earth-Abundant Solar Cell Absorbers. *Adv. Mater* 25 (11), 1522–1539. doi:10.1002/adma.201203146

Chen, W., Huang, X., Cheng, Q., Chen, C., Yun, D., and Zhang, F. (2016). Simulation Analysis of Heterojunction ZnO/CdS/Cu(In,Ga)Se_2 Thin-Film Solar Cells Using Wxamps. *Optik* 127 (1), 182–187. doi:10.1016/j.ijleo.2015.09.198

Cho, J. Y., Kim, S. Y., Nandi, R., Jang, J., Enkhbayar, E., Lee, D-K., et al. (2020). Achieving over 4% Efficiency for SnS/CdS Thin-Film Solar Cells by Improving the Heterojunction Interface Quality. *J. Mat. Chem. A* 8, 20658–20665. doi:10.1039/D0TA06937J

Contreras, M. A., Egaas, B., Dippo, P., Webb, J., Asher, S., Swartzlander, A., et al. (1998). Effects of Na Incorporation in CIGS Absorbers. *Inst. Phys. Conf. Ser.* 152, 333–337.

Courel, M., Andrade-Arvizu, J. A., and Vigil-Galán, O. (2015). Loss Mechanisms Influence on Cu_2ZnSnS_4/CdS-Based Thin Film Solar Cell Performance. *Solid-State Electron.* 111, 243–250. doi:10.1016/j.sse.2015.05.038

Courel, M., Andrade-Arvizu, J. A., and Vigil-Galán, O. (2014). Towards a CdS/Cu_2ZnSnS_4 Solar Cell Efficiency Improvement: a Theoretical Approach. *Appl. Phys. Lett.* 105 (23), 233501. doi:10.1063/1.4903826

Dai, X., Zhou, A., Feng, L., Wang, Y., Xu, J., and Li, J. (2014). Molybdenum Thin Films with Low Resistivity and Superior Adhesion Deposited by Radio-Frequency Magnetron Sputtering at Elevated Temperature. *Thin Solid Films* 567, 64–71. doi:10.1016/j.tsf.2014.07.043

Davies, D. W., Butler, K. T., Skelton, J. M., Xie, C., Oganov, A. R., and Walsh, A. (2018). Computer-aided Design of Metal Chalcohalide Semiconductors: from Chemical Composition to Crystal Structure. *Chem. Sci.* 9, 1022–1030. doi:10.1039/C7SC03961A

Davies, D. W., Butler, K. T., and Walsh., A. (2019). Data-driven Discovery of Photoactive Quaternary Oxides Using First-Principles Machine Learning. *Chem. Mat.* 31 (18), 7221–7230. doi:10.1021/acs.chemmater.9b01519

Davis, J. R., Rohatgi, A., Hopkins, R. H., Blais, P. D., Rai-Choudhury, P., McCormick, J. R., et al. (1980). Impurities in Silicon Solar Cells. *IEEE Trans. Electron Devices* 27 (4), 677–687. doi:10.1109/T-ED.1980.19922

De Angelis, F. (2014). Modeling Materials and Processes in Hybrid/organic Photovoltaics: From Dye-Sensitized to Perovskite Solar Cells. *Acc. Chem. Res.* 47 (11), 3349–3360. doi:10.1021/ar500089n

Dimoulas, A., Tsipas, P., Sotiropoulos, A., and Evangelou, E. K. (2006). Fermi-level Pinning and Charge Neutrality Level in Germanium. *Appl. Phys. Lett.* 89 (25), 252110. doi:10.1063/1.2410241

Dross, F., Robbelein, J., Vandevelde, B., Van Kerschaver, E., Gordon, I., Beaucarne, G., et al. (2007). Stress-Induced Large-Area Lift-Off of Crystalline Si Films. *Appl. Phys. A* 89 (1), 149–152. doi:10.1007/s00339-007-4195-2

Eames, C., Frost, J. M., Barnes, P. R., O'Regan, B. C., Walsh, A., and Islam, M. S. (2015). Ionic Transport in Hybrid Lead Iodide Perovskite Solar Cells. *Nat. Commun.* 6 (1), 7497–7498. doi:10.1038/ncomms8497

Edward, T. Y., McCaldin, J. O., and McGill, T. C. (1992). Band Offsets in Semiconductor Heterojunctions. *Solid state Phys.* 46, 1–146. doi:10.1016/S0081-1947(08)60397-5

Egger, D. A., Kronik, L., and Rappe, A. M. (2015). Theory of Hydrogen Migration in Organic-Inorganic Halide Perovskites. *Angew. Chem. Int. Ed.* 54 (42), 12437–12441. doi:10.1002/anie.201502544

Elbar, M., and Tobbeche, S. (2015). Numerical Simulation of CGS/CIGS Single and Tandem Thin-Film Solar Cells Using the Silvaco-Atlas Software. *Energy Procedia* 74, 1220–1227. doi:10.1016/j.egypro.2015.07.766

Even, J., Pedesseau, L., Tea, E., Almosni, S., Rolland, A., Robert, C., et al. (2014). Density Functional Theory Simulations of Semiconductors for Photovoltaic Applications: Hybrid Organic-Inorganic Perovskites and III/V Heterostructures. *Int. J. Photoenergy* 2014, 1–11. doi:10.1155/2014/649408

Fell, A., and Altermatt, P. P. (2018). A Detailed Full-Cell Model of a 2018 Commercial Perc Solar Cell in Quokka3. *IEEE J. Photovoltaics* 8 (6), 1443–1448. doi:10.1109/jphotov.2018.2863548

Fell, A. (2012). A Free and Fast Three-Dimensional/two-Dimensional Solar Cell Simulator Featuring Conductive Boundary and Quasi-Neutrality Approximations. *IEEE Trans. Electron Devices* 60 (2), 733–738. doi:10.1109/TED.2012.2231415

Feng, Y., Lunt, T., Sardei, F., and Zha, X. (2013). Implicit Coupling of Impurity Transport at the SOL-Core Interface. *Comput. Phys. Commun.* 184 (6), 1555–1561. doi:10.1016/j.cpc.2013.02.003

Franciosi, A, and Van de Walle, C. G. (1996). Heterojunction Band Offset Engineering. *Surf. Sci. Rep.* 25 (1-4), 1–140. doi:10.1016/0167-5729(95)00008-9

Francis Mott, N. (1939). The Theory of Crystal Rectifiers. *Proc. R. Soc. Lond. Ser. A. Math. Phys. Sci.* 171, 27–38. doi:10.1098/rspa.1939.0051

Fritsche, J., Kraft, D., Thissen, A., Mayer, T., Klein, A., and Jaegermann, W. (2001). Interface Engineering of Chalcogenide Semiconductors in Thin Film Solar Cells: CdTe as an Example. *MRS Online Proc. Libr. Opl.* 668, 66. doi:10.1557/proc-668-h6.6

Froitzheim, A., Stangl, R., Elstner, L., Kriegel, M., and Fuhs, W. (2003). "Afors-het: a Computer-Program for the Simulation of Heterojunction Solar Cells to Be Distributed for Public Use," in 3rd World Conference onPhotovoltaic Energy Conversion, 2003. Proceedings of (IEEE), 279–282.

Fritsche, J., Klein, A., and Jaegermann, W. (2005). Thin Film Solar Cells: Materials Science at Interfaces. *Adv. Eng. Mat.* 7, 914–920. doi:10.1002/ADEM.200500126

Führer, M., Farrell, D., and Ekins-Daukes, N. (2013). "Cpv Modelling with Solcore: An Extensible Modelling Framework for the Rapid Computational Simulation and Evaluation of Solar Cell Designs and Concepts," in AIP Conference Proceedings (American Institute of Physics), 34.

Gueymard, C. (1995). *SMARTS2: A Simple Model of the Atmospheric Radiative Transfer of Sunshine: Algorithms and Performance Assessment*. FL: Florida Solar Energy Center Cocoa.

Gundlach, K. H., and Simmons, J. G. (1969). Range of Validity of the Wkb Tunnel Probability, and Comparison of Experimental Data and Theory. *Thin Solid Films* 4 (1), 61–79. doi:10.1016/0040-6090(69)90021-2

Holmgren, W. F., Hansen, C. W., and Mark, A. (2018). Mikofski. Pvlib python: a python Package for Modeling Solar Energy Systems. *J. Open Source Softw.* 3 (29), 884. doi:10.21105/joss.00884

Holmgren, W. F., Hansen, C. W., and Mark, A. (2018). Mikofski. Pvlib python: a python Package for Modeling Solar Energy Systems. *J. Open Source Softw.* 3 (29), 884. doi:10.21105/joss.00884

Holmgren, W. F., Hansen, C. W., Stein, J. S., and Mikofski, M. A. (2018). "Review of Open Source Tools for Pv Modeling," in 2018 IEEE 7th World Conference on Photovoltaic Energy Conversion (WCPEC) (A Joint Conference of 45th IEEE PVSC, 28th PVSEC 34th EU PVSEC), 2557–2560. doi:10.1109/PVSC.2018.8548231

Houimi, A., Gezgin, S. Y., Mercimek, B., and Kılıç, H. Ş. (2021). Numerical Analysis of CZTS/n-Si Solar Cells Using Scaps-1d. A Comparative Study between Experimental and Calculated Outputs. *Opt. Mater.* 121, 111544. doi:10.1016/j.optmat.2021.111544

Huang, Y., Yu, C., Chen, W., Liu, Y., Li, C., Niu, C., et al. (2019). Band Gap and Band Alignment Prediction of Nitride-Based Semiconductors Using Machine Learning. *J. Mat. Chem. C* 7, 3238–3245. doi:10.1039/C8TC05554H

Itthibenchapong, V., Kokenyesi, R. S., Ritenour, A. J., Zakharov, L. N., Boettcher, S. W., Wager, J. F., et al. (2013). Earth-abundant Cu-Based Chalcogenide Semiconductors as Photovoltaic Absorbers. *J. Mat. Chem. C* 1, 657–662. doi:10.1039/C2TC00106C

Jackson, A. J., and Walsh, A. (2014). Abinitio Thermodynamic Model of Cu_2ZnSnS_4. *J. Mat. Chem. A* 2, 7829–7836. doi:10.1039/C4TA00892H10.1039/C4TA00892H

Jaegermann, W., Klein, A., and Mayer, T. (2009). Interface Engineering of Inorganic Thin-Film Solar Cells - Materials-Science Challenges for Advanced Physical Concepts. *Adv. Mat.* 21, 4196–4206. doi:10.1002/ADMA.200802457

Jain, A., Ong, S. P., Hautier, G., Chen, W., Richards, W. D., Dacek, S., et al. (2013). Commentary: The Materials Project: A Materials Genome Approach to Accelerating Materials Innovation. *Apl. Mater.* 1 (1), 011002. doi:10.1063/1.4812323

Jannat, F., Ahmed, S., and Alim, M. A. (2021). Performance Analysis of Cesium Formamidinium Lead Mixed Halide Based Perovskite Solar Cell with Moox as Hole Transport Material via Scaps-1d. *Optik* 228, 166202. doi:10.1016/j.ijleo.2020.166202

Ju, M.-G., Dai, J., Ma, L., Zhou, Y., and Zeng, X. C. (2020). $AgBiS_2$ as a Low-Cost and Eco-Friendly All-Inorganic Photovoltaic Material: Nanoscale Morphology-Property Relationship. *Nanoscale Adv.* 2, 770–776. doi:10.1039/C9NA00505F

Juan, E. (2022). A Tcad Semiconductor Device Simulator. *J. Open Source Softw.* 7 (70), 3898. doi:10.21105/joss.03898

Karthick, S., Velumani, S., and Bouclé, J. (2020). Experimental and Scaps Simulated Formamidinium Perovskite Solar Cells: A Comparison of Device Performance. *Sol. Energy*, 349–357. doi:10.1016/j.solener.2020.05.041

Kaur, K., Kumar, N., and Kumar, M. (2017). Strategic Review of Interface Carrier Recombination in Earth Abundant Cu–Zn–Sn–S–Se Solar Cells: Current Challenges and Future Prospects. *J. Mat. Chem. A* 5 (7), 3069–3090. doi:10.1039/c6ta10543b

Kephart, J. M., McCamy, J. W., Ma, Z., Ganjoo, A., Alamgir, F. M., and Sampath, W. S. (2016). Band Alignment of Front Contact Layers for High-Efficiency CdTe Solar Cells. *Sol. Energy Mater. Sol. Cells* 157, 266–275. doi:10.1016/j.solmat.2016.05.050

Kim, J., Jang, J., Suryawanshi, M. P., He, M., Heo, J., LeeLee, D. S., et al. (2020). Effect of a Graphene Oxide Intermediate Layer in $Cu_2ZnSn(S,Se)_4$ Solar Cells. *J. Mat. Chem. A* 8 (9), 4920–4930. doi:10.1039/c9ta13080b

Kim, S., Hood, S. N., van Gerwen, P., Whalley, L. D., and Carriercapture, A (2020). Anharmonic Carrier Capture. *J. Open Source Softw.* 5 (47), 2102. doi:10.21105/joss.02102

Kim, J., Park, S., Ryu, S., Oh, J., and Shin, B. (2017). Improving the Open-Circuit Voltage of Cu2ZnSnSe4thin Film Solar Cells via Interface Passivation. *Prog. Photovolt. Res. Appl.* 25, 308–317. doi:10.1002/PIP.2864

Kirklin, S., Saal, J. E., Meredig, B., Thompson, A., Doak, J. W., Aykol, M., et al. (2015). The Open Quantum Materials Database (OQMD): Assessing the Accuracy of DFT Formation Energies. *npj Comput. Mater* 1 (1), 15010. doi:10.1038/npjcompumats.2015.10

Koopmans, M., and Vincent, M. (2022). SIMsalabim: An Open-Source Drift-Diffusion Simulator for Semiconductor Devices. *J. Open Source Softw.* 7 (70), 3727. doi:10.21105/joss.03727

Kroemer, H. (2001). Nobel Lecture: Quasielectric Fields and Band Offsets: Teaching Electrons New Tricks. *Rev. Mod. Phys.* 73, 783–793. doi:10.1103/RevModPhys.73.783

Lanzetta, L., Webb, T., Zibouche, N., Liang, X., Ding, D., Min, G., et al. (2021). Degradation Mechanism of Hybrid Tin-Based Perovskite Solar Cells and the Critical Role of Tin (IV) Iodide. *Nat. Commun.* 12 (1), 2853. doi:10.1038/s41467-021-22864-z

Leijtens, T., Srimath Kandada, A. R., Eperon, G. E., Grancini, G., D'Innocenzo, V., Ball, J. M., et al. (2015a). Modulating the Electron-Hole Interaction in a Hybrid Lead Halide Perovskite with an Electric Field. *J. Am. Chem. Soc.* 137 (49), 15451–15459. doi:10.1021/jacs.5b09085

Leijtens, T., Eperon, G. E., NoelNoel, N. K., Habisreutinger, S. N., Petrozza, A., and Snaith, H. J. (2015b). Stability of Metal Halide Perovskite Solar Cells. *Adv. Energy Mat.* 5 (20), 1500963. doi:10.1002/aenm.201500963

Leijtens, T., Hoke, E. T., Grancini, G., Slotcavage, D. J., Eperon, G. E., Ball, J. M., et al. (2015). Mapping Electric Field-Induced Switchable Poling and Structural Degradation in Hybrid Lead Halide Perovskite Thin Films. *Adv. Energy Mat.* 5 (20), 1500962. doi:10.1002/aenm.201500962

Li, F., and Jen, A. K.-Y. (2022). Interface Engineering in Solution-Processed Thin-Film Solar Cells. *Acc. Mat. Res.* 3 (3), 272–282. doi:10.1021/accountsmr.1c00169

Li, J., Aierken, A., Liu, Y., Zhuang, Y., Yang, X., Mo, J. H., et al. (2021). A Brief Review of High Efficiency Iii-V Solar Cells for Space Application. *Front. Phys.* 8, 631925. doi:10.3389/fphy.2020.631925

Li, J., Mitzi, D. B., and Shenoy, V. B. (2011). Structure and Electronic Properties of Grain Boundaries in Earth-Abundant Photovoltaic Absorber $Cu_2ZnSnSe_4$. *Acs Nano* 5 (11), 8613–8619. doi:10.1021/nn203230g

Limpert, S., Ghosh, K., Wagner, H., Bowden, S., Honsberg, C., Goodnick, S., et al. (2014). "Results from Coupled Optical and Electrical Sentaurus Tcad Models of a Gallium Phosphide on Silicon Electron Carrier Selective Contact Solar Cell," in 2014 IEEE 40th Photovoltaic Specialist Conference (PVSC), pages 0836–0840. IEEE. doi:10.1109/pvsc.2014.6925045

Liu, F., Zeng, Q., Li, J., Hao, X., Ho-Baillie, A., Tang, J., et al. (2020). Emerging Inorganic Compound Thin Film Photovoltaic Materials: Progress, Challenges and Strategies. *Mater. Today* 41, 120–142. doi:10.1016/j.mattod.2020.09.002

Liu, W., Turkani, V. S., Akhavan, V., and Korgel, B. A. (2021). Photonic Lift-Off Process to Fabricate Ultrathin Flexible Solar Cells. *ACS Appl. Mat. Interfaces* 13 (37), 44549–44555. doi:10.1021/acsami.1c12382

Liu, Y., Heinzel, D., and Rockett, A. (2011). "A New Solar Cell Simulator: Wxamps," in 2011 37th IEEE Photovoltaic Specialists Conference, 002753. doi:10.1109/PVSC.2011.6186517

Liu, Y., Sun, Y., and Rockett, A. (2012a). A New Simulation Software of Solar Cells-wxAMPS. *Sol. Energy Mater. Sol. Cells* 98, 124–128. doi:10.1016/j.solmat.2011.10.010

Liu, Y., Sun, Y., and Rockett, A. (2012b). "Batch Simulation of Solar Cells by Using Matlab and Wxamps," in 2012 38th IEEE Photovoltaic Specialists Conference (IEEE). doi:10.1109/pvsc.2012.6317748

Lu, S., Zhou, Q., Ouyang, Y., Guo, Y., Li, Q., and Wang, J. (2018). Accelerated Discovery of Stable Lead-free Hybrid Organic-Inorganic Perovskites via Machine Learning. *Nat. Commun.* 9 (1), 3405. doi:10.1038/s41467-018-05761-w

Mansouri Tehrani, A., Ghadbeigi, L., Brgoch, J., and Sparks, T. D. (2017). Balancing Mechanical Properties and Sustainability in the Search for Superhard Materials. *Integr. Mater Manuf. Innov.* 6 (1), 1–8. doi:10.1007/s40192-017-0085-4

Meloni, S., Moehl, T., Tress, W., Franckevičius, M., Saliba, M., Lee, Y. H., et al. (2016). Ionic Polarization-Induced Current-Voltage Hysteresis in CH3NH3PbX3 Perovskite Solar Cells. *Nat. Commun.* 7 (1), 10334–10339. doi:10.1038/ncomms10334

Michael, S., Bates, A. D., and Green, M. S. (2005). "Silvaco Atlas as a Solar Cell Modeling Tool," in Conference Record of the Thirty-first IEEE Photovoltaic Specialists Conference, 2005 (IEEE), 719–721.

Michael, S. (2005). A Novel Approach for the Modeling of Advanced Photovoltaic Devices Using the Silvaco/atlas Virtual Wafer Fabrication Tools. *Sol. energy Mater. Sol. cells* 87 (1-4), 771–784. doi:10.1016/j.solmat.2004.07.050

Minemoto, T., Matsui, T., Takakura, H., Hamakawa, Y., Negami, T., Hashimoto, Y., et al. (2001). Theoretical Analysis of the Effect of Conduction Band Offset of

Window/CIS Layers on Performance of CIS Solar Cells Using Device Simulation. *Sol. Energy Mater. Sol. Cells* 67 (1-4), 83–88. doi:10.1016/s0927-0248(00)00266-x

Ming, W., Yang, D., Li, T., Zhang, L., and Du, M. H. (2018). Formation and Diffusion of Metal Impurities in Perovskite Solar Cell Material $CH_3 NH_3 PbI_3$: Implications on Solar Cell Degradation and Choice of Electrode. *Adv. Sci.* 5 (2), 1700662. doi:10.1002/advs.201700662

Moayedpour, S., Dardzinski, D., Yang, S., Hwang, A., and Marom, N. (2021). Structure Prediction of Epitaxial Inorganic Interfaces by Lattice and Surface Matching with Ogre. *J. Chem. Phys.* 155 (3), 034111. doi:10.1063/5.0051343

Mosconi, E., Ronca, E., and De Angelis, F. (2014). First-Principles Investigation of the TiO2/organohalide Perovskites Interface: The Role of Interfacial Chlorine. *J. Phys. Chem. Lett.* 5 (15), 2619–2625. doi:10.1021/jz501127k

Mostefaoui, M., Mazari, H., Khelifi, S., Bouraiou, A., and Dabou, R. (2015). Simulation of High Efficiency CIGS Solar Cells with Scaps-1d Software. *Energy Procedia* 74, 736–744. doi:10.1016/j.egypro.2015.07.809

Nakata, A., Baker, J. S., Mujahed, S. Y., PoultonPoulton, J. T. L., Arapan, S., Lin, J., et al. (2020). Large Scale and Linear Scaling Dft with the Conquest Code. *J. Chem. Phys.* 152 (16), 164112. doi:10.1063/5.000507410.1063/5.0005074

Nelson, J. A. (2003). *The Physics of Solar Cells*. London: World Scientific Publishing Company.

Nicholson, A. P., Martinez, U., Shah, A., Thiyagarajan, A., and Sampath, W. S. (2020). Atomistic Modeling of Energy Band Alignment in CdTe(1 0 0) and CdTe(1 1 1) Surfaces. *Appl. Surf. Sci.* 528, 146832. ISSN 0169-4332. doi:10.1016/j.apsusc.2020.146832

Nikander, V., Wei, J., Aho, A., Polojärvi, V., Tukiainen, A., and Guina, M. (2020). "Quasi-3d Optimization of Grid Architecture for Photovoltaic Converters Using Solcore," in 2020 International Conference on Numerical Simulation of Optoelectronic Devices (NUSOD) (IEEE), 51–52. doi:10.1109/nusod49422.2020.9217763

Nishimura, T., Kita, K., and Toriumi, A. (2007). Evidence for Strong Fermi-Level Pinning Due to Metal-Induced Gap States at Metal/Germanium Interface. *Appl. Phys. Lett.* 91 (12), 123123. doi:10.1063/1.2789701

Oba, F., and Kumagai, Y. (2018). Design and Exploration of Semiconductors from First Principles: A Review of Recent Advances. *Appl. Phys. Express* 11 (6), 060101. doi:10.7567/apex.11.060101

Oba, F., Togo, A., Tanaka, I., Paier, J., and Kresse, G. (2008). Defect Energetics in ZnO: A Hybrid Hartree-Fock Density Functional Study. *Phys. Rev. B* 77, 245202. doi:10.1103/PhysRevB.77.245202

Park, J.-S., Calbo, J., Jung, Y.-K., Whalley, L. D., and Walsh, A. (2019). Accumulation of Deep Traps at Grain Boundaries in Halide Perovskites. *ACS Energy Lett.* 4 (6), 1321–1327. doi:10.1021/acsenergylett.9b00840

Park, J.-S., Jung, Y.-K., Butler, K. T., and Walsh, A. (2018). Quick-start Guide for First-Principles Modelling of Semiconductor Interfaces. *J. Phys. Energy* 1 (1), 016001. doi:10.1088/2515-7655/aad928

Park, J.-S., and Walsh, A. (2021). Modeling Grain Boundaries in Polycrystalline Halide Perovskite Solar Cells. *Annu. Rev. Condens. Matter Phys.* 12 (1), 95–109. doi:10.1146/annurev-conmatphys-042020-025347

Passeri, D., Moscatelli, F., Morozzi, A., and Bilei, G. M. (2016). Modeling of Radiation Damage Effects in Silicon Detectors at High Fluences Hl-Lhc with Sentaurus Tcad. *Nucl. Instrum. Methods Phys. Res. Sect. A Accel. Spectrom. Detect. Assoc. Equip.*, 443–445. doi:10.1016/j.nima.2015.08.039

Pauling, L. (1929). The Principles Determining the Structure of Complex Ionic Crystals. *J. Am. Chem. Soc.* 51 (4), 1010–1026. doi:10.1021/ja01379a006

Pearce, P., and Ekins-Daukes, N. (2019). "Open-source Integrated Optical Modelling with Rayflare," in 2019 IEEE 46th Photovoltaic Specialists Conference (PVSC), 2627–2633. doi:10.1109/PVSC40753.2019.8980868

Peng, H., Scanlon, D. O., Stevanovic, V., Vidal, J., Watson, G. W., and Lany, S. (2013). Convergence of Density and Hybrid Functional Defect Calculations for Compound Semiconductors. *Phys. Rev. B*, 88:115201. doi:10.1103/PhysRevB.88.115201

Pelatt, B. D., Ravichandran, R., Wager, J. F., and Keszler, D. A. (2011). Atomic Solid State Energy Scale. *J. Am. Chem. Soc.* 133 (42), 16852–16860. doi:10.1021/ja204670s

Peressi, M., Binggeli, N., and Baldereschi, A. (1998). Band Engineering at Interfaces: Theory and Numerical Experiments. *J. Phys. D. Appl. Phys.* 31 (11), 1273–1299. doi:10.1088/0022-3727/31/11/002

Polizzotti, A., RepinsRepins, I. L., Noufi, R., Wei, S.-H., and Mitzi, D. B. (2013). The State and Future Prospects of Kesterite Photovoltaics. *Energy Environ. Sci.* 6 (11), 3171–3182. doi:10.1039/c3ee41781f

Prabhakar, T., and Jampana, N. (2011). Effect of Sodium Diffusion on the Structural and Electrical Properties of Cu_2ZnSnS_4 Thin Films. *Sol. Energy Mater. Sol. Cells* 95 (3), 1001–1004. doi:10.1016/j.solmat.2010.12.012

Prentice, J. C. A., Aarons, J., Womack, J. C., Allen, A. E. A., Andrinopoulos, L., Anton, L., et al. (2020). The Onetep Linear-Scaling Density Functional Theory Program. *J. Chem. Phys.* 152 (17), 174111. doi:10.1063/5.0004445

Qi, Y.-F., Kou, D.-X., Zhou, W.-H., Zhou, Z.-J., Tian, Q.-W., Meng, Y.-N., et al. (2017). Engineering of Interface Band Bending and Defects Elimination via a Ag-Graded Active Layer for Efficient $(Cu,Ag)_2ZnSn(S,Se)_4$ Solar Cells. *Energy Environ. Sci.* 10 (11), 2401–2410. doi:10.1039/c7ee01405h

Qu, Y., Zoppi, G., and Beattie, N. S. (2016a). Selenization Kinetics in $Cu_2ZnSn(S,Se)_4$ Solar Cells Prepared from Nanoparticle Inks. *Sol. Energy Mater. Sol. Cells* 158, 130–137. doi:10.1016/j.solmat.2015.12.016

Qu, Y., Zoppi, G., and Beattie, N. S. (2016b). The Role of Nanoparticle Inks in Determining the Performance of Solution Processed Cu_2 $ZnSn(S,Se)_4$ Thin Film Solar Cells. *Prog. Photovolt. Res. Appl.* 24 (6), 836–845. doi:10.1002/pip.2756

Ratcliff, L. E., Dawson, W., Fisicaro, G., Caliste, D., Mohr, S., Degomme, A., et al. (2020). Flexibilities of Wavelets as a Computational Basis Set for Large-Scale Electronic Structure Calculations. *J. Chem. Phys.* 152 (19), 194110. doi:10.1063/5.0004792

Raymand, D., van Duin, A. C. T., Baudin, M., Hermansson, K., and Hermansson, K. (2008). A Reactive Force Field (Reaxff) for Zinc Oxide. *Surf. Sci.* 602 (5), 1020–1031. doi:10.1016/j.susc.2007.12.023

Raymond, T., and Kronik, L. (2018). Charge Density and Band Offsets at Heterovalent Semiconductor Interfaces. *Adv. Theory Simulations* 1 (1), 1700001. doi:10.1002/adts.201700001

Refaei, M. (2017). *Modeling and Simulation of III-Nitride-Based Solar Cells Using NextnanoRTM*. Fayetteville: Master's thesis, University of Arkansas, Little Rock.

Richter, A., Jan, B., Frank, F., Fell, A., Martin, H., and Glunz, S. W. (2017). n-Type Si Solar Cells with Passivating Electron Contact: Identifying Sources for Efficiency Limitations by Wafer Thickness and Resistivity Variation. *Sol. Energy Mater. Sol. Cells* 173, 96–105. doi:10.1016/j.solmat.2017.05.042

Rolf, S., Kriegel, M., and Schmidt, M. (2006). "Afors-het, Version 2.2, a Numerical Computer Program for Simulation of Heterojunction Solar Cells and Measurements," in 2006 IEEE 4th World Conference on Photovoltaic Energy Conference (IEEE), 1350–1353.

Rondiya, S., Jadhav, Y., Nasane, M., Jadkar, S., and Dzade, N. Y. (2019). Interface Structure and Band Alignment of CZTS/CdS Heterojunction: An Experimental and First-Principles Dft Investigation. *Mater. (Basel)* 12 (24), 4040. doi:10.3390/ma12244040

Rondiya, S. R., Jadhav, Y., Dzade, N. Y., Ahammed, R., Goswami, T., De Sarkar, A., et al. (2020). Experimental and Theoretical Study into Interface Structure and Band Alignment of the $Cu_2Zn_{1-x}Cd_xSnS_4$ Heterointerface for Photovoltaic Applications. *ACS Appl. Energy Mat.* 3 (6), 5153–5162. doi:10.1021/acsaem.9b02314

Sai, G., Senftle, T. P., and Carter, E. A. (2018). Understanding the Effects of Cd and Ag Doping in Cu_2ZnSnS_4 Solar Cells. *Chem. Mat.* 30 (14), 4543–4555. doi:10.1021/acs.chemmater.8b00677

Salomé, P. M. P., Malaquias, J., Fernandes, P. A., and Cunha, A. F. d. (2010). Mo Bilayer for Thin Film Photovoltaics Revisited. *J. Phys. D. Appl. Phys.* 43 (34), 345501. doi:10.1088/0022-3727/43/34/345501

Sayre, L., Camarillo Abad, E., Pearce, P., Chausse, P., Pierre-Marie, C., Shields, P., et al. (2022). Ultra-thin GaAs Solar Cells with Nanophotonic Metal-Dielectric Diffraction Gratings Fabricated with Displacement Talbot Lithography. *Prog. Photovoltaics Res. Appl.* 30 (1), 96–108. doi:10.1002/pip.3463

Schleife, A., Fuchs, F., Rödl, C., Furthmüller, J., and Bechstedt, F. (2009). Branch-point Energies and Band Discontinuities of III-Nitrides and III-/II-oxides from Quasiparticle Band-Structure Calculations. *Appl. Phys. Lett.* 94 (1), 012104. doi:10.1063/1.3059569

Scragg, J. J., Dale, P. J., Colombara, D., and Peter, L. M. (2012a). Thermodynamic Aspects of the Synthesis of Thin-Film Materials for Solar Cells. *ChemPhysChem* 13 (12), 3035–3046. doi:10.1002/cphc.201200067

Scragg, J. J., Wätjen, J. T., Edoff, M., Ericson, T., Kubart, T., and Platzer-Björkman, C. (2012b). A Detrimental Reaction at the Molybdenum Back Contact in $Cu_2ZnSn(S,Se)_4$ Thin-Film Solar Cells. *J. Am. Chem. Soc.* 134 (47), 19330–19333. doi:10.1021/ja308862n

Shin, B., Zhu, Y., Bojarczuk, N. A., Chey, S. J., and Guha, S. (2012). Control of an Interfacial MoSe2 Layer in Cu2ZnSnSe4 Thin Film Solar Cells: 8.9% Power Conversion Efficiency with a Tin Diffusion Barrier. *Appl. Phys. Lett.* 101 (5), 053903. doi:10.1063/1.4740276

Silva, B., Paul, L., Theristis, M., and Hubert, S. (2022). Pypvrpm: Photovoltaic Reliability and Performance Model in python. *J. Open Source Softw.* 7 (71), 4093. doi:10.21105/joss.04093

Simya, O. K., Mahaboobbatcha, A., and Balachander, K. (2015). A Comparative Study on the Performance of Kesterite Based Thin Film Solar Cells Using Scaps Simulation Program. *Superlattices Microstruct.* 82, 248–261. doi:10.1016/j.spmi.2015.02.020

Singh-Miller, N. E., and Marzari, N. (2009). Surface Energies, Work Functions, and Surface Relaxations of Low-Index Metallic Surfaces from First Principles. *Phys. Rev. B* 80, 235407. doi:10.1103/PhysRevB.80.235407

Sun, W., and Ceder, G. (2013). Efficient Creation and Convergence of Surface Slabs. *Surf. Sci.* 617, 53–59. doi:10.1016/j.susc.2013.05.016

Suryawanshi, M. P., GhorpadeGhorpade, U. V., Suryawanshi, U. P., He, M., Kim, J., Gang, M. G., et al. (2017). Aqueous-Solution-Processed $Cu_2ZnSn(S,Se)_4$ Thin-Film Solar Cells via an Improved Successive Ion-Layer-Adsorption-Reaction Sequence. *ACS omega* 2 (12), 9211–9220. doi:10.1021/acsomega.7b00967

Sutanto, A. A., Szostak, R., Drigo, N., Queloz, V. I. E., Marchezi, P. E., Germino, J. C., et al. (2020). *In Situ* Analysis Reveals the Role of 2D Perovskite in Preventing Thermal-Induced Degradation in 2D/3D Perovskite Interfaces. *Nano Lett.* 20 (5), 3992–3998. doi:10.1021/acs.nanolett.0c01271

Tabor, D. P., Roch, L. M., Saikin, S. K., Kreisbeck, C., Sheberla, D., Montoya, J. H., et al. (2018). Accelerating the Discovery of Materials for Clean Energy in the Era of Smart Automation. *Nat. Rev. Mater* 3 (5), 5–20. doi:10.1038/s41578-018-0005-z

Tamura, T., Karasuyama, M., Kobayashi, R., Arakawa, R., Shiihara, Y., and Takeuchi, I. (2017). Fast and Scalable Prediction of Local Energy at Grain Boundaries: Machine-Learning Based Modeling of First-Principles Calculations. *Model. Simul. Mat. Sci. Eng.* 25 (7), 075003. doi:10.1088/1361-651x/aa8276

Thomas, M., Kronik, L., Hodes, G., and Cahen, D. (2016). Hybrid Organic—Inorganic Perovskites: Low-Cost Semiconductors with Intriguing Charge-Transport Properties. *Nat. Rev. Mater.* 1 (1), 1–16. doi:10.1038/natrevmats.2015.7

Thompson, A. P., Swiler, L. P., and Trott, C. R. (2015). Spectral Neighbor Analysis Method for Automated Generation of Quantum-Accurate Interatomic Potentials. *J. Comput. Phys.* 285, 316. doi:10.1016/j.jcp.2014.12.018

Toroker, M. C., Kanan, D. K., Alidoust, N., Isseroff, L. Y., Liao, P., and Carter, E. A. (2011). First Principles Scheme to Evaluate Band Edge Positions in Potential Transition Metal Oxide Photocatalysts and Photoelectrodes. *Phys. Chem. Chem. Phys.* 13, 16644–16654. doi:10.1039/C1CP22128K

Tucher, N., Eisenlohr, J., Gebrewold, H., Kiefel, P., Höhn, O., Hauser, H., et al. (2016). Optical Simulation of Photovoltaic Modules with Multiple Textured Interfaces Using the Matrix-Based Formalism Optos. *Opt. Express* 24 (14), A1083. doi:10.1364/OE.24.0A1083

van der Giessen, E., Schultz, P. A., Bertin, N., Bulatov, V. V., Cai, W., Csányi, G., et al. (2020). Roadmap on Multiscale Materials Modeling. *Model. Simul. Mat. Sci. Eng.* 28 (4), 043001. doi:10.1088/1361-651x/ab7150

Verschraegen, J., and Burgelman, M. (2007). Numerical Modeling of Intra-band Tunneling for Heterojunction Solar Cells in Scaps. *Thin Solid Films* 515 (15), 6276–6279. doi:10.1016/j.tsf.2006.12.049

Wada, T., Kohara, N., Nishiwaki, S., and Negami, T. (2001). Characterization of the Cu(In,Ga)Se_2 /Mo Interface in CIGS Solar Cells. *Thin Solid Films* 387, 118–122. doi:10.1016/S0040-6090(00)01846-0

Walsh, A., and Zunger, A. (2017). Instilling Defect Tolerance in New Compounds. *Nat. Mater* 16 (10), 964–967. doi:10.1038/nmat4973

Wang, L., Chen, F., and Ai, Y. (2011). Simulation of High Efficiency Heterojunction Solar Cells with Afors-Het. *J. Phys. Conf. Ser.* 276, 012177. doi:10.1088/1742-6596/276/1/012177

Wang, Y., Sumpter, B. G., Huang, J., Zhang, H., Liu, P., Yang, H., et al. (2015). Density Functional Studies of Stoichiometric Surfaces of Orthorhombic Hybrid Perovskite $CH_3NH_3PbI_3$. *J. Phys. Chem. C* 119 (2), 1136–1145. doi:10.1021/jp511123s

Wei, H. M., Gong, H. B., Chen, L., Zi, M., and Cao, B. Q. (2012). Photovoltaic Efficiency Enhancement of Cu_2O Solar Cells Achieved by Controlling Homojunction Orientation and Surface Microstructure. *J. Phys. Chem. C* 116 (19), 10510–10515. doi:10.1021/jp301904s

Wei, S.-H., and Zunger, A. (1998). Calculated Natural Band Offsets of All II-VI and III-V Semiconductors: Chemical Trends and the Role of Cation D Orbitals. *Appl. Phys. Lett.* 72 (16), 2011–2013. doi:10.1063/1.121249

Weston, L., and Stampfl, C. (2018). Machine Learning the Band Gap Properties of Kesterite I2–II–IV–V4 Quaternary Compounds for Photovoltaics Applications. *Phys. Rev. Mater.* 2, 085407. doi:10.1103/PhysRevMaterials.2.085407

Wilson, H. F., Tang, C., and Barnard, A. S. (2016). Morphology of Zinc Oxide Nanoparticles and Nanowires: Role of Surface and Edge Energies. *J. Phys. Chem. C* 120 (17), 9498–9505. doi:10.1021/acs.jpcc.6b01479

Wu, H.-M., Liang, S.-C., Lin, Y.-L., Ni, C.-Y., Bor, H.-Y., Tsai, D.-C., et al. (2012). Structure and Electrical Properties of Mo Back Contact for Cu(In, Ga)Se_2 Solar Cells. *Vacuum* 86 (12), 1916–1919. doi:10.1016/j.vacuum.2012.04.036

Wu, J., Liu, S.-C., Li, Z., Wang, S., Xue, D.-J., Lin, Y., et al. (2021). Strain in Perovskite Solar Cells: Origins, Impacts and Regulation. *Natl. Sci. Rev.* 8 (8), 03. doi:10.1093/nsr/nwab047

Wu, Y-C., and Jhan, Y-R. (2018). "Introduction of Synopsys Sentaurus Tcad Simulation," in *3D TCAD Simulation for CMOS Nanoeletronic Devices* (Springer). doi:10.1007/978-981-10-3066-6_1

Xiao, Z., Yuan, Y., Shao, Y., Wang, Q., Dong, Q., Bi, C., et al. (2015). Giant Switchable Photovoltaic Effect in Organometal Trihalide Perovskite Devices. *Nat. Mater* 14 (2), 193–198. doi:10.1038/nmat4150

Xu, J., Buin, A., Ip, A. H., Li, W., Voznyy, O., Comin, R., et al. (2015). Perovskite-fullerene Hybrid Materials Suppress Hysteresis in Planar Diodes. *Nat. Commun.* 6 (1), 7081–7088. doi:10.1038/ncomms8081

Xu, X., Qu, Y., Barrioz, V., Zoppi, G., and Beattie, N. S. (2018). Reducing Series Resistance in $Cu_2ZnSn(S,Se)_4$ Nanoparticle Ink Solar Cells on Flexible Molybdenum Foil Substrates. *RSC Adv.* 8 (7), 3470–3476. doi:10.1039/c7ra13336g

Xu, X., Qu, Y., Campbell, S., Le Garrec, M., Ford, B., Barrioz, V., et al. (2019). Solution Processing Route to Na Incorporation in CZTSSe Nanoparticle Ink Solar Cells on Foil Substrate. *J. Mater Sci. Mater Electron* 30 (8), 7883–7889. doi:10.1007/s10854-019-01108-3

Yan, Y., Jiang, C.-S., Noufi, R., Wei, S.-H., Moutinho, H. R., and Al-Jassim, M. M. (2007). Electrically Benign Behavior of Grain Boundaries in PolycrystallineCuInSe2Films. *Phys. Rev. Lett.* 99 (23), 235504. doi:10.1103/physrevlett.99.235504

Yang, T.-Y., Gregori, G., Pellet, N., Grätzel, M., and Maier, J. (2015). The Significance of Ion Conduction in a Hybrid Organic-Inorganic Lead-Iodide-Based Perovskite Photosensitizer. *Angew. Chem.* 127 (27), 8016–8021. doi:10.1002/ange.201500014

Yao, Y., Xu, X., Zhang, X., Zhou, H., Gu, X., and Xiao, S. (2018). Enhanced Efficiency in Bifacial Hit Solar Cells by Gradient Doping with Afors-Het Simulation. *Mater. Sci. Semicond. Process.* 77, 16–23. doi:10.1016/j.mssp.2018.01.009

Yaşar, S., Kahraman, S., Çetinkaya, S., Apaydın, Ş., İsmail, B., and Uluer, İ. (2016). Numerical Thickness Optimization Study of CIGS Based Solar Cells with Wxamps. *Optik* 127 (20), 8827–8835. doi:10.1016/j.ijleo.2016.06.094

Yuan, Z.-K., Chen, S., Xiang, H., Gong, X.-G., Walsh, A., Park, J.-S., et al. (2015). Engineering Solar Cell Absorbers by Exploring the Band Alignment and Defect Disparity: The Case of Cu- and Ag-Based Kesterite Compounds. *Adv. Funct. Mat.* 25 (43), 6733–6743. doi:10.1002/adfm.201502272

Zhao, Y.-C., Zhou, W.-K., Zhou, X., Liu, K.-H., Yu, D.-P., and Zhao, Q. (2017). Quantification of Light-Enhanced Ionic Transport in Lead Iodide Perovskite Thin Films and its Solar Cell Applications. *Light Sci. Appl.* 6 (5), e16243. doi:10.1038/lsa.2016.243

Zhao, Y., Zhou, W., Ma, W., Meng, S., Li, H., Wei, J., et al. (2016). Correlations between Immobilizing Ions and Suppressing Hysteresis in Perovskite Solar Cells. *ACS Energy Lett.* 1 (1), 266–272. doi:10.1021/acsenergylett.6b00060

Zoppi, G., Beattie, N. S., Major, J. D., Miles, R. W., and Forbes, I. (2011). Electrical, Morphological and Structural Properties of Rf Magnetron Sputtered Mo Thin

Films for Application in Thin Film Photovoltaic Solar Cells. *J. Mater Sci.* 46 (14), 4913–4921. doi:10.1007/s10853-011-5404-0

Zur, A., and McGill, T. C. (1984). Lattice Match: An Application to Heteroepitaxy. *J. Appl. Phys.* 55 (2), 378–386. doi:10.1063/1.333084

Conflict of Interest: The authors declare that the research was conducted in the absence of any commercial or financial relationships that could be construed as a potential conflict of interest.

Publisher's Note: All claims expressed in this article are solely those of the authors and do not necessarily represent those of their affiliated organizations, or those of the publisher, the editors and the reviewers. Any product that may be evaluated in this article, or claim that may be made by its manufacturer, is not guaranteed or endorsed by the publisher.

frontiers | Frontiers in Chemistry

PERSPECTIVE
published: 27 June 2022
doi: 10.3389/fchem.2022.938353

Pyrrolopyrrole-Based Aza-BODIPY Small Molecules for Organic Field-Effect Transistors

Daohai Zhang[1]†, Dongxu Liang[2]†, Liang Gu[2] and Haichang Zhang[2]**

[1]School of Chemical Engineering of Guizhou Minzu University, Guiyang, China, [2]Key Laboratory of Rubber-Plastics of Ministry of Education/Shandong Province (QUST), School of Polymer Science and Engineering, Qingdao University of Science and Technology, Qingdao, China

Diketopyrrolopyrrole (DPP), due to its good planarity, π-conjugate structure, thermal stability, and structural modifiability, has received much attention from the scientific community as an excellent semiconductor material for its applications in the field of optoelectronics, such as organic solar cells, organic photovoltaics, and organic field effect transistors. In this study, a new small molecule, pyrrolopyrrole aza-BODIPY (PPAB), based on the thiophene-substituted DPP structure was developed using the Schiff-base formation reaction of DPP and heteroaromatic amines. Absorption spectroscopy, electrochemistry, X-ray diffraction, molecular theoretical simulation calculation were performed, and organic field-effect transistor properties based on PPAB were investigated. It was found that PPAB exhibits a broad absorption range in the visible and near-infrared regions, which is attributed to its long-range conjugate structure. In addition, it is worth noting that PPAB has multiple F atoms resulting in the low LUMO level, which is conducive to the injection and transportation of charge carriers between the semiconductor layer and the electrode. Meanwhile, its hole carrier mobility is up to 1.3×10^{-3} cm^2 V^{-1} s^{-1} due to its large conjugate structure, good intramolecular charge transfer effect, and high degree of coplanarity. In this study, a new chromophore with electron-deficient ability for designing high-performance semiconductors was successfully synthesized.

Keywords: pyrrolopyrrole-based aza-BODIPY, electron-deficient, conjugated materials, hole transport mobility, organic field-effect transistor

OPEN ACCESS

Edited by:
Yue Liu,
Liaoning Technical University, China

Reviewed by:
Yalong Wang,
Hainan University, China
Detebg Zhang,
Qingdao University, China

***Correspondence:**
Daohai Zhang
zhangdaohai6235@163.com
Haichang Zhang
haichangzhang@hotmail.com

†*These authors have contributed equally to this work*

Specialty section:
This article was submitted to Electrochemistry, a section of the journal Frontiers in Chemistry

Received: *07 May 2022*
Accepted: *16 May 2022*
Published: *27 June 2022*

Citation:
Zhang D, Liang D, Gu L and Zhang H (2022) Pyrrolopyrrole-Based Aza-BODIPY Small Molecules for Organic Field-Effect Transistors Front. Chem. 10:938353 doi: 10.3389/fchem.2022.938353

INTRODUCTION

Diketopyrrolopyrrole (DPP), ever since it was first discovered in the 1970s, has great potential as an excellent semiconductor material for optoelectronic devices (Yao et al., 2015; Mitchell and Jones, 2018) because of its excellent molecular structural characteristics such as excellent planarity, large conjugated molecular skeleton, structural modifiability, and good stability, which has attracted extensive research interest (Rochat et al., 1985; Guo et al., 2014; Zhao et al., 2016; Huang et al., 2017; Zhang et al., 2017). Recently, in-depth research was conducted on the DPP structure and hundreds of DPP derivatives were reported. These DPP derivatives show excellent performance in various electronic devices because of their unique molecular core structure, which greatly promotes the development of organic electronic device materials (Luo et al., 2016; Oh et al., 2016).

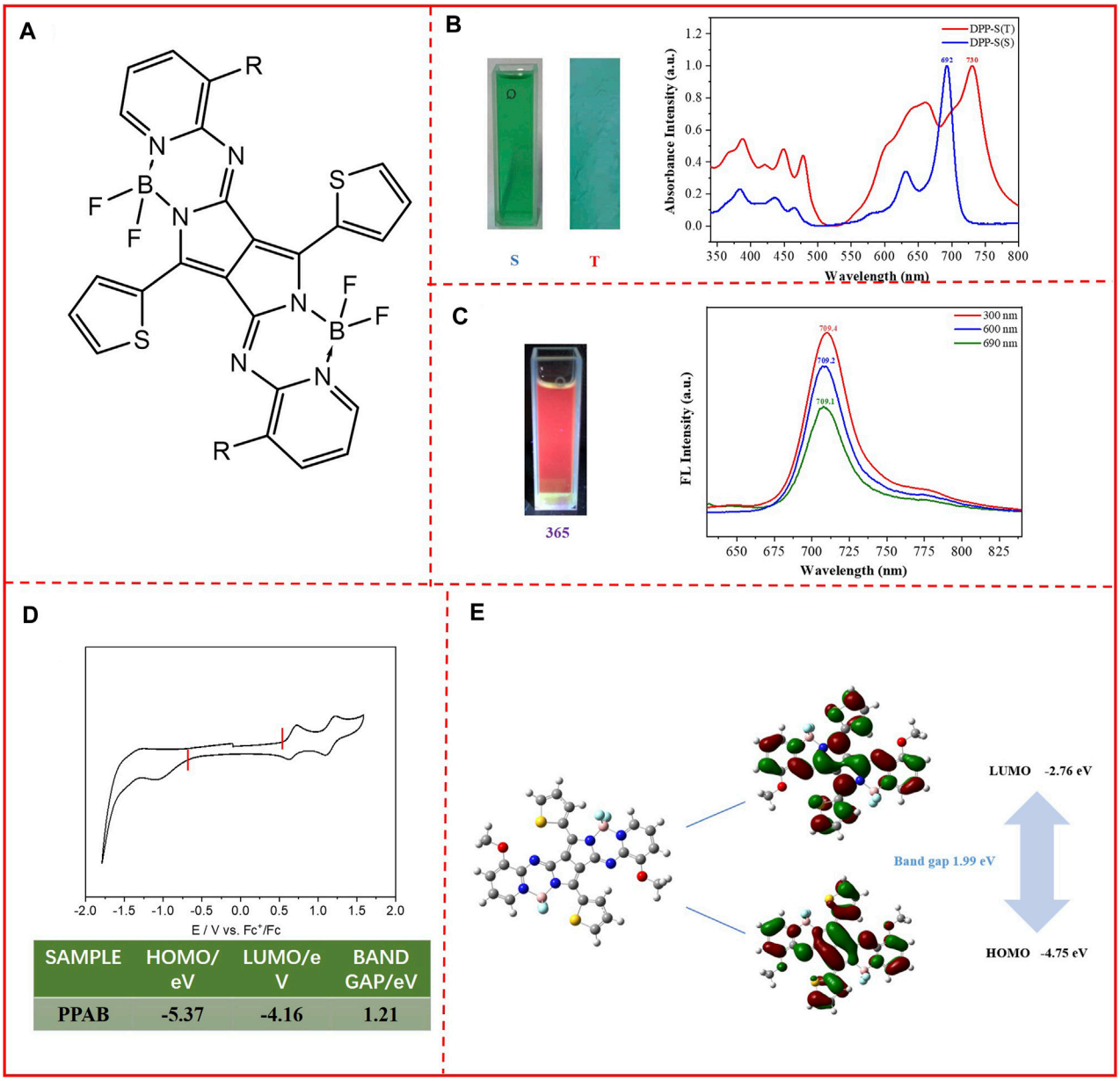

SAMPLE	HOMO/eV	LUMO/eV	BAND GAP/eV
PPAB	-5.37	-4.16	1.21

FIGURE 1 | (A) Chemical structure of PPAB; **(B)** photos of PPAB in the chloroform solution (left) and in the thin film state (right). UV/vis absorption spectra of PPAB in the chloroform solution (S) and thin films (T); **(C)** photos of PPAB in the chloroform solution excited by 365 nm light; PL spectra of PPAB in chloroform, excited by 300, 600, and 690 nm; **(D)** cyclic voltammograms of PPAB. Electrolyte: 0.1 M $TBAPF_6$ in acetonitrile. Potential calculated vs. ferrocene. Scan rate: 100 mV s^{-1}; $T = 25°C$; **(E)** computational calculations of the simplified PPAB obtained at the B3LYP/6-31G* level and molecular orbital surfaces of the HOMO and LUMO energy levels and the band gap of PPAB.

The organic field-effect transistor (OFET) is a kind of device that relies on the external electric field to induce current on the surface of the semiconductor layer, which can be changed by regulating the intensity of the external enhanced electric field (Zhang et al., 2020). Because of its small size, light weight, low power consumption, and special variable conductivity, OFET has become one of the most important components in the microelectronics industry. Charge carrier mobility is one of the most critical parameters used to characterize the device performance, which directly reflects the carrier movement in the semiconductor material layer (Zhao et al., 2016; Shi et al., 2020). To obtain OFETs with high performance and high electron mobility, the designed semiconductor layer molecules generally need to have a longer conjugate structure, good planarity and π–π stacking structure, and an excellent intramolecular charge transfer (ICT) effect, which is beneficial to match the energy level of the metal electrode. Therefore, the DPP structure is one of the best candidate structures (Qu and Tian, 2012; Yuto et al.,

2018). In addition, in order to ensure a lower LUMO level, it is necessary to introduce atoms or groups with greater polarity, such as nitrogen atoms, fluorine atoms, and cyano groups (Jo et al., 2015). These groups can be introduced in the process of structural modification of DPP. At the same time, they can also give it better planarity and conjugate structure. Although molecules with high carrier mobility have been developed recently, the continuous development of new strategies for high-carrier-mobility molecules is still an important topic.

In this study, a new small molecule (pyrrolopyrrole aza-BODIPY, or PPAB; **Figure 1A**) based on the DPP structure was synthesized using the Schiff-base formation reaction between thiophene-substituted DPP and heteroaromatic amines, and in this structure, four fluorine atoms and a large number of N atoms are also introduced, which are in favor of reducing the LUMO level (Donaghey et al., 2013; Wiktorowski et al., 2014; Lin et al., 2018; Lee et al., 2019). The 3,6 positions of the DPP structure were replaced with thiophene groups to improve the electron enrichment of molecules (Sonar et al., 2012; Murlidhar, 2018; Li et al., 2014; Jiang et al., 2017; Li et al., 2017). More importantly, the extension was performed using the B—N bridge in the longitudinal direction of the structure to improve the π–π stacking area (Dou et al., 2016; Long et al., 2016). The results indicate that PPAB shows a lower LUMO level of about −2.76 eV. OFET devices were also prepared with PPAB as the semiconductor layer, and the carrier mobility measured was up to $1.3 \times 10^{-3}\ cm^2\ V^{-1}\ s^{-1}$, which is mainly due to the synergy between its large conjugate structure that is conducive to carrier transport and good planarity that is beneficial to improving the π–π stacking area (Yuto et al., 2018; Bao et al., 2020). This study also has great potential not only in designing small molecules but also in the block construction of polymers.

RESULTS AND DISCUSSION

Optical Properties

The molecule presents a green color in both the chloroform solution and film state (**Figure 1B**). In order to investigate the optical properties of PPAB, the absorption spectra of PPAB in the thin film state and in the chloroform solution were measured. It was found that PPAB exhibits a broad absorption range between 550 and 800 nm. In the chloroform solution, the maximum absorption peak occurs at 692 nm, while in the solid film, the maximum absorption peak shifts to 730 nm. This red shift of nearly 40 nm can be attributed to the aggregation and tight packing of molecules in the solid film compared to the solution, and PPAB tends to exist in the form of single molecules in the solution. From the onset optical absorption, the optical band gap is calculated to be 1.55 eV. In addition, the chloroform solution of PPAB can exhibit an obvious red color with the excitation of 365 nm light as shown in **Figure 1C**. The photoluminescence (PL) spectra were also recorded; due to its wide range of absorption, three different wavelengths of light (300, 600, and 690 nm) were chosen to excite it. The results are shown in **Figure 1C**; the emission peaks of PPAB are observed at 709 nm, with a red shift of nearly 20 nm relative to 692 nm corresponding to the maximum absorption peak. The experiment of fluorescence emission was also carried out in the thin film, but it did not show fluorescence emission, which might be caused by the aggregation-induced quenching effect. This indicates the PPAB thin film with a strong aggregation between molecules and the formation of excimer association complexes or excimer complexes by π–π interactions, which consumes the energy of excited states.

Electrochemical Properties and Molecular Theoretical Simulation

According to the initial reduction potential and oxidation potential, the LUMO/HOMO energy level of the monomer can be estimated. In **Figure 1D**, the PPAB monomer shows a reversible and redox curve, and the first initial oxidation and reduction positions appear at 0.57 and −0.64 V, respectively. Based on this, the HOMO and LUMO energy levels are −5.37 eV and −4.16 eV, respectively. The energy band gap is about 1.21 eV, which is 0.33 eV smaller compared to the optical band gap. It is worth noting that the four fluorine atoms and a deal of nitrogen atoms introduced play an important role in the reduction of LUMO energy level as the result of increasing the electron-deficient ability of the molecular skeleton, which is in favor of matching with the metal electrode.

In order to further determine the characteristics of the molecular structure, computation calculations were performed by density-functional theory (DFT) at the B3LYP/6-31 (d,p) level using simplified chromophores with the methyl group instead of the alky chain. It was found that the molecular skeleton has good coplanarity, which is conducive to the formation of π–π stacking between adjacent molecules (**Figure 1E**). Furthermore, the electrons in the HOMO orbitals were mainly localized at the thiophene DPP with part of the core of the backbone, while the LUMO orbitals were mainly localized at the core of PPAB with part of the electron wave function along the conjugation backbone structure, and the HOMO and LUMO orbitals show a relatively even state, which means that the molecule has a potentially strong ICT effect. The PPAB measured by cyclic voltammetry may have a certain degree of molecular aggregation, which leads to a level different from the HOMO and LUMO energy levels calculated by theoretical simulation. The narrow band gap measured by the cyclic voltammetry shows the strong interaction of molecules in the aggregated state, which is conducive to the effective extension of conjugation for carrier transportation to a certain extent.

X-Ray Diffraction

In order to better understand the structure of this small molecule, X-ray diffraction (XRD) was used to investigate and to characterize the structure of the PPAB thin film (**Figure 2A**). The XRD patterns of PPAB exhibit primary diffraction peaks at $2\theta = 1.56^{\circ}$, 5.56°, and 11.78° for PPAB, which correspond to the inter-lamellar distance of 1.935 nm. The peak shape also indicates that the molecule will have a preferential growth trend during aggregation, which is consistent with the flake state of the molecule. In addition, this relatively compact structure is

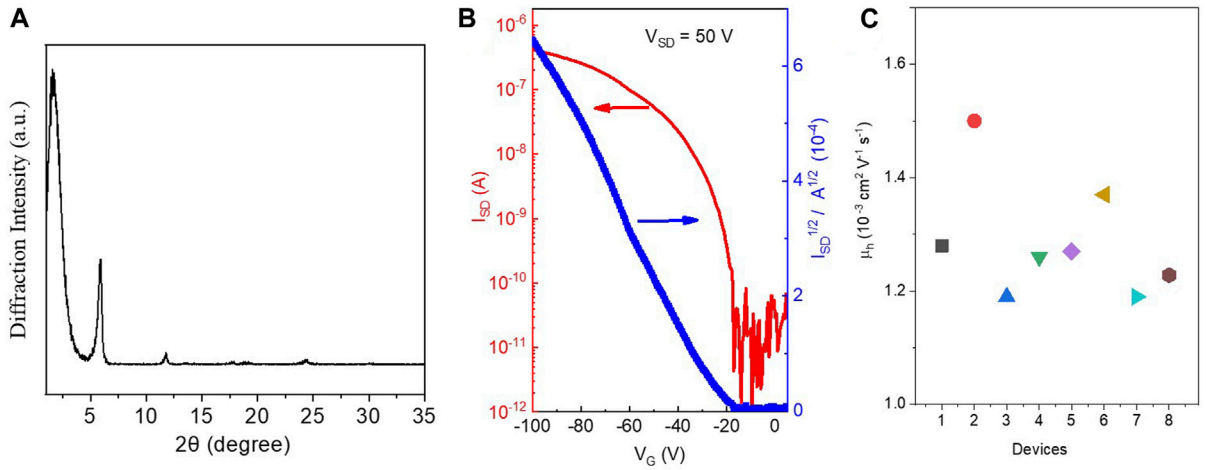

FIGURE 2 | (A) Transmission XRD diagrams of PPAB; **(B)** characteristics of the OFET devices of PQ1; **(C)** hole transport mobility obtained from eight different devices.

consistent with the results of molecular theoretical simulation mentioned above.

Organic Field-Effect Transistors

The charge transport properties of PPAB were evaluated by fabricating OFET devices of PPAB in a bottom-gate and bottom-contact configuration on a silicon wafer using a layer of 300 nm SiO_2 as the dielectric material. The devices with chromophores were fabricated by directly drop-coating the chloroform solution of the compound onto the octadecyltrichlorosilane-treated silicon wafer with pre-patterned gold source and drain electrodes. The devices were measured under the vacuum condition after thermal annealing at 50°C for 5 min in an argon-filled glove box to remove the remaining residual solvent. The PPAB-based device exhibits p-type semiconductor properties with an average hole transport mobility (μ_h) of around 1.3×10^{-3} cm^2 V^{-1} s^{-1} (the highest μ_h of 1.5×10^{-3} cm^2 V^{-1} s^{-1}; **Figures 2B,C**). The high charge carrier mobility of PPAB is mainly ascribed to two factors: 1) PPAB shows a high degree of coplanarity of the molecular core and the large π-conjugation system, which is beneficial for the charge transport within the individual molecules; 2) the PPAB film features strong aggregation, which is an advantage for the charge transport between the adjacent molecules. The I_{on}/I_{off} ratio for the IIDG-AB-based OFETs is in the range of 10^5~10^6, and the threshold voltage for the device operation is −19 V.

CONCLUSION

In summary, an electron-deficient chromophore, namely, PPAB, was successfully synthesized by a Schiff-base reaction between thiophene-substituted DPP and heteroaromatic amines in the presence of titanium tetrachloride. The PPAB compound shows an ultra-low LUMO level (only around −4.16 eV). The study of optical properties indicates that there is around 40 nm bathochromic shift for PPAB from the solution to the thin film state, which indicates a strong aggregation with a broad optical absorption range between 500 and 800 nm, which makes it a potential light absorber for photovoltaic applications. The OFETs constructed by PPAB as the semiconductor layer present a clear p-type behavior with a maximum electron mobility of 1.5×10^{-3} cm^2 V^{-1} s^{-1}. Our results indicate that PPAB is a promising electron-deficient chromophore to construct semiconductors for OFETs. In addition, we believe that this study can pave the way for future molecular design and engineering to fabricate high-performing semiconductor materials.

DATA AVAILABILITY STATEMENT

The original contributions presented in the study are included in the article/**Supplementary Material**; further inquiries can be directed to the corresponding authors.

AUTHOR CONTRIBUTIONS

DZ designed and characterized the molecule. In addition, the manuscript was revised by him. DL synthesized and characterized the materials. In addition, part of the manuscript was written by him. LG help synthesized the materials. HZ designed the manuscript. In addition, part of the manuscript was written and revised by him.

FUNDING

HZ acknowledges the support from Young Taishan Scholars under Grant no. 201909120. The Natural Science Foundation of China (Grant no. 52163001), Guizhou Province Science and

Technology Plan Projects (Grant nos. CXTD [2021]005, [2018]1012), Baiyun district Science and Technology Plan Projects (Grant no. [2020]28), and the Polymer Composites Engineering Research Center of Guizhou Minzu University (Grant no. GZMUGCZX [2021]01) are acknowledged.

REFERENCES

Bao, W. W., Li, R., Dai, Z. C., Tang, J., Shi, X., Geng, J. T., et al. (2020). Diketopyrrolopyrrole (DPP)-based Materials and its Applications: a Review. *Front. Chem.* 8, 679. doi:10.3389/fchem.2020.00679

Donaghey, J. E., Sohn, E.-H., Ashraf, R. S., Anthopoulos, T. D., Watkins, S. E., Song, K., et al. (2013). Pyrroloindacenodithiophene Polymers: the Effect of Molecular Structure on OFET Performance. *Polym. Chem.* 4, 3537–3544. doi:10.1039/c3py00335c

Dou, C., Long, X., Ding, Z., Xie, Z., Liu, J., and Wang, L. (2016). An Electron-Deficient Building Block Based on the B←N Unit: An Electron Acceptor for All-Polymer Solar Cells. *Angew. Chem.* 128, 1458–1462. doi:10.1002/ange.201508482

Fusco, S., Barra, M., Bonomo, M., Cassinese, A., Centore, R., Chiarella, F., et al. (2021). Novel DPP Derivatives Functionalized with Auxiliary Electron-Acceptor Groups and Characterized by Narrow Bandgap and Ambipolar Charge Transport Properties. *Dyes Pigments* 186, 109026. doi:10.1016/j.dyepig.2020.109026

Guo, X., Puniredd, S. R., He, B., Marszalek, T., Baumgarten, M., Pisula, W., et al. (2014). Combination of Two Diketopyrrolopyrrole Isomers in One Polymer for Ambipolar Transport. *Chem. Mat.* 26, 3595–3598. doi:10.1021/cm5017245

Huang, Y., Chen, H., Yang, J., Tian, W., and Wang, W. (2017). 3D-Printed OFETs of the 1,4-Bis(3-Phenylquinoxalin-2-Yl)benzene-Based Polymer Semiconductors. *Polym. Chem.* 8, 4878–4886. doi:10.1039/C7PY00810D

Jiang, Z., Ni, Z., Wang, H., Wang, Z., Zhang, J., Qiu, G., et al. (2017). Versatile Asymmetric Thiophene/benzothiophene Flanked Diketopyrrolopyrrole Polymers with Ambipolar Properties for OFETs and OSCs. *Polym. Chem.* 8, 5603–5610. doi:10.1039/C7PY00940B

Jo, J. W., Bae, S., Liu, F., Russell, T. P., and Jo, W. H. (2015). Comparison of Two D–A Type Polymers with Each Being Fluorinated on D and A Unit for High Performance Solar Cells. *Adv. Funct. Mat.* 25, 120–125. doi:10.1002/adfm.201402210

Kage, Y., Mori, S., Ide, M., Saeki, A., Furuta, H., and Shimizu, S. (2018). Blackening of Aza-BODIPY Analogues by Simple Dimerization: Panchromatic Absorption of a Pyrrolopyrrole Aza-BODIPY Dimer. *Mat. Chem. Front.* 2, 112–120. doi:10.1039/C7QM00438A

Lee, S. M., Lee, H. R., Dutta, G. K., Lee, J., Oh, J. H., and Yang, C. (2019). Furan-flanked Diketopyrrolopyrrole-Based Chalcogenophene Copolymers with Siloxane Hybrid Side Chains for Organic Field-Effect Transistors. *Polym. Chem.* 10, 2854–2862. doi:10.1039/C9PY00448C

Li, W., Roelofs, W. S. C., Turbiez, M., Wienk, M. M., and Janssen, R. A. J. (2014). Polymer Solar Cells with Diketopyrrolopyrrole Conjugated Polymers as the Electron Donor and Electron Acceptor. *Adv. Mat.* 26, 3304–3309. doi:10.1002/adma.201305910

Li, Z., Xu, X., Zhang, W., Genene, Z., Mammo, W., Yartsev, A., et al. (2017). High-photovoltage All-Polymer Solar Cells Based on a Diketopyrrolopyrrole-Isoindigo Acceptor Polymer. *J. Mat. Chem. A* 5, 11693–11700. doi:10.1039/C6TA09379E

Lin, F.-J., Lin, S.-D., Chin, C.-H., Chuang, W.-T., and Hsu, C.-S. (2018). Novel Conjugated Polymers Based on Bis-Dithieno[3,2-B;2′,3′-D]pyrrole Vinylene Donor and Diketopyrrolopyrrole Acceptor: Side Chain Engineering in Organic Field Effect Transistors. *Polym. Chem.* 9, 28–37. doi:10.1039/C7PY01340J

Liu, Q., Sun, H., Blaikie, C., Caporale, C., Manzhos, S., Feron, K., et al. (2018). Naphthalene Flanked Diketopyrrolopyrrole Based Organic Semiconductors for High Performance Organic Field Effect Transistors. *New J. Chem.* 42, 12374–12385. doi:10.1039/C8NJ01453A

Long, X., Ding, Z., Dou, C., Zhang, J., Liu, J., and Wang, L. (2016). Polymer Acceptor Based on Double B←N Bridged Bipyridine (BNBP) Unit for High-Efficiency All-Polymer Solar Cells. *Adv. Mat.* 28, 6504–6508. doi:10.1002/adma.201601205

Luo, H., Yu, C., Liu, Z., Zhang, G., Geng, H., Yi, Y., et al. (2016). Remarkable Enhancement of Charge Carrier Mobility of Conjugated Polymer Field-Effect Transistors upon Incorporating an Ionic Additive. *Sci. Adv.* 2, e1600076. doi:10.1002/adma.20120146410.1126/sciadv.1600076

Mitchell, V. D., and Jones, D. J. (2018). Advances toward the Effective Use of Block Copolymers as Organic Photovoltaic Active Layers. *Polym. Chem.* 9, 795–814. doi:10.1039/C7PY01878A

Oh, J. Y., Rondeau-Gagné, S., Chiu, Y.-C., Chortos, A., Lissel, F., Wang, G.-J. N., et al. (2016). Intrinsically Stretchable and Healable Semiconducting Polymer for Organic Transistors. *Nature* 539, 411–415. doi:10.1038/nature20102

Qu, S., and Tian, H. (2012). Diketopyrrolopyrrole (DPP)-based Materials for Organic Photovoltaics. *Chem. Commun.* 48, 3039–3051. doi:10.1039/C2CC17886A

Rochat, A. C., Iqbal, A., Pfenninger, J., and Casser, L. (1985). *Process for Dyeing a High Molecular Organic Material, Polycyclic Compounds and Their Preparation*. Switzerland: European Patent.

Shi, D., Liu, Z., Ma, J., Zhao, Z., Tan, L., Lin, G., et al. (2020). Half-Fused Diketopyrrolopyrrole-Based Conjugated Donor-Acceptor Polymer for Ambipolar Field-Effect Transistors. *Adv. Funct. Mat.* 30, 1910235. doi:10.1002/adfm.201910235

Sonar, P., Foong, T. R. B., Singh, S. P., Li, Y., and Dodabalapur, A. (2012). A Furan-Containing Conjugated Polymer for High Mobility Ambipolar Organic Thin Film Transistors. *Chem. Commun.* 48, 8383–8385. doi:10.1039/c2cc33093h

Wiktorowski, S., Rosazza, C., Winterhalder, M. J., Daltrozzo, E., and Zumbusch, A. (2014). Water-soluble Pyrrolopyrrole Cyanine (PPCy) NIR Fluorophores. *Chem. Commun.* 50, 4755–4758. doi:10.1039/c4cc01014k

Yao, J., Yu, C., Liu, Z., Luo, H., Yang, Y., Zhang, G., et al. (2015). Significant Improvement of Semiconducting Performance of the Diketopyrrolopyrrole-Quaterthiophene Conjugated Polymer through Side-Chain Engineering via Hydrogen-Bonding. *J. Am. Chem. Soc.* 138, 173–185. doi:10.1021/jacs.5b09737

Zhang, H., Deng, R., Wang, J., Li, X., Chen, Y.-M., Liu, K., et al. (2017). Crystalline Organic Pigment-Based Field-Effect Transistors. *ACS Appl. Mat. Interfaces* 9, 21891–21899. doi:10.1021/acsami.7b03170

Zhang, H., Li, R., Deng, Z., Cui, S., Wang, Y., Zheng, M., et al. (2020). π-Conjugated Oligomers Based on Aminobenzodifuranone and Diketopyrrolopyrrole. *Dyes Pigments* 181, 108552. doi:10.1016/j.dyepig.2020.108552

Zhao, N., Ai, N., Cai, M., Wang, X., Pei, J., and Wan, X. (2016). Thiophene-fused Isoindigo Based Conjugated Polymers for Ambipolar Organic Field-Effect Transistors. *Polym. Chem.* 7, 235–243. doi:10.1039/C5PY01488C

SUPPLEMENTARY MATERIAL

The Supplementary Material for this article can be found online at: https://www.frontiersin.org/articles/10.3389/fchem.2022.938353/full#supplementary-material

Conflict of Interest: The authors declare that the research was conducted in the absence of any commercial or financial relationships that could be construed as a potential conflict of interest.

Publisher's Note: All claims expressed in this article are solely those of the authors and do not necessarily represent those of their affiliated organizations or those of the publisher, the editors, and the reviewers. Any product that may be evaluated in this article or claim that may be made by its manufacturer is not guaranteed or endorsed by the publisher.

frontiers | Frontiers in Chemistry

PERSPECTIVE
published: 28 June 2022
doi: 10.3389/fchem.2022.919552

High Lithium Storage Performance of Co Ion-Doped $Li_4Ti_5O_{12}$ Induced by Fast Charge Transport

M. Wang[1,2], Y. Chen[1], C. X. Yang[1], Y. H. Zeng[1], P. F. Fang[1], W. Wang[1] and X. L. Wang[1,2]*

[1]School of Materials Science and Engineering, Liaoning Technical University, Fuxin, China, [2]Key Laboratory of Mineral High Value Conversion and Energy Storage Materials of Liaoning Province, Fuxin, China

In this study, Co_3O_4-doped $Li_4Ti_5O_{12}$ (LTO) composite was designed and synthesized by the hydrothermal reduction method and metal doping modification method. The microstructure and electrochemical performance of the Co_3O_4-doped $Li_4Ti_5O_{12}$ composite were characterized by XRD, SEM, TEM, electrochemical impedance spectroscopy, and galvanostatic tests. The results showed that $Li_4Ti_5O_{12}$ particles attached to lamellar Co_3O_4 constituted a heterostructure and Co ion doped into $Li_4Ti_5O_{12}$ lattice. This Co ion-doped microstructure improved the charge transportability of $Li_4Ti_5O_{12}$ and inhibited the gas evolution behavior of $Li_4Ti_5O_{12}$, which enhanced the lithium storage performance. After 20 cycles, the discharge specific capacity reached stability, and the capacity retention maintained 99% after 1,000 cycles at 0.1 A/g (compared to the capacity at the 20th cycle). It had an excellent rate performance and long cycle stability, in which the capacity reached 174.6 mA h/g, 2.2 times higher than that of $Li_4Ti_5O_{12}$ at 5 A/g.

Keywords: metallic ion doping, Li4Ti5O12, charge transport, lithium storage performance, the microstructure

OPEN ACCESS

Edited by:
Meng Zheng,
Qingdao Haiwan Science and Technology Industry Research Institute Co., Ltd., China

Reviewed by:
Xiao Lyu,
Shenyang Ligong University, China
Yong Yan,
Beijing University of Technology, China

****Correspondence:***
M. Wang
wangming@lntu.edu.cn

Specialty section:
This article was submitted to Electrochemistry, a section of the journal Frontiers in Chemistry

Received: *13 April 2022*
Accepted: *26 April 2022*
Published: *28 June 2022*

Citation:
Wang M, Chen Y, Yang CX, Zeng YH, Fang PF, Wang W and Wang XL (2022) High Lithium Storage Performance of Co Ion-Doped $Li_4Ti_5O_{12}$ Induced by Fast Charge Transport. Front. Chem. 10:919552. doi: 10.3389/fchem.2022.919552

INTRODUCTION

Lithium-ion batteries have the advantages of high energy density, high charge transport rate, long cycle life, high security, and no memory effect. Therefore, it has been widely used in the field of consumer electronics and electric vehicles (Chen et al., 2013; Liu et al., 2013; Yang et al., 2015a; Yang et al., 2015b; Liu et al., 2015; Li Z et al., 2016; Li H. Z et al., 2016; Li S et al., 2016; Qu et al., 2018; Lu et al., 2019). $Li_4Ti_5O_{12}$ (LTO) was widely studied as anode material for lithium-ion batteries due to its good electrochemical performance (Zhang et al., 2013; Sun et al., 2014; Yan, 2014; You et al., 2018; Wang, 2020; Wang, 2021). However, the low theoretical specific capacity, the low charge transport rate, and the poor electrical conductivity led to serious polarization during rapid charge and discharge, which greatly limited its wide application (Shen et al., 2012; Kim et al., 2013; Zettsu et al., 2014; Tan and Xue, 2018). In recent years, many researchers have carried out several modification studies of pure LTO, including carbon coating, ion doping, and nanocrystallization. (Tang et al., 2009; Cheng et al., 2010; Shi et al., 2011; Li et al., 2013; Ma et al., 2013; Wang et al., 2013; Cheng et al., 2014; Li et al., 2014; Liu et al., 2014; Zhang et al., 2021). In this study, layered Co_3O_4 and spherical LTO heterostructures with large specific surface area and short ion diffusion length were prepared by the ion doping method. The composite has excellent electrochemical performance using the microstructure characterization and electrochemical performance test.

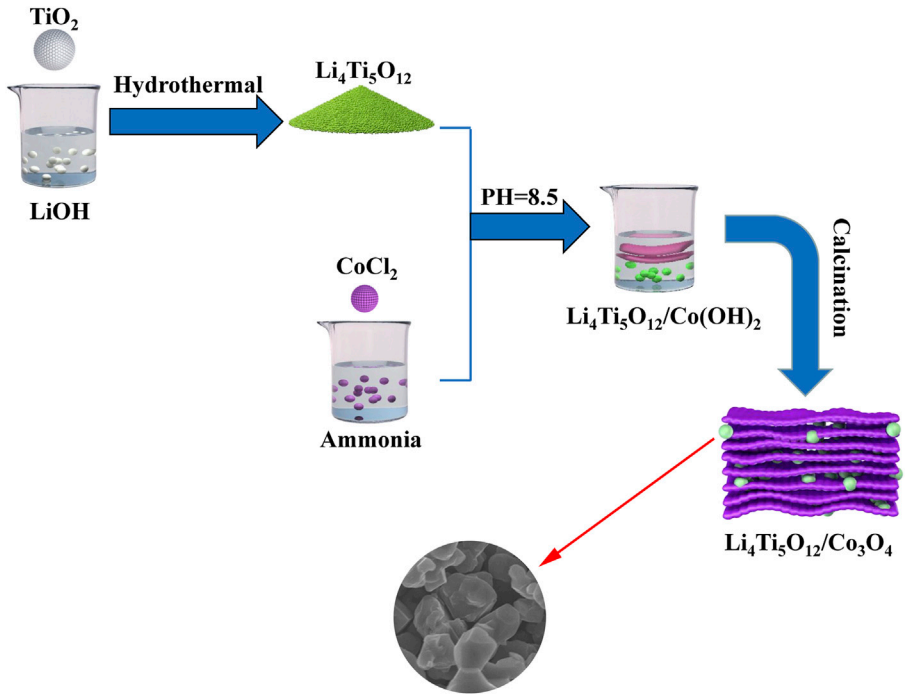

FIGURE 1 | Schematic diagrams of the synthesis of the $Li_4Ti_5O_{12}/Co_3O_4$ composite.

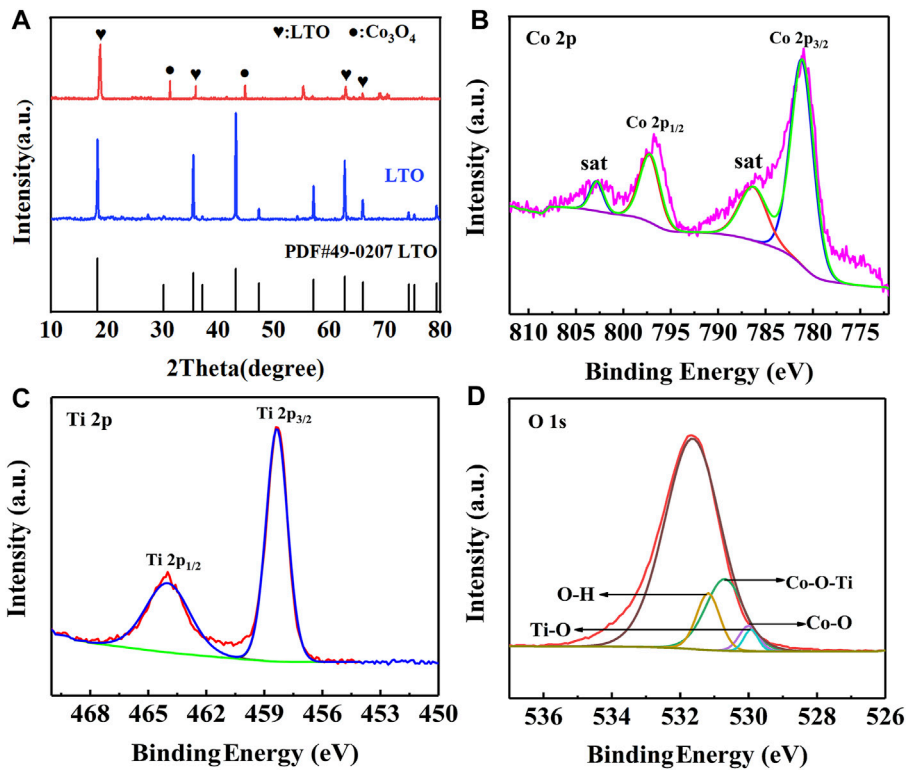

FIGURE 2 | (A) XRD patterns of $Li_4Ti_5O_{12}$ and $Li_4Ti_5O_{12}/Co_3O_4$ composite. **(B–D)** XPS patterns of $Li_4Ti_5O_{12}/Co_3O_4$ composite. **(B)** Co 2p; **(C)** Ti 2p; **(D)** O 1s.

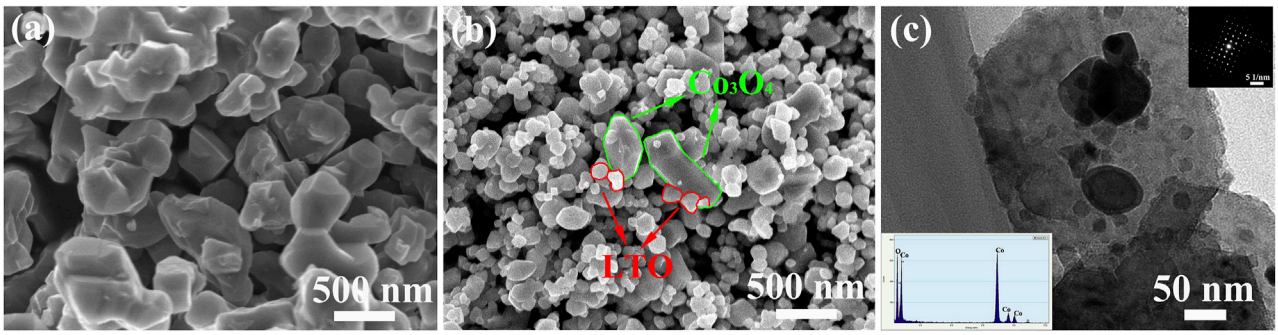

FIGURE 3 | (A) SEM image of $Li_4Ti_5O_{12}$ particles; **(B)** SEM image of $Li_4Ti_5O_{12}/Co_3O_4$ composites; **(C)** TEM morphology of $Li_4Ti_5O_{12}/Co_3O_4$ composites (inset: EDS of the Co_3O_4 sheet and SAED pattern of $Li_4Ti_5O_{12}$ particle).

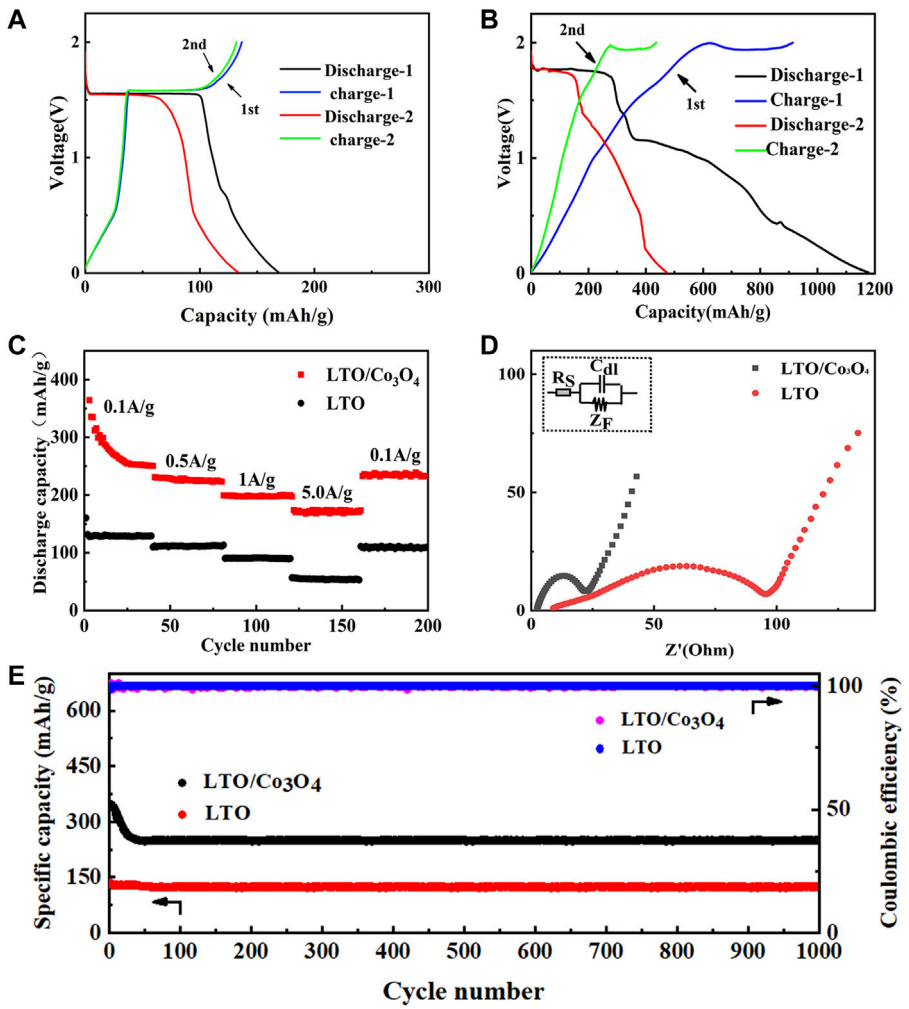

FIGURE 4 | (A) The first and second charge/discharge curves of $Li_4Ti_5O_{12}$. **(B)** The first and second charge/discharge curves of $Li_4Ti_5O_{12}/Co_3O_4$. **(C)** The rate performance comparison of $Li_4Ti_5O_{12}$ and $Li_4Ti_5O_{12}/Co_3O_4$. **(D)** The EIS (AC impedance) diagram of $Li_4Ti_5O_{12}$ and $Li_4Ti_5O_{12}/Co_3O_4$. **(E)** Cycle performance curves comparison of $Li_4Ti_5O_{12}$ and $Li_4Ti_5O_{12}/Co_3O_4$ at 0.1A/g.

EXPERIMENTAL

Firstly, 1.5 mg of $CoCl_2$ was dissolved in 30 ml dilute ammonia solution (0.3 mol/L). The pH value of the above solution was adjusted to 8.5 by concentrated ammonia solution and stood for 12 h. The formed precipitate (α-$Co(OH)_2$) was filtered and dried. Then, a certain mass of α-$Co(OH)_2$, LiOH, and TiO_2 was mixed and placed in a 100 ml Teflon-lined stainless steel autoclave and heated at 90°C for 12 h. After the temperature was cooled to room temperature, the solution was filtered and dried. The precursors were heated at 800°C for 4 h in a tube furnace. The obtained product was LTO/Co_3O_4 powder. Finally, CR2025-type coin cells were assembled in a high-purity Ar-filled ZKX glovebox. The schematic diagram of the synthesis of the LTO/Co_3O_4 composite is shown in **Figure 1**.

The phase composition of the specimen was characterized by XRD (SHIMADZU XRD-6100). The microstructure and morphology of the specimen were analyzed by SEM (JSM-7500F) and FEI TEM (Tecnai G2T20). The charge and discharge performance, rate performance, cycle performance, and Coulombic efficiency, among others, were tested on the battery performance test system (NEWARE). Electrochemical impedance spectroscopy (EIS) was tested on the CHI660E electrochemical workstation.

RESULTS AND DISCUSSION

The XRD pattern of LTO and LTO/Co_3O_4 composites prepared by the hydrothermal method is shown in **Figure 2**. It was found that the diffraction peak of the LTO/Co_3O_4 composite at 18.3°, 35.6°, 62.8°, and 66.1° corresponded to the crystal planes of (111), (311), (440), and (531), respectively. The characteristic diffraction peak of Co_3O_4 at 31.3° and 44.8° corresponded to the crystal planes of (220) and (440), respectively. In addition, it was observed that the diffraction peak of the LTO/Co_3O_4 composite shifted significantly to the right. For the (111) crystal plane of LTO, when Co ions were doped into the LTO lattice, the diffraction peak of the composite shifted to the right at approximately 0.5°; the reason for the radius of the Co atom (1.26 Å) was less than that of the Ti atom (1.45 Å), indicating that LTO and Co_3O_4 have a good combination.

The surface chemical composition and interfacial bonding state of the LTO/Co_3O_4 composite were analyzed by XPS, as shown in **Figure 2**. The high-resolution spectra of Co 2p, Ti 2p, and O 1s are shown in **Figures 2B–D**, respectively. It can be seen from **Figure 2B** that the two signal peaks located at 795.7 and 779.8 eV corresponded to the Co $2p_{3/2}$ and Co $2p_{1/2}$ of Co 2p, respectively, and each diffraction peak was accompanied by a satellite peak (Yang et al., 2022). The two characteristic peaks of Ti 2p at 464.3 and 458.6 eV were the spin-orbital peaks of Ti $2p_{1/2}$ and Ti $2p_{3/2}$, respectively (see **Figure 2C**), which was consistent with Zhou's results (Zhou et al., 2006). In addition, **Figure 2D** shows the Ti-O, Co-O, O-H, and Co-O-Ti bonds, four diffraction peaks, corresponding to 529.9, 530.0, 532.1, and 530.7 eV, respectively. The formation of the Co-O-Ti bond was successfully induced by hydrothermal synthesis of the LTO/Co_3O_4 composite, which was consistent with the reports in the literature (Xu et al., 2020). There is a synergistic effect between the surface of LTO and Co_3O_4, which can effectively improve the electrochemical performance of the composite. At the same time, the unsaturated O atoms in the composite combined with H atoms in water to form an O-H bond. It can also be seen from **Figure 2D** that the peak intensity of the Ti-O bond was significantly lower than that of the Co-O-Ti bond; the reason for the formation of the Co-O-Ti bond weakened the Ti-O bond, indicating that Co ions were successfully doped into LTO lattice.

Figure 3 shows the SEM morphology and the TEM morphology of LTO and LTO/Co_3O_4 composite. **Figure 3A** shows that the diameters of pure LTO nanoparticles were approximately 200 nm. It can be seen from **Figure 3B** that LTO spherical nanoparticles were uniformly attached to the surface and interlayer of Co_3O_4, in which the particle size of LTO was approximately 50 ± 20 nm and the lamellar diameter of Co_3O_4 was approximately 150 ± 50 nm. The addition of Co_3O_4 effectively inhibited the growth of LTO nanoparticles. The grain refinement would improve the specific surface area of the composite (Li et al., 2018). **Figure 3C** shows that the LTO nanoparticles were uniformly dispersed on the layered surface of Co_3O_4, indicating that LTO and Co_3O_4 combined well. In addition, EDS analysis showed that the composite contained Co and O elements, indicating the existence of Co_3O_4 in the composite (see the inset of **Figure 3C**).

The first and second charge/discharge curves of LTO and LTO/Co_3O_4 composite at 0.1 A/g are shown in **Figures 4A,B**, respectively. It can be seen that the first discharge specific capacity of LTO and LTO/Co_3O_4 composite was 175 and 1,178.0 mA h/g, and the first Coulomb efficiency was 76.3% and 77.6%, respectively. The addition of Co_3O_4 improved the ion diffusion rate of the composite, increasing the first discharge specific capacity of the composite. In addition, the second discharge specific capacity of LTO and LTO/Co_3O_4 composite was 133.2 and 473 mA h/g, respectively. The first and second discharge specific capacity of LTO and LTO/Co_3O_4 composite was quite different. The reason was that the anode material would form SEI film at the electrode/electrolyte interface after the first cycle, which consumed part of Li^+, causing irreversible capacity loss. Compared with LTO (1.55 V vs. Li/Li^+ (Wang et al., 2016)), the discharge voltage platform of the LTO/Co_3O_4 composite was 1.75 V (vs. Li/Li^+). The higher discharge voltage platform was beneficial in inhibiting the growth of lithium dendrites and forming a stable SEI film, which improves the cycle performance of the composite. **Figure 4C** shows the rate performance of LTO and LTO/Co_3O_4 composite for 200 cycles at different current densities. The discharge specific capacity of LTO/Co_3O_4 composite was higher than that of LTO at different current densities, indicating better rate performance. The discharge specific capacity of LTO at 20, 60, 100, and 140 cycles corresponded to 128.8, 110.9, 91.1, and 53.6 mA h/g, respectively. After 160 cycles, the discharge specific capacity was stable at 111.1 mA h/g, and the capacity retention rate was 86.3% (compared to the capacity at the 20th cycle). The discharge specific capacity of LTO/Co_3O_4 at 20, 60, 100, and

140 cycles corresponded to 274.5, 226.2, 201.1, and 174.6 mA h/g, respectively. After 160 cycles, the discharge specific capacity was stable at 230.6 mA h/g, and the capacity retention rate was 84% (compared to the capacity at the 20th cycle). The EIS (AC impedance) test results of LTO and LTO/Co_3O_4 composite are shown in **Figure 4D**. The curve in **Figure 4D** was fitted by an analog circuit, where R_S is ohmic resistance, C_{dl} is the double capacitance between electrode and electrolyte, and Z_F is the series connection between R_{CT} (charge transfer resistance) and Z_W (Warburg resistance). The results showed that the internal resistance of LTO and LTO/Co_3O_4 composite was 9.0 and 2.5 Ω, and the charge transfer resistance was 95.4 and 19.5 Ω, respectively. Compared with pure LTO, the LTO/Co_3O_4 composite has lower resistance because the incorporation of Co_3O_4 provided more charge transfer channels, improving the charge transport rate of the LTO/Co_3O_4 composite. The long cycle performance of the LTO/Co_3O_4 composite at 0.1 A/g for 1,000 cycles is shown in **Figure 4E**. **Figure 4E** shows that the discharge specific capacity of the composite decreased significantly in the first 20 cycles due to the continuous formation of SEI, leading to the continuous decomposition of Li^+. With the increase in the cycle number, the SEI film gradually tended to be stable and the discharge specific capacity loss was smaller. After 1,000 cycles, the discharge specific capacity of the LTO and LTO/Co_3O_4 composite was maintained at 124.3 and 248.4 mA h/g, and the capacity retention rate reached 96.5% and 99% (compared to the capacity at the 20th cycle), respectively. The LTO/Co_3O_4 composite combined with the advantage of Co_3O_4 (the high discharge specific capacity) and LTO (the good cycle stability).

The geometric structure model of LTO, Co_3O_4, and LTO/Co_3O_4 was optimized based on the density functional theory. As shown in **Supplementary Figure S1A**, 0 eV was defined as the Fermi level. The bandgap between the conduction band and the valence band was 0.8 eV, indicating that the composite exhibited semi-metallic properties. In addition, the energy value of the LTO/Co_3O_4 composite was higher than that of LTO and Co_3O_4 at the Fermi level (see **Supplementary Figure S1B**). The synergistic effect between LTO and Co_3O_4 significantly increased the probability of electrons appearing in the LTO/Co_3O_4 composite at the Fermi level, which was more conducive to electron transfer, improving the charge transfer rate of the LTO/Co_3O_4 composite.

CONCLUSION

The Co ion-doped LTO composite was prepared using the hydrothermal method. The combination of LTO and Co_3O_4 by the Co-O-Ti bond not only maintained the structural stability of the composite but also improved the electron/ion diffusion rate of the composite. Compared with LTO, LTO/Co_3O_4 has a higher first discharge specific capacity, good rate performance, and better cycle stability. The first specific capacity was 1,178 mA h/g at 0.1 A/g. After 1,000 cycles, the discharge specific capacity was 248.4 mA h/g and the capacity retention rate was 99% (compared to the capacity at the 20th cycle). At the same time, the LTO/Co_3O_4 composite also has a higher discharge specific capacity at high current density (the discharge specific capacity was 174.6 mA h/g at 5 A/g), which was 2.2 times that of pure LTO.

DATA AVAILABILITY STATEMENT

The original contributions presented in the study are included in the article/**Supplementary Material**. Further inquiries can be directed to the corresponding author.

AUTHOR CONTRIBUTIONS

MW: resources, writing—review and editing, supervision, project administration, funding acquisition. YC and CXY: designing and completing experiments, writing—original draft. YHZ, PFF, and WW: investigation, writing—review and editing. XLW: funding acquisition.

FUNDING

This work was financially supported by the National Natural Science Foundation of China (51974152), General Project of Science Research Foundation of Liaoning Province (LJKZ0363), Central Government Guiding Local Project of Science and Technology Development Foundation (2022JH6/100100047), and Discipline Innovation Team Project of Liaoning Technical University (LNTU20TD-09 and LNTU20TD-16).

SUPPLEMENTARY MATERIAL

The Supplementary Material for this article can be found online at: https://www.frontiersin.org/articles/10.3389/fchem.2022.919552/full#supplementary-material

Supplementary Figure S1 | (A) The energy band diagram of $Li_4Ti_5O_{12}/Co_3O_4$ and **(B)** the density of states of $Li_4Ti_5O_{12}$, Co_3O_4, and $Li_4Ti_5O_{12}/Co_3O_4$.

REFERENCES

Chen, Z., Belharouak, I., Sun, Y.-K., and Amine, K. (2013). Titanium-Based Anode Materials for Safe Lithium-Ion Batteries. *Adv. Funct. Mat.* 23 (8), 959–969. doi:10.1002/adfm.201200698

Cheng, J., Che, R., Liang, C., Liu, J., Wang, M., and Xu, J. (2014). Hierarchical Hollow $Li_4Ti_5O_{12}$ Urchin-like Microspheres with Ultra-high Specific Surface Area for High Rate Lithium Ion Batteries. *Nano Res.* 7 (7), 1043–1053. doi:10.1007/s12274-014-0467-2

Cheng, L., Yan, J., Zhu, G.-N., Luo, J.-Y., Wang, C.-X., and Xia, Y.-Y. (2010). General Synthesis of Carbon-Coated Nanostructure $Li_4Ti_5O_{12}$as a High Rate

Electrode Material for Li-Ion Intercalation. *J. Mat. Chem.* 20 (3), 595–602. doi:10.1039/b914604k

Kim, J.-G., Shi, D., Park, M.-S., Jeong, G., Heo, Y.-U., Seo, M., et al. (2013). Controlled Ag-Driven Superior Rate-Capability of $Li_4Ti_5O_{12}$ Anodes for Lithium Rechargeable Batteries. *Nano Res.* 6 (5), 365–372. doi:10.1007/s12274-013-0313-y

Li, H., Shen, L., Wang, J., Ding, B., Nie, P., Xu, G., et al. (2014). Design of a Nitrogen-Doped, Carbon-Coated $Li_4Ti_5O_{12}$ Nanocomposite with a Core-Shell Structure and its Application for High-Rate Lithium-Ion Batteries. *ChemPlusChem* 79 (1), 128–133. doi:10.1002/cplu.201300316

Li, H. Z., Yang, L. Y., Liu, J., Li, S. T., Fang, L. B., Lu, Y. K., et al. (2016). Improved Electrochemical Performance of Yolk-Shell Structured SnO 2 @void@C Porous Nanowires as Anode for Lithium and Sodium Batteries. *J. Power Sources* 324, 780–787. doi:10.1016/j.jpowsour.2016.06.011

Li, N., Zhou, G., Li, F., Wen, L., and Cheng, H.-M. (2013). A Self-Standing and Flexible Electrode of $Li_4Ti_5O_{12}$ Nanosheets with a N-Doped Carbon Coating for High Rate Lithium Ion Batteries. *Adv. Funct. Mat.* 23 (43), 5429–5435. doi:10.1002/adfm.201300495

Li, S., Liu, G., Liu, J., Lu, Y., Yang, Q., Yang, L.-Y., et al. (2016). Carbon Fiber cloth@ VO_2(B): Excellent Binder-free Flexible Electrodes with Ultrahigh Mass-Loading. *J. Mat. Chem. A* 4 (17), 6426–6432. doi:10.1039/c6ta00728g

Li, W., Wang, F., Ma, M., Zhou, J., Liu, Y., and Chen, Y. (2018). Preparation of SiO_2 Nanowire Arrays as Anode Material with Enhanced Lithium Storage Performance. *RSC Adv.* 8 (59), 33652–33658. doi:10.1039/c8ra06381h

Li, Z., Ding, F., Zhao, Y., Wang, Y., Li, J., Yang, K., et al. (2016). Synthesis and Electrochemical Performance of $Li_4Ti_5O_{12}$ Submicrospheres Coated with TiN as Anode Materials for Lithium-Ion Battery. *Ceram. Int.* 42, 15464–15470. doi:10.1016/j.ceramint.2016.06.198

Liu, J., Lu, P.-J., Liang, S., Liu, J., Wang, W., Lei, M., et al. (2015). Ultrathin Li_3VO_4 Nanoribbon/graphene Sandwich-like Nanostructures with Ultrahigh Lithium Ion Storage Properties. *Nano energy* 12, 709–724. doi:10.1016/j.nanoen.2014.12.019

Liu, J., Song, K., van Aken, P. A., Maier, J., and Yu, Y. (2014). Self-Supported $Li_4Ti_5O_{12}$-C Nanotube Arrays as High-Rate and Long-Life Anode Materials for Flexible Li-Ion Batteries. *Nano Lett.* 14 (5), 2597–2603. doi:10.1021/nl5004174

Liu, J., Tang, S., Lu, Y., Cai, G., Liang, S., Wang, W., et al. (2013). Synthesis of Mo_2N Nanolayer Coated MoO_2 Hollow Nanostructures as High-Performance Anode Materials for Lithium-Ion Batteries. *Energy Environ. Sci.* 6 (9), 2691–2697. doi:10.1039/c3ee41006d

Lu, Y., Zhang, Q., and Chen, J. (2019). Recent Progress on Lithium-Ion Batteries with High Electrochemical Performance. *Sci. China Chem.* 62 (5), 533–548. doi:10.1007/s11426-018-9410-0

Ma, Y., Ding, B., Ji, G., and Lee, J. Y. (2013). Carbon-Encapsulated F-Doped $Li_4Ti_5O_{12}$ as a High Rate Anode Material for Li+ Batteries. *ACS Nano* 7 (12), 10870–10878. doi:10.1021/nn404311x

Qu, X. L., Pu, K. C., Gao, M. X., Liu, Y. F., and Pan, H. G. (2018). Nanostructuring and Alloying of Si-Based Anode Materials. *Materials China* 037 (004), 254–263.

Shen, L., Zhang, X., Uchaker, E., Yuan, C., and Cao, G. (2012). $Li_4Ti_5O_{12}$ Nanoparticles Embedded in a Mesoporous Carbon Matrix as a Superior Anode Material for High Rate Lithium Ion Batteries. *Adv. Energy Mat.* 2 (6), 691–698. doi:10.1002/aenm.201100720

Shi, Y., Wen, L., Li, F., and Cheng, H.-M. (2011). Nanosized $Li_4Ti_5O_{12}$/graphene Hybrid Materials with Low Polarization for High Rate Lithium Ion Batteries. *J. Power Sources* 196 (20), 8610–8617. doi:10.1016/j.jpowsour.2011.06.002

Sun, X., Hegde, M., Wang, J., Zhang, Y., Liao, J., Radovanovic, P. V., et al. (2014). Structural Analysis and Electrochemical Studies of Carbon Coated $Li_4Ti_5O_{12}$ Particles Used as Anode for Lithium-Ion Battery. *ECS Trans.* 58 (14), 79–88. doi:10.1149/05814.0079ecst

Tan, Y., and Xue, B. (2018). Research Progress of Lithium Titanate as Anode Material for Lithium Ion Battery. *J. Inorg. Mater.* 33 (05), 475–482. doi:10.15541/jim20170330

Tang, Y., Yang, L., Qiu, Z., and Huang, J. (2009). Template-free Synthesis of Mesoporous Spinel Lithium Titanate Microspheres and Their Application in High-Rate Lithium Ion Batteries. *J. Mat. Chem.* 19 (33), 5980–5984. doi:10.1039/b907480e

Wang, D. D. (2020). Studies of Ti-Based Oxide Anode Materials for Lithium Ion Battery. Doctoral Dissertation. Tianjin: Tianjin University.

Wang, J., Zhao, H., Yang, Q., Wang, C., Lv, P., and Xia, Q. (2013). $Li_4Ti_5O_{12}$-TiO_2 Composite Anode Material for Lithium-Ion Batteries. *J. Power Sources* 222, 196–201. doi:10.1016/j.jpowsour.2012.08.082

Wang, Q., Geng, J., Yuan, C., Kuai, L., and Geng, B. (2016). Mesoporous Spherical $Li_4Ti_5O_{12}$/TiO_2 Composites as an Excellent Anode Material for Lithium-Ion Batteries. *Electrochimica Acta* 212, 41–46. doi:10.1016/j.electacta.2016.06.153

Wang, Y. J. (2021). Preparation and Electrochemical Properties of Titanate Anode Materials for Lithium Ion Batteries. MS Dissertation. Wulumuqi: Xinjiang Normal University.

Xu, Z., Yin, Q., Li, X., Meng, Q., Xu, L., Lv, B., et al. (2020). Self-assembly of a Highly Stable and Active Co_3O_4/H-TiO_2 Bulk Heterojunction with High-Energy Interfacial Structures for Low Temperature CO Catalytic Oxidation. *Catal. Sci. Technol.* 10 (24), 8374–8382. doi:10.1039/d0cy01477j

Yan, J. D. (2014). Development Status and Prospect Analysis of Lithium-Ion Battery. *J. Aeronautics* 35 (10), 2767–2775.

Yang, L. Y., Li, H. Z., Liu, J., Sun, Z. Q., Tang, S. S., and Lei, M. (2015). Dual Yolk-Shell Structure of Carbon and Silica-Coated Silicon for High-Performance Lithium-Ion Batteries. *Sci. Rep.* 5 (1), 10908–10909. doi:10.1038/srep10908

Yang, L. Y., Li, H. Z., Liu, J., Tang, S. S., Lu, Y. K., Li, S. T., et al. (2015). $Li_4Ti_5O_{12}$ Nanosheets as High-Rate and Long-Life Anode Materials for Sodium-Ion Batteries. *J. Mat. Chem. A* 3 (48), 24446–24452. doi:10.1039/c5ta07403g

Yang, X., Xu, C., Li, S., Wu, Y. P., Wu, X. Q., Yin, Y. M., et al. (2022). Thermal Treatment for Promoting Interfacial Interaction in Co-BDC/$Ti_3C_2T_X$ Hybrid Nanosheets for Hybrid Supercapacitors. *J. Colloid Interface Sci.* 617, 633–640. doi:10.1016/j.jcis.2022.03.015

You, S. L., Fang, L., Xu, H. T., and Wang, Y. (2018). Progress in the Research on Anode Material $Li_4Ti_5O_{12}$ for Li-Ion Batteries. *J. Chongqing Univ.* 41 (12), 92–100. doi:10.1183/j.issn.1000-582X.2018.12.011

Zettsu, N., Mizuno, Y., Kojima, H., Yubuta, K., Sakaguchi, T., Saito, T., et al. (2014). Direct Fabrication of Densely Packed Idiomorphic $Li_4Ti_5O_{12}$ Crystal Layers on Substrates by Using a LiCl-NaCl Mixed Flux and Their Additive-free Electrode Characteristics. *Cryst. Growth & Des.* 14 (11), 5634–5639. doi:10.1021/cg5009279

Zhang, C., Zhang, Y., Wang, J., Wang, D., He, D., and Xia, Y. (2013). $Li_4Ti_5O_{12}$ Prepared by a Modified Citric Acid Sol-Gel Method for Lithium-Ion Battery. *J. Power Sources* 236, 118–125. doi:10.1016/j.jpowsour.2013.01.135

Zhang, J., Wang, S., and Xu, G. (2021). Assembly of Multifunctional $Li_4Ti_5O_{12}$@ Co_3O_4 Heterostructures for High-Performance Li-Ion Half/full Batteries[J]. *J. Alloys Compd.* 856, 158110. doi:10.1016/j.jallcom.2020.158110

Zhou, G. W., Lee, D. K., Kim, Y. H., Kim, C. W., and Kang, Y. S. (2006). Preparation and Spectroscopic Characterization of Ilmenite-Type $CoTiO_3$ Nanoparticles. *Bull. Korean Chem. Soc.* 27 (3), 368–372.

Conflict of Interest: The authors declare that the research was conducted in the absence of any commercial or financial relationships that could be construed as a potential conflict of interest.

Publisher's Note: All claims expressed in this article are solely those of the authors and do not necessarily represent those of their affiliated organizations or those of the publisher, the editors, and the reviewers. Any product that may be evaluated in this article, or claim that may be made by its manufacturer, is not guaranteed or endorsed by the publisher.

frontiers | Frontiers in Chemistry

MINI REVIEW
published: 08 July 2022
doi: 10.3389/fchem.2022.944029

Cationic Interstitials: An Overlooked Ionic Defect in Memristors

Zhemi Xu[1], *Peiyuan Guan*[2], *Tianhao Ji*[1], *Yihong Hu*[3], *Zhiwei Li*[4], *Wenqing Wang*[3] *and Nuo Xu*[3]*

[1]College of Chemistry and Material Engineering, Beijing Technology and Business University, Beijing, China, [2]School of Materials Science and Engineering, University of New South Wales, Sydney, NSW, Australia, [3]College of Computer, National University of Defense Technology, Changsha, China, [4]College of Electronic Science and Technology, National University of Defense Technology, Changsha, China

Metal oxide-based memristors are promising candidates for breaking through the limitations in data storage density and transmission efficiency in traditional von Neumann systems, owing to their great potential in multi-state data storage and achievement of the in-memory neuromorphic computing paradigm. Currently, the resistive switching behavior of those is mainly ascribed to the formation and rupture of conductive filaments or paths formed by the migration of cations from electrodes or oxygen vacancies in oxides. However, due to the relatively low stability and endurance of the cations from electrodes, and the high mobility and weak immunity of oxygen vacancies, intermediate resistance states can be hardly retained for multilevel or synaptic resistive switching. Herein, we reviewed the memristors based on cationic interstitials which have been overlooked in achieving digital or analog resistive switching processes. Both theoretical calculations and experimental works have been surveyed, which may provide reference and inspiration for the rational design of multifunctional memristors, and will promote the increments in the memristor fabrications.

Keywords: resistive switching (RS), cationic interstitials, metal oxides, memristor, conductive filament

OPEN ACCESS

Edited by:
Meng Zheng,
Qingdao Haiwan Science and Technology Industry Research Institute Co., Ltd, China

Reviewed by:
Chuanyu Sun,
University of Padua, Italy
Wenwen Fei,
Anhui University, China

***Correspondence:**
Nuo Xu
xunuo@nudt.edu.cn

Specialty section:
This article was submitted to Electrochemistry, a section of the journal Frontiers in Chemistry

Received: *14 May 2022*
Accepted: *08 June 2022*
Published: *08 July 2022*

Citation:
Xu Z, Guan P, Ji T, Hu Y, Li Z, Wang W and Xu N (2022) Cationic Interstitials: An Overlooked Ionic Defect in Memristors. Front. Chem. 10:944029. doi: 10.3389/fchem.2022.944029

INTRODUCTION

As the memories and CPUs are separated in the current von Neumann computer system, the data have to be transferred between them through the limited bandwidth buses, which limits the time and energy efficiencies in the data processing. Such issue could be addressed by achieving an in-memory computing paradigm, for which the memristor is a suitable device because of its higher data storage density (Cheng et al., 2017; Chen et al., 2019) and excellent physical characteristics of conditional switching and physical MAC operation (Yang et al., 2017; Zhou et al., 2019; Xu et al., 2021; Li et al., 2022). Meanwhile, they can also bridge various electrical devices and be applied in energy storage, remote sensing, low-power applications, *etc.* (Chen, 2017; Han et al., 2020; Wang et al., 2020; Zhang and Sun, 2021) Thus, memristors are crucial for non-volatile memory, logic operations, Internet of Things, and neuromorphic computing in the big data era (Qin et al., 2020; Xu et al., 2020; Yao et al., 2020; Huang et al., 2021).

The memristor is a two-terminal electrical device that regulates the flow of electrical current in a circuit and remembers the amount of charge that has previously flowed through it even after removing the bias voltage (Fu et al., 2020). The original concept for memristors was proposed by Leon Chua in 1971, which was described as a nonlinear, passive two-terminal electrical component that linked electric charge and magnetic flux (Chua, 1971). This conceptual device has been firstly

linked to a kind of physical resistive switching device (ReRAM) by HP labs in 2008 (Strukov et al., 2008). Nowadays, the definition of memristor has been broadened to the arbitrary form of non-volatile memory with the foundation principle of resistance switching.

So far, the state transition phenomenon in different material systems is employed to trigger the resistive switching (RS) behavior and further construct the different types of memristors. Except for the well-studied RS behavior in metal-oxide materials (Illarionov et al., 2020; Liu et al., 2021; Wang et al., 2021), phase change materials (Hazra et al., 2021), organic materials (Chen, 2017; Cheng et al., 2017), ferroelectric materials (Guan et al., 2017), and magnetic materials (Park et al., 2018) are also reported to exhibit the macroscopic RS behavior because of the transition of crystalline phase, ferroelectric polarization, and spin polarization respectively. Among these numerous material systems, the metal-oxide-based memristors are promising owing to their low cost, simple process, and high compatibility with complementary metal-oxide-semiconductor (CMOS) technology (Mohammad et al., 2016; Illarionov et al., 2020; Nili et al., 2020).

However, compared to the basic metal-oxide-semiconductor (MOS) transistor which is the foundation device of constructing the current computing system, the memristor is still suffering from the relatively low reliability caused by device fluctuation, limited stability, and durability to maintain the resistance value or to improve repeated erasable times. Therefore, rational design and optimization of the memristor active layer through material engineering for enhancing the performance of memristors are expected. The works on metal-oxide-based RS have been mainly focused on the migration or ionization of oxygen vacancies (V_O) or cations from active electrodes (Waser et al., 2009; Chen et al., 2013; Kamiya et al., 2014; Tang et al., 2015). However, due to the high mobility of V_O and relative low endurance of cation-based resistive random-access memories (RRAM), it is a challenge to maintain stable intermediate states, which greatly limited the applications of memristors in multi-level RS and artificial synapses.

Compared to Vo and cations from electrodes, another common ionic defect in metal oxides, cationic interstitial (C_{int}) can also contribute to the successful RS, which has been less focused on previously. In the limited reports, C_{int}s have shown great potential in enhancing the performance of memristors with better stability and endurance, higher ON/OFF ratio, lower operation voltage, *etc*. Multi-level RS and synaptic RS have also been realized *via* modulating C_{int}s in memristors. Hence, in this mini-review, we focused on studying the C_{int}-induced RS behaviors from the previous reports. Both theoretical and experimental works have been investigated, which may provide reference and inspiration for the rational design of multifunctional memristors from a new perspective and may shed some light on the increments in memristors.

REVIEW OF THE WORKS RELATED TO THE FIRST-PRINCIPLE STUDIES

First-principles calculations have been always employed to investigate the mechanism of the RS behavior through some calculations in terms of formation energy, the density of states, partial charge densities, *etc*. For C_{int}s-induced RS, there are two main contributions from C_{int}s to realize or enhance the RS: forming a conductive path and promoting charge transfer in the metal oxides. Related works have been summarized in **Table 1**.

Gu et al. have compared the formation possibility of conductive paths with Cu interstitials (Cu_{int}) and Vo in the Ta_2O_5 atomic switch through first-principles studies (Gu et al., 2010): **Figure 1A** shows that Cu_{int} can form an effective conduction channel in the Ta_2O_5, as the formation of $Cu_{int,}$ may connect the two adjacent Ta-O planes through the simulation process, while Vo failed to form such a conductive channel. But it should be noted that the conductive path formed by C_{int}s is sensitive to the concentrations of interstitials, which need to be tuned carefully in the experiments.

The formation of the conductive path with C_{int}s is sensitive to the valences of the doped cations as well. Li et al. have systematically calculated the TiO_2 and ZrO_2 with different C_{int}s and investigated how C_{int}s with different valence states may affect the transport coefficients (Li et al., 2015). **Figure 1B** illustrates the deformation electron densities for the TiO_2 with Cu_{int}, Ti_{int}, and Zr_{int}, respectively. The blue region around Cu_{int} indicates that the loss of e^- from Cu could form ionic bonds with nearby O atoms, while such a phenomenon has not been observed in the situation of Ti_{int} and Zr_{int}. The calculation results indicate that the transport coefficients of the materials with Ti_{int} and Zr_{int} are higher than that with Cu_{int}. To optimize the RS behavior, the doping of metals with +4 or higher valences could be employed as it may enhance the transport properties.

Similarly, Zr_{int} and Ti_{int} in CeO_2 and Ta_{int} in Ta_2O_5 have also been confirmed to contribute to the formation of conductive paths in memristor. As it is shown in **Figure 1C**, Ti_{int} can form a more obvious conductive path in CeO_2 compared to the Ti substitution (Ti_{sub}). And then, Ti_{int} and Zr_{int} have been introduced in experiments and successfully improved the RS performance of CeO_2 RRAMs (Hussain et al., 2018). Zhu et al. compared the V_O and Ta_{int} in the Ta_2O_5-based RRAM and confirmed the contribution of Ta_{int} in realizing RS under oxygen-poor conditions (Zhu et al., 2016). Thus, it is concluded that the C_{int}s can introduce more defect states to above metal oxides than that of Vo, and the C_{int}-induced RS can be enhanced under an electric field.

The synergistic effects of Vo and C_{int}s for achieving RS have also been identified in memristors. In the Au-doped HfO_2, it has been confirmed that both Vo and Au_{int} are involved in the formation of conductive filaments (Tan et al., 2018). Similarly, Abdelouahed et al. compared the TiO_2 with Vo and Ti_{int} and revealed the co-formation of both defects, which induced a net dipole moment, and enhanced RS behavior under an electric field (Abdelouahed and Mckenna, 2015).

REVIEW OF EXPERIMENTAL WORKS

C_{int}-induced or enhanced RS behavior in memristors has also been confirmed in experimental works (as summarized in **Table 2**).

TABLE 1 | Theoretical works on the C_{int}-induced RS behavior.

Materials	Interstitials	Effects	Ref
Ta_2O_5	Cu_{int}	Forming conductive path	Gu et al. (2010)
TiO_2	Ti_{int} or Zr_{int}	Promoting charge transfer	Li et al. (2015)
CeO_2	Ti_{int} or Zr_{int}	Forming conductive path	Hussain et al. (2018)
Ta_2O_5	Ta_{int}	Forming conductive path	Zhu et al. (2016)
HfO_2	Au_{int} + Vo	Forming filaments	Tan et al. (2018)
TiO_2	Ti_{int} + Vo	Forming net dipole moment	Abdelouahed and Mckenna, (2015)

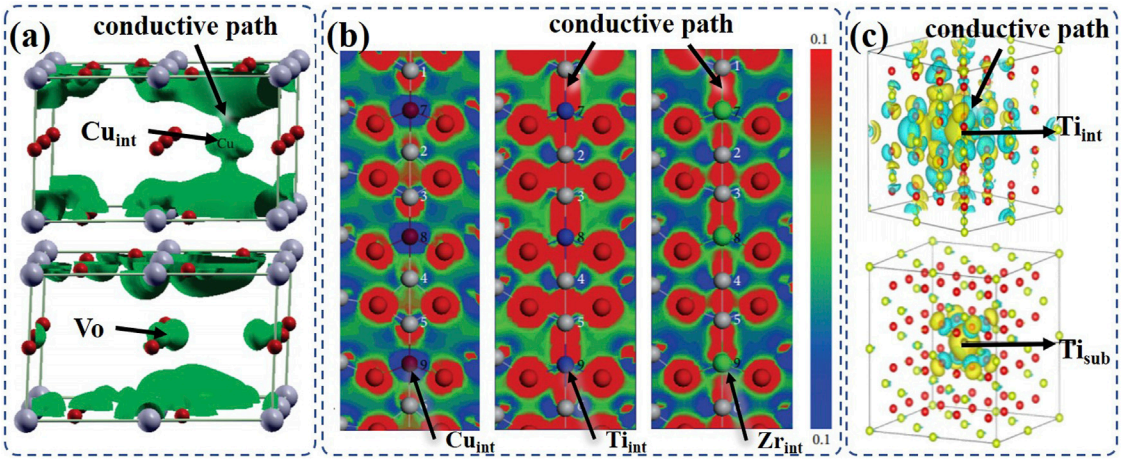

FIGURE 1 | (A) Isosurface plot of the partial charge density corresponding to the defect state induced by the interstitial Cu_{int} and Vo in Ta_2O_5 (reproduced with permission (Gu et al., 2010). Copyright 2010, American Chemical Society); **(B)** deformation electron density in [110] for the defected TiO_2 with the Cu_{int}, $Ti_{int,}$ and Zr_{int} (reproduced with permission (Li et al., 2015). Copyright 2015, Lei Li et al.); **(C)** isosurface plots of Ti_{int} and Ti_{sub} (reproduced with permission (Hussain et al., 2018). Copyright 2018, Springer-Verlag GmbH Germany).

TABLE 2 | Experimental works on the C_{int}-induced RS behavior.

Materials	Interstitials	C_{int} forming conditions	Effects	Ref
Cu_xO	Cu_{int}	Annealing in Ar environment	Enhanced RS	Rehman et al. (2018)
ZnO_x	Zn_{int}	Sputtering under high oxygen partial pressure	Change bipolar (with O_{int}) into unipolar (with Zn_{int}) RS	Wu et al. (2014)
ZnO/Al_2O_3	Zn_{int}	PLD, rapid thermal annealing	Change TCSC conduction (with Vo) into diode-like RS (with Zn_{int})	Sekhar et al. (2015)
$NiO:SnO_2$	Ru_{int} + Al_{int}	Sol-gel, Ru, and Al co-doping	Enhanced RS with a higher ON/OFF ratio	Li et al. (2014)
CeO_2	Ti_{int}	Depositing Ti as a buffer layer in CeO_2/Ti/CeO_2	Improved stability, endurance, and ON/OFF ratio, lowered SET voltage	Rana et al. (2017)
SnO_2	Mn_{int}	Hydrothermally synthesized Mn-doped SnO_2	Intrinsic multi-level RS, improved stability and endurance	Xu et al. (2018)
TiO_2	Ti_{int} + Vo	Thermally-induced self-doping and phase transformation	Improved stability, endurance, and ON/OFF ratio, lowered SET voltage	Hazra et al. (2021)
MoO_3	Mo_{int} + Vo	Hydrothermally synthesized hexagonal MoO_3	Multi-level RS	Patil et al. (2021)
ZnO	Zn_{int} + Vo	2 wt% Cu-doped ZnO	Enhanced electric controlled RS and light-modulable RS	Saini et al. (2021)
TiO_2	Ti_{int} + Ag^+ + K^+	Fabricate Ag/TiO_2-LPE/FTO device	Enhanced stability and endurance, lowered SET voltage, bipolar RS	Abbasi et al. (2020)
$LaAlO_3$	B_{int}	B-doped $LaAlO_3$	Enhanced RS behavior, realized ferromagnetic ionic-electronic conductor	Park et al. (2018)

·The formation of C_{int}s and C_{int}-induced RS behavior

The C_{int}s can be introduced to metal oxides by modifying the synthesis parameters, such as the annealing conditions, oxygen partial pressure, doping concentration, *etc*. For example, by changing the annealing temperature and improving the oxygen concentration during the annealing process, Cu_{int}s have been successfully formed in the Cu_xO, and the RS can be enhanced by

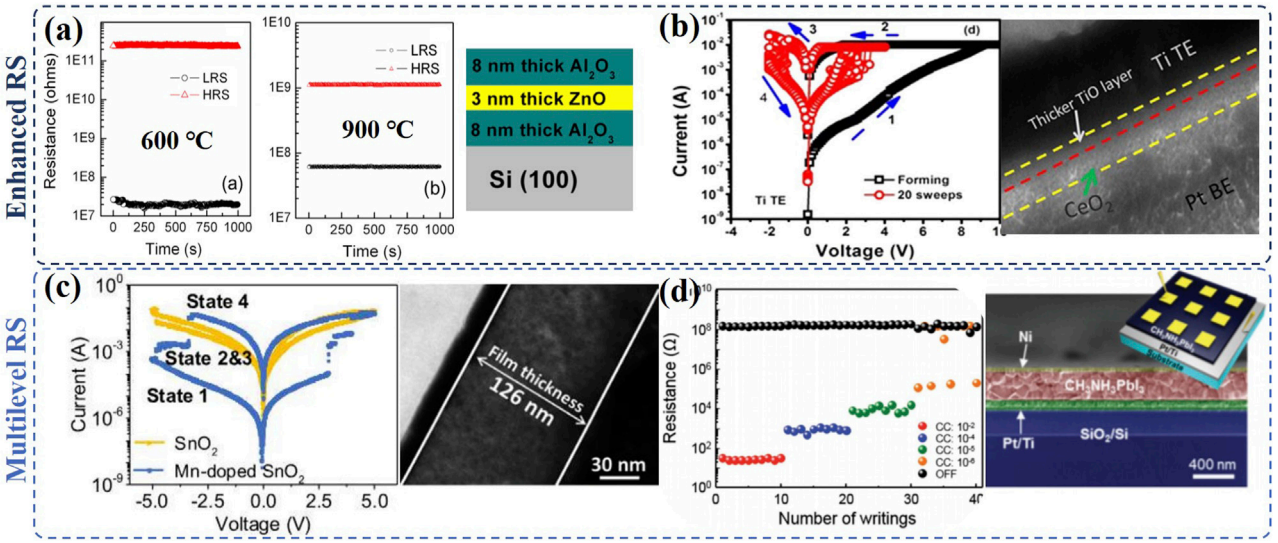

FIGURE 2 | Enhanced RS performance and the cross-section images of the device based on **(A)** $Al_2O_3/ZnO/Al_2O_3$ memristors (reproduced with permission (Sekhar et al., 2015). Copyright 2015, Elsevier B.V.) and **(B)** $CeO_2/Ti/CeO_2$ (reproduced with permission (Rana et al., 2017). Copyright 2017, Anwar Manzoor Rana et al.); the multilevel RS and the cross-section images of the device based on **(C)** Mn-doped SnO_2 (reproduced with permission (Xu et al., 2018). Copyright 2018, Elsevier Ltd.) and **(D)** $CH_3NH_3PbI_3$ thin films (reproduced with permission (Choi et al., 2016). Copyright 2016, John Wiley & Sons, Inc.).

tuning the Cu_{int}s in the memristors (Rehman et al., 2018). In the sputtering process, by adjusting the oxygen partial pressure, the formation of O_{int} or Zn_{int} could be controlled, and interestingly, it is found that the bipolar and unipolar RS behavior can be tuned by forming O_{int} and Zn_{int} in the $Al/ZnO_x/Al$ memory device, respectively (Wu et al., 2014). In the pulsed laser deposition (PLD), rapid thermal annealing may also change the defects in ZnO/Al_2O_3 memristor: the trap-controlled-space-charge (TCSC) limited conduction mechanism has been observed when Vo dominates, while, diode-like RS behavior has been identified in the case of Zn_{int} dominating. In the latter, the stability, endurance, and ON/OFF ratio of the memristor have been significantly improved as it is shown in **Figure 2A** (Sekhar et al., 2015). Such transition is ascribed to the formation of $ZnAL_2O_4$ as an interlayer, which acts as the e^- trapping/detrapping area and achieved successful RS.

In the memristors fabricated from solution-processed, C_{int}s are usually introduced *via* doping. In the $NiO:SnO_2$ memristor, Ru_{int}, and Al_{int} can be achieved through Ru and Al co-doping in the sol-gel process (Li et al., 2014). Compared to the Vo induced RS, the RS behavior conducted by Ru_{int} and Al_{int} could be greatly improved and show a larger ON/OFF ratio. The enhanced RS is ascribed to the increased trapped states between the equilibrium Fermi level and conduction band by Ru_{int} and Al_{int} (Li et al., 2014). Mn_{int}s have been achieved in SnO_2 by increasing the Mn-doping level to 12.5 mol% in the liquid-liquid interface hydrothermal process and compared to the pure SnO_2 with Vo, Mn-doped SnO_2 memristor shows more effective and stable RS with significantly larger ON/OFF ratio and better intermediate state retention (Xu et al., 2018).

Adding a buffer layer is another method to introduce the C_{int}s. As it is illustrated in **Figure 2B**, Ti_{int}s have been introduced by a Ti buffer layer in the $TaN/CeO_2/Ti/CeO_2/Pt$ memory device, in which Ti_{int}s assisted the formation of conductive filaments in CeO_2. Compared to the device without the Ti buffer layer, the device's stability and endurance could be significantly improved alongside the lower SET voltage and larger memory window (Rana et al., 2017). Similarly, by alternately depositing the SnO_2 layer with Vo and Mn-doped SnO_2 layer with Mn_{int}, Mn_{int}s have been introduced to the SnO_2-based RRAMs, which significantly enhance the RS behavior with a higher ON/OFF ratio and better stability and endurance (Xu et al., 2017).

·C_{int}-induced Multi-level RS

Multilevel RS has also been investigated in C_{int}-induced memristors. Intrinsic multi-state RS behavior with good endurance and stability has been observed in Mn-doped SnO_2-based memristor by increasing the Mn-doping concentration, as it is illustrated in **Figure 2C** (Xu et al., 2018). By comparing the RS behavior of Mn-doping, Al-doping, and In-doping in SnO_2 together with the XPS results and the calculated defect formation energies, the multi-level RS has been ascribed to Mn_{int} instead of Vo. Iodine interstitials induced multi-level RS has also been achieved in the $Ag/CH_3NH_3PbI_3/Pt$ cells as shown in **Figure 2D** (Choi et al., 2016). Owing to the relatively low activation energies, the migration of I_{int} enables filament formation and annihilation at a relative operation voltage.

·Synergistic RS induced by C_{int} and other defects

Furthermore, the synergistic effect of C_{int}s with other ionic defects in memristor has been confirmed in experiments more

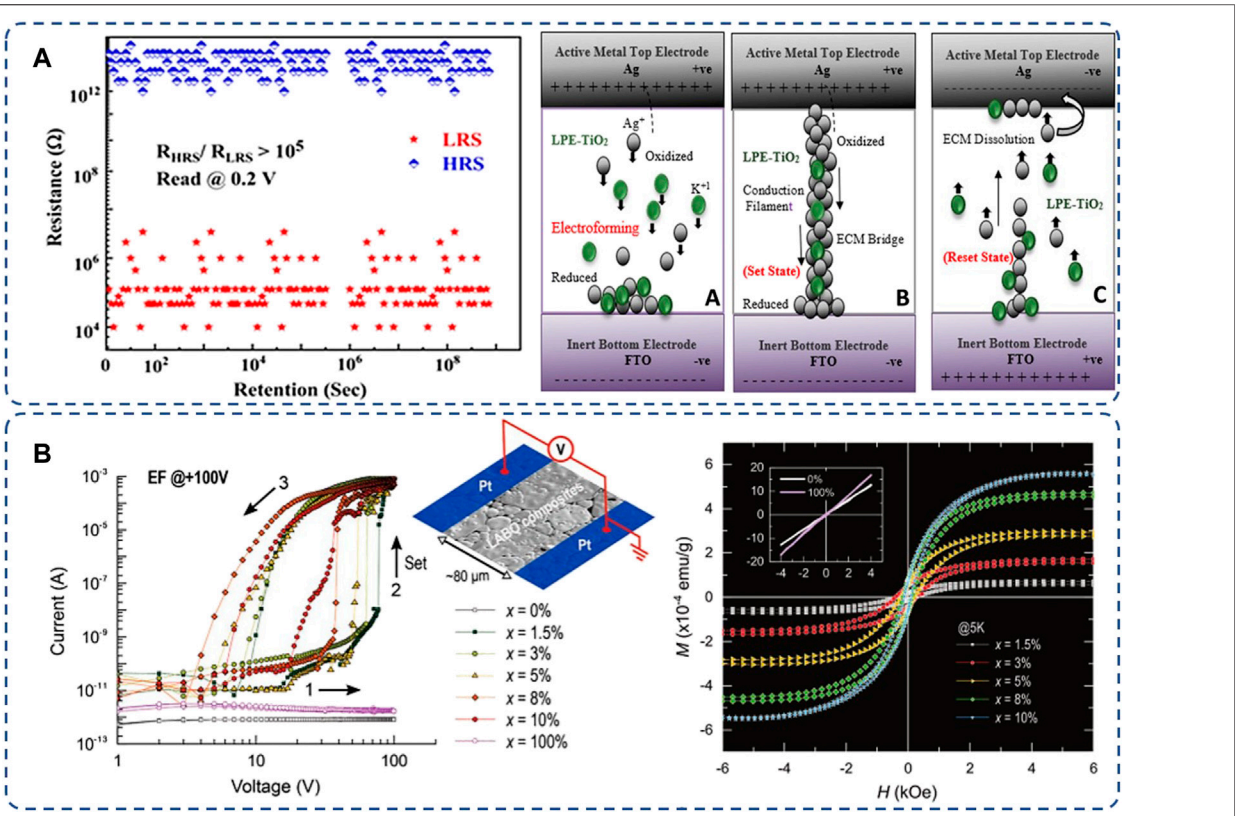

FIGURE 3 | (A) Enhanced retention and the schematic of Ti_{int} assisted the conductive filament with Ag^+ and K^+ (reproduced with permission (Abbasi et al., 2020). Copyright 2020, American Chemical Society); **(B)** the remarkably enhanced RS and ferromagnetic behavior by B_{int} in $LaAlO_3$(1-x):$LaBO_3$(x) (reproduced with permission (Park et al., 2018). Copyright 2018, John Wiley & Sons, Inc.).

than the theoretical results above (Lee et al., 2021). The synergistic effect of Ti_{int} with Vo has been confirmed in the Au/TiO_2 nanotube/Ti memory (Hazra et al., 2021). In the Ti/MoO_3/FTO memory cell, it is identified that Mo_{int}, surface defects, and Vo have contributed together to the multilevel RS behavior (Patil et al., 2021). Zn_{int} together with Vo enables the formation and rupture of conducting filaments in the Cu-doped ZnO, and both electric controlled and white light modulated RS has been achieved (Saini et al., 2021). Similarly, Vo and I_{int} assisted RS *via* a Schottky barrier tuning has also been verified in the Au/$CH_3NH_3PbI_3$/TiO_2/FTO memory device (Lee et al., 2021).

In addition, C_{int} can act as assistance or a game-changer in metal oxides. **Figure 3A** illustrates the defect-abundant memory device of Ag/TiO_2-LPE (known as lime peel extract)/FTO, in which Ti_{int} from TiO_2, Ag^+ oxidized from the Ag electrode, and K^+ from the LPE synergistically contribute to the RS behavior. Ti_{int}s provide active paths for cation migrations, which enhanced the stability and endurance of bipolar RS of the memory cell with low operation voltage and high ON/OFF ratio (Abbasi et al., 2020). In the B-doped $LaAlO_3$, B_{int}s realized charge injection into the neighboring cations, which enables remarkable electrical RS and transformed the oxide into a ferromagnetic ionic-electronic conductor at the same time, as it is shown in **Figure 3B**. This extends applications of C_{int}s to contribute to energy-efficient and spin-based devices (Park et al., 2018).

SUMMARY AND OUTLOOK

In summary, the cationic interstitials induced RS behavior in metal-oxide-based memories has been summarized. For a defect that has been less focused, there are very few reports on the formation, contribution, and mechanism of C_{int}-induced RS behavior compared to those on Vo or active electrodes. However, from both theoretical and experimental aspects, the C_{int}-induced or enhanced RS behavior has been confirmed in recent years. As discussed above, diversified C_{int}s provide more opportunities to tailor the metal oxides for different electronic devices. The rational fabrication of memristors with C_{int}s may give rise to remarkable enhancement in RS performance with better stability and endurance, lower operation voltage, higher ON/OFF ratio, faster device speed, *etc*. However, C_{int}-based memristors are sensitive to the concentration and valence state of C_{int}, which makes the formation of C_{int} in metal oxide synthesis need to be carefully modulated. By adjusting the C_{int}s, suitable electric structures would be established in the

metal oxides, which helps improve the performance of the electronic devices.

AUTHOR CONTRIBUTIONS

All authors listed have made a substantial, direct, and intellectual contribution to the work, and approved it for publication.

FUNDING

ZX acknowledges financial support from the Beijing Technology and Business University (Grant No. 19005902140). YH, WW, and NX acknowledge financial support from the National Natural Science Foundation of China (Grant No. 61832007) and the Research Foundation from the National University of Defense Technology (Grant No. ZK20-02).

REFERENCES

Abbasi, M. S., Irshad, M. S., Arshad, N., Ahmed, I., Idrees, M., Ahmad, S., et al. (2020). Biomaterial-Induced Stable Resistive Switching Mechanism in TiO2 Thin Films: The Role of Active Interstitial Sites/Ions in Minimum Current Leakage and Superior Bioactivity. *ACS Omega* 5, 19050–19060. doi:10.1021/acsomega.0c02410

Abdelouahed, S., and Mckenna, K. P. (2015). Relevance of Non-equilibrium Defect Generation Processes to Resistive Switching in TiO2. *J. Appl. Phys.* 118, 134103. doi:10.1063/1.4932225

Chen, E. T. (2017). *Nanostructured Biomimetic Sensing and Energy Storage: Organic Memristor/Memcapacitors. Dekker Encyclopedia of Nanoscience and Nanotechnology*. 3rd Edition. Boca Raton: CRC Press.

Chen, J.-Y., Hsin, C.-L., Huang, C.-W., Chiu, C.-H., Huang, Y.-T., Lin, S.-J., et al. (2013). Dynamic Evolution of Conducting Nanofilament in Resistive Switching Memories. *Nano Lett.* 13, 3671–3677. doi:10.1021/nl4015638

Chen, Z., Huang, W., Zhao, W., Hou, C., Ma, C., Liu, C., et al. (2019). Ultrafast Multilevel Switching in Au/YIG/n-Si RRAM. *Adv. Electron. Mat.* 5, 1800418. doi:10.1002/aelm.201800418

Cheng, X.-F., Xia, S.-G., Hou, X., Xiao, X., He, J.-H., Ren, Z.-G., et al. (2017). Racemic Effect on the Performance of Organic Multilevel Memory: beyond Molecular Design. *Adv. Mat. Technol.* 2, 1700202. doi:10.1002/admt.201700202

Choi, J., Park, S., Lee, J., Hong, K., Kim, D.-H., Moon, C. W., et al. (2016). Organolead Halide Perovskites for Low Operating Voltage Multilevel Resistive Switching. *Adv. Mat.* 28, 6562–6567. doi:10.1002/adma.201600859

Chua, L. (1971). Memristor-The Missing Circuit Element. *IEEE Trans. Circuit Theory* 18, 507–519. doi:10.1109/tct.1971.1083337

Fu, Y., Dong, B., Su, W.-C., Lin, C.-Y., Zhou, K.-J., Chang, T.-C., et al. (2020). Enhancing LiAlOX Synaptic Performance by Reducing the Schottky Barrier Height for Deep Neural Network Applications. *Nanoscale* 12, 22970–22977. doi:10.1039/d0nr04782a

Gu, T., Tada, T., Watanabe, S., Watanabe, S., Watanabe, S., and Watanabe, S. (2010). Conductive Path Formation in the Ta2O5 Atomic Switch: First-Principles Analyses. *ACS Nano* 4, 6477–6482. doi:10.1021/nn101410s

Guan, P., Sun, Y., Wan, T., Lin, X., Xu, Z., and Chu, D. (2017). Development of Ferroelectric Oxides Based Resistive Switching Materials. *Mater. Sci. Technol.* 33, 2010–2023. doi:10.1080/02670836.2017.1366712

Han, X., Xu, Z., Wu, W., Liu, X., Yan, P., and Pan, C. (2020). Recent Progress in Optoelectronic Synapses for Artificial Visual-Perception System. *Small Struct.* 1, 2000029. doi:10.1002/sstr.202000029

Hazra, A., Tripathi, A., Jan, A., Kundu, S., and Boppidi, P. K. R. (2021). Multiple Nano-Filaments Based Efficient Resistive Switching in TiO2 Nanotubes Array Influenced by Thermally Induced Self-Doping and Anatase to Rutile Phase Transformation. *Nanotechnology* 32, 115201. doi:10.1088/1361-6528/abd05c

Huang, C., Xu, N., Qiu, K., Zhu, Y., Ma, D., and Fang, L. (2021). Efficient and Optimized Methods for Alleviating the Impacts of IR-Drop and Fault in RRAM Based Neural Computing Systems. *IEEE J. Electron Devices Soc.* 9, 645–652. doi:10.1109/jeds.2021.3093478

Hussain, F., Imran, M., Rana, A. M., Khalil, R. M. A., Khera, E. A., Kiran, S., et al. (2018). An Insight into the Dopant Selection for CeO2-Based Resistive-Switching Memory System: a DFT and Experimental Study. *Appl. Nanosci.* 8, 839–851. doi:10.1007/s13204-018-0751-7

Illarionov, G. A., Morozova, S. M., Chrishtop, V. V., Einarsrud, M. A., and Morozov, M. I. (2020). Memristive TiO2: Synthesis, Technologies, and Applications. *Front. Chem.* 8, 724. doi:10.3389/fchem.2020.00724

Kamiya, K., Yang, M. Y., Magyari-Kpe, B., Nishi, Y., Shiraishi, K., and Shiraishi, K. (2014). Modeling of Resistive Random Access Memory (RRAM) Switching Mechanisms and Memory Structures. *Woodhead Publ.* 8, 262. doi:10.1533/9780857098092.2.262

Lee, S., Wolfe, S., Torres, J., Yun, M., and Lee, J.-K. (2021). Asymmetric Bipolar Resistive Switching of Halide Perovskite Film in Contact with TiO2 Layer. *ACS Appl. Mat. Interfaces* 13, 27209–27216. doi:10.1021/acsami.1c06278

Li, J.-C., Cao, Q., and Hou, X.-Y. (2014). Ru-Al Codoping to Mediate Resistive Switching of NiO:SnO2 Nanocomposite Films. *Appl. Phys. Lett.* 104, 113511. doi:10.1063/1.4869231

Li, L., Xia, C., Li, W., Ji, A., Zhu, C., Zhang, L., et al. (2015). Nature of the Interstitials in Titanium Dioxide and Their Impact on Transmission Coefficient: Ab Initio Calculations. *J. Nanomater.* 2015, 574752.doi:10.1155/2015/574752

Li, Z., Long, H., Zhu, X., Wang, Y., Liu, H., Li, Q., et al. (2022). Error Detection and Correction Method toward Fully Memristive Stateful Logic Design. *Adv. Intell. Syst.* 1, 2100234.doi:10.1002/aisy.202100234

Liu, Z., Cheng, P., Li, Y., Kang, R., Zhang, Z., Zuo, Z., et al. (2021). High Temperature CsPbBrxI3-X Memristors Based on Hybrid Electrical and Optical Resistive Switching Effects. *ACS Appl. Mat. Interfaces* 13, 58885–58897. doi:10.1021/acsami.1c13561

Mohammad, B., Jaoude, M. A., Kumar, V., Al Homouz, D. M., Nahla, H. A., Al-Qutayri, M., et al. (2016). State of the Art of Metal Oxide Memristor Devices. *Nanotechnol. Rev.* 5, 311–329. doi:10.1515/ntrev-2015-0029

Nili, H., Vincent, A., Prezioso, M., Mahmoodi, M. R., Kataeva, I., and Strukov, D. (2020). Comprehensive Compact Phenomenological Modelling of Integrated Metal-Oxide Memristors. *IEEE Trans. Nanotechnol.* 19, 344–349. doi:10.1109/TNANO.2020.2982128

Park, D.-S., Rees, G. J., Wang, H., Rata, D., Morris, A. J., Maznichenko, I. V., et al. (2018). Electromagnetic Functionalization of Wide-Bandgap Dielectric Oxides by Boron Interstitial Doping. *Adv. Mat.* 30, 1802025. doi:10.1002/adma.201802025

Patil, S. R., Mullani, N. B., Kamble, B. B., Tayade, S. N., Kamat, R. K., Park, T. J., et al. (2021). Forming-free and Multilevel Resistive Switching Properties of Hydrothermally Synthesized Hexagonal Molybdenum Oxide Microrods. *J. Mater Sci. Mater Electron* 32, 12490–12502. doi:10.1007/s10854-021-05883-w

Qin, Y.-F., Bao, H., Wang, F., Chen, J., Li, Y., and Miao, X.-S. (2020). Recent Progress on Memristive Convolutional Neural Networks for Edge Intelligence. *Adv. Intell. Syst.* 2, 2000114. doi:10.1002/aisy.202000114

Rana, A. M., Akbar, T., Ismail, M., Ahmad, E., Hussain, F., Talib, I., et al. (2017). Endurance and Cycle-To-Cycle Uniformity Improvement in Tri-layered CeO2/Ti/CeO2 Resistive Switching Devices by Changing Top Electrode Material. *Sci. Rep.* 7, 39539. doi:10.1038/srep39539

Rehman, S., Hur, J.-H., and Kim, D.-K. (2018). Resistive Switching in Solution-Processed Copper Oxide (Cu_xO) by Stoichiometry Tuning. *J. Phys. Chem. C* 122, 11076–11085. doi:10.1021/acs.jpcc.8b00432

Saini, M., Kumar, M., Mandal, R., Mitra, A., and Som, T. (2021). White Light Modulated Forming-free Multilevel Resistive Switching in ZnO:Cu Films. *Appl. Surf. Sci.* 563, 150271. doi:10.1016/j.apsusc.2021.150271

Sekhar, K. C., Kamakshi, K., Bernstorff, S., and Gomes, M. J. M. (2015). Effect of Annealing Temperature on Photoluminescence and Resistive Switching Characteristics of ZnO/Al2O3 Multilayer Nanostructures. *J. Alloys Compd.* 619, 248–252. doi:10.1016/j.jallcom.2014.09.067

Strukov, D. B., Snider, G. S., Stewart, D. R., and Williams, R. S. (2008). The Missing Memristor Found. *Nature* 453, 80–83. doi:10.1038/nature06932

Tan, T., Cao, A., and Zha, G. (2018). A First-Principles Study of the Effects of Au Dopants in HfO2-Based RRAM. *Superlattices Microstruct.* 121, 38–44. doi:10.1016/j.spmi.2018.07.022

Tang, Z., Fang, L., Xu, N., and Liu, R. (2015). Forming Compliance Dominated Memristive Switching through Interfacial Reaction in Ti/TiO2/Au Structure. *J. Appl. Phys.* 118, 185309. doi:10.1063/1.4935622

Wang, S., Wang, C.-Y., Wang, P., Wang, C., Li, Z.-A., Pan, C., et al. (2020). Networking Retinomorphic Sensor with Memristive Crossbar for Brain-Inspired Visual Perception. *Natl. Sci. Rev.* 8, nwaa172. doi:10.1093/nsr/nwaa172

Wang, Y., Gong, Y., Yang, L., Xiong, Z., Lv, Z., Xing, X., et al. (2021). MXene-ZnO Memristor for Multimodal In-Sensor Computing. *Adv. Funct. Mat.* 31, 2100144. doi:10.1002/adfm.202100144

Waser, R., Dittmann, R., Staikov, G., Szot, K., Szot, K., and Szot, K. (2009). Redox-Based Resistive Switching Memories - Nanoionic Mechanisms, Prospects, and Challenges. *Adv. Mat.* 21, 2632–2663. doi:10.1002/adma.200900375

Wu, X., Xu, Z., Liu, B., Sun, T., Zhao, W., Liu, S., et al. (2014). Effect of Cation and Anion Defects on the Resistive Switching Polarity of ZnO X Thin Films. *Appl. Phys. A* 114, 847–852. doi:10.1007/s00339-013-7704-5

Xu, Z., Guan, P., Younis, A., Chu, D., Li, S., and Li, S. (2017). Manipulating Resistive States in Oxide Based Resistive Memories through Defective Layers Design. *RSC Adv.* 7, 56390–56394. doi:10.1039/c7ra11681k

Xu, Z., Younis, A., Cazorla, C., Yi, J., Chu, D., and Li, S. (2018). Engineering Cationic Defects in Transparent Tin Oxide Superlattices. *Mater. Des.* 155, 71–76. doi:10.1016/j.matdes.2018.05.061

Xu, N., Park, T. G., Kim, H. J., Shao, X., Yoon, K. J., Park, T. H., et al. (2020). A Stateful Logic Family Based on a New Logic Primitive Circuit Composed of Two Antiparallel Bipolar Memristors. *Adv. Intell. Syst.* 2, 1900082. doi:10.1002/aisy.201900082

Xu, N., Park, T., Yoon, K. J., and Hwang, C. S. (2021). In-Memory Stateful Logic Computing Using Memristors: Gate, Calculation, and Application. *Phys. Rapid Res. Ltrs* 15, 2100208. doi:10.1002/pssr.202100208

Yang, C.-S., Shang, D.-S., Chai, Y.-S., Yan, L.-Q., Shen, B.-G., and Sun, Y. (2017). Electrochemical-reaction-induced Synaptic Plasticity in MoOx-Based Solid State Electrochemical Cells. *Phys. Chem. Chem. Phys.* 19, 4190–4198. doi:10.1039/c6cp06004h

Yao, P., Wu, H., Gao, B., Tang, J., Zhang, Q., Zhang, W., et al. (2020). Fully Hardware-Implemented Memristor Convolutional Neural Network. *Nature* 577, 641–646. doi:10.1038/s41586-020-1942-4

Zhang, H., and Sun, C. (2021). Cost-effective Iron-Based Aqueous Redox Flow Batteries for Large-Scale Energy Storage Application: A Review. *J. Power Sources* 493, 229445. doi:10.1016/j.jpowsour.2020.229445

Zhou, L., Yang, S., Ding, G., Yang, J.-Q., Ren, Y., Zhang, S.-R., et al. (2019). Tunable Synaptic Behavior Realized in C3N Composite Based Memristor. *Nano Energy* 58, 293–303. doi:10.1016/j.nanoen.2019.01.045

Zhu, L., Zhou, J., Guo, Z., Sun, Z., Sun, Z., and Sun, Z. (2016). Synergistic Resistive Switching Mechanism of Oxygen Vacancies and Metal Interstitials in Ta2O5. *J. Phys. Chem. C* 120, 2456–2463. doi:10.1021/acs.jpcc.5b11080

Conflict of Interest: The authors declare that the research was conducted in the absence of any commercial or financial relationships that could be construed as a potential conflict of interest.

Publisher's Note: All claims expressed in this article are solely those of the authors and do not necessarily represent those of their affiliated organizations, or those of the publisher, the editors, and the reviewers. Any product that may be evaluated in this article, or claim that may be made by its manufacturer, is not guaranteed or endorsed by the publisher.

frontiers | Frontiers in Chemistry

PERSPECTIVE
published: 12 July 2022
doi: 10.3389/fchem.2022.943925

Fluorescence Enhancement of Dicyanomethylene-4H-Pyran Derivatives in Solid State for Visualization of Latent Fingerprints

*Yi Cai[1], Ting-Ting Hou[1], Cai-Yun Wang[1], Ying-Hao Tang[1], Zhen-Yu Zhang[1], Deteng Zhang[2], Ming-Qiang Zhu[3] and Ya-Long Wang[1,3,4]**

[1]Key Laboratory of Biomedical Engineering of Hainan Province, School of Biomedical Engineering, Hainan University, Haikou, China, [2]Institute of Neuroregeneration and Neurorehabilitation, Qingdao University, Qingdao, China, [3]Wuhan National Laboratory for Optoelectronics, Huazhong University of Science and Technology, Wuhan, China, [4]One Health Institute, Hainan University, Haikou, China

The efficient development of latent fingerprint (LFP) is attractively important for criminal investigation. The low-cost and high-contrast developer is still a challenge. In this study, we designed and synthesized dicyanomethylene-4H-pyran (DCM) derivatives PZ-DCM and Boc-PZ-DCM by introducing of large steric hindrance group Boc, the solid-state fluorescence of DCM derivatives was greatly enhanced. The low-cost fluorescent LFP developers were prepared by blending with different proportion of montmorillonite (MMT). As a result, clear and high contrast fingerprint patterns were obtained with dusting method by the developer with 3% content of Boc-PZ-DCM. Furthermore, we employed the developer with 3% content of Boc-PZ-DCM to develop the sweat latent fingerprints on different substrates by powder dusting, and collected clear fingerprint patterns, indicating that the developer is universal. In a word, the Boc-PZ-DCM/MMT powder is a promising candidate for LFP developer.

Keywords: latent fingerprints (LFP), fluorescent imaging, dicyanomethylene-4H-pyran (DCM), D-π-A structure, fluorescence enhancement

OPEN ACCESS

Edited by:
Yue Liu,
Liaoning Technical University, China

Reviewed by:
Huizhi Lu,
Qingdao University of Science and Technology, China
Shian Ying,
Shandong University of Science and Technology, China

****Correspondence:***
Ya-Long Wang
ylwang@hainanu.edu.cn

Specialty section:
This article was submitted to Electrochemistry, a section of the journal Frontiers in Chemistry

Received: *14 May 2022*
Accepted: *23 June 2022*
Published: *12 July 2022*

Citation:
Cai Y, Hou T-T, Wang C-Y, Tang Y-H, Zhang Z-Y, Zhang D, Zhu M-Q and Wang Y-L (2022) Fluorescence Enhancement of Dicyanomethylene-4H-Pyran Derivatives in Solid State for Visualization of Latent Fingerprints. Front. Chem. 10:943925. doi: 10.3389/fchem.2022.943925

INTRODUCTION

Fingerprint is a complex pattern composed of ridges (raised papillary line) and furrows (sunken wrinkles) through interval distribution (Wang et al., 2017). This unique pattern is different for each person and does not change throughout one's life (Becue, 2016; Tian et al., 2022). Based on its uniqueness, fingerprint has been used as a person's ID card for identification in criminal cases (Wang et al., 2017; Wang Y. et al., 2018). Latent fingerprint (LFP), the imprint of a real fingerprint, is crucial evidence for individual identification in forensic science. However, as the most common evidence at a crime scene, LFP is invisible to the naked eye without any treatment. Hence, the efficient visualization of LFP is very important for criminal investigation (Wei et al., 2016; Zhang et al., 2017). Powder dusting, reagent fuming and chemical staining are traditional methods of LFP development (Wang et al., 2017; Li et al., 2020; Lv et al., 2021). The common developers of reagent fuming and chemical staining methods are iodine, cyanoacrylate, silver nitrate, ninhydrin and 1-diazafene-9-one (DFO). These chemical reagents can react with amino acids in LFPs and seriously damage skin, eyes, mucous membrane, and DNA (Wang et al., 2017). Powder dusting method is the most commonly used method due to its simplicity and high efficiency. The tools used are usually

special brush and fine powder in contrast to the substrate. When the special brush gently sweeps on the surface of latent fingerprints (LFPs), the powders are adhered to the ridges of latent fingerprints (LFPs), hence the LFPs can be seen by the naked eyes (Li et al., 2020). Traditional powder developers, such as toner, aluminum, copper, magnetic powder, are not suitable for substrates with similar color and often show low signal-to-noise ratio and low resolution. Hence, high contrast powder developer is an urgent problem to be solved. Fluorescent materials have been widely studied due to their various colors, high brightness and high contrast. Fluorescence visualization of LFPs has become a new research hotspot (Wang et al., 2020). Up to now, a variety of fluorescent materials have been employed in LFPs fluorescence development, such as up-conversion nanoparticles (UCNPs) (Wang et al., 2015; Marappa et al., 2018; Kanodarwala et al., 2021), metal–organic frame-works (Wang M. et al., 2018), quantum dots (QDs) (Raju et al., 2017; Sandhyarani et al., 2017; Shi et al., 2018), gold nanoparticles (Cheng et al., 2016), carbon dots (Fernandes et al., 2015), and semiconductor polymer dots (Cui et al., 2015). Compared with traditional developers, fluorescent developers greatly improve the contrast of development patterns of LFPs. However, these fluorescent materials showed some limitations, such as complex preparation process, large consumption of developers, exorbitant price, poor safety and so on (Wang et al., 2020). Recently, Pro Fu and Pro Tang prepared LFP fluorescent developer by blending fluorescent dyes with MMT (Li et al., 2020; Lv et al., 2021). These novel fluorescent developers reduced the dye content to 10%, which greatly reduced the consumption of developers and enhanced the safety. At present, there are few studies on fluorescent dye/MTT developers. Novel fluorescent materials for fluorescent dye/MTT developers with lower material consumption and high performance of LFPs development need to be developed.

As one of the typical fluorophores, DCM derivatives possess excellent photophysical and photochemical properties, such as large Stokes shift, excellent photostability, tunable near-infrared emission, etc. However, the fluorescence of DCM derivatives in solid state is usually very weak, suffering from aggregation-caused quenching (ACQ) effect. Herein, DCM derivative Boc-PZ-DCM with strong emission in solid state was successfully synthesized by introducing Boc group into the core of DCM. By blending Boc-PZ-DCM with MMT, fluorescence developer for LFP was successfully prepared, reducing the dosage of fluorescent material to 3%. This paper provides a strategy for fluorescence enhancement of dyes in solid state and its application in efficient fluorescence visualization of LFP.

MATERIALS AND METHODS

Synthesis of (*E*)-2-(2-methyl-6-(4-(piperazin-1-yl)styryl)-4H-pyran-4-ylidene)malononitrile (PZ-DCM). A solution of 2-(2,6-dimethyl-4H-pyran-4-ylidene)malononitrile (200 mg, 1.16 mmol, 1 eq.) and 4-(piperazin-1-yl)benzaldehyde (221 mg, 1.16 mmol, 1 eq.) and piperidine (20 μl, cat.) in EtOH (15 ml) was

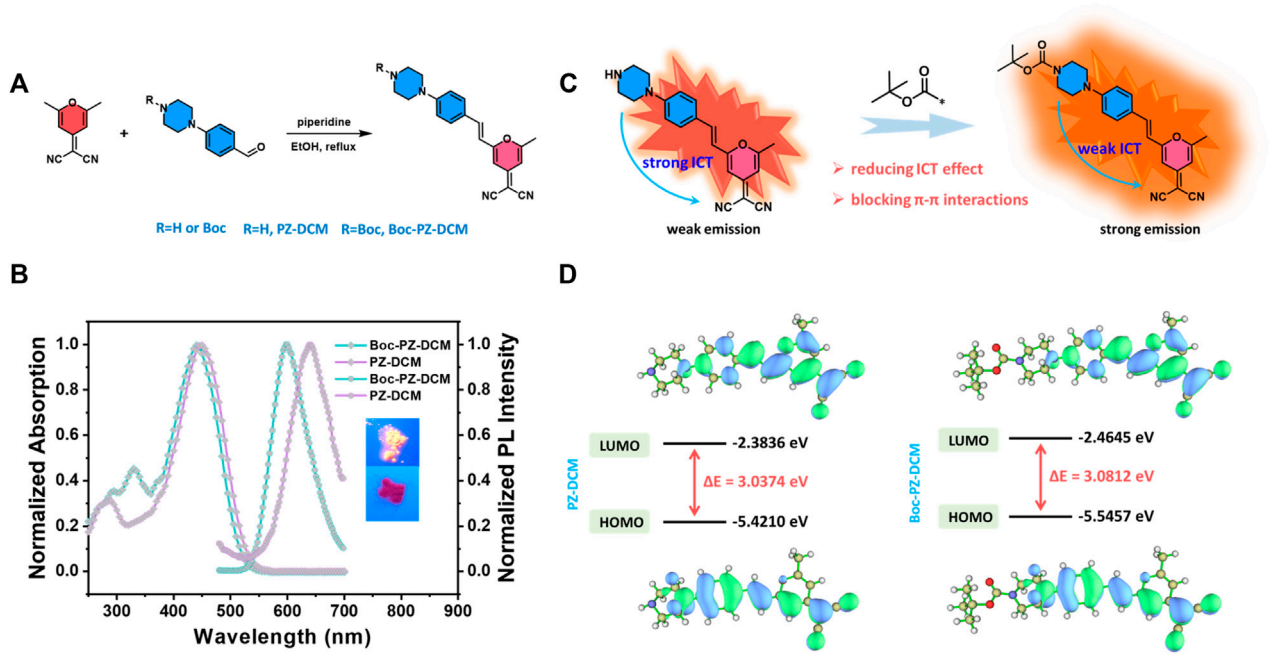

FIGURE 1 | (A) The synthetic route of compounds PZ-DCM and Boc-PZ-DCM. **(B)** Normalized absorption and fluorescence spectra of PZ-DCM and Boc-PZ-DCM. The absorption spectra were measured in THF solution with the dye concentration of 10 μM. The fluorescence spectra were measured in solid state under 410 nm excitation. Inset: Fluorescent photographs of PZ-DCM (bottom) and Boc-PZ-DCM (top) under 365 nm irradiation. **(C)** Schematic diagram for fluorescence properties of PZ-DCM and Boc-PZ-DCMS affect by ICT effect. **(D)** HOMO and LUMO energy levels of PZ-DCM and Boc-PZ-DCM. Molecular orbital amplitude plots of HOMO and LUMO energy levels calculated using the B3LYP/6-31G(d) basis set in the Gaussian 09 program. ΔE (energy gap) = LUMO–HOMO.

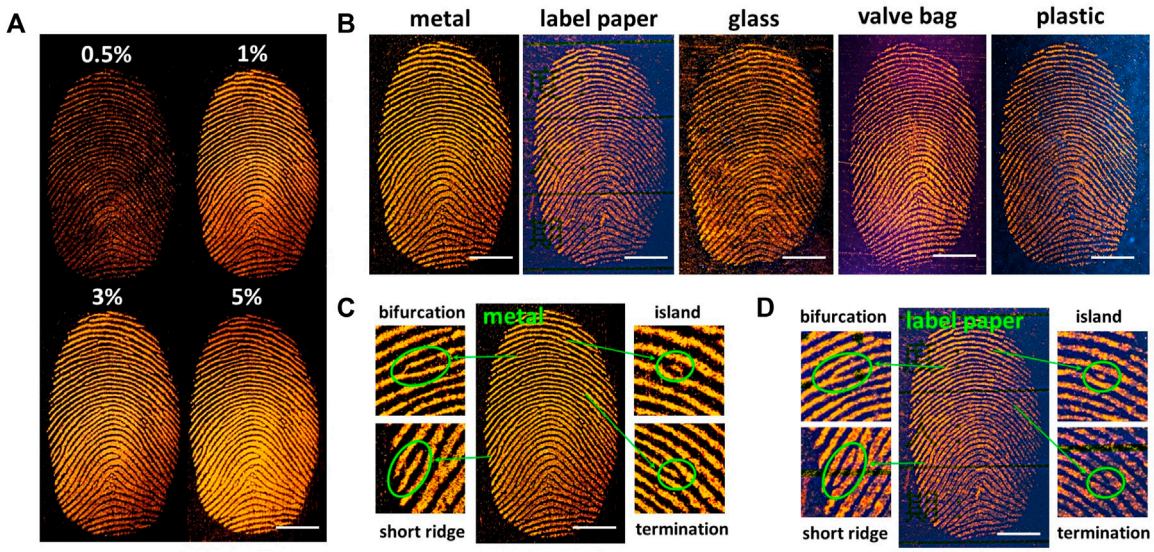

FIGURE 2 | (A) Images of LFPs developed by the mixing powder of Boc-PZ-DCM/MMT with dye content of 0.5%, 1%, 3%, 5%, respectively, under 365 nm irradiation. **(B)** Images of LFPs on different substrates developed by the mixing powder of Boc-PZ-DCM/MMT with dye content of 3%. **(C)** Level 2 details of LFP on metal developed by the mixing powder of Boc-PZ-DCM/MMT with dye content of 3%. **(D)** Level 2 details of LFP on labelled paper developed by the mixing powder of Boc-PZ-DCM/MMT with dye content of 3%. Scale bar, 5 mm.

stirred at 80°C for 16 h. The solvent was evaporated under vacuum. The residue was purified by flash column chromatography (DCM/MeOH = 0–15%) to afford **PZ-DCM** (160 mg, 40%) as an orange solid. ^{1}H NMR (400 MHz, Chloroform-d_3) δ 7.46–7.42 (m, 2H), 7.37 (d, J = 15.9 Hz, 1H), 6.91 (d, J = 8.9 Hz, 2H), 6.61 (d, J = 2.1 Hz, 1H), 6.56–6.47 (m, 2H), 3.33–3.23 (m, 4H), 3.07–2.97 (m, 4H), 2.39 (s, 3H). ^{13}C NMR (101 MHz, DMSO-d_6) δ 164.32, 161.29, 157.14, 153.05, 138.53, 130.08, 124.75, 116.22, 114.74, 114.70, 106.04, 105.99, 48.35, 45.78, 19.86.

Synthesis of tert-butyl (*E*)-4-(4-(2-(4-(dicyanomethylene)-6-methyl-4H-pyran-2-yl)vinyl)phenyl)piperazine-1-carboxylate (Boc-PZ-DCM). A solution of 2-(2,6-dimethyl-4H- pyran-4-ylidene)malononitrile (500 mg, 2.91 mmol, 1 eq.) and tert-butyl 4-(4-formylphenyl)piperazine-1-carboxylate (844 mg, 2.91 mmol, 1 eq.) and piperidine (40 μl, cat.) in EtOH (30 ml) was stirred at 80°C for 16 h. The solvent was evaporated under vacuum. The residue was purified by flash column chromatography (DCM/MeOH = 0–10%) to afford **Boc-PZ-DCM** (810 mg, 63%) as a red solid. ^{1}H NMR (600 MHz, Chloroform-d_3) δ 7.46–7.42 (m, 2H), 7.37 (d, J = 15.9 Hz, 1H), 6.91 (dd, J = 8.7, 5.9 Hz, 2H), 6.62 (d, J = 2.1 Hz, 1H), 6.57–6.48 (m, 2H), 3.59 (t, J = 5.4 Hz, 4H), 3.29 (t, J = 5.2 Hz, 4H), 2.36 (s, 3H), 1.49 (s, 9H). ^{13}C NMR (101 MHz, DMSO-d_6) δ 164.37, 161.19, 157.16, 154.33, 138.37, 131.96, 130.06, 126.90, 125.30, 116.18, 115.23, 113.88, 106.58, 106.14, 79.55, 47.30, 46.61, 28.53, 19.86, 19.78.

Preparation of Boc-PZ-DCM/MMT developers. Boc-PZ-DCM/MMT developers were prepared by grinding Boc-PZ-DCM and MMT with a mortar. 10 mg Boc-PZ-DCM and 1990 mg MMT were thoroughly ground to prepared 0.5% Boc-PZ-DCM/MMT developer. 1%, 3%, 5% Boc-PZ-DCM/MMT developers were prepared by grinding 20 mg Boc-PZ-DCM and 1980 mg MMT, 60 mg Boc-PZ-DCM and 1940 mg MMT, 100 mg Boc-PZ-DCM and 1900 mg MMT, respectively.

RESULTS AND DISCUSSION

PZ-DCM and Boc-PZ-DCM were synthesized by simple Knoevenagel condensation (**Figure 1A**). The detailed synthesis procedures of PZ-DCM and Boc-PZ-DCM and the target compounds are described in section of materials and methods. The target compounds were characterized by ^{1}H NMR, ^{13}C NMR. The UV-vis absorption spectra of PZ-DCM and Boc-PZ-DCM were measured in THF solution. The maximum UV-vis absorption peaks of PZ-DCM and Boc-PZ-DCM are located at 450 and 440 nm, respectively (**Figure 1B**). Compared with PZ-DCM, the maximum absorption peak of Boc-PZ-DCM blue-shifted 10 nm. This is probably attributed to the introduction of the Boc electron-withdrawing group. The photoluminescence (PL) spectra of PZ-DCM in solid state located at 640 nm and the solid of PZ-DCM showed weak red emission (**Figure 1B**). However, Boc-PZ-DCM emitted strong orange fluorescence in solid state and the emission peak located at 598 nm (**Figure 1B**). The emission peak showed a large blue-shift of 42 nm for Boc-PZ-DCM compared with PZ-DCM in solid. This is mainly attributed to the electron-withdrawing effect and steric effect of Boc group. To understand their geometries and electronic structures at the molecular level, density functional theory (DFT) calculations of PZ-DCM and Boc-PZ-DCM were carried out (Lu and Chen, 2012). The optimized geometries of PZ-DCM and Boc-PZ-DCM are shown in **Figure 1D**. The computerized energy gap (ΔEg) of PZ-DCM and Boc-PZ-DCM are 3.0374 and

3.0812 eV, respectively. Combined with the calculation results, it can be inferred that, firstly, the electron-withdrawing effect of Boc group reduces the electron donating capacity of the piperazine group, hence, the ICT effect of Boc-PZ-DCM is weakened (**Figures 1C,D**). Secondly, the large steric hindrance of the Boc group prevents strong intermolecular π-π stacking of Boc-PZ-DCM. This means the Boc group can greatly affect the luminescence properties of DCM derivatives.

Fluorescent materials have been used for LFP visualization with powder dusting method due to its high contrast and low background. However, the traditional fluorescent developer is high consumption in LFP visualization. Recently Tang et al. (Li et al., 2020) and Fu et al. (Lv et al., 2021) prepared LFP fluorescent developer by blending fluorescent materials with MMT. This method reduces the use of fluorescent materials to 10%. The excellent optical performance of Boc-PZ-DCM is conducive to the application of LFPs fluorescent development. Hence, Boc-PZ-DCM/MMT fluorescent developers were prepared by mixing Boc-PZ-DCM and MMT with dye content of 0.5%, 1%, 3%, 5%, respectively. Next, the LFPs were developed by dusting method with the prepared fluorescent developers. As shown, when the dye content was 0.5%, the developed fingerprint pattern showed poor contrast (**Figure 2A**). When the dye ratio was between 1% and 5%, the fingerprint pattern was clearly visible, showing excellent contrast (**Figure 2A**). Subsequently, Boc-PZ-DCM/MMT developer with 3% dye content was employed to develop LFPs on different substrates (**Figure 2B**). Clear fingerprint patterns can be obtained with high resolution. Level 2 details, generally divided into termination, bifurcation, island, short ridge, lake and so on, are often used to recognize an individual's identity due to the unique features of individual. To verify the fingerprint details, level 2 details of the fingerprints on metal and label paper were analyzed. As shown, the bifurcation, short ridge, island and termination are clearly visible by the naked eye, which can provide reliable evidence for the reorganization of individual identity (**Figures 2C,D**). The results show that Boc-PZ-DCM/MMT developer possesses high development ability and multi-substrates universality.

CONCLUSION

In conclusion, we have successfully prepared DCM derivatives with strong emission in solid state by introducing Boc group, which provides strategies for the fluorescence enhancement of ACQ dyes in solid state. In view of this, LFP fluorescent developers were prepared by blending Boc-PZ-DCM with MMT. As a result, LFP can be clearly developed by dusting method with 3% dye content Boc-PZ-DCM/MMT developer. The level 2 fingerprint features are clearly visible, resulting in a clear, high-contrast fingerprint pattern. Boc-PZ-DCM/MMT developer for LFP reduces the content of fluorescent materials to 3%, greatly reducing the consumption of fluorescent materials and increasing the safety of LFP fluorescent developer.

DATA AVAILABILITY STATEMENT

The original contributions presented in the study are included in the article/Supplementary Material, further inquiries can be directed to the corresponding author.

AUTHOR CONTRIBUTIONS

YC, T-TH carried out the experiment and prepared the article. C-YW, Y-HT, Z-YZ participated in the work of data collection. DZ revised the language of the article. M-QZ, Y-LW supervised the whole work. All authors discussed and commented on the article.

FUNDING

This work was supported by National Key R&D Program of China (2021ZD0201004), the National Natural Science Foundation of China (22165008 and 22077037), Hainan Provincial Natural Science Foundation of China (521RC506), the Open Project Program of Wuhan National Laboratory for Optoelectronics (No. 2020WNLOKF018).

ACKNOWLEDGMENTS

We also thank Analytical and Testing Center of Hainan University for use of their facilities.

REFERENCES

Bécue, A. (2016). Emerging Fields in Fingermark (Meta)detection - a Critical Review. *Anal. Methods* 8 (45), 7983–8003. doi:10.1039/c6ay02496c

Cheng, Y.-H., Zhang, Y., Chau, S.-L., Lai, S. K.-M., Tang, H.-W., and Ng, K.-M. (2016). Enhancement of Image Contrast, Stability, and SALDI-MS Detection Sensitivity for Latent Fingerprint Analysis by Tuning the Composition of Silver-Gold Nanoalloys. *ACS Appl. Mat. Interfaces* 8 (43), 29668–29675. doi:10.1021/acsami.6b09668

Cui, J., Xu, S., Guo, C., Jiang, R., James, T. D., and Wang, L. (2015). Highly Efficient Photothermal Semiconductor Nanocomposites for Photothermal Imaging of Latent Fingerprints. *Anal. Chem.* 87 (22), 11592–11598. doi:10.1021/acs.analchem.5b03652

Fernandes, D., Krysmann, M. J., and Kelarakis, A. (2015). Carbon Dot Based Nanopowders and Their Application for Fingerprint Recovery. *Chem. Commun.* 51 (23), 4902–4905. doi:10.1039/c5cc00468c

Kanodarwala, F. K., Moret, S., Spindler, X., Lennard, C., and Roux, C. (2021). Novel Upconverting Nanoparticles for Fingermark Detection. *Opt. Mater.* 111, 110568. doi:10.1016/j.optmat.2020.110568

Li, J., Jiao, Z., Zhang, P., Wan, X., Song, C., Guo, Z., et al. (2020). Development of AIEgen-Montmorillonite Nanocomposite Powders for Computer-Assisted Visualization of Latent Fingermarks. *Mat. Chem. Front.* 4 (7), 2131–2136. doi:10.1039/d0qm00059k

Lu, T., and Chen, F. (2012). Multiwfn: A Multifunctional Wavefunction Analyzer. *J. Comput. Chem.* 33 (5), 580–592. doi:10.1002/jcc.22885

Lv, Z., Man, Z., Xu, Z., Li, S., Liao, Q., and Fu, H. (2021). Highly Emissive Near-Infrared Solid Organic Fluorophores for Visualization of Latent Fingerprints Based on the Powder Dusting Method. *J. Mat. Chem. C* 9 (23), 7345–7350. doi:10.1039/d1tc01183a

Marappa, B., Rudresha, M. S., Basavaraj, R. B., Darshan, G. P., Prasad, B. D., Sharma, S. C., et al. (2018). EGCG Assisted Y2O3:Eu3+ Nanopowders with 3D Micro-architecture Assemblies Useful for Latent Finger Print Recognition and Anti-counterfeiting Applications. *Sensors Actuators B Chem.* 264, 426–439. doi:10.1016/j.snb.2018.02.133

Sandhyarani, A., Kokila, M. K., Darshan, G. P., Basavaraj, R. B., Daruka Prasad, B., Sharma, S. C., et al. (2017). Versatile Core-Shell SiO 2 @SrTiO 3 :Eu 3+ , Li + Nanopowders as Fluorescent Label for the Visualization of Latent Fingerprints and Anti-counterfeiting Applications. *Chem. Eng. J.* 327, 1135–1150. doi:10.1016/j.cej.2017.06.093

Seeta Rama Raju, G., Park, J. Y., Nagaraju, G. P., Pavitra, E., Yang, H. K., Moon, B. K., et al. (2017). Evolution of CaGd2ZnO5:Eu3+ Nanostructures for Rapid Visualization of Latent Fingerprints. *J. Mat. Chem. C* 5 (17), 4246–4256. doi:10.1039/c7tc00852j

Shi, Y., Ye, J., Qi, Y., Akram, M. A., Rauf, A., and Ning, G. (2018). An Anionic Layered Europium(iii) Coordination Polymer for Solvent-dependent Selective Luminescence Sensing of Fe3+ and Cu2+ Ions and Latent Fingerprint Detection. *Dalton Trans.* 47 (48), 17479–17485. doi:10.1039/c8dt04042g

Tian, R., Wang, Y.-L., Li, C., and Zhu, M.-Q. (2022). Turn-on Green Fluorescence Imaging for Latent Fingerprint Applications. *Mat. Chem. Front.* 6 (9), 1188–1193. doi:10.1039/d2qm00107a

Wang, M., Guo, L., and Cao, D. (2018). Metal-organic Framework as Luminescence Turn-On Sensor for Selective Detection of Metal Ions: Absorbance Caused Enhancement Mechanism. *Sensors Actuators B Chem.* 256, 839–845. doi:10.1016/j.snb.2017.10.016

Wang, M., Li, M., Yang, M., Zhang, X., Yu, A., Zhu, Y., et al. (2015). NIR-Induced Highly Sensitive Detection of Latent Fingermarks by NaYF4:Yb,Er Upconversion Nanoparticles in a Dry Powder State. *Nano Res.* 8 (6), 1800–1810. doi:10.1007/s12274-014-0686-6

Wang, M., Li, M., Yu, A., Zhu, Y., Yang, M., and Mao, C. (2017). Fluorescent Nanomaterials for the Development of Latent Fingerprints in Forensic Sciences. *Adv. Funct. Mat.* 27 (14), 1606243. doi:10.1002/adfm.201606243

Wang, Y.-L., Li, C., Qu, H.-Q., Fan, C., Zhao, P.-J., Tian, R., et al. (2020). Real-Time Fluorescence *In Situ* Visualization of Latent Fingerprints Exceeding Level 3 Details Based on Aggregation-Induced Emission. *J. Am. Chem. Soc.* 142 (16), 7497–7505. doi:10.1021/jacs.0c00124

Wang, Y., Wang, J., Ma, Q., Li, Z., and Yuan, Q. (2018). Recent Progress in Background-free Latent Fingerprint Imaging. *Nano Res.* 11 (10), 5499–5518. doi:10.1007/s12274-018-2073-1

Wei, Q., Zhang, M., Ogorevc, B., and Zhang, X. (2016). Recent Advances in the Chemical Imaging of Human Fingermarks (A Review). *Analyst* 141 (22), 6172–6189. doi:10.1039/c6an01121g

Zhang, S., Liu, R., Cui, Q., Yang, Y., Cao, Q., Xu, W., et al. (2017). Ultrabright Fluorescent Silica Nanoparticles Embedded with Conjugated Oligomers and Their Application in Latent Fingerprint Detection. *ACS Appl. Mat. Interfaces* 9 (50), 44134–44145. doi:10.1021/acsami.7b15612

Conflict of Interest: The authors declare that the research was conducted in the absence of any commercial or financial relationships that could be construed as a potential conflict of interest.

Publisher's Note: All claims expressed in this article are solely those of the authors and do not necessarily represent those of their affiliated organizations, or those of the publisher, the editors and the reviewers. Any product that may be evaluated in this article, or claim that may be made by its manufacturer, is not guaranteed or endorsed by the publisher.

frontiers | Frontiers in Chemistry

MINI REVIEW
published: 22 July 2022
doi: 10.3389/fchem.2022.954419

Organic Electroluminescent Materials Possessing Intra- and Intermolecular Hydrogen Bond Interactions: A Mini-Review

Xinyong Liu[1], *Jingwei Li*[1], *Xu Qiu*[1]* *and Yuyu Pan*[2]*

[1]College of Materials Science and Engineering, Shandong University of Science and Technology, Qingdao, China, [2]School of Petrochemical Engineering, Shenyang University of Technology, Liaoyang, China

Organic light-emitting diodes (OLEDs) have become the predominant technology in display applications because of their superior light weight, flexibility, power conservation, and environmental friendliness, among other reasons. The device's performance is determined by the intrinsic properties of organic emitters. The aggregation structure of emitters, in particular, is crucial for color purity and efficiency. Intra- and intermolecular interactions, such as hydrogen bonds (H-bonds), can reduce structural vibrations and torsions, which affect the stability of emitting layer films and optoelectronic properties of emitting materials. Hence, by regulating the H-bond interaction, the desired properties could be obtained. This mini-review focuses on the influence of intra- and intermolecular H-bond interactions on the optoelectronic properties of high-performance emitters.

Keywords: hydrogen bond, intra- and intermolecular interaction, charge transfer, organic emitter, optoelectronic property

OPEN ACCESS

Edited by:
Meng Zheng,
Qingdao Haiwan Science and Technology Industry Research Institute Co., Ltd., China

Reviewed by:
Huizhi Lu,
Qingdao University of Science and Technology, China
Haichang Zhang,
Qingdao University of Science and Technology, China

***Correspondence:**
Xu Qiu
tlqiux2014@163.com
Yuyu Pan
panyu0422@sut.edu.cn

Specialty section:
This article was submitted to Electrochemistry, a section of the journal Frontiers in Chemistry

Received: *27 May 2022*
Accepted: *21 June 2022*
Published: *22 July 2022*

Citation:
Liu X, Li J, Qiu X and Pan Y (2022) Organic Electroluminescent Materials Possessing Intra- and Intermolecular Hydrogen Bond Interactions: A Mini-Review. Front. Chem. 10:954419. doi: 10.3389/fchem.2022.954419

INTRODUCTION

As stated in the pioneering work of Tang and VanSlyke et al., organic light-emitting diodes (OLEDs) have attracted considerable scientific and industrial interests (Tang and VanSlyke, 1987). Extensive research has been conducted to promote OLEDs in commercial applications as flat panel displays and lighting sources due to their lightweight, flexibility, power saving, and environmental friendliness (Chen and Xu, 2021; Zhang et al., 2021; Zhu et al., 2021). Red, green, and blue (RGB) emitters with nearly comparable stability, efficiency, and color purity are necessary to fabricate full-color flat panel displays. Therefore, developing emitters with good comprehensive performance is crucial for the new generation of full-color flat panel display applications.

Organic emitters are one of the indispensable parts of OLEDs; not only the properties of the monomolecular state but also those of the aggregated state can influence device performance. The aggregation structure of emitters is crucial for device color purity and electroluminescence (EL) efficiency (Guo et al., 2017; Han et al., 2020). Intra- and intermolecular interactions, such as hydrogen bonds (H-bonds), could have a vital effect on the stability of emitting layer films and optoelectronic properties of emitting materials. The desired optoelectronic properties could be obtained by regulating the H-bond interactions. Hence, in this mini-review, we focus on the organic emitting materials from the influence of intra- and intermolecular H-bond interactions on optoelectronic properties.

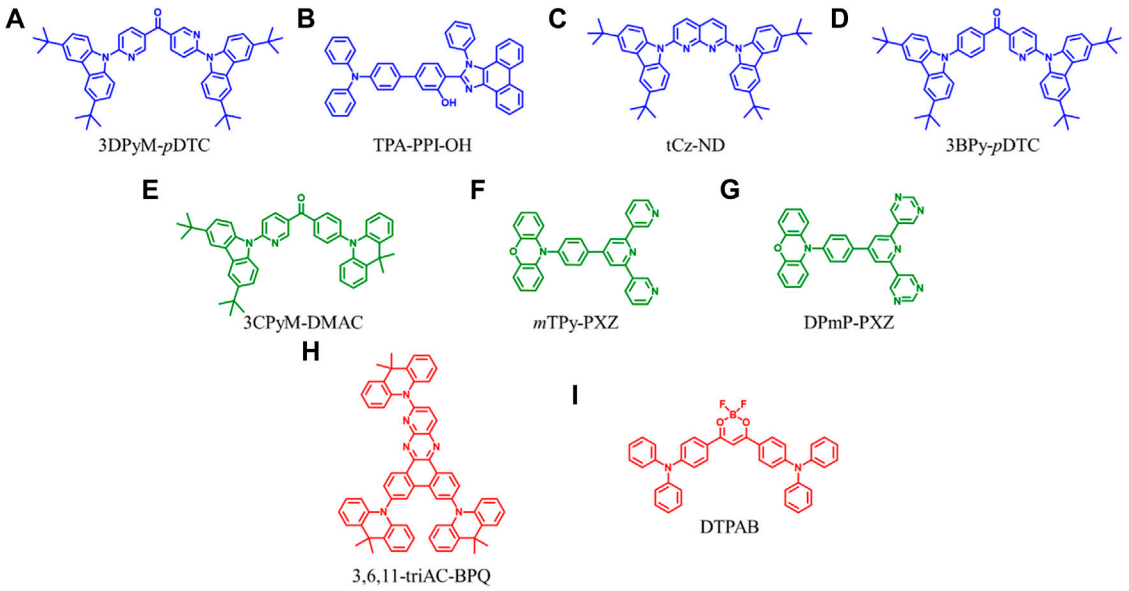

FIGURE 1 | Chemical structures of the OLED materials possessing intra/intermolecular H-bond interactions.

INTRA- AND INTERMOLECULAR H-BOND INTERACTIONS IN DIFFERENT EMITTING MATERIALS

The intra- and intermolecular interactions in optoelectronic materials can influence their arrangement and aggregation behaviors, which could further influence, for example, carrier mobility, color purity, and efficiency. This section mainly discusses the influence of intra- and intermolecular H-bond interactions on the optoelectronic properties of RGB organic emitting materials.

H-bond Interactions in Organic Blue Emitters

An efficient deep-blue emitter can lower the power consumption, increase the color gamut of full-color OLEDs, and create other visible emissions and white light through the energy transfer processes (Lv et al., 2021; Xu et al., 2021). However, deep-blue emitters have a naturally broad bandgap, leading to a significant charge injection barrier and unbalanced charge injection and transportation in the device (Xue et al., 2017; Zhang et al., 2020; Zhang et al., 2022). Therefore, there is an essential and significant need to develop deep-blue emitters with high EL efficiency and narrow-band emission.

To simultaneously enhance color purity, out-coupling efficiency, and internal quantum efficiency of OLEDs, two isomers, 2DPyM-*m*DTC and 3DPyM-*p*DTC (**Figure 1A**), have been designed by Cheng et al. The crystal structure of 3DPyM-*p*DTC showed that the intramolecular H-bonding between the two pyridine nitrogen atoms and the proximal C–H-bonds of the tert-butylcarbazole groups with a C–H···N of 2.5 Å was found (**Figure 2A**). The presence of C–H···N hydrogen bonding should limit rotation between the donor and acceptor groups in the molecule and increase the photoluminescence quantum yield (PLQY) in the solid state. The device based on 3DPyM-*p*DTC, with a nearly planar structure, shows a very high PLQY of 98%, EQE of 31%, and corresponding blue emission with full width at half-maximum (FWHM) of 62 nm and CIE of (0.14, 0.18) compared with 2DPyM-*m*DTC (Rajamalli et al., 2017).

Ma et al. reported TPA-PPI-OH (**Figure 1B**), a deep-blue fluorescent emitter with phenol group as a π-bridge (Qiu et al., 2019). The endowed intra- and intermolecular H-bonds interactions proved beneficial in suppressing the structural vibrations and thereby caused a narrower FWHM PL emission of TPA-PPI-OH. A non-doped OLED device based on TPA-PPI-OH exhibited highly efficient EL performance and achieved an EQE of 7.37% with narrow emission (FWHM: 58 nm). Kazlauskas et al. exploited carbazole–naphthyridine (donor-acceptor) based blue-emitting compounds, which were designed using both the H-bonding and sterically controlled charge-transfer interactions between D and A units. None methyl-substituted naphthyridine (tCz-ND, **Figure 1C**) exhibited deep-blue (λ_{max} < 460 nm) and narrow-band EL (FWHM = 66 nm), whereas the more twisted methyl-substituted compound (MetCz-ND) expressed broader band (FWHM >80 nm) sky-blue (λ_{max} ≈ 480 nm) emission. (Kreiza et al., 2020). Recently, Rajamalli et al. demonstrated the role of the donor substitution position in a thermally activated delayed fluorescence (TADF) emitter to achieve deep-blue emission with improved color purity without reducing the device performance. A novel 3BPy-*p*DTC (**Figure 1D**) was synthesized, where two tert-butyl carbazolyl (DTC) donors linearly connected at the para position of the benzoyl pyridine (3BPy) acceptor core. 3BPy-*p*DTC shows higher color purity in deep-blue emission than the meta-substituted counterpart (3BPy-*m*DTC) due to the locked geometry *via* intramolecular H-bonding (**Figure 2B**) (Sk et al., 2022).

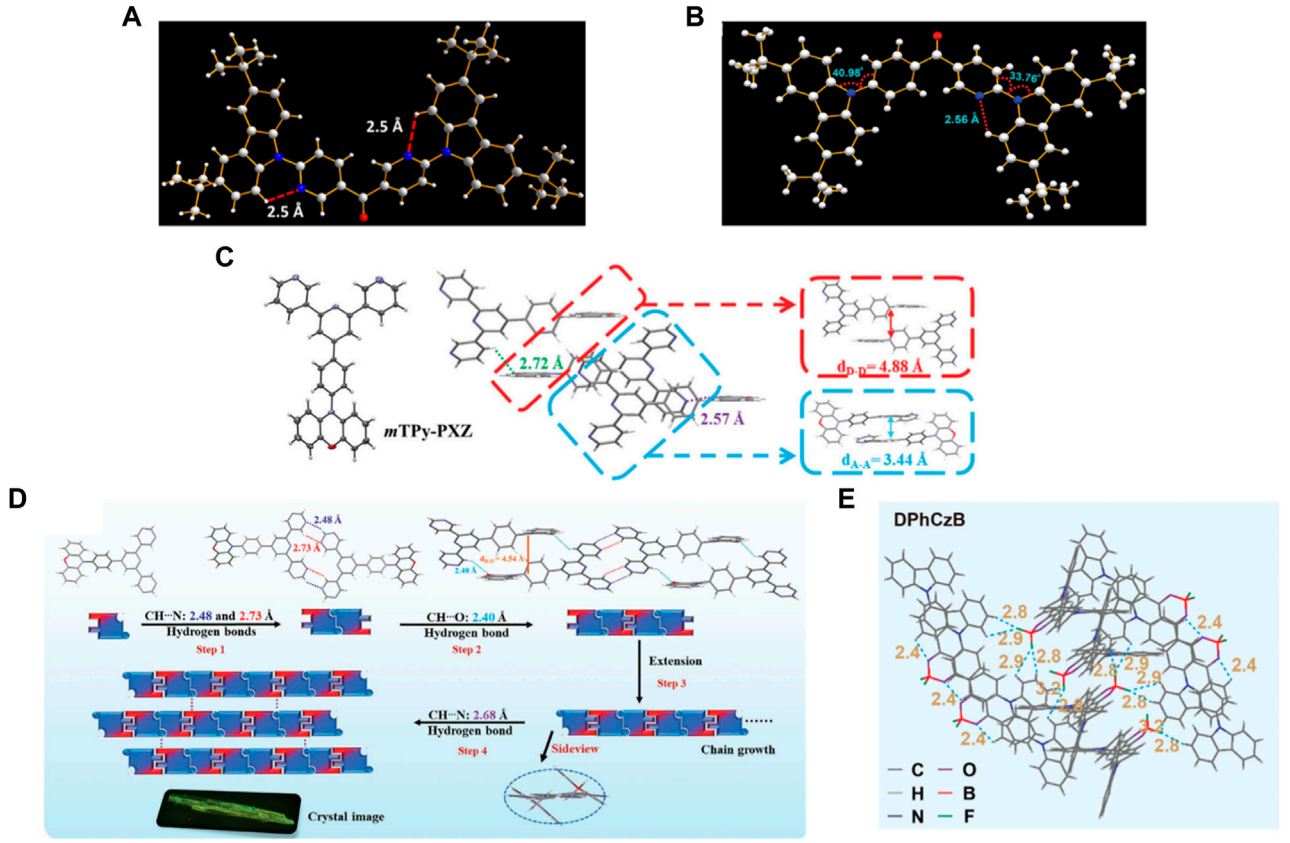

FIGURE 2 | The H-bond interactions in different OLED materials. **(A)** Crystal structure of 3DPyM-*p*DTC. **(B)** The molecular structure and packing diagram of 3BPy-*p*DTC obtained from single-crystal X-ray diffraction analysis displaying the intramolecular H-bonding interaction and the donor-acceptor dihedral angles. **(C)** Thermal ellipsoid drawings at the 50% probability level and intermolecular geometries of *m*TPy-PXZ in the single crystals were determined by X-ray analysis. **(D)** Intermolecular packing geometries of DPmP-PXZ in the single crystal determined by X-ray analysis. **(E)** Molecular packing and inter- and intramolecular interactions in the DPhCzB crystal.

H-Bond Interactions in Organic Green Emitters

TADF materials are urgently needed for fabricating OLEDs because of the high exciton usage efficiency and metal-free molecular frameworks (Liu et al., 2018). The narrowing singlet-triplet splitting energy (ΔE_{st}) is important for the up-conversion process from triplet to singlet excitons in devices, resulting in theoretically high internal quantum efficiencies. Qi et al. discovered that the existence of intramolecular hydrogen bonding is conducive to diminish the energy difference (ΔE_{st}) between a singlet and a triplet, suppressing nonradiative decay and increasing the luminescence efficiency (Ma et al., 2020). They found that, for the crystals of CBM-PXZ and 3CPyM-PXZ, multiple H-bonds of C=O···H with the distances of 2.57–3.57 Å can be observed, which were conducive to locking the movement within molecules and rigidifying the geometric structures of molecules. Therefore, the nonradiative decay process can be suppressed, and luminescence efficiency will be enhanced in the solid state. Therefore, solution-processed non-doped OLEDs adopted 3CPyM-DMAC (**Figure 1E**) as an emitter exhibiting a maximum CE and EQE of 33 cd A^{-1} and 11.4%.

Due to quenching caused by intermolecular triplet contact, non-doped OLEDs always result in significant efficiency roll-off. Zhang et al. reported a green fluorescent material of *m*TPy-PXZ (**Figure 1F**), revealing a novel strategy of tuning intermolecular H-bonds for high-performance non-doped electroluminescence (Shi et al., 2020). Suitable intermolecular H-bond interaction enables the 3D supramolecular framework formation (**Figure 2C**), which limits the nonradiative process and suppresses the triplet exciton quenching caused by π–π stacking of triplets but also favors the horizontal molecular orientations, especially in their non-doped states. The non-doped OLED based on the *m*TPy-PXZ with such suitable intermolecular H-bonds exhibits the state-of-the-art performance with maximum EQE of up to 23.6% with only 7.2% roll-off at 1,000 cd m^{-2}. Recently, they designed a new TADF emitter, DPmP-PXZ (**Figure 1G**), composed of 2,6-di (pyrimidin-5-yl) pyridine (DPmP) as electron-acceptor and phenoxazine (PXZ) as electron-donor (Shi et al., 2021). Further intermolecular hydrogen bonding between the DPmP and PXZ groups favors the formation of extended linear chains of molecules instead of 3D frameworks (**Figure 2D**). It is further shown that the 1D structure would help separate electron-rich

PXZ cores in neighboring molecules. This leads to suppression of exciton annihilation between molecules, and the extended 1D chain structure improves the carrier mobility balance and optical out-coupling. The non-doped device based on DPmP-PXZ realized an excellent maximum EQE of 21.8% with little efficiency roll-off. These findings contribute to a better understanding of the role of hydrogen bonding in molecular packing and expand the possibilities for using varied hydrogen bonding to regulate molecular packing in non-doped systems.

H-Bond Interactions in Organic Red Emitters

The design of high-performance red emitters remains a great challenge due to their small energy bandgaps with severe nonradiative decay for low luminous efficiency. Introducing rigid and fused coplanar molecular structure to suppress the vibrational relaxation and show a horizontal molecular orientation in the film, enhancing the luminescence efficiency of organic red emitters, is an effective technique. Tang et al. fabricated an emitter, 3,6,11-triAC-BPQ (**Figure 1H**), containing a rigid planar dibenzo[*f,h*]pyrido[2,3-*b*]quinoxaline (BPQ) core and three 9,9-dimethyl-9,10-dihydroacridine (Ac) donors (Xie et al., 2020). They found that a 3,6,11-triAC-BPQ intramolecular H-bond refined the dihedral angle, which can hybrid the local and charge transfer excited state. Finally, a device with 3,6,11-triAC-BPQ as an emitter exhibited a high EQE of 22.0%.

Introducing rigid and fused moieties is an effective way to enhance the red emitters' luminescence. Still, the solubility is significantly reduced, inevitably prohibiting their applications in solution-processed OLEDs. Hence, Chen et al. proposed an intermolecular locking strategy to improve the solution processibility and photoluminescence efficiency of red emitters using a highly soluble flexible difluoroboron β-diketonate unit with exposed and easily reachable fluorines that can form H-bonds in the solid state to induce strong intermolecular locking for high luminescent efficiency (Jin et al., 2021). Due to the exposed difluoroboron β-diketonate group with multiple fluorine and oxygen atoms in forming hydrogen bonds, abundant intra- and intermolecular interactions with short distances can be observed with strong intermolecular hydrogen bonds of C–H···F and C–H···O in the single-crystal structure analyses of DPhCzB (**Figure 2E**). Hence, the solution-processed OLED based on DTPAB (**Figure 1I**) exhibits exceptional high performance, with a maximum EQE of 8.2%. These results demonstrated that the intermolecular locking strategy by directly addressing the internal conflicts between solubility and luminescent efficiency provides important clues in developing highly efficient and solution-processable red emitters for high-performance OLEDs.

CONCLUSION

One of the most promising technologies for future lighting and flat panel display applications is highly efficient OLEDs. In this mini-review, we have mainly discussed the RGB emitting materials possessing intra- and intermolecular H-bonds interactions that potentially affect optoelectronic performance. There are mainly two aspects ascribed to the interactions based on exploiting the intra- and intermolecular H-bonds interactions and analyzing the performance of different materials: 1) restricting the rotation between different donor/acceptor moieties and inhibiting the vibrational coupling of excited states, which could obtain high luminous efficiency and color purity; 2) the multiple H-bonds interactions could further enhance horizontal orientation in amorphous organic semiconductor films and significantly increase hole and electron mobilities, which is beneficial for efficiency stability with negligible roll-off. Although the H-bond interaction is weaker than a covalent interaction, it is critical in promoting the development of high-performance OLEDs. Optoelectronic materials with hydrogen bonding interactions will, predictably, attract increasing interest and attention in the future.

AUTHOR CONTRIBUTIONS

XL prepared the article. JL participated in the work of data collection. XQ and YP supervised the whole work. All authors discussed and commented on the manuscript.

FUNDING

This work was financially supported by the Natural Science Foundation of Shandong Province of China (ZR2021QE050).

ACKNOWLEDGMENTS

We thank the Project of Shandong Province Higher Educational Young Innovative Talent Introduction and Cultivation Team [Environment function material innovation team].

REFERENCES

Chen, S., and Xu, H. (2021). Electroluminescent Materials toward Near Ultraviolet Region. *Chem. Soc. Rev.* 50 (15), 8639–8668. doi:10.1039/d0cs01580f

Guo, J., Li, X.-L., Nie, H., Luo, W., Gan, S., Hu, S., et al. (2017). Achieving High-Performance Nondoped OLEDs with Extremely Small Efficiency Roll-Off by Combining Aggregation-Induced Emission and Thermally Activated Delayed Fluorescence. *Adv. Funct. Mat.* 27 (13), 1606458. doi:10.1002/adfm.201606458

Han, P., Lin, C., Ma, D., Qin, A., and Tang, B. Z. (2020). Violet-Blue Emitters Featuring Aggregation-Enhanced Emission Characteristics for Nondoped OLEDs with CIEy Smaller Than 0.046. *ACS Appl. Mat. Interfaces* 12 (41), 46366–46372. doi:10.1021/acsami.0c12722

Jin, J., Wang, W., Xue, P., Yang, Q., Jiang, H., Tao, Y., et al. (2021). Intermolecular Locking Design of Red Thermally Activated Delayed Fluorescence Molecules for High-Performance Solution-Processed Organic Light-Emitting Diodes. *J. Mat. Chem. C* 9 (7), 2291–2297. doi:10.1039/d0tc05624c

Kreiza, G., Banevičius, D., Jovaišaitė, J., Juršėnas, S., Javorskis, T., Vaitkevičius, V., et al. (2020). Realization of Deep-Blue TADF in Sterically Controlled Naphthyridines for Vacuum- and Solution-Processed OLEDs. *J. Mat. Chem. C* 8 (25), 8560–8566. doi:10.1039/d0tc01637c

Liu, Y., Li, C., Ren, Z., Yan, S., and Bryce, M. R. (2018). All-organic Thermally Activated Delayed Fluorescence Materials for Organic Light-Emitting Diodes. *Nat. Rev. Mater* 3 (4), 18020. doi:10.1038/natrevmats.2018.20

Lv, X., Xu, L., Yu, Y., Cui, W., Zhou, H., Cang, M., et al. (2021). High External Quantum Efficiency and Low Efficiency Roll-Off Achieved Simultaneously in Nondoped Pure-Blue Organic Light-Emitting Diodes Based on a Hot-Exciton Fluorescent Material. *Chem. Eng. J.* 408, 127333. doi:10.1016/j.cej.2020.127333

Ma, F., Zhao, G., Zheng, Y., He, F., Hasrat, K., and Qi, Z. (2020). Molecular Engineering of Thermally Activated Delayed Fluorescence Emitters with Aggregation-Induced Emission via Introducing Intramolecular Hydrogen-Bonding Interactions for Efficient Solution-Processed Nondoped OLEDs. *ACS Appl. Mat. Interfaces* 12 (1), 1179–1189. doi:10.1021/acsami.9b17545

Qiu, X., Xu, Y., Wang, C., Hanif, M., Zhou, J., Zeng, C., et al. (2019). Synergistic Effects of Hydrogen Bonds and the Hybridized Excited State Observed for High-Efficiency, Deep-Blue Fluorescent Emitters with Narrow Emission in OLED Applications. *J. Mat. Chem. C* 7 (18), 5461–5467. doi:10.1039/c9tc00357f

Rajamalli, P., Senthilkumar, N., Huang, P.-Y., Ren-Wu, C.-C., Lin, H.-W., and Cheng, C.-H. (2017). New Molecular Design Concurrently Providing Superior Pure Blue, Thermally Activated Delayed Fluorescence and Optical Out-Coupling Efficiencies. *J. Am. Chem. Soc.* 139 (32), 10948–10951. doi:10.1021/jacs.7b03848

Shi, Y., Wang, K., Tsuchiya, Y., Liu, W., Komino, T., Fan, X., et al. (2020). Hydrogen Bond-Modulated Molecular Packing and its Applications in High-Performance Non-doped Organic Electroluminescence. *Mat. Horiz.* 7 (10), 2734–2740. doi:10.1039/d0mh00952k

Shi, Y. Z., Wang, K., Fan, X. C., Chen, J. X., Ou, X. M., Yu, J., et al. (2021). High-Performance Nondoped Organic Light-Emitting Diode Based on a Thermally Activated Delayed Fluorescence Emitter with 1D Intermolecular Hydrogen Bonding Interactions. *Adv. Opt. Mater.* 9 (16), 2100461. doi:10.1002/adom.202100461

Sk, B., Ravindran, E., Deori, U., Yadav, N., Nanda, G. P., and Rajamalli, P. (2022). A Deep Blue Thermally Activated Delayed Fluorescence Emitter: Balance between Charge Transfer and Color Purity. *J. Mat. Chem. C* 10 (12), 4886–4893. doi:10.1039/d1tc05027c

Tang, C. W., and VanSlyke, S. A. (1987). Organic Electroluminescent Diodes. *Appl. Phys. Lett.* 51 (12), 913–915. doi:10.1063/1.98799

Xie, F.-M., Zeng, X.-Y., Zhou, J.-X., An, Z.-D., Wang, W., Li, Y.-Q., et al. (2020). Intramolecular H-Bond Design for Efficient Orange-Red Thermally Activated Delayed Fluorescence Based on a Rigid Dibenzo[f,h]pyrido[2,3-B]quinoxaline Acceptor. *J. Mat. Chem. C* 8 (44), 15728–15734. doi:10.1039/d0tc03965a

Xu, Y., Xu, P., Hu, D., and Ma, Y. (2021). Recent Progress in Hot Exciton Materials for Organic Light-Emitting Diodes. *Chem. Soc. Rev.* 50 (2), 1030–1069. doi:10.1039/d0cs00391c

Xue, S., Qiu, X., Ying, S., Lu, Y., Pan, Y., Sun, Q., et al. (2017). Highly Efficient Nondoped Near-Ultraviolet Electroluminescence with an External Quantum Efficiency Greater Than 6.5% Based on a Carbazole-Triazole Hybrid Molecule with High and Balanced Charge Mobility. *Adv. Opt. Mater* 5 (21), 1700747. doi:10.1002/adom.201700747

Zhang, D., Huang, T., and Duan, L. (2020). Emerging Self-Emissive Technologies for Flexible Displays. *Adv. Mat.* 32 (15), 1902391. doi:10.1002/adma.201902391

Zhang, D., Wada, Y., Wang, Q., Dai, H., Fan, T., Meng, G., et al. (2022). Highly Efficient and Stable Blue Organic Light-Emitting Diodes Based on Thermally Activated Delayed Fluorophor with Donor-Void-Acceptor Motif. *Adv. Sci.* 9 (12), 2106018. doi:10.1002/advs.202106018

Zhang, H., Xue, J., Li, C., Zhang, S., Yang, B., Liu, Y., et al. (2021). Novel Deep-Blue Hybridized Local and Charge-Transfer Host Emitter for High-Quality Fluorescence/Phosphor Hybrid Quasi-White Organic Light-Emitting Diode. *Adv. Funct. Mat.* 31 (25), 2100704. doi:10.1002/adfm.202100704

Zhu, X., Li, Y., Wu, Z., Lin, C., Ma, D., Zhao, Z., et al. (2021). Anthracene-based Bipolar Deep-Blue Emitters for Efficient White OLEDs with Ultra-high Stabilities of Emission Color and Efficiency. *J. Mat. Chem. C* 9 (15), 5198–5205. doi:10.1039/d1tc00432h

Conflict of Interest: The authors declare that the research was conducted in the absence of any commercial or financial relationships that could be construed as a potential conflict of interest.

frontiers | Frontiers in Chemistry

TYPE Original Research
PUBLISHED 26 September 2022
DOI 10.3389/fchem.2022.954588

OPEN ACCESS

EDITED BY
Porun Liu,
Griffith University, Australia

REVIEWED BY
Iver Lauermann,
Helmholtz Association of German Research Centers (HZ), Germany
Jincheng Fan,
Changsha University of Science and Technology, China

*CORRESPONDENCE
Yongtao Qu,
y.qu@northumbria.ac.uk
Vincent Barrioz,
vincent.barrioz@northumbria.ac.uk

SPECIALTY SECTION
This article was submitted to Electrochemistry, a section of the journal Frontiers in Chemistry

RECEIVED 27 May 2022
ACCEPTED 19 August 2022
PUBLISHED 26 September 2022

CITATION
Campbell S, Phillips LJ, Major JD, Hutter OS, Voyce R, Qu Y, Beattie NS, Zoppi G and Barrioz V (2022), Routes to increase performance for antimony selenide solar cells using inorganic hole transport layers.
Front. Chem. 10:954588.
doi: 10.3389/fchem.2022.954588

Routes to increase performance for antimony selenide solar cells using inorganic hole transport layers

Stephen Campbell[1], Laurie J. Phillips[2], Jonathan D. Major[2], Oliver S. Hutter[1], Ryan Voyce[1], Yongtao Qu[1]*, Neil S. Beattie[1], Guillaume Zoppi[1] and Vincent Barrioz[1]*

[1]Department of Mathematics, Physics and Electrical Engineering, Northumbria University, Newcastle Upon Tyne, United Kingdom, [2]Department of Physics, University of Liverpool, Liverpool, United Kingdom

Simple compound antimony selenide (Sb_2Se_3) is a promising emergent light absorber for photovoltaic applications benefiting from its outstanding photoelectric properties. Antimony selenide thin film solar cells however, are limited by low open circuit voltage due to carrier recombination at the metallic back contact interface. In this work, solar cell capacitance simulator (SCAPS) is used to interpret the effect of hole transport layers (HTL), i.e., transition metal oxides NiO and MoO_x thin films on Sb_2Se_3 device characteristics. This reveals the critical role of NiO and MoO_x in altering the energy band alignment and increasing device performance by the introduction of a high energy barrier to electrons at the rear absorber/metal interface. Close-space sublimation (CSS) and thermal evaporation (TE) techniques are applied to deposit Sb_2Se_3 layers in both substrate and superstrate thin film solar cells with NiO and MoO_x HTLs incorporated into the device structure. The effect of the HTLs on Sb_2Se_3 crystallinity and solar cell performance is comprehensively studied. In superstrate device configuration, CSS-based Sb_2Se_3 solar cells with NiO HTL showed average improvements in open circuit voltage, short circuit current density and power conversion efficiency of 12%, 41%, and 42%, respectively, over the standard devices. Similarly, using a NiO HTL in TE-based Sb_2Se_3 devices improved open circuit voltage, short circuit current density and power conversion efficiency by 39%, 68%, and 92%, respectively.

KEYWORDS

Sb_2 Se_3, photovoltaic, inorganic hole transport layers, SCAPs, thin films

1 Introduction

Antimony selenide (Sb_2Se_3), as a simple and low-cost compound with a direct energy band gap (~1.18 eV), high absorption coefficient ($> 10^5$ cm^{-1}) and high carrier mobility (~10 cm^2/Vs, is a promising emergent light absorber for photovoltaic (PV) applications (Chen et al., 2015; Chen et al., 2017; Birkett et al., 2018). As a material, Sb_2Se_3 is mainly

composed of $(Sb_4Se_6)_n$ as 1-D ribbon structures, where the ribbons are strongly coupled by covalent bonds running along the c-axis with weaker Van der Waals (VdW) interactions between the ribbons. Thus, stacking of the ribbons occurs due to the weaker VdW bonds (Deringer et al., 2015). Hole mobility is enhanced in the *c*-axis and can reach 45 cm^2/Vs along the ribbons (Black et al., 1957).

A number of studies have reported that Sb_2Se_3 thin films with preferred crystallographic orientation along the (*hk*1) direction, particularly (221), resulted in devices with higher efficiencies (Leng et al., 2014; Yuan et al., 2016; Li et al., 2017). The improved performance is often attributed to increased charge transport through the (*hk*1)-oriented ribbons perpendicular to the substrate and benign grain boundaries in this material (Chen et al., 2017; Williams et al., 2020). Wang and co-workers demonstrated the dependence of Sb_2Se_3 PV device performance on the preferred crystal orientation of the absorber (Wang et al., 2017). In that work, by optimising growth conditions, Sb_2Se_3 solar cells with preferred (211) and (221)-orientations on CdS and ZnO achieved higher efficiencies (5.6% and 6.0%, respectively) than those with (020) and (120)-orientations (3.2% and 4.8%, respectively). For planar Sb_2Se_3 solar cells in substrate orientation, a record efficiency of 6.5% has been reported with the $Cd_{0.75}Zn_{0.25}S$ buffer layer being used as an alternative to CdS (Figure 1A shows standard substrate device). Meanwhile, Sb_2Se_3 devices with this buffer layer but in a superstrate structure (Figure 1B) have achieved an efficiency of 7.6% (Wen et al., 2018). Recently, a record substrate device efficiency of 9.2% was obtained by growing (001)-oriented Sb_2Se_3 nanorod arrays on sputtered molybdenum layers (Li et al., 2019). A conformal interfacial TiO_2 layer was used to mitigate the migration of elemental antimony (Sb) into the CdS buffer layer, as interdiffusion has been shown to create a detrimental CdSe interlayer (Phillips et al., 2019).

In this work, thin transition metal oxides, NiO and MoO_x, are applied as HTLs in substrate Sb_2Se_3 devices to improve carrier selectivity at the back electrode by controlling inter-diffusion and formation of secondary phase materials (such as $MoSe_2$) at the interface. Additionally, NiO and MoO_x HTLs are deposited on superstrate Sb_2Se_3 films before making Au back contacts to alter the energy band alignments at the back contact effectively producing an electron reflector, and minimising carrier recombination.

In the first part of this study, Sb_2Se_3 substrate/superstrate device simulations using solar cell capacitance simulator (SCAPS) are conducted in order to interpret the effect of HTLs on Sb_2Se_3 device characteristics (Burgelman et al., 2000). We then characterise the material properties of MoO_x and NiO thin films deposited at room temperature by electron beam evaporation. At this temperature it was found that NiO formed a crystalline film, unlike MoO_x which was amorphous. Sb_2Se_3 absorber films were then fabricated by close-space sublimation (CSS) and thermal evaporation (TE) techniques and incorporated into superstrate and substrate solar cell configurations. HTLs were inserted at the metal electrode/Sb_2Se_3 absorber interface and their effect on Sb_2Se_3 crystallinity and solar cell performance is comprehensively studied.

2 Experimental section

2.1 Device fabrication

The basic structure of substrate Sb_2Se_3 solar cells was as follows: Soda lime glass (SLG)/Mo/Sb_2Se_3/CdS/ZnO/ITO/Ni-Al. Mo coated soda lime glass (SLG) substrates measuring 7.5 cm^2 × 2.5 cm^2 were used in this study. NiO or MoO_x HTLs were deposited between the Mo electrode and Sb_2Se_3. Thin HTL films of 15 nm thickness were deposited using e-beam evaporation. 500 nm thick Sb_2Se_3 layers were prepared by TE of crystalline/powder Sb_2Se_3 source material (Alfa Aesar, 99.99%) at a deposition rate of ~15 Å/s. The substrates were maintained at a temperature of 300°C throughout the deposition. The Sb_2Se_3 films were subsequently subjected to a heat treatment

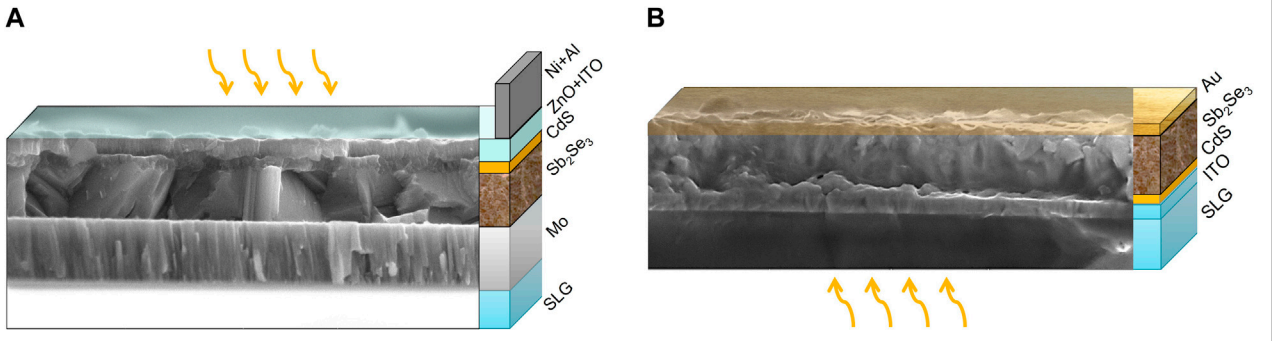

FIGURE 1
Standard planar **(A)** substrate and **(B)** superstrate configuration Sb_2Se_3 solar cells.

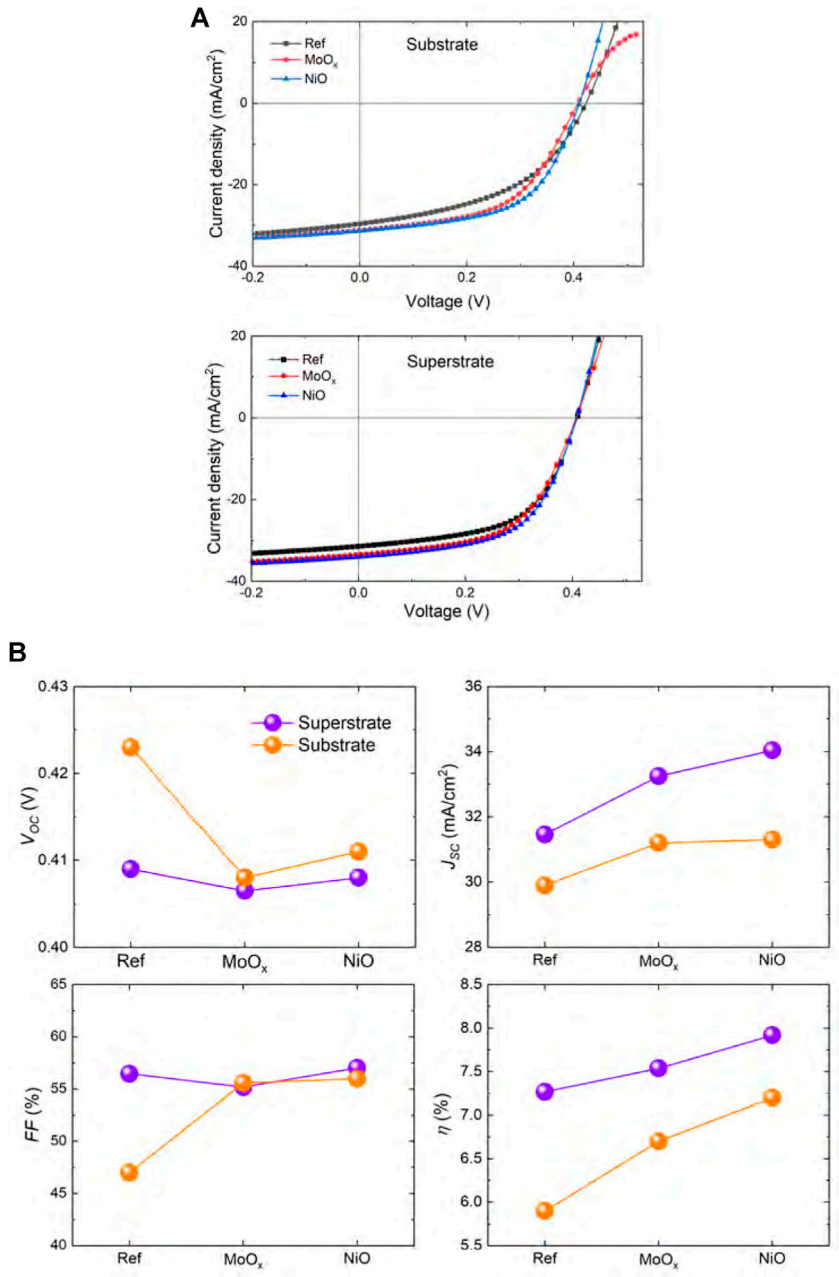

FIGURE 2
(A) *J-V* curves and **(B)** *J-V* parameters of simulated Sb_2Se_3 solar cells with different HTL materials. Roll-over behaviour is observed in the *J-V* curve of substrate devices with MoO_x HTL.

at 300°C for 30 min in Ar atmosphere in a tube furnace to promote recrystallisation. For the CSS Sb_2Se_3 films, a compact seed layer was grown at 0.05 mbar N_2 for 5 min with a source temperature of 350°C, followed by a 30 min growth step at 13 mbar and a source temperature of 450°C to produce a compact and highly orientated grain structure. The substrate was then rapidly cooled with N_2. An *n*-type CdS buffer layer (~60 nm) was deposited by chemical bath deposition followed by DC-pulsed sputtering deposition of an *i*-ZnO (~35 nm) layer plus a transparent conductive window layer ITO (~200 nm). Front contact grids comprising Ni (~50 nm) and Al (~1,000 nm) were deposited through a shadow mask by e-beam evaporation. Finally, 0.16 cm^2 cells were defined by mechanical scribing on each substrate.

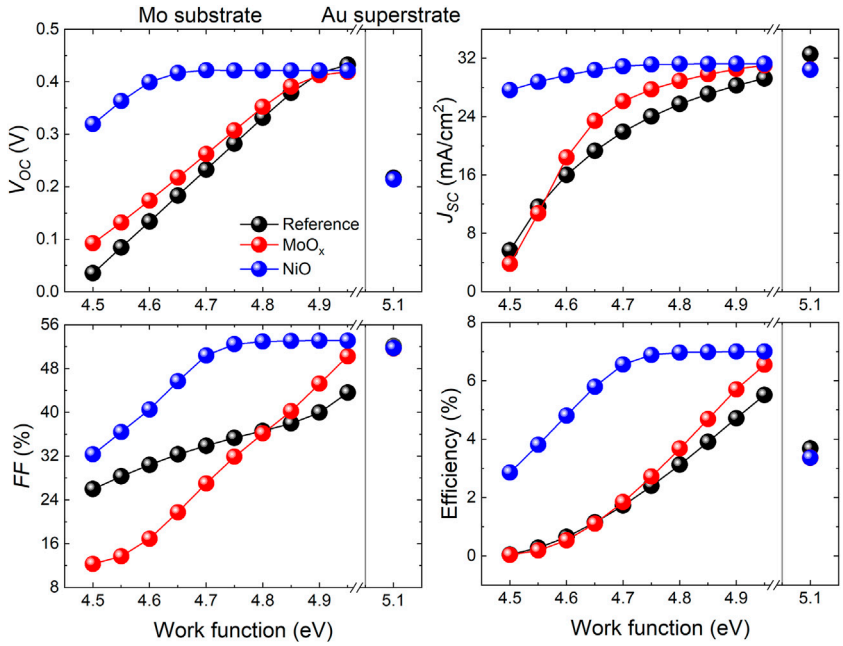

FIGURE 3
J-V parameters of simulated Sb_2Se_3 substrate devices with Mo back contact (varying Mo WF between 4.50–4.95 eV) and simulated Sb_2Se_3 superstrate devices with Au back contact (WF at 5.1 eV).

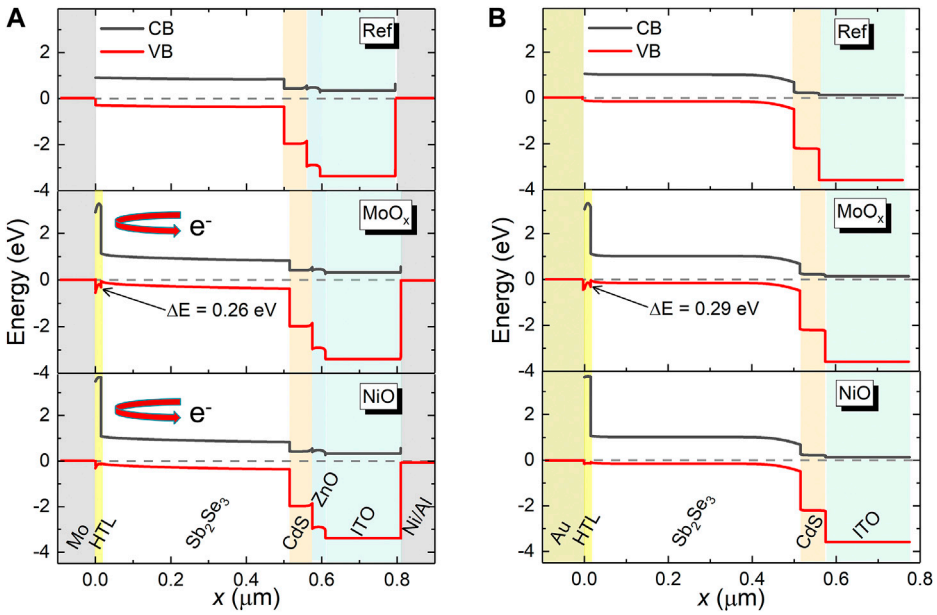

FIGURE 4
Energy level alignment for the devices in substrate **(A)** and superstrate **(B)** orientati1ons. Devices without a hole transport layer (top), with a MoO_x layer (middle) and a NiO layer (bottom) are shown.

Superstrate Sb_2Se_3 solar cells have the following configuration: SLG/ITO/CdS/Sb_2Se_3/Au with NiO or MoO_x HTLs deposited between the metal contact and Sb_2Se_3 absorber. The ITO layer was deposited by DC-pulsed sputtering and Sb_2Se_3 layers were grown by TE and CSS as detailed above. Finally, Au back contacts with an area of 0.07 cm^2 were deposited through a shadow mask by e-beam evaporation.

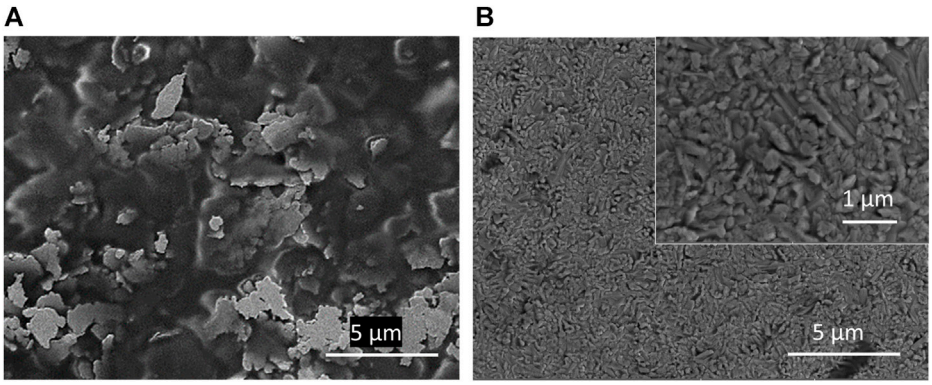

FIGURE 5
Top-down SEM image of a 100 nm **(A)** MoO_x film and **(B)** NiO films on glass. Inset: Higher magnification image of the NiO film, showing the nanostructure.

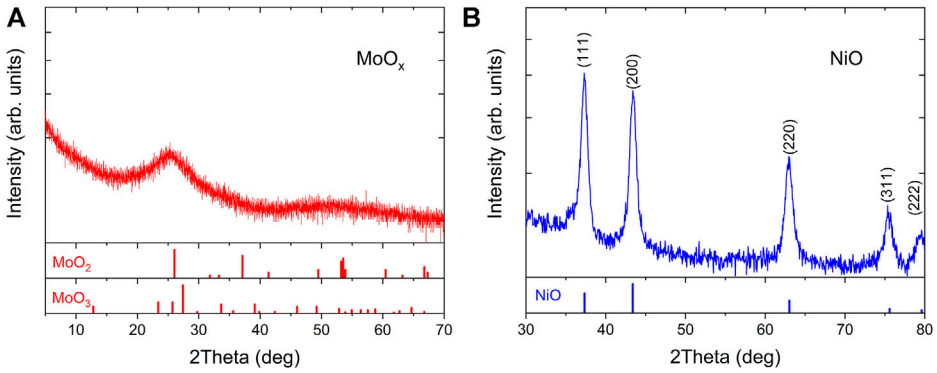

FIGURE 6
XRD pattern of 100 nm films of **(A)** MoOx and **(B)** NiO on soda lime glass (SLG). Reference XRD data for MoO_2, MoO_3 and NiO are shown underneath the XRD with JPDCS card ID 65-5787, 35-0609 and 04-0,835 respectively.

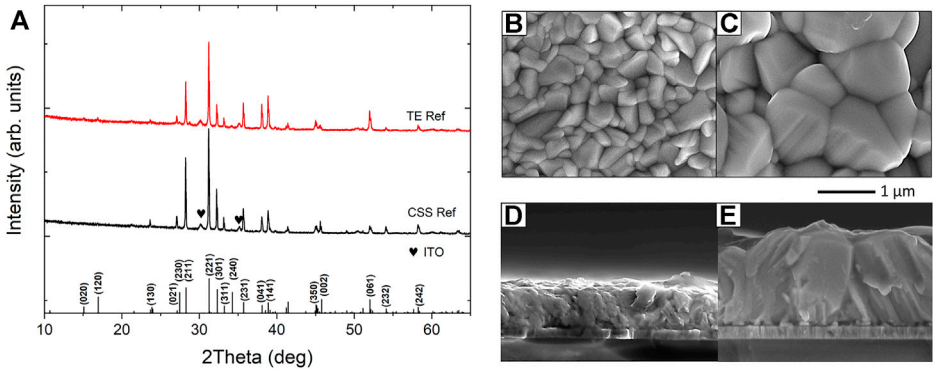

FIGURE 7
(A) XRD patterns of Sb_2Se_3 layers deposited by TE and CSS on ITO/CdS superstrates with standard diffraction pattern for Sb_2Se_3 (JCPDS15-0861) included for reference and SEM images of corresponding TE **(B,D)** and CSS **(C,E)** Sb_2Se_3 samples.

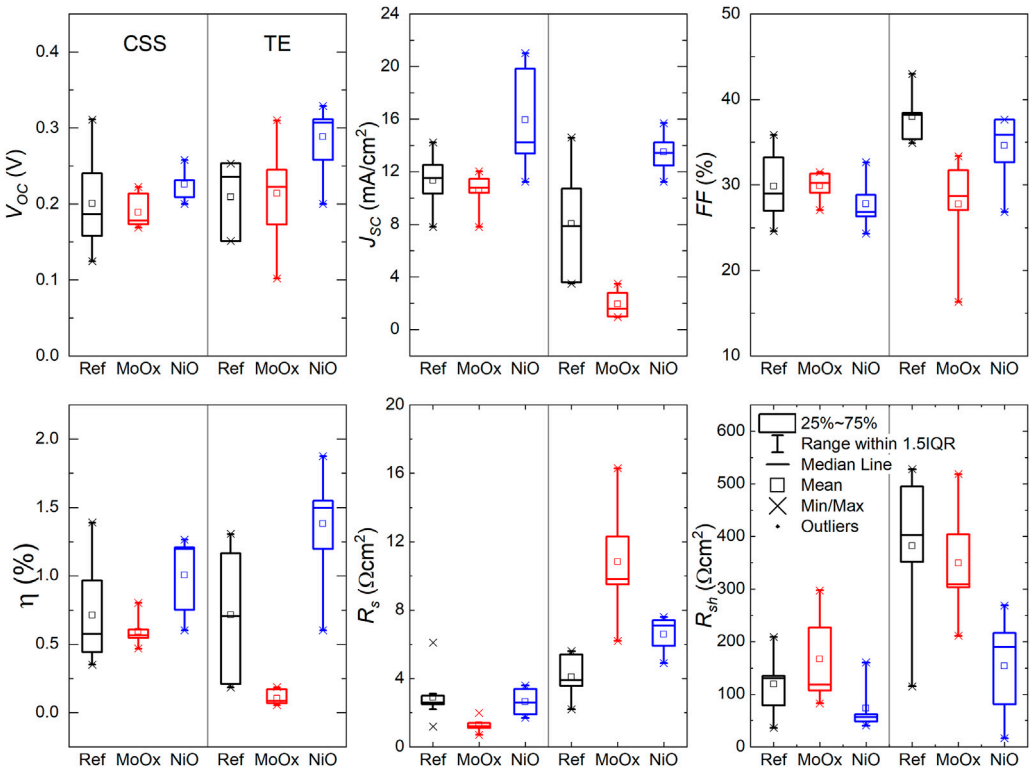

FIGURE 8
J-V parameters of superstrate TE and CSS Sb_2Se_3 devices with incorporated MoO_x and NiO HTLs. □ is the average value and × is the minimum and maximum position. The three horizontal lines of each box stand for the 25%, 50%, and 75% of the reading distribution. The whisker range is determined by the standard deviation of the sampled devices. IQR is the inter-quartile range.

2.2 Material and device characterisation

The crystal structures of Sb_2Se_3 were characterised by X-ray diffraction (XRD) with Cu Kα1 (1.54056 Å) radiation (Rigaku SmartLab SE). The surface morphology and cross-sectional images of Sb_2Se_3 films were taken by scanning electron microscopy (SEM, Tescan Mira 3 FEG-SEM). Optical spectroscopy measurements were performed using a Shimadzu UV-2600 spectrophotometer fitted with an integrating sphere. Kelvin probe force microscopy (KFPM) measurements were done using a KP Technology KP020 single point kelvin probe system fitted with a standard 2 mm Au tip.

Current-density vs. voltage (*J-V*) measurements of Sb_2Se_3 thin film solar cells were performed using an Abet Technologies solar simulator at 1-sun (100 mW/cm^2) illumination equivalent to air mass 1.5 global spectrum with light power density calibrated using a Si reference cell.

2.3 Device simulation

Device simulation was carried out for both substrate and superstrate configuration Sb_2Se_3 solar cell using Solar Cell Capacitance Simulator (SCAPS 1-D), which is based on the solutions to Poisson's equation and continuity equation for electrons and holes in the vertical heterostructure of multilayer thin film PV device (Burgelman et al., 2000). The input parameters of the solar cells were defined with the Sb_2Se_3, HTL and electron transport layer (ETL) semiconducting properties, including experimentally determined bandgaps, electron affinity, density of states (Zeng et al., 2016), mobility of charge carriers (Chen et al., 2017), acceptor/donor concentrations (Wang et al., 2015), and defect state density (Leijtens et al., 2016). Defects were introduced at the Sb_2Se_3/CdS interface to simulate realistic device performance.

3 Results and discussion

3.1 Simulated Sb_2Se_3 devices

Simulation analysis using SCAPS software was implemented to evaluate the performance of reference substrate and superstrate Sb_2Se_3 solar cells and those incorporating MoO_x and NiO as HTLs, subsequently

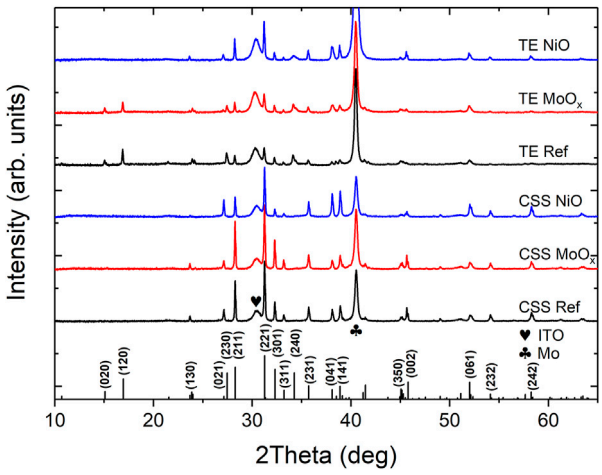

FIGURE 9
XRD patterns of Sb_2Se_3 films deposited by TE or CSS on top of NiO, MoO_x and Mo-coated SLG.

referred to as samples Ref, MoO_x and NiO, respectively (see Table 1 for film properties). Figure 2 shows the *J-V* curves and corresponding box plots of *J-V* parameters of both Sb_2Se_3 device configurations with incorporated HTLs. Regarding the substrate devices, all device parameters are improved, with the exception of V_{oc} which shows a slight decrease for devices with a HTL (down from 0.423 V for the reference device to 0.408 and 0.411 V for MoO_x and NiO devices, respectively). However, devices with MoO_x HTL show evidence of roll-over behaviour. The roll-over phenomenon, which occurs near the V_{oc} in a light *J-V* curve, is due to Schottky energy barrier formed at the absorber/metal interface at a solar cell back contact (Eisenbarth et al., 2011; Hädrich et al., 2011). It acts as a reverse biased diode when the main junction is forward biased, blocking carrier transport for increasing forward bias, resulting in roll-over behaviour in light *J-V* characteristics. The baseline J_{sc} in the reference device was 29.9 mA/cm^2, rising to 31.2 and 31.3 mA/cm^2 in MoO_x and NiO devices, respectively. Addition of HTL films to the reference device demonstrated a notable increase in *FF* for substrate devices. The *FF* in the reference device was 47.0%, rising to a maximum of 55.6% and 56.0% in the MoO_x and NiO devices, respectively. The increase in J_{sc} and *FF* of devices with integrated HTL materials directly translates into improvements in power conversion efficiency, PCE [η = 5.9% (Ref), 6.7% (MoO_x) and 7.2% (NiO)]. The current-blocking energy barrier at the back contact of the MoO_x substrate device could explain the lower PCE in comparison to the device with a NiO HTL. It is important to note that the results shown are not representative of the maximum conversion efficiencies that may be achieved with Sb_2Se_3, as we are focusing solely on the effect of the HTL, while using currently available materials parameters.

For superstrate Sb_2Se_3 solar cells, devices with an incorporated HTL showed an increase in J_{sc} of around 8% from 31.5 mA/cm^2 observed in the reference device to 33.5 and 34.0 mA/cm^2 in the devices with a MoO_x and NiO HTL, respectively. As a result of the improvement in J_{sc}, the PCE of solar cells with a HTL increased to 7.5% (MoO_x) and 8.0% (NiO) from the reference value of 7.3%. Interestingly, no roll-over was seen in the *J-V* curve for the MoO_x device which could be related to the use of Au as metallic back contact rather than Mo in the substrate devices. The work function (WF) of a metal employed as a rear contact on a PV device plays an important role in facilitating hole extraction at the contact (Fleck et al., 2020). Typically, Au is reported to have a WF of 5.10 eV (Michaelson, 1977) and Mo has WFs ranging from 4.50–4.95 eV, depending on the preferred crystal orientation of the metal (Green, 1969; Michaelson, 1977; Hölzl and Schulte, 1979). To illustrate the effect of back contact metal WF on substrate/superstrate Sb_2Se_3 device performance, Figure 3 shows the dependence of *J-V* parameters on the WF of Mo and Au metals. It is apparent that the J-V parameters of all substrate devices are sensitive to variations in the value of Mo WF. In the Ref and MoO_x substrate devices, V_{oc} decreases monotonically with Mo WF where a significant drop is observed from 0.432 V to 0.422 V at WF 4.95 eV to 0.036 V and 0.093 V at WF 4.50 eV for Ref and MoO_x devices, respectively. This is a clear indication of an increasing back contact barrier with decreasing Mo WF. This phenomenon has been observed experimentally in Sb_2Se_3 solar cells previously (Liu et al., 2014; Li et al., 2017). The V_{oc} in the NiO device is less affected by the Mo WF, reducing from 0.422 V at WF 4.95 eV to 0.319 V at WF 4.50 eV. A similar trend is seen in J_{sc}, *FF* and η parameters for the substrate devices. However, a low Mo WF of 4.50 eV causes a notable decrease in *FF* of the MoO_x device (12.3%), compared to the Ref and NiO devices (26.0% and 32.4%).

In order to understand the improvement of the device performance with the introduction of HTLs, it is necessary to consider the energy band alignment at the interfaces at the back of the PV devices. Figure 4 shows the simulated energy band diagrams of substrate and superstrate Sb_2Se_3 devices incorporating NiO and MoO_x HTLs. Due to a small electron affinity (EA = 1.46 eV (NiO), 2.05 eV (MoO_x)) and large band gaps (E_g ~3.80 eV (NiO), 3.50 eV MoO_xx)) in both HTL materials, a large potential energy barrier is formed at the back contact, reflecting electrons. This barrier minimises carrier recombination at the back interfaces with Sb_2Se_3 and improves conductivity at the back electrode. However, it is apparent that a non-negligible hole barrier of 0.26 and 0.29 eV is formed at the MoO_x/Sb_2Se_3 interface of the substrate and superstrate devices, respectively, which can manifest as *J-V* roll-over behaviour seen in the simulated MoO_x substrate device. Thus the SCAPS simulations indicate the incorporation of a MoO_x or NiO HTL into substrate and superstrate configuration Sb_2Se_3 solar cells increases device performance compared to a standard solar cell by the introduction of a high energy barrier to electrons at the rear absorber/metal interface.

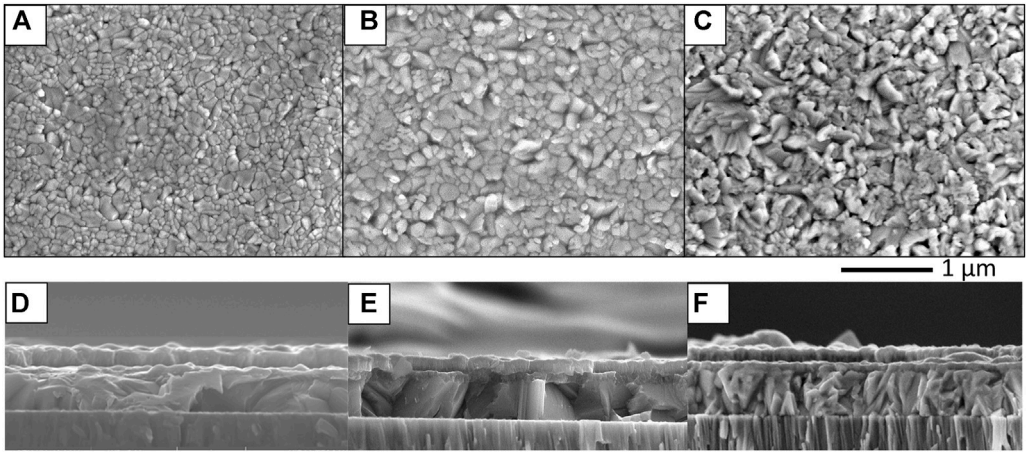

FIGURE 10
Top-down and cross-sectional SEM images of reference substrate **(A,D)**, MoO_x **(B,E)** and NiO **(C,F)** of Sb_2Se_3 films deposited by thermal evaporation.

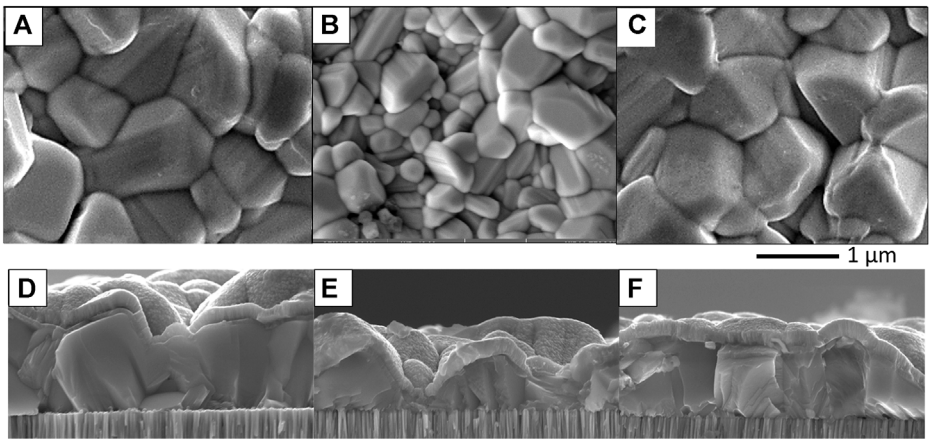

FIGURE 11
Top-down and cross-sectional SEM images of reference substrate **(A,D)**, MoO_x **(B,E)** and NiO **(C,F)** of Sb_2Se_3 films deposited by close-space sublimation.

3.2 Fabricated Sb_2Se_3 devices

100 nm thick films of MoO_x and NiO were deposited on SLG at room temperature to facilitate characterisation of the HTLs. Figure 5 shows surface morphology SEM images of the respective HTLs. The MoO_x film exhibits an amorphous, flake-like structure in comparison to a compact crystalline morphology observed in the NiO film. XRD patterns in Figure 6 confirm the amorphous and crystalline nature of the MoO_x and NiO films, respectively. All the diffraction peaks in the NiO thin film were identified and indexed to cubic NiO (JCPDS number 04-0835) and no diffraction peaks of other impurity phases were observed.

Supplementary Materials S1A shows the spectral transmittance and reflectance of the NiO and MoO_x films on SLG. Both HTLs are highly transparent in the visible and near-infrared wavelength region and their transmittance falls sharply at ultraviolet wavelengths. However, the amorphous MoO_x film has slightly lower transmittance/higher reflectance in the sub-600 nm wavelength region compared to the crystalline NiO film. The bandgap energy (E_g) of the HTL films was calculated by extrapolation of the linear region of the Tauc plot to the x-axis, according to the relation (Tauc et al., 1966):

$$(\alpha h\nu)^2 = A\left(h\nu - E_g\right) \quad (1)$$

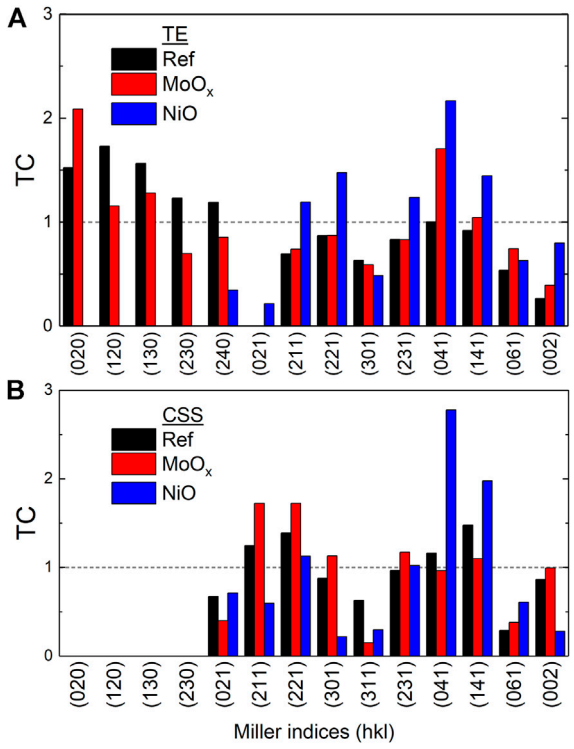

FIGURE 12
Texture coefficient analysis from XRD patterns of Sb_2Se_3 films deposited *via* TE **(A)** and CSS **(B)** with different hole transport layers in substrate configuration. A diffraction peak with a relatively large TC value (>1) indicates a preferred orientation of the grain along this direction.

where α is the absorption coefficient of the semiconductor material, h is Planck's constant, ν is the frequency of the electromagnetic radiation and A is a constant of proportionality. The estimated E_g values of NiO and MoO_x films are 3.95 and 3.85 eV, respectively (see Supplementary Materials S1B). A HTL film thickness of 15 nm was incorporated into the superstrate/substrate device to ensure a conformal coating of the HTL. A HTL requires a thickness sufficient to preserve the desired material properties and not impede charge transport considerably which would detrimentally increase series resistance in the finished devices.

3.3 Superstrate devices

TE and CSS deposition techniques were employed for Sb_2Se_3 film growth on SLG/ITO/CdS superstrates. For TE, the SLG/ITO/CdS superstrates were heated to 300°C prior to Sb_2Se_3 deposition in order to promote the growth of preferred ($hk1$) crystal orientations while minimising ($hk0$) orientations (Zhou et al., 2015) ($hk0$) planes, specifically (120), have been found to be detrimental to carrier transport (Guo et al., 2018; Wen et al., 2018; Li et al., 2019). The ($hk0$)-oriented Sb_2Se_3 nanoribbons are stacked parallel to the ITO/SLG superstrate where conductivity is inhibited by electrically insulating VdW bonds between the stacked nanoribbons. A seed layer is used in Sb_2Se_3 films deposited *via* CSS. This seed layer has a high density of nucleation points for the second stage of growth during the CSS process, which improves uniformity, raising the average efficiency of devices (Hutter et al., 2018a). Transmittance and reflectance data for a representative TE Sb_2Se_3 film was used to determine the E_g from a Tauc plot, which gave a E_g value of 1.17 eV in good agreement with (Birkett et al., 2018), see Supplementary Materials S2A,B. XRD patterns for Sb_2Se_3 films deposited by TE and CSS are shown in Figure 7A. The peaks in both XRD patterns are sharp and well resolved indicating the polycrystalline nature of the Sb_2Se_3 thin films. The lattice planes are cross-referenced to JCPDS card no. 15-0861 confirming the formation of orthorhombic Sb_2Se_3 with space group Pbnm. Both XRD patterns show similar characteristics, exhibiting strong (211) and (221) peaks with minimal contributions from ($hk0$) planes. Figures 7B–E shows the top and cross-sectional SEM images of Sb_2Se_3 thin films deposited by TE and CSS. The different growth techniques result in contrasting Sb_2Se_3 film morphologies. TE produces Sb_2Se_3 films of uniform thickness of ~500 nm and densely packed grains, confirming the good crystallinity of the films, consistent with the XRD results (Figures 7B,D). However, this deposition method did not form a conformal coating of the Sb_2Se_3 film across the entire superstrate with the presence of pinholes observed, see Supplementary Materials S3A.

Conversely, CSS-grown Sb_2Se_3 films have a rough surface morphology with exceptionally large grains in comparison to the TE films and the grains extend the full depth of the layer. Larger grains are a prerequisite for better device performance as charge mobility is faster along the Sb_2Se_3 ribbons than hopping between the ribbons (see Figures 7C,E). The CSS films also showed a degree of porosity but not to the extent observed in the TE films, Supplementary Materials S3B. The presence of pinholes in the Sb_2Se_3 films is detrimental to device performance as shunting pathways may be formed upon subsequent deposition of the Au back contact (Hutter et al., 2018b).

J-V measurements under 1-sun illumination (100 mW/cm^2) were performed on Sb_2Se_3 devices in the standard superstrate configuration and devices incorporating MoO_x and NiO HTLs. The light *J-V* curves were fitted using a single diode model to extract the values of series (R_s) and shunt (R_{sh}) resistances. Figure 8 compares the statistical distribution of the key PV parameters for these devices, where a minimum of 10 cells of each device type were measured. On average, there was a slight increase in V_{oc} when a NiO HTL was incorporated into the CSS device structure. Using a NiO HTL layer increased V_{oc} to 0.226 V from values of 0.201 and 0.186 V for Ref and MoO_x devices, respectively. The mean J_{sc} of NiO cells was also enhanced to

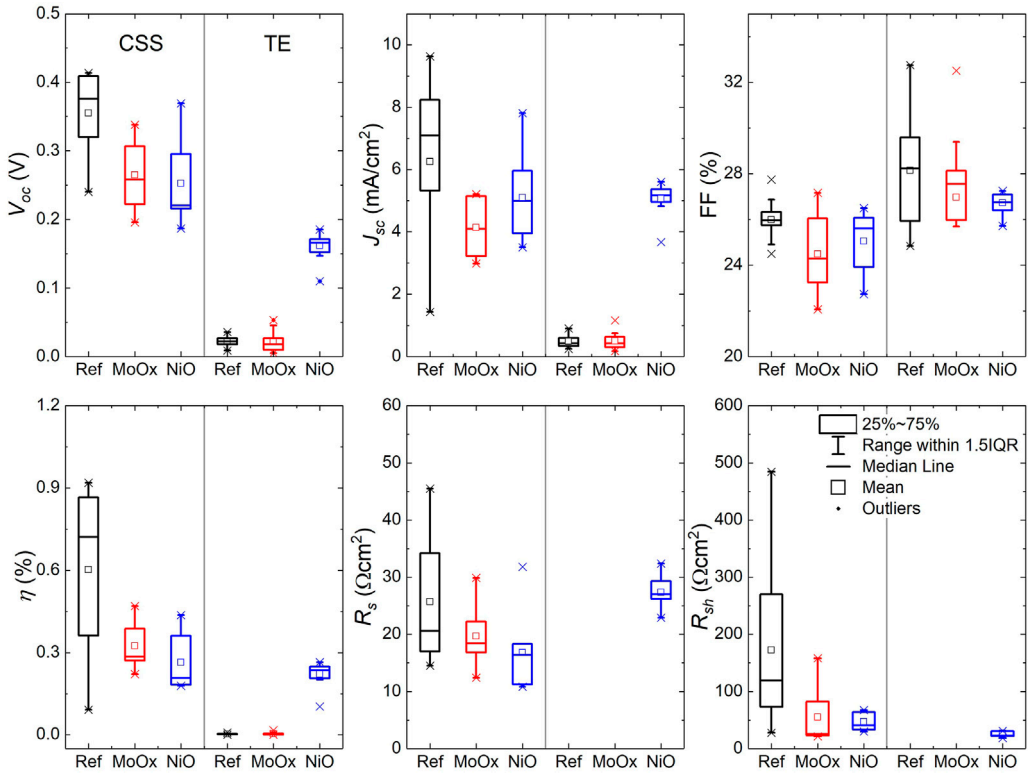

FIGURE 13
J-V parameters of substrate TE and CSS Sb_2Se_3 devices with incorporated MoO_x and NiO HTLs. □ is the average value and × is the minimum and maximum position. The three horizontal lines of each box stand for the 25%, 50% and 75% of the reading distribution. The whisker range is determined by the standard deviation of the sampled devices. IQR is the inter-quartile range.

15.94 mA/cm^2 compared to Ref (11.34 mA/cm^2) and MoO_x (10.54 mA/cm^2) cells despite a slightly lower average *FF* in the NiO devices. This translates into a higher mean NiO CSS device efficiency of 1.01% with Ref and MoO_x devices achieving efficiencies of 0.71 and 0.59% respectively. Notwithstanding the higher average R_s (2.6 Ωcm^2) and lower R_{sh} (74 Ωcm^2) values for NiO CSS solar cells compared to Ref (R_s = 2.9 Ωcm^2, R_{sh} = 119 Ωcm^2) and MoO_x (R_s = 1.3 Ωcm^2, R_{sh} = 167 Ωcm^2) cells, using NiO as a HTL increases performance by boosting J_{sc} in CSS Sb_2Se_3 superstrate devices compared to the standard and MoO_x based devices.

The average *J-V* parameters of TE Sb_2Se_3 superstrate devices followed a similar trend to those observed in the CSS devices [V_{oc}: 0.209 V (Ref) → 0.214 V (MoO_x) → 0.288 V (NiO), J_{sc}: 1.94 mA/cm^2 (MoO_x) → 8.05 mA/cm^2 (Ref) → 13.48 mA/cm^2 (NiO) ⇒ η: 0.10% (MoO_x → 0.72% (Ref) → 1.38% (NiO)]. It is worth noting that the mean *FF* of the Ref TE cells (38.0%) was higher in relation to the cells with a HTL (27.2% MoO_x, 34.6% NiO). This correlates to an increase in R_{sh} of 382 Ωcm^2 in Ref samples from R_{sh} values of 349 Ωcm^2 and 154 Ωcm^2 measured in MoO_x and NiO cells, respectively. In TE superstrate device configuration, the thin MoO_x film appears to form a more resistive layer compared to Ref and NiO devices (R_s: 10.8 Ωcm^2 MoO_x, 4.1 Ωcm^2 Ref and 6.6 Ωcm^2 NiO). Thus, overall device performance in MoO_x based solar cells is negatively impacted by low J_{sc} and high R_s which could be related to the amorphous nature of the MoO_x thin film and the presence of a current-blocking barrier at the back contact highlighted in device simulations. Despite lower *FF* in NiO based solar cells, device efficiencies exceed those of Ref and MoO_x TE devices due to improvements in V_{oc} and J_{sc} showing the benefit of using NiO as a HTL in superstrate Sb_2Se_3 solar cells.

3.4 Substrate devices

Figure 9 shows the XRD patterns of substrate Sb_2Se_3 thin films deposited *via* TE and CSS. All diffraction peaks are in good agreement with the orthorhombic Sb_2Se_3 (JCPDS 15-0861), which presents in the form of (*hk*0), (*hk*1) or (*hk*2). No diffraction peaks of other impurity phases were observed. TE Sb_2Se_3 films on Mo and Mo/MoO_x substrates show (020) and (120) peaks compared to all other Sb_2Se_3 films. The presence of (020) and (120) crystal orientations in thin Sb_2Se_3 films adversely

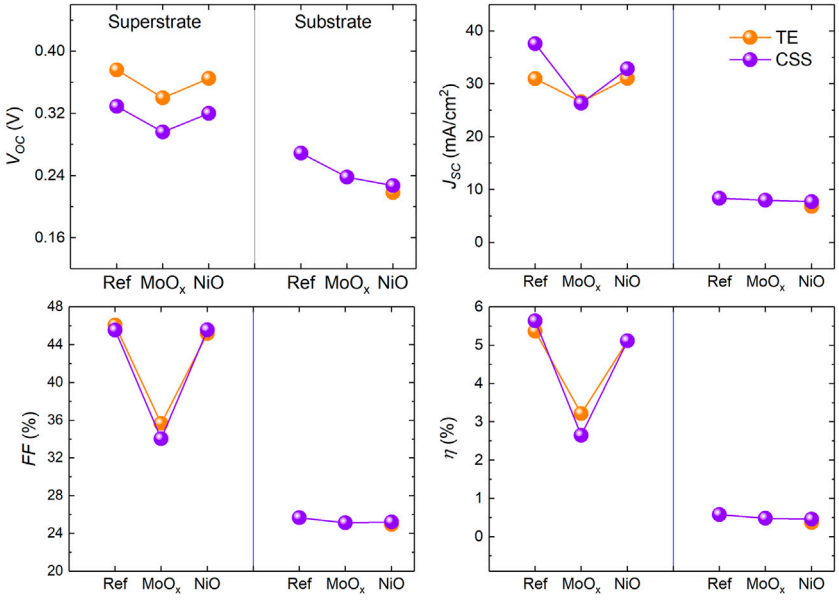

FIGURE 14
Comparison of *J-V* parameters of simulated TE and CSS Sb_2Se_3 solar cells with different HTL materials in substrate and superstrate device configurations.

affects PV device performance (Leng et al., 2014; Yuan et al., 2016; Li et al., 2017). However, when using a NiO HTL in TE Sb_2Se_3 films, it can be observed that the intensity of the diffraction peaks of Sb_2Se_3 is dominated by (221) and (211) crystal plane orientations. Furthermore, when using the Mo/NiO substrate, Sb_2Se_3 film shows an increased peak intensity for the (002) orientation. Since *h* and *k* miller indices have a zero value, it indicates that the $(Sb_4Se_6)_n$ ribbons grow perpendicular to the substrate surface (Li et al., 2019). For CSS Sb_2Se_3 films, Ref and MoO_x samples demonstrate a higher (002) peak intensity than NiO.

Figures 10, 11 show SEM images of Sb_2Se_3 films on Mo-coated SLG deposited by TE and CSS methods, respectively. The top-down SEM images of the TE films (Figures 10A–C) show a difference in morphology depending on the presence of the underlying HTL. The MoO_x sample exhibits larger Sb_2Se_3 grains than the Ref sample and the presence of pinholes in both samples is patently obvious. On the other hand, the Sb_2Se_3 grains in the NiO sample appear more angular in nature although pinholes are still present in the film. The dissimilarity in morphology is emphasised in SEM cross-section images of the TE Sb_2Se_3 films (Figures 10D–F). Voids at the absorber/Mo interface are apparent in the Ref TE sample whereas the MoO_x sample shows a homogenous film with large grains. For the NiO sample, the Sb_2Se_3 grains appear column-like with no voids at the Mo interface. The top-down SEM image of all types of CSS Sb_2Se_3 thin films (Figures 11A–C) show significantly larger grains compared to the TE films. However, Sb_2Se_3 film in the Ref sample is on average thicker (~1,000 nm) than the MoO_x (~550 nm) and NiO (~700 nm), see Figures 11D–F. The NiO sample also has a smoother surface topography.

To quantify the difference in orientations between the substrate Sb_2Se_3 thin films, the texture coefficient (TC) of diffraction peaks of the samples was calculated based on the following equation (Zoppi et al., 2006):

$$TC_{(hkl)} = \frac{\frac{I_{(hkl)}}{I_0\,(hkl)}}{\frac{1}{N}\sum_N \frac{I_{(hkl)}}{I_0\,(hkl)}} \quad (2)$$

where $I_{(hkl)}$ is the measured peak intensity of (*hkl*) plane and I_0 (*hkl*) the intensity in the standard XRD pattern. *N* is the total number of reflections considered for the calculation. A diffraction peak with a relatively large TC value (> 1) indicates a preferred orientation of the grain along this direction. Figure 12 shows the TC for Sb_2Se_3 thin films with HTLs deposited by (A) TE and (B) CSS. It is apparent from Figure 12 that NiO HTL plays a critical role in eliminating the detrimental (*hk*0) planes in the TE samples and at the same time, significantly increases absorber growth in planes, i.e., (211), (221) that are perpendicular to the substrate surface. This further supports the enhanced device performance in solar cells when NiO is used as the HTL. In CSS samples, this templating effect of HTLs is not observed as no (*hk*0) planes are grown in the Ref and MoO_x samples. MoO_x increases the growth of favoured crystal planes including (211), (221), and (002) compared to the Ref substrate sample whereas NiO appears to inhibit the growth of the preferential planes, which may be attributed to rendering the seed layer ineffective but further study will be required to fully understand the reason.

Figure 13 shows the variation in *J-V* parameters measured for a minimum batch size of 10 Sb_2Se_3 solar cells in substrate configuration deposited by TE and CSS incorporating HTLs. The use of MoO_x/NiO HTLs adversely affects all device parameters in CSS-based solar cells. This can be explained by lower average R_{sh} values of 55 Ωcm^2 and 47 Ωcm^2 determined for MoO_x and NiO device types, respectively, compared to 172 Ωcm^2 in the Ref devices. The reason for the reduction in R_{sh} of the substrate devices with a HTL is not obvious. Only working TE devices were achieved by incorporating a NiO HTL, which can be attributed to the templating effect of the NiO film which eliminated the deleterious (*hk*0) crystal planes and promoted the growth of preferred (211) and (221) planes. As highlighted in device simulations, the performance of substrate Sb_2Se_3 solar cells can be dependent on the WF of Mo back contact (see Figure 3). Mo metal typically has a WF in the range of 4.5–4.95 eV. KPFM measurements on Mo coated SLG prior to Sb_2Se_3 deposition determined the Mo WF to be 4.6 eV. According to simulations, device performance of Ref and MoO_x substrate devices is severely impacted at the observed Mo WF. Simulated NiO device performance is affected to a lesser degree.

R_s values for both TE and CSS substrate Sb_2Se_3 devices were significantly higher than their superstrate counterparts and had a detrimental effect on overall substrate device performance. This could be related to a non-optimal sputtered ITO layer in the substrate devices with a typical sheet resistance of ~ 35 Ω/□ (Qu et al., 2016) compared to commercially available ITO-coated glass slides used in superstrate devices with sheet resistances of 8–12 Ω/□ (Sigma Aldrich).

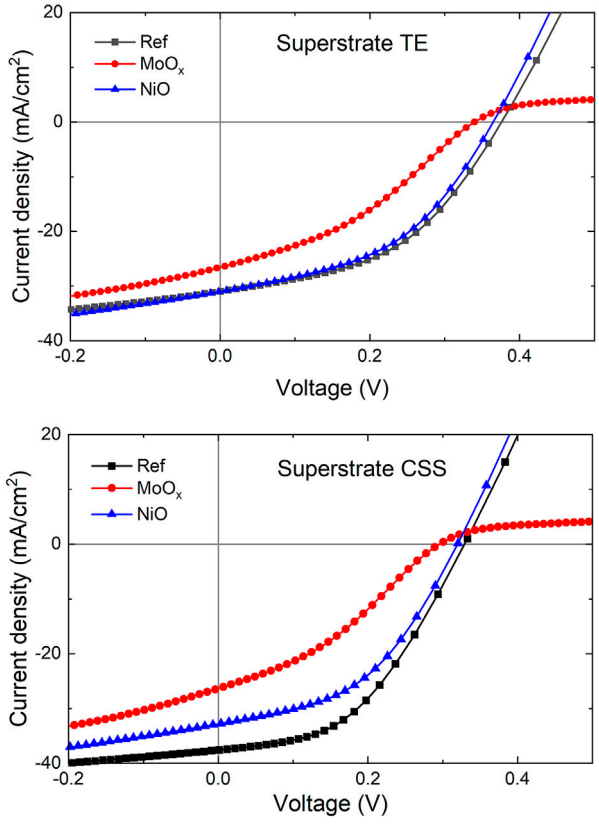

FIGURE 15
J-V curves for simulated TE and CSS Sb_2Se_3 devices with HTLs in superstrate configuration. Roll-over behaviour is evident in both TE and CSS devices with MoO_x HTL indicating a carrier transport barrier at the back contact.

3.5 Simulated and fabricated device comparison

Experimentally determined device parameters, such as R_s and R_{sh} and apparent doping density (N_A) of the Sb_2Se_3 absorber, were incorporated into SCAPS simulations of TE/CSS Sb_2Se_3 devices in superstrate/substrate configurations in order to replicate the observed behaviour of the fabricated devices. For an accurate representation of the fabricated cells, the N_A value for the Sb_2Se_3 absorber in the CSS devices was set to a value previously determined for the same CSS deposition process used in this study with a Sb_2Se_3 absorber thickness of 1 μm (Phillips et al., 2019). An experimentally determined N_A value for a typical 500 nm thick TE Sb_2Se_3 absorber was used in TE device simulations (see Table 1 for TE/CSS Sb_2Se_3 film properties). Figure 14 shows device performance of the simulated TE/CSS Sb_2Se_3 devices with experimentally determined R_s, R_{sh} and N_A values. Similar trends are observed for all device parameters of the simulated and fabricated solar cells in both device configurations indicating the simulated devices are a reasonable representation of actual Sb_2Se_3 solar cells (see Figures 8, 13). However, in superstrate configuration, simulations overestimate all *J-V* parameters, indicating factors other than R_s, R_{sh} and N_A are influencing device performance. Material properties such as carrier lifetimes, defects and band tails states have been cited as having a detrimental effect on overall device performance (Chen and Tang, 2020). In that work, a number of bulk defects in Sb_2Se_3 were identified with energy levels within the Sb_2Se_3 bandgap ranging from 0.18–0.94 eV above the valence band maximum. For simulation purposes, a mid-gap donor defect (0.62 eV) was introduced for the Sb_2Se_3 bulk to reproduce realistic device performance (Wen et al., 2018; Ma et al., 2020). Chen and Tang (2020) also highlighted significant recombination occurring at the *n-p* interface which severely impacts both V_{oc} and J_{sc}. The presence of additional Sb_2Se_3 bulk defects and increased absorber/buffer interface defect concentration could account for the differences observed between the simulated and fabricated devices studied here.

TABLE 1 Device simulation parameters, d: layer thickness, E_g: bandgap, χ: electron affinity, $\varepsilon/\varepsilon_0$: dielectric constant, $N_{C/V}$: effective density of states C: conduction band (CB) V: valence band (VB), $\mu_{e,h}$: carrier mobility, $N_{A/D}$: apparent doping density D: donor A: acceptor, $\sigma_{e,h}$: capture cross section, N_{int}: interface defect concentration, E_t: defect energy level relative to CB/VB and N_{bulk}: bulk defect concentration. Subscripts e and h are electron and hole, respectively.

Properties	MoO_x	NiO	Sb_2Se_3	CdS	*i*-ZnO	ITO
d (nm)	15	15	500 (TE). 1,000 (CSS)	70	35	200
E_g (eV)	3.85[a]	3.95[a]	1.17[a]	2.72[a]	3.37[b]	3.72[c]
χ (eV)	2.20[e]	1.46[f]	4.15[g]	4.70[c]	4.70[c]	4.50[days]
$\varepsilon/\varepsilon_0$	10.0[e]	11.9[f]	14.4[g]	9.0[b]	9.0[b]	9.4[days]
N_C (cm^{-3})	2.2×10^{18}[e]	2.2×10^{18}[f]	2.2×10^{18}[g]	2.1×10^{18}[b]	1.8×10^{19}[b]	4.0×10^{19}[c]
N_V (cm^{-3})	1.8×10^{19}[e]	1.8×10^{19}[f]	1.8×10^{19}[g]	1.7×10^{19}[b]	2.4×10^{18}[b]	1.0×10^{18}[c]
μ_e (cm^2/Vs.)	30[e]	2.8[f]	100[g]	160[b]	200[b]	30[b]
μ_h (cm^2/Vs.)	2.5[e]	2.8[f]	25[g]	15[b]	93[b]	5[b]
$N_{A/D}$ (cm^{-3})	D:3 × 10^{16}[e]	A:3 × 10^{18}[f]	A:1 × 10^{14}[h] (TE). A:1 × 10^{16}[i] (CSS)	D:1 × 10^{17}[b]	D:1 × 10^{18}[b]	D:1 × 10^{21}[b]
Defects at Sb_2Se_3/CdS interface (Gaussian distribution throughout interface)						
N_{int} (cm^{-3})			D: varied	A: varied		
σ_e (cm^2)			10^{-13}	10^{-15}		
σ_h (cm^2)			10^{-15}	10^{-13}		
Bulk Sb_2Se_3 defects (Gaussian distribution throughout bulk)						
N_{bulk} (cm^{-3})			D: 2.6 × 10^{16}[j]	A: 5.0 × 10^{15}[b]		
E_t (eV)			0.62[j]	1.20[b]		
σ_e (cm^2)			10^{-13}	10^{-17}		
σ_h (cm^2)			10^{-15}	10^{-13}		

[a]Experimentally determined from UV-VIS, measurements.
[b]Reference (Kanevce et al., 2015).
[c]Reference (Erkan et al., 2016).
[d]Reference (Kartopu et al., 2019).
[e]Reference (Ni et al., 2019).
[f]Reference (Casas et al., 2017).
[g]Reference (Maurya and Singh, 2021).
[h]Experimentally determined from capacitance-voltage *C-V* measurements.
[i]Reference (Phillips et al., 2019).
[j]Reference (Chen and Tang, 2020).

In addition, it is worth noting actual superstrate devices which incorporate a MoO_x HTL under-perform in relation to standard simulated superstrate devices (see Figure 8). This decrease in performance is not observed in the fabricated substrate Sb_2Se_3 solar cells with a MoO_x HTL. This discrepancy can be accounted for by different processing conditions applied during deposition of substrate and superstrate devices. During deposition of Sb_2Se_3 layer on SLG/Mo/HTL substrate, the substrate temperature is maintained at 300°C which is sufficient to crystallise the MoO_x film, see Supplementary Materials S4. The crystallised MoO_x film consists of a mixture of MoO_2, MoO_3 and intermediate reduced oxide phases. The phase composition affects the electronic and optical properties of the MoO_x film, with MoO_2 content lowering the resistivity, transmittance and bandgap (Inzani et al., 2017). Simulations also show a roll-over in the *J-V* curves for superstrate Sb_2Se_3 devices in both configurations (see Figure 15), indicating the presence of a barrier to carrier transport at the back contact seen in simulated energy band alignments as previously discussed (Figure 4).

4 Conclusion

Numerical simulations of standard planar superstrate and substrate Sb_2Se_3 solar cells along with the effect of incorporating MoO_x and NiO HTLs, demonstrated an increase in device efficiency for cells with a HTL which was achieved by an increase in J_{sc} for both substrate and superstrate device configurations. Both HTLs have high bandgaps and low electron affinities compared to Sb_2Se_3 absorber which manifests as a large barrier for electrons at the metallic back electrode and facilitates hole extraction. However, a roll-over effect was seen in the simulated *J-V* curve of the substrate device with MoO_x HTL, suggesting a current-blocking barrier at the back contact caused by non-optimal energy band alignment. Material characterisation of the HTL materials deposited by E-beam evaporation at room temperature revealed MoO_x formed an amorphous layer while NiO crystallised in cubic crystal orientation. 15 nm thick HTLs were incorporated into superstrate/substrate solar cells with

Sb_2Se_3 absorbers deposited by thermal evaporation and close-space sublimation. For CSS superstrate solar cells with NiO HTL, device efficiency was enhanced by a 40% increase in J_{sc} compared to reference and MoO_x based devices. TE superstrate cells incorporating NiO as HTL also demonstrated improved efficiencies achieved by higher V_{oc} and J_{sc}. In the superstrate TE cells with MoO_x HTL, J_{sc} was severely inhibited which is attributed to MoO_x forming a more resistive layer due to its amorphous nature. Conversely, the presence of a MoO_x or NiO HTL in substrate CSS-deposited Sb_2Se_3 solar cells reduced device performance which is linked to lower average R_{sh} observed in these cells. Optimisation of HTL thickness and/or re-optimisation of the absorber deposition could potentially alleviate this issue. Simulations reveal a connection between the WF of the Mo metal back contact and substrate device performance. For an experimentally determined Mo WF of 4.6 eV, all device *J-V* characteristics are significantly reduced, whereas substrate devices with NiO HTL are only marginally affected. In addition, XRD analysis of TE Sb_2Se_3 films with NiO HTL revealed a templating effect on Sb_2Se_3 crystal orientation where detrimental (020)/(120) crystal planes were eliminated and preferred (211)/(221) planes increased in intensity which resulted in increased device performance of substrate Sb_2Se_3 solar cells. NiO shows more promise as a HTL in Sb_2Se_3 PV devices, and crucially can act as a templating layer when the Sb_2Se_3 deposition method does not already impart the desired structure, as is often the case with TE devices.

Data availability statement

Data is available *via* this link: https://figshare.com/projects/Routes_to_Increase_Performance_for_Antimony_Selenide_Solar_Cells_using_Inorganic_Hole_Transport_Layers/140140.

Author contributions

SC, RV, LP, and JM fabricated absorbers and solar cells, SC conducted material and device characterisation, data analysis and device simulations. SC wrote the manuscript with contribution from OH. OH, YQ, VB, NB, and GZ discussed results and contributed to manuscript mofification and finalisation. VB and YQ supervised the project.

Acknowledgments

The authors acknowledge the EPSRC Centre for Doctoral Training in Renewable Energy Northeast Universities (ReNU) for funding through grant EP/S023836/1. The authors also appreciate the support from North East Centre for Energy Materials (NECEM) (EP/R021503/1) and British Council Newton Fund Institutional Links Grant in Ultralight Absorber for Remote Energy Source (U-AREs, No. 623804307). Discussions regarding NiO thin film deposition with Prof. Elizabeth Gibson, School of Natural and Environmental Sciences, Newcastle University is acknowledged.

Conflict of interest

The authors declare that the research was conducted in the absence of any commercial or financial relationships that could be construed as a potential conflict of interest.

Publisher's note

Supplementary material

The Supplementary Material for this article can be found online at: https://www.frontiersin.org/articles/10.3389/fchem.2022.954588/full#supplementary-material

References

Birkett, M., Linhart, W. M., Stoner, J., Phillips, L. J., Durose, K., Alaria, J., et al. (2018). Band gap temperature-dependence of close-space sublimation grown Sb_2Se_3 by photo-reflectance. *Apl. Mater.* 6, 084901. doi:10.1063/1.5027157

Black, J., Conwell, E., Seigle, L., and Spencer, C. (1957). Electrical and optical properties of some M2v–bN3vi–b semiconductors semiconductors. *J. Phys. Chem. Solids* 2, 240–251. doi:10.1016/0022-3697(57)90090-2

Burgelman, M., Nollet, P., and Degrave, S. (2000). Modelling polycrystalline semiconductor solar cells. *Thin Solid Films* 361-362, 527–532. doi:10.1016/S0040-6090(99)00825-1

Casas, G., Cappelletti, M., Cédola, A., Soucase, B. M., and Peltzer y Blancá, E. (2017). Analysis of the power conversion efficiency of perovskite solar cells with different materials as Hole-Transport Layer by numerical simulations. *Superlattices Microstruct.* 107, 136–143. doi:10.1016/j.spmi.2017.04.007

Chen, C., Bobela, D. C., Yang, Y., Lu, S., Zeng, K., Ge, C., et al. (2017). Characterization of basic physical properties of Sb_2Se_3 and its relevance for photovoltaics. *Front. Optoelectron.* 10, 18–30. doi:10.1007/s12200-017-0702-z

Chen, C., Li, W., Zhou, Y., Chen, C., Luo, M., Liu, X., et al. (2015). Optical properties of amorphous and polycrystalline Sb_2Se_3 thin films prepared by thermal evaporation. *Appl. Phys. Lett.* 107, 043905. doi:10.1063/1.4927741

Chen, C., and Tang, J. (2020). Open-circuit voltage loss of antimony chalcogenide solar cells: Status, origin, and possible solutions. *ACS Energy Lett.* 5, 2294–2304. doi:10.1021/acsenergylett.0c00940

Deringer, V. L., Stoffel, R. P., Wuttig, M., and Dronskowski, R. (2015). Vibrational properties and bonding nature of Sb_2Se_3 and their implications for chalcogenide materials. *Chem. Sci.* 6, 5255–5262. doi:10.1039/C5SC00825E

Eisenbarth, T., Caballero, R., Nichterwitz, M., Kaufmann, C. A., Schock, H.-W., and Unold, T. (2011). Characterization of metastabilities in Cu(In, Ga)Se_2 thin-film solar cells by capacitance and current-voltage spectroscopy. *J. Appl. Phys.* 110, 094506. doi:10.1063/1.3656453

Erkan, M. E., Chawla, V., and Scarpulla, M. A. (2016). Reduced defect density at the CZTSSe/CdS interface by atomic layer deposition of Al_2O_3. *J. Appl. Phys.* 119, 194504. doi:10.1063/1.4948947

Fleck, N., Hutter, O. S., Phillips, L. J., Shiel, H., Hobson, T. D. C., Dhanak, V. R., et al. (2020). How oxygen exposure improves the back contact and performance of antimony selenide solar cells. *ACS Appl. Mat. Interfaces* 12, 52595–52602. doi:10.1021/acsami.0c14256

Green, M. (1969). Solid state surface science volume 1. *J. Macromol. Sci. Part B* 3, 366. doi:10.1080/00222346908205102

Guo, L., Zhang, B., Qin, Y., Li, D., Li, L., Qian, X., et al. (2018). Tunable quasi-one-dimensional ribbon enhanced light absorption in Sb_2Se_3 thin-film solar cells grown by close-space sublimation. *Sol. RRL* 2, 1800128. doi:10.1002/solr.201800128

Hädrich, M., Heisler, C., Reislöhner, U., Kraft, C., and Metzner, H. (2011). Back contact formation in thin cadmium telluride solar cells. *Thin Solid Films* 519, 7156–7159. doi:10.1016/j.tsf.2010.12.144

Hölzl, J., and Schulte, F. K. (1979). "Work function of metals," in *Solid surface physics*. 2nd Edn, Editor J. Hölzl, F.K. Schulte, and H. Wagner (Berlin, Heidelberg: Springer), vol. 85, 1–150.

Hutter, O. S., Phillips, L. J., Durose, K., and Major, J. D. (2018a). 6.6% efficient antimony selenide solar cells using grain structure control and an organic contact layer. *Sol. Energy Mater. Sol. Cells* 188, 177–181. doi:10.1016/j.solmat.2018.09.004

Hutter, O. S., Phillips, L. J., Yates, P. J., Major, J. D., and Durose, K. (2018b). "CSS antimony selenide film morphology and high efficiency PV devices," in 2018 IEEE 7th World Conference on Photovoltaic Energy Conversion (WCPEC)(A Joint Conference of 45th IEEE PVSC, 28th PVSEC & 34th EU PVSEC) (IEEE).

Inzani, K., Nematollahi, M., Vullum-Bruer, F., Grande, T., Reenaas, T. W., and Selbach, S. M. (2017). Electronic properties of reduced molybdenum oxides. *Phys. Chem. Chem. Phys.* 19, 9232–9245. doi:10.1039/C7CP00644F

Kanevce, A., Repins, I., and Wei, S.-H. (2015). Impact of bulk properties and local secondary phases on the $Cu_2(Zn, Sn)Se_4$ solar cells open-circuit voltage. *Sol. Energy Mater. Sol. Cells* 133, 119–125. doi:10.1016/j.solmat.2014.10.042

Kartopu, G., Williams, B., Zardetto, V., Gürlek, A., Clayton, A., Jones, S., et al. (2019). Enhancement of the photocurrent and efficiency of CdTe solar cells suppressing the front contact reflection using a highly-resistive ZnO buffer layer. *Sol. Energy Mater. Sol. Cells* 191, 78–82. doi:10.1016/j.solmat.2018.11.002

Leijtens, T., Eperon, G. E., Barker, A. J., Grancini, G., Zhang, W., Ball, J. M., et al. (2016). Carrier trapping and recombination: The role of defect physics in enhancing the open circuit voltage of metal halide perovskite solar cells. *Energy Environ. Sci.* 9, 3472–3481. doi:10.1039/c6ee01729k

Leng, M., Luo, M., Chen, C., Qin, S., Chen, J., Zhong, J., et al. (2014). Selenization of Sb_2Se_3 absorber layer: An efficient step to improve device performance of CdS/Sb_2Se_3 solar cells. *Appl. Phys. Lett.* 105, 083905. doi:10.1063/1.4894170

Li, Z., Chen, X., Zhu, H., Chen, J., Guo, Y., Zhang, C., et al. (2017). Sb_2Se_3 thin film solar cells in substrate configuration and the back contact selenization. *Sol. Energy Mater. Sol. Cells* 161, 190–196. doi:10.1016/j.solmat.2016.11.033

Li, Z., Liang, X., Li, G., Liu, H., Zhang, H., Guo, J., et al. (2019). 9.2%-efficient core-shell structured antimony selenide nanorod array solar cells. *Nat. Commun.* 10, 125. doi:10.1038/s41467-018-07903-6

Liu, X., Chen, J., Luo, M., Leng, M., Xia, Z., Zhou, Y., et al. (2014). Thermal evaporation and characterization of Sb_2Se_3 thin film for substrate Sb_2Se_3/CdS solar cells. *ACS Appl. Mat. Interfaces* 6, 10687–10695. doi:10.1021/am502427s

Ma, Y., Tang, B., Lian, W., Wu, C., Wang, X., Ju, H., et al. (2020). Efficient defect passivation of Sb_2Se_3 film by tellurium doping for high performance solar cells. *J. Mat. Chem. A* 8, 6510–6516. doi:10.1039/D0TA00443J

Maurya, K., and Singh, V. (2021). Sb_2Se_3 versus Sb_2S_3 solar cell: A numerical simulation. *Sol. Energy* 228, 540–549. doi:10.1016/j.solener.2021.09.080

Michaelson, H. B. (1977). The work function of the elements and its periodicity. *J. Appl. Phys.* 48, 4729–4733. doi:10.1063/1.323539

Ni, M., Liu, J.-M., Li, Z.-Q., Shen, Q., Feng, Y.-Z., and Feng, X.-D. (2019). Simulation of graded bandgap on backwall superstrate CIGS solar cells with MoO_x electron reflection layer. *Mat. Res. Express* 6, 116441. doi:10.1088/2053-1591/ab4c5c

Phillips, L. J., Savory, C. N., Hutter, O. S., Yates, P. J., Shiel, H., Mariotti, S., et al. (2019). Current enhancement via a TiO_2 window layer for CSS Sb_2Se_3 solar cells: Performance limits and high V_{oc}. *IEEE J. Photovolt.* 9, 544–551. doi:10.1109/jphotov.2018.2885836

Qu, Y., Zoppi, G., and Beattie, N. S. (2016). The role of nanoparticle inks in determining the performance of solution processed $Cu_2ZnSn(S, Se)_4$ thin film solar cells. *Prog. Photovolt. Res. Appl.* 24, 836–845. doi:10.1002/pip.2756

Tauc, J., Grigorovici, R., and Vancu, A. (1966). Optical properties and electronic structure of amorphous germanium. *Phys. Stat. Sol.* 15, 627–637. doi:10.1002/pssb.19660150224

Wang, L., Li, D.-B., Li, K., Chen, C., Deng, H.-X., Gao, L., et al. (2017). Stable 6%-efficient Sb_2Se_3 solar cells with a ZnO buffer layer. *Nat. Energy* 2, 17046. doi:10.1038/nenergy.2017.46

Wang, Y., Xia, Z., Liang, J., Wang, X., Liu, Y., Liu, C., et al. (2015). Towards printed perovskite solar cells with cuprous oxide hole transporting layers: A theoretical design. *Semicond. Sci. Technol.* 30, 054004. doi:10.1088/0268-1242/30/5/054004

Wen, X., Chen, C., Lu, S., Li, K., Kondrotas, R., Zhao, Y., et al. (2018). Vapor transport deposition of antimony selenide thin film solar cells with 7.6% efficiency. *Nat. Commun.* 9, 2179. doi:10.1038/s41467-018-04634-6

Williams, R. E., Ramasse, Q. M., McKenna, K. P., Phillips, L. J., Yates, P. J., Hutter, O. S., et al. (2020). Evidence for self-healing benign grain boundaries and a highly defective Sb_2Se_3–cds interfacial layer in Sb_2Se_3 thin-film photovoltaics. *ACS Appl. Mat. Interfaces* 12, 21730–21738. PMID: 32314567. doi:10.1021/acsami.0c03690

Yuan, C., Zhang, L., Liu, W., and Zhu, C. (2016). Rapid thermal process to fabricate Sb_2Se_3 thin film for solar cell application. *Sol. Energy* 137, 256–260. doi:10.1016/j.solener.2016.08.020

Zeng, K., Xue, D.-J., and Tang, J. (2016). Antimony selenide thin-film solar cells. *Semicond. Sci. Technol.* 31, 063001. doi:10.1088/0268-1242/31/6/063001

Zhou, Y., Wang, L., Chen, S., Qin, S., Liu, X., Chen, J., et al. (2015). Thin-film Sb_2Se_3 photovoltaics with oriented one-dimensional ribbons and benign grain boundaries. *Nat. Photonics* 9, 409–415. doi:10.1038/nphoton.2015.78

Zoppi, G., Durose, K., Irvine, S. J. C., and Barrioz, V. (2006). Grain and crystal texture properties of absorber layers in MOCVD-grown CdTe/CdS solar cells. *Semicond. Sci. Technol.* 21, 763–770. doi:10.1088/0268-1242/21/6/009

Frontiers in Chemistry

Explores all fields of chemical science across the periodic table

Advances our understanding of how atoms, ions, and molecules come together and come apart. It explores the role of chemistry in our everyday lives - from electronic devices to health and wellbeing.

Discover the latest Research Topics

See more →

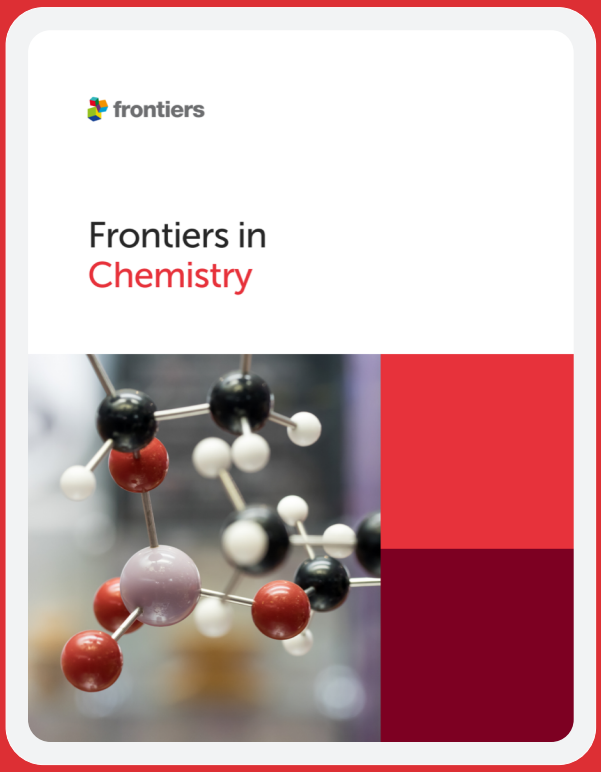

Frontiers

Avenue du Tribunal-Fédéral 34
1005 Lausanne, Switzerland
frontiersin.org

Contact us

+41 (0)21 510 17 00
frontiersin.org/about/contact